SHOCK ATTENUATION IN TWO-PHASE (GAS-LIQUID) JETS FOR INERTIAL FUSION APPLICATIONS

A Thesis
Presented to
The Academic Faculty

by

Céline C. Lascar

In Partial Fulfillment
of the Requirements for the Degree
Doctor of Philosophy in the
School of Mechanical Engineering

Georgia Institute of Technology
December 2007

SHOCK ATTENUATION IN TWO-PHASE (GAS-LIQUID) JETS FOR INERTIAL FUSION APPLICATIONS

Approved by:

Professor Said I. Abdel-Khalik,
Committee Chair
School of Mechanical Engineering
Georgia Institute of Technology

Professor Cyrus K. Aidun
School of Mechanical Engineering
Georgia Institute of Technology

Professor S. Mostafa Ghiaasiaan
School of Mechanical Engineering
Georgia Institute of Technology

Professor Daniel W. Tedder
School of Chemical and Biomolecular Engineering
Georgia Institute of Technology

Professor Donald R. Webster
School of Civil Engineering
Georgia Institute of Technology

Date Approved: 20 August 2007

À mon Chéri, qui se reconnaîtra.

Merci pour ton amour.

ACKNOWLEDGEMENTS

The successful completion of this thesis would not have been possible without the support and the guidance of many individuals. Foremost, I would like to thank my advisor and committee chairman, Dr. Said I. Abdel-Khalik. His invaluable advice and support throughout these past three years are greatly appreciated. I would also like to thank the additional members of my thesis committee, Dr. Cyrus K. Aidun, Dr. S. Mostafa Ghiaasiaan, Dr. Daniel W. Tedder, and Dr. Donald Webster for their recommendations and support.

A special thanks is due to Mr. Dennis L. Sadowski for his efforts in this project. I am very grateful for his inexhaustible efforts in the design, construction, and operation of the experimental apparatus. I would also like to thank my laboratory colleagues whose support and camaraderie have been indispensable: Tim Koehler, Lorenzo Crosatti, Dr. Sam Durbin, Brandon Weathers, Chad Dillon, Tony Jones, Joseph Hu, Bo Lu and Dr. Vladimir Novak.

Most importantly, I wish to express my deepest appreciation to my parents, Catherine and Jean-Luc, my grand-mother, Gigi, and my brother, Guillaume, without whom all my achievements would have been impossible. I would especially like to thank Lee for his support, patience, and understanding.

TABLE OF CONTENTS

LIST OF TABLES

LIST OF FIGURES

NOMENCLATURE

α	void fraction [-]
α_C	average one-dimensional homogeneous void fraction across the container [-]
α_e	average one-dimensional homogeneous void fraction of the jet at the nozzle exit [-] or [%]
α_{jet}	measured average one-dimensional homogeneous void fraction of the jet [-]
β	homogeneous equilibrium void fraction [-]
δ	measured jet thickness [m]
δ_C	inner length of the container cross section for void fraction measurements [m]
δ_{CLT}	jet collapsed liquid thickness [m]
δ_e	length of the exit cross section for the planar nozzle [m]
δ_i	length of the inlet cross section for the planar nozzle [m]
δ_{jet}	actual jet measured thickness [m]
γ	specific heat ratio [-]
μ	mean two-phase dynamic viscosity [N.s/m^2]
μ_l	liquid dynamic viscosity [N.s/m^2]
ν_l	liquid kinematic viscosity [m^2/s]
ϕ^2	two-phase friction multiplier [-]
$\varphi_{e,i}$	inner diameter of the exit cross section for the annular nozzle [m]

$\varphi_{e,o}$ outer diameter of the exit cross section for the annular nozzle [m]

ϕ_e diameter of the exit cross section for the circular nozzle [m]

ϕ_i diameter of the inlet cross section for the circular nozzle [m]

ρ_g gas density [kg/m^3]

ρ_l liquid density [kg/m^3]

σ surface tension between the liquid and the gas [N/m] or sample standard deviation

C_0 distribution parameter for the Drift Flux Model [-]

C_D drag coefficient [-]

$d_{b,max}$ maximum axe of a bubble approximated by a spheroid [m]

$d_{b,min}$ minimum axe of a bubble approximated by a spheroid [m]

$d_{b,s}$ equivalent spherical bubble diameter [m]

D_{bubble} bubble diameter [m]

$D_{d,max}$ maximum distorted bubble limit [m]

$D_{h,planar}$ hydraulic diameter of the planar nozzle [m]

$D_{Laplace}$ Laplace length scale [m]

d_{Sauter} Sauter mean bubble diameter [m]

f_{TP} friction factor for two-phase flow [-]

Fr_g gas Froude number at the nozzle exit, defined in Equation 4.12 [-]

Fr_l liquid Froude number at the nozzle exit, defined in Equation 4.8 [-]

G mass flux [kg/s.m^2]

g gravitational acceleration [m/s^2]

h_C inner height of the container for void fraction measurements [m]

I absorption of a collimated beam [photons$\cdot m^{-2} \cdot s$]

I_0 initial intensity of a collimated beam [photons$\cdot m^{-2} \cdot s$]

$I_{2-phase}$ absorption of a collimated beam through a two-phase flow [photons$\cdot m^{-2} \cdot s$]

$I_{g,avg}$ averaged absorption of a collimated beam through a gas [photons$\cdot m^{-2} \cdot s$]

I_g absorption of a collimated beam through a gas [photons$\cdot m^{-2} \cdot s$]

$I_{l,avg}$ averaged absorption of a collimated beam through a liquid [photons$\cdot m^{-2} \cdot s$]

I_l absorption of a collimated beam through a liquid [photons$\cdot m^{-2} \cdot s$]

$j_{g,e}$ gas superficial velocity at the nozzle exit [m/s]

j_g gas superficial velocity [m/s]

j_{gj} drift flux [m/s]

$j_{l,e}$ liquid superficial velocity at the nozzle exit [m/s]

$j_{l,h}$ liquid superficial velocity within the honeycomb section [m/s]

j_l liquid superficial velocity [m/s]

k_c multiplier computed from an appropriate distribution such that 95% of the data should fall within statistical fluctuations [-]

L distance between the exploding wire mid-point and the transducer location [m]

$L_{j,1}$ left-handed distance from the screw head to the side of the jet thickness tester when the jet is on [m]

$L_{j,2}$ right-handed distance from the screw head to the side of the jet thickness tester when the jet is on [m]

$L_{s,1}$ left-handed distance from the screw head to the side of the jet thickness tester when the jet is off [m]

$L_{s,2}$ right-handed distance from the screw head to the side of the jet thickness tester when the jet is off [m]

M Mach number, defined in Equation 4.50 [-]

$\dot{m}_g$ gas mass flow rate [kg/s]

$\dot{m}_l$ liquid mass flow rate [kg/s]

P_{atm} atmospheric pressure [psig]

P_M pressure at the pressure gauge (M), referring to Figure 3.1 [psig]

R_{air} gas constant for air [-]

Re_l liquid Reynolds number at the nozzle exit, defined in Equation 4.6 [-]

S slip ratio [-]

Su_l liquid Suratman number at the nozzle exit, defined in Equation 4.13 [-]

T gas temperature [^{o}C]

t time between pulser trigger and arrival of first peak at the transducer location [s]

U uncertainty

U_A imprecision, due to statistical fluctuations

U_B inaccuracy, due to the inaccuracy of the instrumentation

U_C total uncertainty, calculated using the rule for combining uncertainties

U_g gas phase velocity [m/s]

U_l liquid phase velocity [m/s]

U_{rise} bubble rise velocity, defined in Equation 4.47 [m/s]

$\dot{V}_{g,e}$ gas volume flow rate at the nozzle exit $[m^3/s]$

$\dot{V}_{g,P_M}$ gas flow rate at pressure P_M [l/min]

V_{gj} effective drift velocity of the gas [m/s]

$\dot{V}_{l,e}$ liquid volume flow rate at the nozzle exit $[m^3/s]$

w measured jet width [m]

w_C inner width of the container cross section for void fraction measurements [m]

w_e width of the exit cross section for the planar nozzle [m]

w_i width of the inlet cross section for the planar nozzle [m]

We_l liquid Weber number at the nozzle exit, defined in Equation 4.7 [-]

x quality [-] or x-coordinate, streamwise flow direction [m]

y y-coordinate [m]

z z-coordinate [m]

SUMMARY

Z-Pinch IFE (Inertial Fusion Energy) reactor designs will likely utilize high yield targets ($\sim$ 3 GJ) at low repetition rates ($\sim$ 0.1 Hz). Appropriately arranged thick liquid jets can adequately protect the cavity walls from the target X-rays, ions, and neutrons. However, the shock waves and mechanical loadings produced by rapid heating and evaporation of incompressible liquid jets may be challenging to accommodate within a small reactor cavity. This investigation examines the possibility of using two-phase compressible (liquid/gas) jets to protect the cavity walls in high yield IFE systems, thereby mitigating the mechanical consequences of rapid energy deposition within the jets.

Two-phase, free, vertical jets with different cross sections (planar, circular, and annular) were examined over wide ranges of liquid velocities and void fractions. The void fraction and bubble size distributions within the jets were measured; correlations to predict variations of the slip ratio and the Sauter mean diameter were developed. An exploding wire system was used to generate a shock wave at the center of the annular jets. Attenuation of the shock by the surrounding single- or two-phase medium was measured. The results show that stable coherent jets can be established and steadily maintained over a wide range of inlet void fractions and liquid velocities, and that significant attenuation in shock strength can be attained with relatively modest void fractions ($\sim$ 1%); the compressible two-phase jets effectively convert and dissipate mechanical energy into thermal energy within the gas bubbles. The experimental characteristics of single- and two-phase jets were compared against predictions of a state-of-art CFD code ($FLUENT$®). The data obtained in this investigation will allow reactor system designers to predict the behavior of single- and two-phase jets

and quantify their effectiveness in mitigating the consequences of shock waves on the cavity walls in high yield IFE systems.

CHAPTER I

INTRODUCTION

Nuclear fusion holds the promise of becoming a significant future energy source with several highly desirable characteristics:

- *A Virtually Inexhaustible Fuel Supply.*

  The basic fuels for fusion are deuterium and tritium. Both deuterium and lithium, from which tritium can be generated, are plentifully and inexpensively available.

- *Minimal Environmental Impact.*

  Fusion does not yield greenhouse gases or other significant effluents that threaten environmental harm. Compared to other competitive energy sources, fusion energy does not produce air pollution and carbon dioxide emissions like fossil fuel combustion or emissions from the production of large quantities of concrete, steel, glass, and other materials to collect dilute solar energy. Unlike some solar and wind technologies, fusion energy would make minimal demands on land use.

  Moreover, the fusion fuel cycle does not involve any input of radioactive material and does not generate radioactive waste directly. Radioactivity is present in the form of the intermediate fuel, tritium, and as radioactivity generated in structural materials by the absorption of neutrons. Suitable choices of design and materials can reduce the radioactivity to achieve low hazard potential. Radioactive wastes from the operation of a fusion plant should not require isolation from the environment for a geological timespan and therefore should

not constitute a burden for future generations.

- *Safety.*

  The stored fuel energy contained in the reactor would likely be equivalent to only fractions of a second in the case of inertial fusion energy. Therefore, the worst possible accidents would not threaten wide-ranging impact or constitute any major hazard to populations outside the plant perimeter that might result in evacuation.

Nevertheless, there remain significant barriers to the realization of fusion as a significant contributor to the world's energy supply. Progress requires advancing fundamental scientific knowledge (e.g., enhancing target design to increase the fusion energy gain), resolving very difficult materials issues (e.g., developing a vessel that can withstand high temperatures and intense neutron flux), finding answers to difficult engineering challenges (e.g., constructing a reliable and repairable system), and proving economic feasibility.

1.1 Energy from Fusion

During the twentieth century, scientists discovered that fusion is the process that powers the sun and the stars. While nuclear fission obtains energy by splitting large heavy atoms, nuclear fusion produces energy by "joining" together small light atoms. The concept behind any fusion reaction is to bring the reactive atoms close enough that the strong nuclear force in their nuclei will turn them together into a larger atom. If two light nuclei fuse, they will generally form a single nucleus with a slightly smaller mass than the sum of their original masses. The difference in mass is released as energy according to Einstein's equation $E = m \cdot c^2$. In order to bring the atoms close enough to fuse despite their mutual electrostatic repulsion, also called "Coulomb barrier", some external source of energy must be supplied. The easiest way to do this is to heat and pressurize the atoms at very high temperatures (100 million degrees

Celsius or more) and high pressures. This is known as the Lawson's Criterion. At such high temperatures, all the electrons of light atoms become separated from the nuclei, in a process of separation called ionization. The hot gas containing negatively charged free electrons and positively charged nuclei or ions is known as a plasma (see Figure 1.1). If this plasma is held together (i.e., confined) long enough, the sheer number of fusion reactions may produce more energy than what is required to heat the gas, generating excess energy that can be used for other applications.(Wikipedia, 2007; Nuttall, 2005)

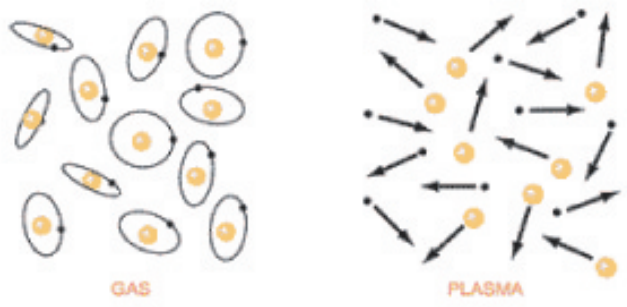

Figure 1.1: Plasma illustration (from `http://www.pppl.gov/fusion_basics/pages/fusion_conditions.html`)

The sun confines its hot plasma through the force of gravity. On earth, scientists cannot use gravity but are instead experimenting with magnetic confinement and inertial confinement (see Figure 1.2).

Magnetic confinement (e.g., ITER program) uses the physics principle that charged particles tend to follow magnetic field lines. Therefore a strong magnetic field can hold the ionized atoms together while they are heated by microwaves or other energy sources.

Inertial confinement (e.g., Z-Pinch program) keeps the plasma together by inertial forces alone. A tiny pellet of frozen Deuterium and Tritium is compressed and heated by intense radiation, such as a laser beam, so quickly that fusion occurs before the atoms can fly apart.

The easiest reaction for nuclear fusion power according to the Lawson's Criterion

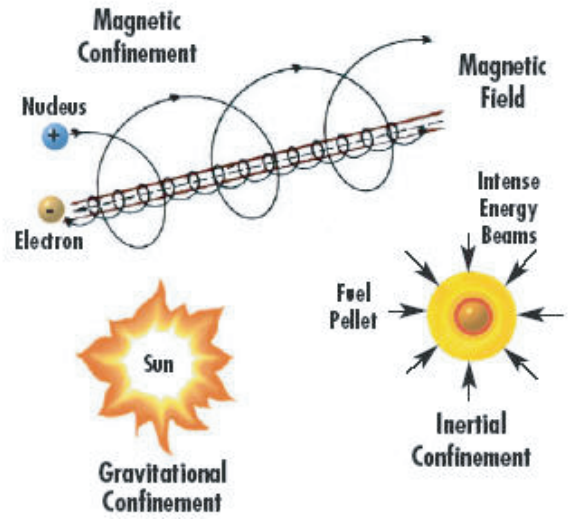

Figure 1.2: Different possible Inertial Fusion Confinements (from `http://www.ofes.fusion.doe.gov/whatisfusion.shtml`)

is the one to one mix of *Deuterium and Tritium*, which are both heavy isotopes of Hydrogen. *Deuterium* is a naturally occurring isotope of Hydrogen and the processes to obtain Deuterium and manufacture "Heavy Water" are well developed and rather easy compared to the Uranium enrichment process. *Tritium* occurs naturally only in negligible amounts due to its radioactive half-life of 12 years. Therefore, it is necessary to breed Tritium from Lithium using one of the following reactions:

$$n + {}^{6}Li \rightarrow T + {}^{4}He$$

$$n + {}^{7}Li \rightarrow T + {}^{4}He + n$$

The supply of lithium is more limited than that of Deuterium, but still large enough to supply the world's energy demand for hundreds of years (Stacey, 1984).

When Deuterium and Tritium fuse, they form for a brief instant an atom of Helium ^{5}He, and then burst apart, thereby giving an Helium nucleus ^{4}He with 3.5 MeV (5.08×10^{-13} J) of kinetic energy and a neutron with four times as much energy, i.e., 14.1 MeV (2.259×10^{-12} J), as shown in Figure 1.3. With its positive charge, the Helium nucleus ^{4}He, more commonly called "alpha particle", interacts strongly with surrounding materials and stops instantaneously, thereby depositing the 3.5 MeV

of heat close to the site of the fusion reaction within a thin surface layer. In the case of Inertial Confinement, the neutrons stop within a thick blanket of material that contains Lithium and breeds the the Tritium necessary for the fusion reaction (Peterson, 1998).

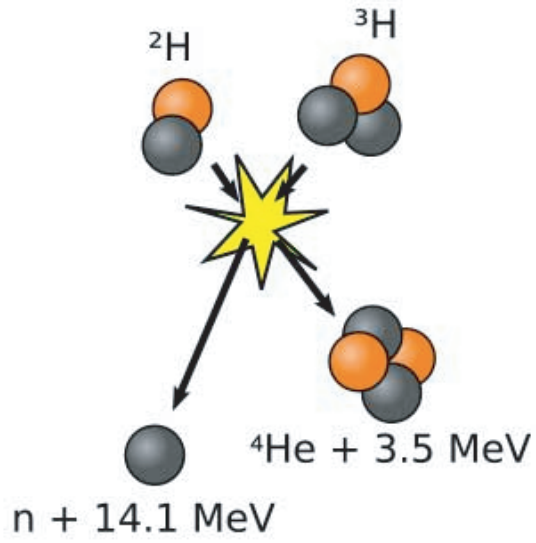

Figure 1.3: D-T Fusion reaction (from `www.answers.com/topic/fusion-power`)

1.1.1 Principles of Inertial Fusion Energy (IFE)

In Inertial Fusion Energy (IFE), the burning fusion reaction is ignited by illuminating and compressing a target, viz. a pellet that contains deuterium and tritium, by the use of a driver that focuses beams of accelerated ions or intense laser light. Every IFE system requires a major driver (lasers, heavy ions, and Z-pinches), a target, and a chamber. An IFE power plant would have separate areas for the driver, a factory for making the targets, a target chamber where the fusion reactions occur, and a power cycle to generate electricity (see Figure 1.4). This provides design flexibility and staged development, and allows the driver and target factory to be protected from the fusion radiation environment (Olson et al., 2005b). Most power reactors operate by igniting several such pellets per second to produce the desired power level

in the chamber (Wikipedia, 2006).

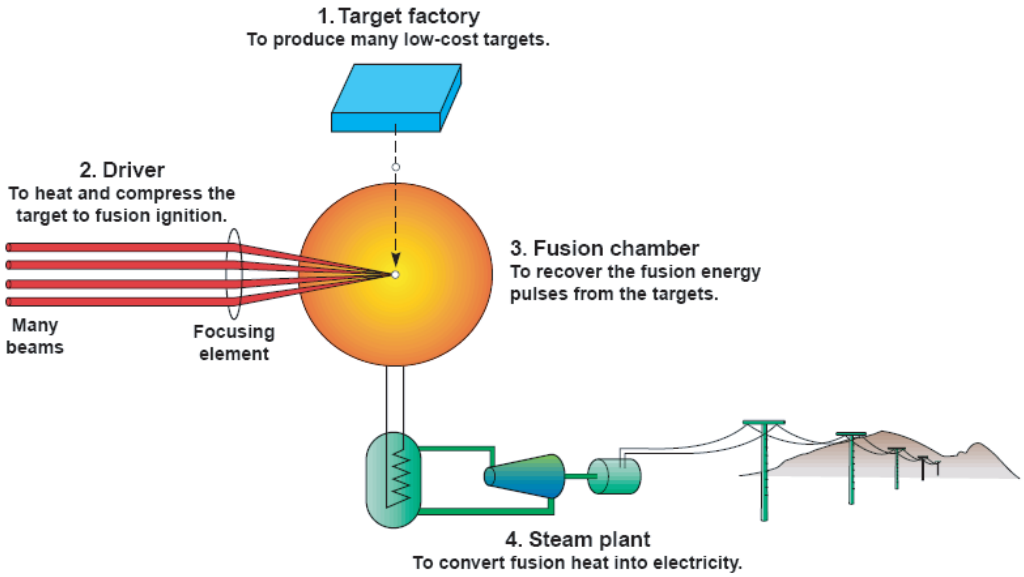

Figure 1.4: Global View of IFE Power Plant (from `http://www.llnl.gov/nif/library/ife.pdf`)

The target ignition is done according to the following process and as it is illustrated on Figure 1.5:

1. *Target Heating.* A pulse of radiation through the driver (light, x-rays, or ions) rapidly heats the outer layers of the target.

2. *Compression.* The fuel is rapidly compressed by the rocket-like blow-off of hot surface material.

3. *Ignition.* During the final part of the capsule implosion, the fuel core reaches 20 times the density of lead and ignites at $100,000,000\,^{\circ}\mathrm{C}$.

4. *Burn.* In a target which has been heated and compressed to the point of thermonuclear ignition, energy can then heat the surrounding fuel to cause it to fuse as well, thereby creating a chain reaction that burns the fuel load.

The total fusion energy released per pulse is about equal to the energy released by burning thirty pounds of coal (LLNL, 1997).

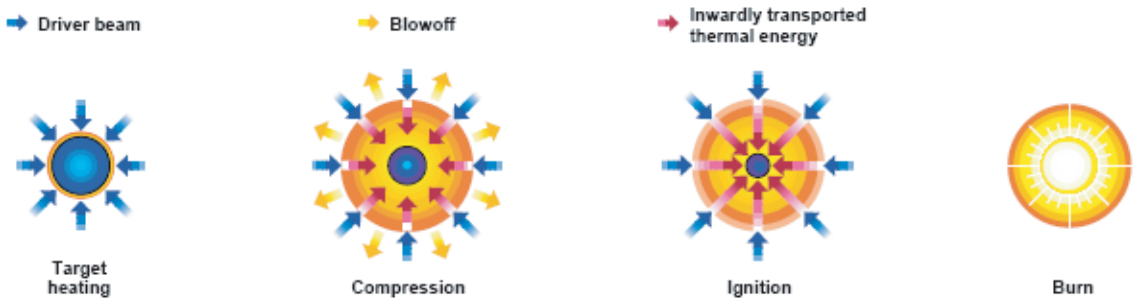

Figure 1.5: Target Ignition (from `http://www.llnl.gov/nif/library/ife.pdf`)

1.1.2 Z-Pinch IFE Chamber

Z-Pinch Inertial Fusion Energy (Z-IFE) is a repetitive, high yield, power plant scenario that can be used for the production of electricity, transmutation of nuclear waste, hydrogen production, etc., all with no CO_2 production and no long-lived radioactive nuclear waste. Different Z-pinch IFE reactors have been proposed; the most recent design is based on the Recyclable Transmission Line (RTL) concept. In this scheme, an RTL connects the pulsed power driver directly to the target, and the fusion explosions are contained in a thick-liquid wall chamber as shown schematically in Figure 1.6. The RTL/target assembly is inserted through a single opening at the top of the thick liquid wall power plant chamber (see Figure 1.7). The shot is fired; portions of the RTL are vaporized and end up mixed with the coolant to be recycled; the upper remnant of the RTL is removed, and the cycle is repeated every 10 seconds. The RTL concept eliminates the problems of optic, high-speed target injection, as well as pointing and tracking beams. The coolant, e.g. Flibe (F_4Li_2Be) or liquid lithium, is approximately one meter thick; it absorbs the fusion neutron energy, breeds tritium to fuel the targets, shields the structural wall from neutron damage, and absorbs the x-rays and ions produced by the explosion to protect the first wall (Olson et al., 2005a). Use of thick liquid jets eliminates the need for the blanket normally placed behind the first wall. Because of the need to replace the RTL

after each explosion, Z-Pinch IFE reactor designs utilize high-yield targets ($\sim$ 3 GJ which is equivalent to one ton of TNT) at low repetition rates ($\sim$ 0.1 Hz). The fusion yield of 3 GJ is typically distributed between neutrons ($\sim$ 65%), x-rays ($\sim$ 30%), and debris ions ($\sim$ 5%). The neutrons heat the liquid blanket volumetrically, whereas the x-rays and the ions deposit their energy in a very thin layer at the edge of the liquid wall. For a chamber radius of 5 m, and a RTL entrance hole of radius 1 m, the RTL opening is only 1% of the surface area of the chamber. This means that essentially 99% of the blast will see thick-liquid walls. Appropriately-arranged "thick" liquid jets (circular, planar, or annular) can adequately protect the cavity walls from the target X-rays, ions, and neutrons. Attenuation of the fusion neutrons within the liquid jets can significantly reduce or eliminate radiation damage to the first wall, so that it may be possible to design cavity structures to last the entire reactor life. However, the shock waves and mechanical loadings produced by rapid heating and evaporation of the nearly-incompressible liquid jets due to the X-rays and ions may be challenging to accommodate within a small reactor cavity. For a multi-GJ yield with 1.6 GJ in x-rays and a Flibe liquid wall starting at a distance of 1 m from the target, the peak instantaneous pressure in the edge of the liquid wall will be or order 80 Mbar, and the impulse will be of order 60 ktaps (1 ktap = 1 Mbar.ns). By carefully selecting the liquid wall structure, it is envisioned that the shock can be reduced to a small enough level, so that when it reaches the structural wall it will not damage it. The liquid wall should reduce the impulse by a a factor of 2.4 or more Olson et al. (2005b).

To this end, "compressible," two-phase, liquid/gas jets have been proposed as a means of protecting the Z-Pinch cavity walls from the target photons, ions, and neutrons. Two-phase jets could also attenuate the shock waves, thereby limiting and mitigating the mechanical consequences of rapid energy deposition within the liquid. Such attenuation would allow the Z-Pinch IFE reactor to use a much smaller, i.e., more economical, reactor cavity to contain the high yield, low repetition rate

explosions. The concept is made possible by the Z-Pinch reactor cavity's relatively high allowable pressure ($\sim$ 10-20 torr), which makes it possible to introduce a gas within the wall-protection jets, without excessively increasing the vacuum pumping requirements (Olson, 2004).

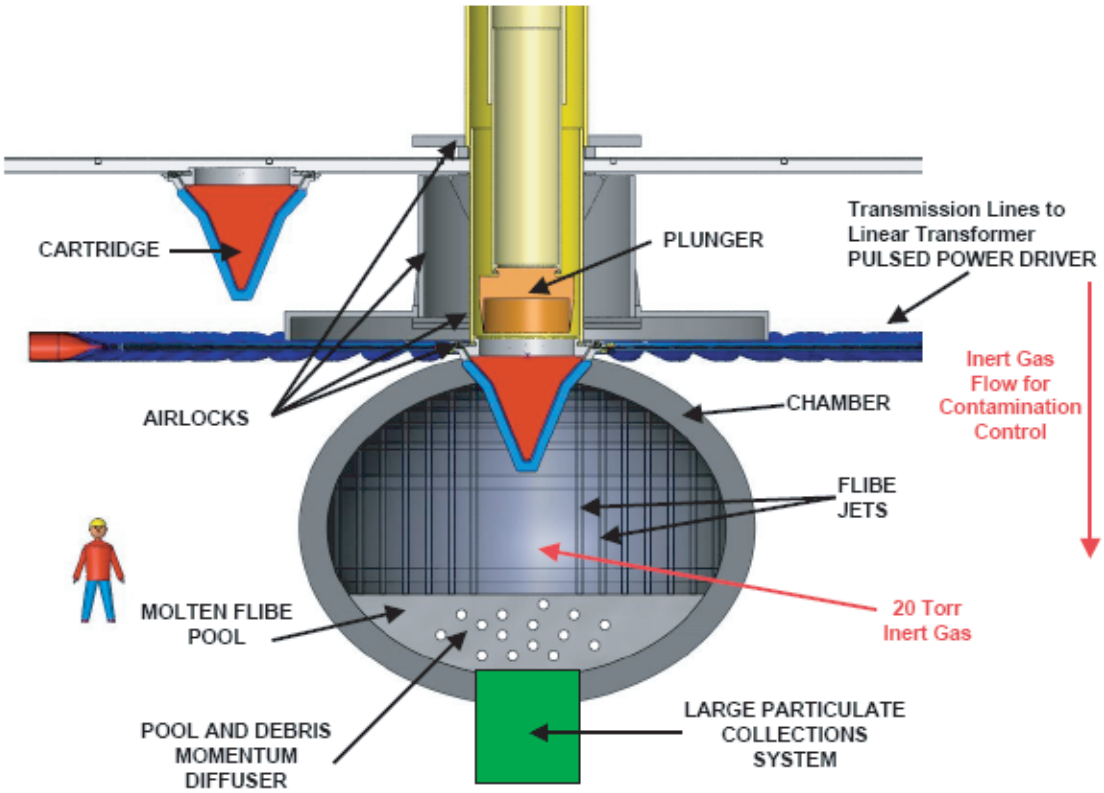

Figure 1.6: Z-Pinch IFE chamber (Olson et al., 2005b)

Z-Pinch IFE is relatively new and has become part of the IFE community over the last eight years. Z-Pinch IFE was part of the 1999 Snowmass Fusion Summer Study, the IAEA Cooperative Research Project on IFE Power Plants (2001), the 2002 Snowmass Fusion Summer Study, the FESAC 35-year Plan Panel Report (2003), the FESAC IFE Panel Report (2004), the 21^{st} IEEE/NPSS Symposium on Fusion Engineering SOFE 2005, and the 17^{th} Topical Meeting on the Technology Fusion Energy TOFE 2006.

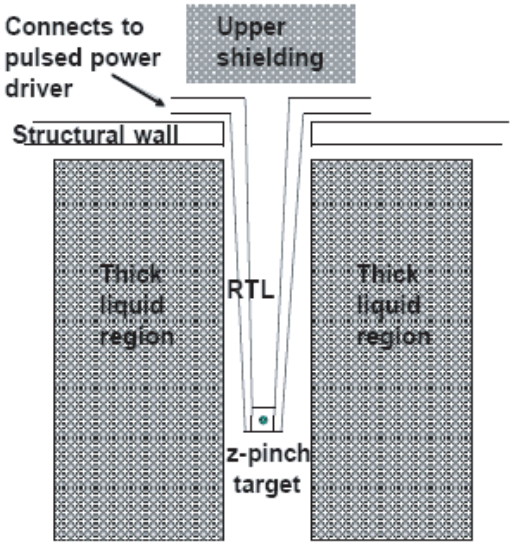

Figure 1.7: The Recyclable Transmission Line (RTL) concept (Olson et al., 2005b)

The long-range goal of the Z-Pinch IFE program is to produce an economically-attractive power plant for production of electricity. A development path for Z-Pinch IFE has been created; research has been conducted in the areas of: (1) RTLs, (2) repetitive pulsed power drivers, (3) shock mitigation, (4) planning for a proof-of-principle full RTL cycle demonstration, (5) IFE target studies for multi-GJ yield targets, and (6) Z-pinch IFE power plant engineering and technology development Olson et al. (2005a).

1.2 Objectives

The goal of this research is to quantify the extent by which two-phase (gas/liquid) jets can attenuate shock waves by conducting experimental and numerical studies. The different steps to be undertaken are:

- *Work on the behavior and the structure of two-phase jets.* Experiments will be conducted to examine the influence of gas void fraction and nozzle/flow conditioning system design on the behavior and stability of a two-phase jet as it is discharged into an open cavity. Planar, circular, and annular jets will be

examined over wide ranges of liquid velocities and void fractions. Bubble size, void fraction, and slip ratio within planar and circular jets will measured. The aim is to determine the parameter ranges over which stable, coherent, two-phase jets can be maintained.

- *Shock mitigation by a two-phase jet.* Experiments will be conducted to quantify the extent by which a shock wave can be attenuated by a two-phase jet. Annular two-phase (water/air) jets with different velocities, void fractions, and initial shock strength will be used. The shock will be produced using an exploding wire located along the jet axis. The axisymmetric jet geometry used in these experiments has been selected because it simplifies data collection and future model validation. Different confinement geometries and scale effects will be considered in the experiments. The transient pressure history at the boundary will be measured to quantify the extent of shock mitigation.

- *Numerical simulations and comparison with experimental results.* A state-of-the art, two-phase, CFD code, such as FLUENT, will be used to model the experimental conditions; the data and model prediction will be compared. The ultimate goal is to obtain an experimentally-validated design tool to allow system designers to evaluate the mechanical design of jet-protected-IFE reactor cavities.

The remainder of this thesis is organized as follows. Chapter 2 gives a brief overview of the literature available on shock mitigation in Z-Pinch IFE reactors, dynamics of vertical annular jet two-phase flow models, different techniques for the measurement of void fraction, theory of wave propagation in two-phase media, and pressure wave due to an exploding wire. Chapter 3 details the equipment and procedures used in the current investigation. Experimental results characterizing the behavior and the stability of two-phase jets and their capability to attenuate shock

waves are reported in Chapter 4. The numerical model representing the experimental conditions is discussed in Chapter 5. Chapter 6 summarizes the conclusions of this investigation and offers recommendations for future research on vertical two-phase jets. Appendix A presents the photographs of the two-phase circular and annular jets examined in this investigation. The *bubble.m* $MATLAB^{®}$ program used to measure the equivalent spherical bubble diameters is listed in Appendix B, while the bubble size distributions within the two-phase planar jets examined in this investigation are presented in Appendix C. Additional experimental results for the void fraction and slip ratio distributions and the pressure histories are included in Appendix D and E, respectively. Error analysis is examined in Appendix F. Finally, Appendix G presents the single- and two-phase jet detailed numerical models.

CHAPTER II

LITERATURE REVIEW

In this chapter, previous work in areas related to this current research is reviewed. Section 2.1 deals with the dynamics and stability of vertical jets. Section 2.2 deals with wave propagation in two-phase media; work related to shock mitigation in Z-Pinch IFE reactors is described in Section 2.3. Pressure waves produced by an exploding wire (the method used in this study) are discussed in Section 2.4. Section 2.5 provides a brief overview of two-phase flow models while Section 2.6 describes the methods used to measure the void fraction in two-phase (gas/liquid) systems.

2.1 Dynamics of Vertical Annular Jet

The hydrodynamics and stability of annular jets has been extensively studied because of their numerous applications in a broad range of disciplines, including aerodynamics, combustion and mixing, cooling and mass transfer, industrial processes, and nuclear engineering. In the 1970's, Hovingh (Hovingh, 1976) and Maniscalo *et al.* (Maniscalco et al., 1979), suggested using an annular jet to act as a renewable first wall blanket for Inertial Confinement Fusion (ICF), or laser fusion power reactors. The required annular jet parameters for that application appeared formidable: about half a meter for the jet thickness and a few meters for the jet radius and closing length. The closing length of such a thick liquid jet was shown to be considerably longer than the chamber height (Hovingh, 1977). Stability of an annular jet discharging in the ambient is the primary concern. Liquid jets in the form of annular jets and water bells have been studied for more than a hundred years, including the work of Baird and Davidson (Baird and Davidson, 1962), Binnie and Squire (Binnie and Squire, 1941), and Boussinesq (Boussinesq, 1869). The numerical method suggested by Boussinesq

(Boussinesq, 1869) for working out the shape of an annular liquid jet from the basic momentum equation is cumbersome, as pointed out by Baird and Davidson (Baird and Davidson, 1962). Several studies have made various assumptions to obtain simplified equations for the annular jet shape. Among the simplifying assumptions are: (a) the effect of gravity is negligible; (b) the radius of axial curvature is much larger than the jet meridian radius; (c) the jet velocity is high and the closing length is large such that the jet surface can be considered to be nearly vertical; and (d) pressures inside and outside the annular jet are equal. Binnie and Squire (Binnie and Squire, 1941) solved for the jet profile using all four of these assumptions. Baird and Davidson (Baird and Davidson, 1962) used the first three assumptions while allowing for a pressure difference between the inside and outside of the annular jet. These two last analyses obtained nonlinear differential equations considering the assumptions mentioned earlier.

These theoretical predictions have been compared to experimental results. In general, the analyses overestimated the observed convergence lengths, with larger errors at low flow velocities. The authors attributed the disparities to "meniscus effects" as the jet approaches the convergent point. Hovingh's analysis accounts for the influence of gravity (Hovingh, 1977). The third and fourth assumptions were used by Hoffman *et al.* (Hoffman et al., 1980) in estimating the closing length of an annular liquid jet. Hoffman *et al.* used the theory of "water bells", which resemble annular jets, to generalize Hovingh's analysis by improving the treatment of surface tension forces and allowing for the existence of a radial component of flow at the inlet to the jet. Hoffman *et al.* also conducted experiments, in which theory and experiment generally agreed, except at high flow velocities where the predicted convergence lengths were reduced. This was thought to be caused by a flow-induced pressure decrease inside the jet. Tuck (Tuck, 1982) conducted an analytical and numerical study of annular water jets with and without the effect of gravity but neglected the surface tension

effect.

Water bells were previously studied by Dumbleton (Dumbleton, 1969), Lance and Perry (Lance and Perry, 1953), Shoji (Shoji, 1971), and Taylor (Taylor, 1959). Hasan, Mitsutake, and Monde (Hasan et al., 1997) conducted analytical and experimental studies to determine the shape of a vertical, axisymmetric, annular liquid jet; the objectives of their work were to analytically solve for the shape of the jet without invoking the four assumptions mentioned above, and to verify the analytical prediction by experimental observation. The forces acting on the jet are the inertial forces, gravity, pressure, axial curvature, and meridian curvature (surface) forces. The following assumptions were made: (a) the annular jet is vertical and axisymmetric; (b) there is no energy loss due to friction with the surrounding medium; (c) jet radius is always very large compared to its thickness; and (d) the velocity profile relaxes quickly upon exit from the nozzle and does not affect the shape of the jet. An annular jet converges, diverges, or maintains its original radius depending upon the magnitude of the difference between the inside and outside pressure. The jet converges when the pressure due to the meridian surface tension is greater than the difference between the inside and the outside pressures, and it diverges if it is smaller.

Esser and Abdel-Khalik (Esser and Abdel-Khalik, 1984) conducted a numerical study of annular liquid jets at high Reynolds numbers, accounting for both surface tension and viscosity. They used a boundary layer approximation, assumed the jet to be axisymmetric, and accounted for gravity and radial pressure gradients, while ignoring the axial pressure gradients. Comparison between their numerical predictions and previous experimental results showed variable agreement. The differences were attributed to incomplete or inaccurate specification of the boundary conditions. Ramos (Ramos, 1998) started from the previous study and used an asymptotic method to derive the leading order equations of axisymmetric, incompressible, laminar, immiscible annular liquid jets using a long wavelength approximation as a function of Reynolds,

Froude, and Weber numbers. Inertia, capillarity, free surface flows, and axial pressure gradients were considered. Ramos' numerical results and previous experimental results agreed well (Ramos, 1998; Duda and Vrentas, 1967).

Majumdar and Shambaugh (Majumdar and Shambaugh, 1991) determined the velocity and temperature profiles in a single, free, annular jet for different Reynolds numbers, initial temperatures, and nozzle dimensions. Their studies showed that the temperature and velocity profiles are independent of the Reynolds number, length-to-diameter ratio, operating temperature, and annulus inner diameter. They concluded that, since the profiles of an annular jet are independent of its inner diameter, it can be treated as a jet emerging from a circular orifice plate in the region of fully developed flow. The experiment conducted by Aly and Rashed (Aly and Rashed, 1991) confirmed these results; the mean velocity profiles were shown to be similar to those of a single jet at a distance 3.24 times the outer diameter downstream from the nozzle.

Annular liquid jets may, however, become unstable and, eventually, turbulent. They have been found experimentally to be sensitive to small perturbations caused by acoustic feedback, external perturbations, and oscillations in the liquid's mass injection rate, etc., especially at high speeds (Ramos, 1998), thereby leading to instability and break-up.

Kendall (Kendall, 1986) showed that a liquid annular jet surrounding a flowing gas in its core is extremely unstable. Periodic, axisymmetric oscillations arise spontaneously within the cylindrical sheet emerging from the nozzle. They grow with such rapidity along the axial dimension that sealing-off and encapsulation of the core gas occurs within a few jet diameters. This is closely followed by a pinchoff of the liquid between adjacent bubbles. Li (Li and Shen, 2001) expanded this work and demonstrated that the jet breakup process has three different regimes, namely, bubble formation, annular jet formation, and atomization. Both the jet breakup length

and the wavelength for bubble formation decrease as the air-to-water velocity ratio is increased. Sivakumar (Sivakumar and Raghunandan, 1997), studying atomizers, observed the possibility of a tulip-shaped liquid bulb; the convergence length of the tulip increases with the liquid mass flow rate due to increased inertial forces. Oscillations can occur for converging annular flow, which may be attributed to the dynamic unbalance between the surface tension and inertia forces in the jet. A further increase in the mass flow rate produces a diverging annular jet as the disruptive inertial and aerodynamics forces dominate over surface tension forces. Numerous other studies have been reported on two-phase (bubbly) flows in channels.

2.2 Wave Propagation in Two-Phase Media

In the early 1960's, non-equilibrium mathematical models describing wave propagation in liquids with gas or vapor bubbles were presented independently in the USSR by Iordansky (Iordansky, 1960) and Kogarko (Kogarko, 1961), and in the Netherlands by van Wijngaarden (Van Wijngaarden, 1968). The general ideas of these models were: (a) the conservation laws were written for the average pressure, density and mass velocity; and (b) the state of two-phase medium was described by a dynamic sub-system including the Rayleigh (Rayleigh, 1917) equation for the bubble radius and the relationships for the density, volumetric gas concentration, and radius. The processes of bubble formation and bubble collapse were not considered in these models. The distances between the bubbles were assumed to be large enough to prevent collisions, so that the interactions between bubbles were due only to pressure changes. The Rayleigh equation was used to represent the oscillations of a single bubble, where the pressure at infinity was replaced by the pressure of the mixture. The fluid was assumed to be incompressible. The use of such an assumption was justified by the great compressibility of a bubble compared to the surrounding liquid and by its size. The void fraction was assumed to be small enough ($\alpha \ll 1$), so that the mixture could

be considered as a medium with the density approximately equal to $\rho_l \cdot (1 - \alpha)$. In other words, the mass of the gas was neglected compared to the mass of the fluid. Viscosity and heat conductivity were significant only in the processes of interaction between the phases, and they could be neglected in a macroscopic transfer of energy and momentum (Grimshaw and Khusnutdinova, 2004). This model can predict the conditions for the shock waves to be attenuated or amplified (Kedrinskii, 1997-1998).

Numerical methods have been developed based on the previous theoretical model. The work of Prosperetti indicated that complex heat transfer would occur inside the bubbles (Prosperetti and Kim, 1988). A new model considering a difference in pressure and velocity between the two phases has been developed by Zhilin (Zhilin et al., 1996). In this case, velocities and pressure before and after the shock front were separately determined for the liquid and the gas bubbles.

The Kortege-de-Vries equation, which describes frictionless processes, can also be added to the system of equations of multiphase hydrodynamics when dissipation is compensated by energy transfer (Elperin et al., 1994). This equation can describe the evolution of long-wave disturbances in an ideal liquid with adiabatic bubbles. Short-wave modulation in polydisperse bubbly mixtures can be modeled by the non-linear Schrödinger equation. Despite different length scales, long and short waves can interact with the possibility of long-wave/short-wave resonance. A new dispersion relation is then required (Khismatullin and Akhatov, 2001).

Numerous papers from the USSR and Russia are available on the subject of wave propagation in gas-liquid media. Unfortunately, most have not yet been translated to English. Nakoryakov's book (Nakoriakov et al., 1993) is an excellent reference as a summary of the Russian literature.

2.3 Shock Mitigation in Z-Pinch IFE Reactors

The envisioned target yields for Z-Pinch IFE are about 3 GJ or larger, compared to other IFE approaches that typically use targets with yields $\leq$ 0.4 GJ. Containment of the blast and shock mitigation must be studied in order to assure integrity of the chamber structural wall. The leading cavity design approach utilizes a thick liquid wall to mitigate shocks because it offers both x-ray and neutron protection for the chamber wall (Olson et al., 2007).

Several different, but relatively simple models have been used to scope out the problem of shock generation, propagation, and attenuation in an IFE environment. One dimensional shock propagation and attenuation in water has been examined as an approximation to the same phenomena in a Flibe liquid wall in an IFE chamber. The effects of geometry, equation of state, and shock parameters were investigated.

Using available properties of Flibe, the deposition of the x-ray energy in Flibe was calculated and used to estimate the blow-off impulse generated in the Flibe (Lawrence, 2006). For a multi-GJ yield with 1.6 GJ in x-rays and a Flibe liquid wall starting at a distance of 1 meter from the target, the peak instantaneous pressure in the edge of the liquid wall will be of the order of 80 Mbar, and the impulse will be of the order 60 ktaps (1 ktap = 1 Mbar.ns).

If there were no liquid wall, the peak instantaneous pressure and the impulse would be reduced at the structural wall at 5 m by about a geometric factor of 5^2, to 3.2 Mbar and 2.4 ktaps (1 ktap = 1 Mbar.ns), respectively. By carefully selecting the liquid wall structure, it is envisioned that the shock strength can be sufficiently reduced, so that when the shock reaches the structural wall it will not damage it. The thick liquid wall should reduce the peak instantaneous pressure by a factor of 2.4 or more (Olson et al., 2005a, 2006).

The research performed on shock mitigation for Z-IFE reactors since 2004 has been conducted under the guidance of Sandia National Laboratories. Analytical

calculations, several computer code simulations, and several scaled experiments have been conducted (Olson et al., 2006).

Abbott (Abbott, 2005) summarized the dynamic response of the shielding liquid to pulsed explosions. The liquid shielding geometry proposed for the Z-Pinch reactor chamber is quite similar to the concepts employed in previous IFE reactors studies. Consequently, much of the analysis previously carried out to understand the dynamics of these chambers can be reapplied (Abbott, 2005). The nominal deflection angle that the liquid curtain will have after a fusion explosion can be determined. The liquid jets can be designed to avoid direct line-of-sight bombardment of the first wall by the target debris and neutrons (Olson et al., 2005b).

Shock mitigation has been modeled in scaled experiments with a shock tube, single or multiple water layers, and different Mach Numbers (Olson et al., 2005a; Meekunnasombat et al., 2005). The results of these studies indicated that the speed of the transmitted shock wave can be reduced by 50% and is a weak function of the numbers of layers. The pressure of the reactor chamber is significantly increased due to the presence of the liquid layer (Meekunnasombat et al., 2005, 2003). However, this pressure is substantially reduced when multiple liquid layers are used (Meekunnasombat et al., 2005). Helium, as well as some other gases, can be used between the layers to mitigate shocks.

The UCB code VIRTUAL TSUNAMI was used to model the gas dynamics inside a thick-liquid protected Z-IFE chamber for a 4 GJ yield target. VIRTUAL TSUNAMI simulations of ablation and venting were performed for two liquid jet chamber configurations proposed by LLNL for Z-IFE - a "closed" configuration consisting of a large circular array of many layers of circular jets, and an "open" configuration consisting of a similar array but with curved slices of jets removed to allow outward venting. Peak impulse loads close to 10^6 Pa were reported for both configurations (Debonel, 2006).

X-ray energy deposition in Flibe was studied with BUCKL simulations at SNL, which show that 80% of the x-ray energy is deposited within the 10 microns of the surface. Subsequent ALEGRA simulations of the deposited energy showed that a strong shock is launched at the surface, and attenuates as it propagates in the Flibe. The use of low density Flibe droplets or mist extends the physical x-ray deposition length. It is suggested that energy deposited in the mists or droplets would cause the droplets or mists to explode into their surroundings voids, and that would help dissipate the initial shock (Rodriguez et al., 2006).

The Vacuum Hydraulics experiment (VHEX) facility at UCB was upgraded with a large annular inlet nozzle system to produce a large annular porous water curtain to study Z-IFE response (Peterson, 2006). An explosive (28 g of C-4) was set off in the center of the annular curtain, and imaged at 1600 fps. The response demonstrated that the crushing of porous liquid structures is effective in dissipating kinetic energy and transferring momentum uniformly into the blanket mass. No significant high-speed jetting or spall was observed exiting the shock liquid structure. The results suggest that porous liquid structures can provide effective mitigation of blast shock loading for Z-IFE (Peterson, 2006).

Shock attenuation by a Flibe liquid pool at the bottom of the chamber, and also by Flibe liquid walls, subjected to a 3 GJ fusion yield was investigated with the LSTC-Dyna2d code at General Atomics. For a 50%-foamed liquid pool, the pressure pulse is reduced by a factor of 36, but the bottom of the vessel would still have excessive strains and deformations. It also appears that the high peak pressures and very short pressure pulse tend to collapse the bubbles in the foamed Flibe pool, making them less effective than expected (Olson et al., 2005b). Further meaningful calculations can be performed using momentum deposition to approximate the impulse from x-ray surface ablation, and to include the effects of volumetric neutron energy deposition as initial energy in the equation of state. Preliminary results show that bubbles (50%)

in the bottom pool appear to substantially mitigate the downward shock (Charmin et al., 2006). Shock attenuation in a foamed liquid has also been investigated with the ALEGRA code. The results show that increasing the number of gas regions while maintaining a constant 50% gas / 50% liquid mixture, or decreasing the size of each region, reduces the peak pressure transmitted through the system (Vigil and Rodriguez, 2005).

Solid, foamed Flibe has been proposed to protect the top of the chamber, directly above the RTL. Solid Al foam may be used to model solid foamed Flibe to gain an understanding of shock attenuation. Foamed Aluminum samples were tested on a shock tube facility at the University of Wisconsin. Results show a 35% pressure reduction when a shock interacts with the 1-inch thick samples and a 50% pressure reduction when a shock interacts with a double layer configuration (Anderson et al., 2005). High porosity (0.89) foam samples (stack of two, 25.4 cm square, 10.2 cm high) of three different cell size (10, 20, and 40 pores per inch) were compressed with a strong shock (M = 6) in a 25 kPa atmosphere of air and SF_6. The presence of the foam was found to decrease the impulse due to the shock/foam interaction with the largest pore size being the most effective at impulse reduction; the impulse was reduced by a factor of approximately 1.3 (Anderson et al., 2006).

Shock attenuation in foamed solids has been investigated with code simulations at SNL and General Atomics. Simulations using the ALEGRA and DYNA3D codes were done to study the behavior of shocked metallic foams. Results from code simulations have been compared to experimental results. Wave speed is reduced significantly as it passes through the foam, energy is well-absorbed, and the incident shock degenerates into a discontinuous compression wave in the two-phase foam but results in greater peak pressures (Olson et al., 2005b; Vigil and Rodriguez, 2005; Anderson et al., 2005; Charmin et al., 2006).

Preliminary studies conducted in 2004 and 2005 by various institutions in support

of Sandia's Z-pinch reactor suggest that thick liquid walls can be used to attenuate the shock from a 3 GJ explosion. There are different options to consider, namely, Flibe liquid sheets or jets in the sideways direction, a foamed Flibe pool at the bottom of the chambers, possibly foamed Flibe in the upward direction , solid foamed Flibe to protect the top of the chamber, and possibly mists or droplets within the chamber (Olson et al., 2005b, 2006).

In 2006, the shock mitigation work focused on attenuating the high energy x-rays before they reached the chamber wall. Three possible x-ray absorbing methods were investigated: thick liquid curtains, aerosols, and gas. Two possible chamber designs were proposed based on these proposed shock mitigation schemes. The first was a thick liquid blanket design and the second was a first wall design. However, the thick liquid curtain design remains the prime candidate for shock mitigation for Z-IFE (Olson et al., 2007).

2.4 Pressure Wave due to an Exploding Wire

Exploding wires are observed when high density current is fed into wire conductors. The phase of the metal wire changes from solid-liquid-gas to plasma with high temperature and pressure in a short time (several microseconds). Numerous studies of exploding wire phenomena were reported in the 1950's and 1960's. From 1959 to 1967, four international conferences dealing with exploding wire phenomena were held in Boston (Chace, 1968, 1964, 1962, 1959). These early studies are very helpful in understanding the characteristics of electric exploding wires (Chace, 1968, 1964, 1962, 1959).

In recent years, since the development of Pulse Power Technology, studies on applications of exploding wires appear to be on the rise (Mankowski and Kristiansen, 2000). The main characteristic of an exploding wire is the production of a high-temperature, high-pressure channel. Along with the expansion of the plasma channel,

a shock wave spreads in arbitrary directions. The waveforms of voltage-drops across the wire and currents through the wire were reported (Vijayan and Rohatgi, 1985; Kolesnikov et al., 1970; Ripoche, 1961). Numerous studies dealing with underwater explosions have been reported (Shoji et al., 1996; Zhang et al., 2004; Otsuka et al., 2004). The pressure characteristics of the pulsed underwater discharge have been studied; the waveforms of pressure were detected by a high dynamic pressure sensor and recorded by a waveform recorder. Different techniques, including holography and high speed cameras, have been used to record the physical changes of the wire during the explosion (Rockett and Bach, 1979; Lisitsyn et al., 1997).

2.5 Two-Phase Flow Models

The general equations for two-phase flows have received considerable attention and have been derived in a number of forms; the work done in that area includes that reported by Bouré (Bouré, 1978), Bouré and Reocreux (Bouré and Reocreux, 1972), Ishii (Ishii, 1990), and Delhaye (Delhaye, 1990). The equations (conservation of mass, conservation of momentum, and conservation of energy) may be written in terms of the local instantaneous conditions or in terms of some space-or-time-average conditions. The two most important models - the "Homogeneous Equilibrium Mixture"(HEM) model and the "separated flow" model - are briefly presented. The "Homogeneous Equilibrium Mixture" model considers the two-phases to flow as a single phase possessing mean fluid properties. The assumptions in this model are the following: (a) equal gas and liquid velocities; (b) thermodynamic equilibrium between the phases; and (c) the use of a suitable defined single-phase friction factor f_{TP} for two-phase flow. The friction factor f_{TP} is assumed to be equal either to the one if the total flow was considered to be all liquid, or to one calculated using a mean two-phase viscosity μ. It can also be correlated. The "Homogeneous Equilibrium Mixture" model has been used for different flow patterns in the steam generation,

petroleum, and refrigeration industries for a considerable time (Collier and Thome, 1994). For the "Homogeneous Equilibrium Mixture" model, the void fraction α can be easily expressed as a function of the quality x and the densities of the two phases ρ_g and ρ_l as illustrated in Equation 2.1. When ρ_l/ρ_g is large, the void fraction rises rapidly once the quality rises even slightly above zero.

$$\alpha = \frac{1}{1 + \left(\frac{1-x}{x} \cdot \frac{\rho_g}{\rho_l}\right)} \tag{2.1}$$

The "separated flow" model considers the phases to be artificially segregated into two streams: one of liquid, and one of gas. In the model's simplest form each stream is assumed to travel at a mean velocity. For the case where the mean velocities of the two phases are equal, the equations reduce to those of the "Homogeneous Equilibrium Mixture" model.

The "separated" model was initially developed in 1944 by Lockhart and Martinelli (Lockhart and Martinelli, 1949). The assumptions in this model are the following: (a) constant but not necessarily equal velocities for the gas and liquid phases, (b) thermodynamic equilibrium between the phases, and (c) the use of empirical correlations or simplified concepts to relate the two-phase friction multiplier ϕ^2 and the void fraction α to the independent variables of the flow (Collier and Thome, 1994). In the "separated flow" model the general equation for the void fraction is expressed in Equation 2.2 as a function of the slip ratio $S = \frac{U_g}{U_l}$, which is usually greater than one for two-phase channel flow.

$$\alpha = \frac{1}{1 + \left(\frac{U_g}{U_l} \cdot \frac{1-x}{x} \cdot \frac{\rho_g}{\rho_l}\right)} \tag{2.2}$$

The "Homogeneous Equilibrium Mixture" model and the "separated flow" model are the most widely used and tested treatments of two-phase flow. However, a larger number of other empirical and semi-empirical methods have been suggested. These methods have to be used in conjunction with some methods defining the flow regime such as a flow pattern map.

The "Bankoff (Bankoff, 1960) variable density model" for bubbly flow corresponds to an "Homogeneous Equilibrium Mixture" model with correction for two-dimensional effects. The model treats the case where radial gradients exist in the concentration of gas bubbles across the channel. The concentration is assumed to be maximum at the center of the channel and zero at the walls. No relative motion is assumed between the gas bubbles and the liquid at any radial position. A power law distribution is assumed for both the velocity and the void fraction (Collier and Thome, 1994). Most void fraction correlations are actually correlations of the slip ratio S. Experimentally, it was found that slip ratio depends on (in decreasing order of importance): (a) physical properties (usually expressed as ρ_l/ρ_g); (b) quality x; (c) mass flux G; and (d) relatively minor variables such as tube diameter, inclination of the tube, length, heat flux, and flow patterns (Whalley, 1987). All the correlations are through the ratio $\frac{U_g}{U_l}$.

Both Smith (Smith, 1969-1970) and Chisholm (Chisholm, 1983) have derived simple and useful expressions for the slip ratio. Smith (Smith, 1969-1970) proposed a simple model for annular two-phase flow with a fraction e of the liquid entrained in the gas core. He postulated equal momentum flux in the film and the core.

Zivi (Zivi, 1964), Levy (Levy, 1960), Thom (Thom, 1964), and Marchaterre and Hoglund (Marchaterre and Hoglund, 1968) have published other equations or graphical methods. Following a suggestion by Bankoff, Hughmark (Hughmark, 1962) developed his void fraction correlation (Collier and Thome, 1994). Much more general, but considerably more complicated correlations have also suggested. Each is based on the analysis of a large data bank. The first was produced by Premoli *et al.* (Premoli et al., 1971) at CISE. HTFS at Harwell have produced another correlation in terms of empirically chosen parameters; the details are proprietary and are only available to subscribers (Azzopardi and Hills, 2003).

The "drift flux" model has been developed principally by Zuber and Findlay in

1965 (Zuber and Findlay, 1965), Wallis in 1969 (Wallis, 1969), and Ishii in 1975 and 1977 (Ishii, 1975, 1977). The drift flux j_{gj} physically represents the volumetric rate at which gas is passing forwards (in up-flow) or backwards (in down-flow) through unit area of a plane normal to the channel axis already traveling with the flow at a velocity j. The "drift flux" model introduces a parameter called the drift velocity, which is the velocity of the gas relative to the gas-liquid mixture (Azzopardi and Hills, 2003). It is valuable only when the drift velocity is significant compared with the total volumetric flux (i.e., bubbly, slug, and churn flow patterns) (Collier and Thome, 1994). In the case of co-current downflow, increasing the gas velocity j_g leads to an increase in the void fraction, and increasing the liquid velocity j_l leads to a decrease in the void fraction.

Zuber and Findlay (Zuber and Findlay, 1965) developed a series of correlations and suggested that the void fraction α is a function of the quality x, the mass flux of the mixture G, and the effective drift velocity of the vapor V_{gj}, introducing a distribution parameter C_0:

$$\alpha = \frac{1}{C_0 \cdot \left(1 + \frac{1-x}{x} \cdot \frac{\rho_l}{\rho_g}\right) + \frac{V_{gj} \cdot \rho_g}{x \cdot G}} \tag{2.3}$$

C_0 accounts for non-uniformities in the distribution of velocity and voidage. One possible advantage of the drift flux model is its ability to provide a means of correlating the effects of flow directions, with V_{gj} being positive for upflow, negative for downflow, and zero for horizontal flow. The "drift flux" model is only suited to liquid-phase continuous flows, for which x does not reach high values (Azzopardi and Hills, 2003).

In 1995, Kocamustafaogullari and Ishii (Kocamustafaogullari and Ishii, 1995) developed the interfacial area transport equation from the statistical model of fluid particle number transport equations. This approach allows the development of closure relations which describe physical mechanisms such as breakup and coalescence. The changes in the flow regime can be predicted mechanistically by the interfacial

area transport equation. The effects of the initial and boundary conditions on the flow structure (e.g., bubble size) can be modeled by this approach (Kocamustafaogullari and Ishii, 1995).

The Beggs and Brill's correlation (Beggs and Brill, 1973) is of particular significance as it is very popular in the oil industry having been derived from a data base involving tests from inclined pipes. It starts from the homogeneous void fraction and the Froude number. A large number of other empirical and semi-empirical correlations are available in the literature for two-phase flow with various features. The most recognized ones were presented here.

2.6 Measurements of Void Fraction

Hewitt (Hewitt, 1978) provides a review of void fraction measurement techniques. The main methods used are radioactive absorption and scattering, impedance and volume measurement. Measurement of the attenuation of a beam of gamma rays in the flow is probably the most widely used technique. It is based on the interaction between the fluid and either radiation or particles. Since particles or the radiation wave length are very small as compared with atoms, interaction with matter occurs only if they hit, or at least pass very close to an atom; as a result, the particle may deviate, bounce, or hit and eventually destroy the atom (Bertola, 2003). The absorption of a collimated beam of initial intensity I_0 (photons$\cdot m^{-2} \cdot s$) is described by an exponential absorption beam as follows:

$$I = I_0 \cdot \exp(-\mu \cdot z) \tag{2.4}$$

where μ is the linear absorption coefficient and z is the distance traveled through the absorbing media. Since the linear absorption coefficient is different for different fluids, a radiation beam can be used to measure the one dimensional void fraction in two-phase flow. Experimentally, there are three contributions to the beam attenuation, those of the two fluids and that of the pipe walls (Bertola, 2003). When the liquid

and the gas exist in layers parallel to the beam, the void fraction is determined by:

$$\alpha = \frac{I_{2-phase} - I_l}{I_g - I_l} \tag{2.5}$$

where $I_{2-phase}$ is the measured intensity and I_l and I_g are the intensities measured for the case of the duct full of liquid or gas, respectively (Hewitt, 1978). For the opposite case, when the liquid and gas exist in layers perpendicular to the beam, the void fraction is determined by:

$$\alpha = \frac{\ln\left(\frac{I_{2-phase}}{I_l}\right)}{\ln\left(\frac{I_g}{I_l}\right)} \tag{2.6}$$

Both the source and the detectors must be properly shielded in order to protect the operators from exposure to radiations. The most common radiation source is ^{137}Cs, which generates γ-rays at 662 keV, requiring a lead shielding 10 cm thick; a less common (and more expensive) source is ^{241}Am, which releases a weaker radiation (60 keV), and needs only a 2 mm thick lead shielding. X-rays can be used instead of γ-rays because they can be produced with much higher intensities. On the other hand, X-ray generators are less stable and less monochromatic (Bertola, 2003).

By replacing the beam with a linear source, one can measure the cross sectional average two dimensional void fraction, but preliminary long calibrations are required in this case. Densitometers with up to five or more beams can be used to determine the cross sectional void fraction (Bertola, 2003). There is a fundamental inaccuracy in the measurement of void fraction due to the normal photon statistical fluctuations. This error can be minimized by using long counting times or strong sources. The statistical error is inversely proportional to the square root of the number of counts. A detailed discussion of statistical errors is given by Piper (Piper, 1974). The statistical error, the dynamic fluctuations of the flow field, the geometric void distribution assumption, and the systematic errors of the measurement contribute to the total uncertainty in the experimental data (Stahl and von Rohr, 2004). Gamma rays are an attractive non-invasive method, but the radioactive source strengths required are quite high.

The second most widely used class of methods for void fraction are those involving the measurement of resistance and capacitance. The electrical impedance of a two-phase flow depends on the composition and the concentration of the phases, and on the spatial distribution of the different components (i.e., flow pattern). The method is attractive since it gives instantaneous response (Hewitt, 1978). The measurement principle of the multi-sensor conductivity probe for local time averaged interfacial area concentration was first described by Ishii in 1975 (Ishii, 1975). The main limitation for using electrical resistance is that the probes must be in contact with a conductive fluid. The large measurement area and the large spacing between the sensors can cause a significant number of bubbles to miss some of the sensors. Electrical capacitance sensors provide a fully non-intrusive way to measure the void fraction. Unlike resistance, capacitance is not very sensitive to temperature. Unfortunately, for gas-liquid flow measurements, capacitances are very small; thus, proper shielding against stray capacitances and a good signal to noise are mandatory (Bertola, 2003).

A third common class of void-fraction measurement techniques is the direct or indirect measurement of the volume of the liquid and gas within the channel. Direct volume measurement can be achieved by the use of "quick-closing valves." The volumes of liquid and gas trapped when the two valves are simultaneously closed enables the void fraction to be calculated. Indirect volume measurement relies on the fact that, in a closed circuit, the generation of voids must be accompanied by some expulsion of the liquid phase of the circuit (Hewitt, 1978).

Optical probes show great promise. The technique is based on the well-known behavior of electromagnetic waves in the interface between two different media, where both reflection and refraction occur simultaneously. The optical probe is an instrument that makes it possible to distinguish two fluids of different refractive index, thanks to the abrupt change in the reflection coefficient. The probe consists of a glass optical fiber connected to one end to an infra-red source and to a photo-diode,

whereas the free end is placed inside the fluid (Bertola, 2003). These methods remain tedious and complex. Light scattering techniques have been also used to measure the concentration of the dispersed phase (Hewitt, 1978).

Numerous other methods have been used for void fractions measurements: (a) acoustic techniques since the velocity of sound in a two-phase mixture is highly sensitive to the void fraction; (b) measurements of average phase velocities; (c) microwave absorption; and (d) magnetic resonance (Hewitt, 1978).

CHAPTER III

EXPERIMENTAL APPARATUS AND PROCEDURES

In this chapter, the experimental apparatus and procedures used in this investigation are described. The small-scale experimental loop and its components are presented in Section 3.1, while those of the large-scale experimental loop are presented in Section 3.2. The settings of both experimental loops are described in Section 3.3. Sections 3.4 and 3.5 detail the procedures for measuring the void fraction and slip ratio distribution and the shock attenuation, respectively.

Two different scale experimental test facilities have been constructed with the general goal of producing steady, two-phase, liquid/gas, jets with controllable velocities and gas void fractions. The jets are formed by allowing a homogeneous mixture of liquid and gas with the appropriate volumetric flow rates and flow regime (liquid or bubbly flow) to flow through a flow conditioner and converging nozzle before being discharged into the ambient air. The open-loop test facility is instrumented to allow the liquid superficial velocity at the nozzle exit and the average (one-dimensional) gas void fraction within the jet to be measured and controlled. Different jet cross sections, viz. rectangular, circular, and annular, were produced. For rectangular and circular jets, the void fraction and slip ratio distributions were measured. For annular jets, an exploding wire placed along the axis was used to produce a shock wave. Attenuation of the shock by the surrounding annular jet was measured.

3.1 Small-Scale Experimental Loop

3.1.1 Small-Scale Loop Components

The overall schematic of the test loop is shown in Figure 3.1. The main components of the flow loop are identified by letters; a detailed list of these components is given

in Table 3.1. Referring to Figure 3.1, a 1000 liter open tank (A) is used as a reservoir. Filtered water from the reservoir is allowed to enter a centrifugal pump (B) through the 5.08 cm (2") pipe size suction line. The pump discharge line includes a water flow meter (C), a control/shutoff valve (D), a mixing "Y" where gas (air) is introduced into the water stream (H), a flexible rubber coupling (I), a flow conditioner, and finally, a nozzle (J). The jet issuing from the nozzle is discharged into the ambient air, thereby returning the liquid to the reservoir. Baffles are placed in the reservoir to prevent the gas contained in the returning liquid from entering the pump suction line.

Filtered air is supplied to the test loop by an air regulator (P) connected to a regulated house line. The gas supply line includes two flow meters (L and N) connected in series to allow accurate measurement over a wide range of gas flow rates. Pressure gauges (K and M) are placed at the exit of each flow meter in order to accurately correct for gas density variations. The gas supply line terminates in a stainless steel porous tube (F) placed with the mixing "Y" in the 5.08 cm (2") pump discharge line. The porous tube has an outer diameter of 7.9 mm (5/16") and an inner diameter of 4.8 mm (3/16"); it consists of a 13 cm long non-porous entry section welded to a 20 cm long porous tube. The porous tube end is plugged (G) so that all of the supply air can be uniformly dispersed into the water stream along the entire 20-cm length of the porous section. The porous tube is positioned along the axis of the 5.08 cm (2") pipe size water line to ensure uniformity of mixing. An air shut-off valve (E) is placed immediately upstream of the porous tube.

3.1.2 Flow Conditioner and Nozzle Design for a Planar Jet

The planar nozzle and the associated flow conditioner used in the experiments are designed according to the recommendations of Durbin *et al.* (Durbin, 2005). The purpose of the flow conditioner is to reduce cross-flow and turbulence by breaking

Table 3.1: Detailed list of the small-scale experimental loop components

Label	Description	Manufacturer	Model
A	Open tank, 1000 liter capacity		
B	Centrifugal pump with 1.0 HP (746 W), 3450 RPM Motor	BALDOR ELECTRIC CO.	CL3509 / 35C12-180
C	Machined acrylic metering tube rotameter $8 - 80$ GPM, Water	KING INSTRUMENT CO.	7205-0241W
D	Manual shut-off valve, 175 psi	MILWAUKEE VALVE CO. INC.	BB2
E	Solid brass 3-way diverter valve	WHITEY	B-45XF8
F	20-cm long stainless steel porous tube, 7.9 mm (5/16") OD, 4.8 mm (3/16") inner diameter		
G	Stainless steel plug		
H	Air/Water mixing column		
I	Flexible rubber coupling, 7.62 cm (3") to 10.16 cm (4")connection	Mc Master	
J	Flow conditioner and nozzle	In house construction	
K	Process pressure gauge, 0-15 psig	WEISS INSTRUMENTS	NF4UGY1 NON-FILLED
L	Air rotameter, 0-4.8 l/min at STP	BROOKS	1355-01C1AAA
M	Pressure gauge, 0-60 psig	ASHCROFT	
N	Air rotameter, 0-44 l/min at STP	BROOKS	1355-01C1AAA
O	6.35 cm Industrial all stainless steel process pressure gauge 0-60 psig	WIKA	232.53
P	Compressed air regulator	WILKERSON	R26-04-000 0874

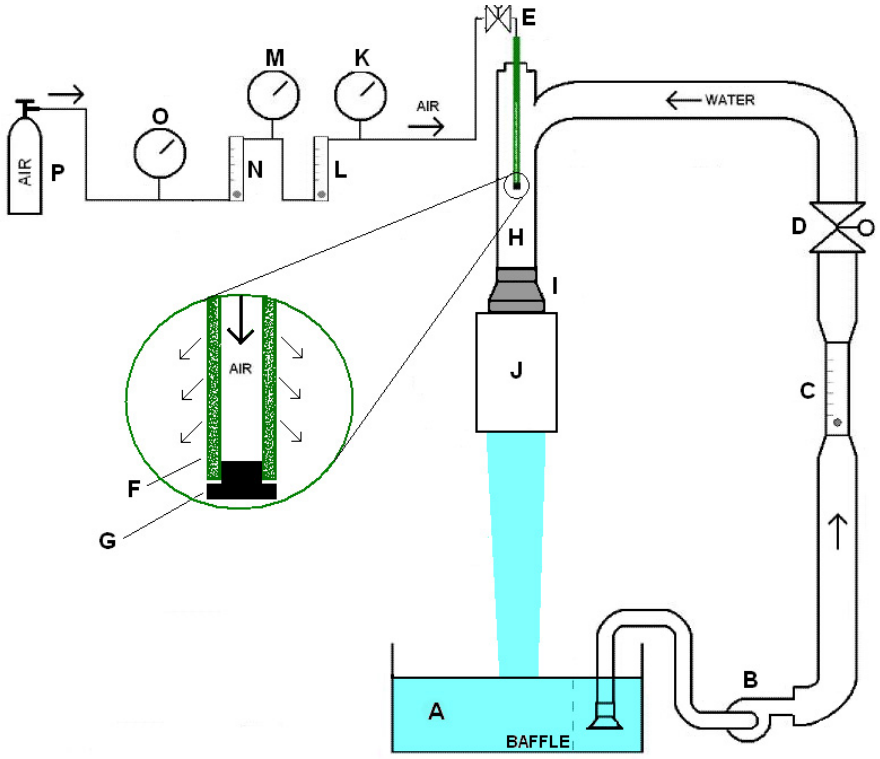

Figure 3.1: Schematic of the small-scale experimental facility

large-scale eddies, thereby increasing the rate of dissipation of turbulent kinetic energy. It is composed of multiple sections, facilitating the insertion and the cleaning of components such as perforated plate, honeycomb, and fine screen, and allowing the use of different materials. The multiple sections are manufactured by stereolithography rapid prototyping at the Georgia Tech Rapid Prototyping and Manufacturing Institute. A photograph of the flow conditioner and nozzle assembly is shown in Figure 3.2. The lists of the different flow conditioner and nozzle sections, and the flow conditioner components are provided in Tables 3.2 and 3.3, respectively.

The 7.62 cm round to 10 cm $\times$ 3 cm rectangle adapter and the nozzle are produced from Vantico SL 7510 resin using stereolithography rapid prototyping at the Georgia Tech Rapid Prototyping and Manufacturing Institute. Photographs of the adapter and the nozzle are shown in Figures 3.3 and 3.4, respectively. The coordinate system associated with this nozzle is presented in Figure 3.2. The origin is located at the

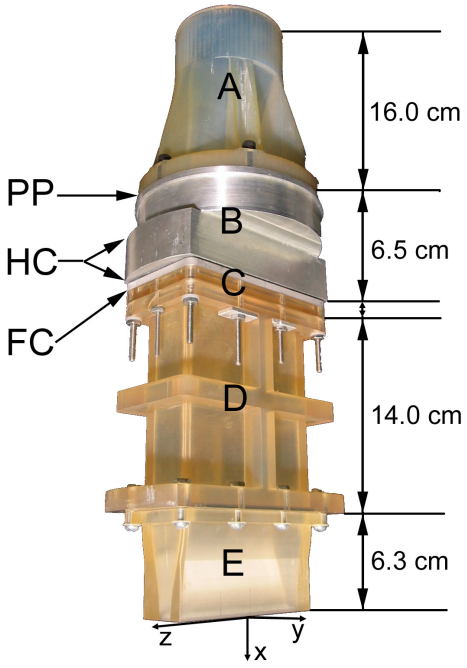

Figure 3.2: Photograph of the flow conditioner assemblies with the attached nozzle for the planar jet

Table 3.2: Detailed list of flow conditioner and nozzle sections for the planar jet

Label	Description	Material	Dimensions (length)
A	7.62 cm round to 10 cm ×3 cm rectangle adapter	Vantico SL 7510 resin	16 cm
B	Section containing the perforated plate and the honeycomb	Aluminum	6.5 cm
C	Sandwiched section containing the fine screen	Aluminum/Vantico SL 7510 resin	1.5 cm
D	10 cm × 3 cm rectangle calming chamber	Vantico SL 7510 resin	14cm
E	10 cm × 3 cm to 10 cm × 1 cm nozzle	Vantico SL 7510 resin	6.3cm

Table 3.3: Detailed list of flow conditioner components for the planar jet

Label	Component type	Description
PP	Perforated plate	50% open area with 4.8 mm staggered holes
HC	Honeycomb	3.2 mm dia. × 26 mm long circular cells
FC	Fine screen (30 × 30)	40.96% open area, 0.30 mm wire dia. w/ cell width 0.56 mm

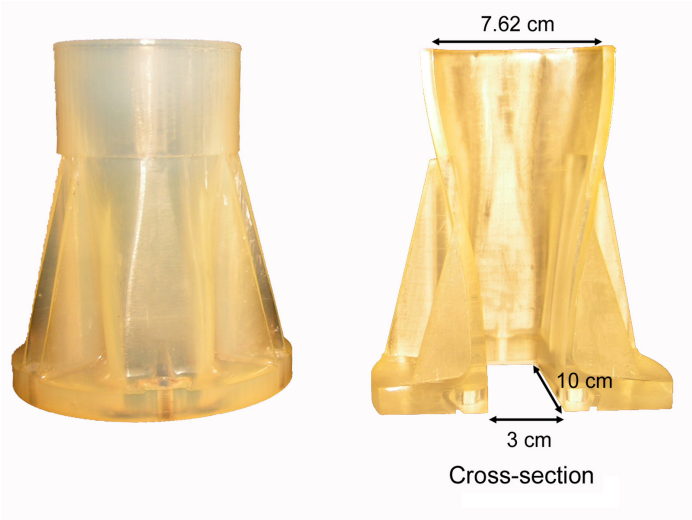

Figure 3.3: Photograph of the 7.62 cm round to 10 cm × 3 cm rectangle adapter

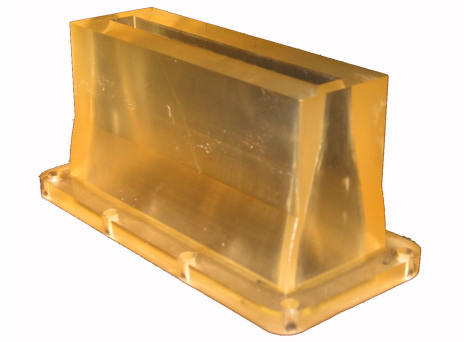

Figure 3.4: Photograph of the planar jet nozzle

center of the nozzle exit with the x-axis along the flow direction. The y- and z-axes are respectively along the short (length) and long (width) dimensions of the nozzle exit. The nozzle contracts from a rectangular cross section of $\delta_i = 3$ cm $\times$ $w_i = 10$ cm to an exit cross section of $\delta_e = 1$ cm $\times$ $w_e = 10$ cm. The two-dimensional contraction along its y-dimension follows a 5^{th} order polynomial which satisfies the Equations 3.1, 3.2, 3.3, and 3.4. The nozzle has a slight taper at its exit with a slope of 4^o.

Inlet (x = -6.3 cm): $f\ (x) = 1.5$ cm;

$$\frac{df}{dx} = 0 \tag{3.1}$$

$$\frac{d^2f}{dx^2} = 0 \tag{3.2}$$

Exit (x = 0 cm): $f\ (x) = 0.5$ cm;

$$\frac{df}{dx} = -tan(4^o) \tag{3.3}$$

$$\frac{d^2f}{dx^2} = 0 \tag{3.4}$$

Durbin *et al.* (Durbin, 2005) showed that the surface roughness has negligible effects on the free-surface fluctuations which are much greater than the measured nozzle surface roughness.

3.1.3 Flow Conditioner and Nozzle Design for a Circular Jet

The circular nozzle and the associated flow conditioner used in the experiments are designed according to the aforementioned recommendations. The flow conditioner is adapted to the new dimensions of the nozzle, while retaining the same components (perforated plate, honeycomb, thin screen). A photograph of the flow conditioner and nozzle assembly is shown in Figure 3.5. The lists of the different flow conditioner and nozzle sections, and the flow conditioner components are provided in Tables 3.4 and 3.5, respectively.

The nozzle is milled from a 6.03 cm diameter circular PVC block. Referring to Figure 3.1, the 7.62 cm to 10.16 cm rubber coupling (I) is replaced by a 5.08 cm (2”)

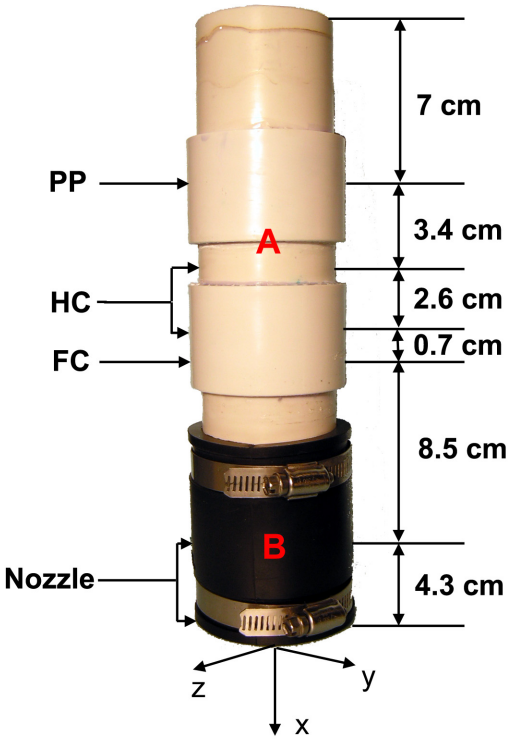

Figure 3.5: Photograph of the flow conditioner assemblies with the attached nozzle for the circular jet

Table 3.4: Detailed list of flow conditioner and nozzle sections for the circular jet

Label	Description	Material	Dimensions (length)
A	5.08 cm (2") pipe assembly	PVC	22.2 cm
B	Mc Master flexible rubber coupling 5.08 cm (2") to 5.08 cm (2") connection	rubber	8.7 cm

Table 3.5: Detailed list of flow conditioner components for the circular jet

Label	Component type	Description
PP	Perforated plate	50% open area with 4.8 mm staggered holes
HC	Honeycomb	3.2 mm dia. 25.4 mm circular cells
FC	Fine screen	37.1% open area, 0.33 mm wire dia. w/ cell width 0.51 mm

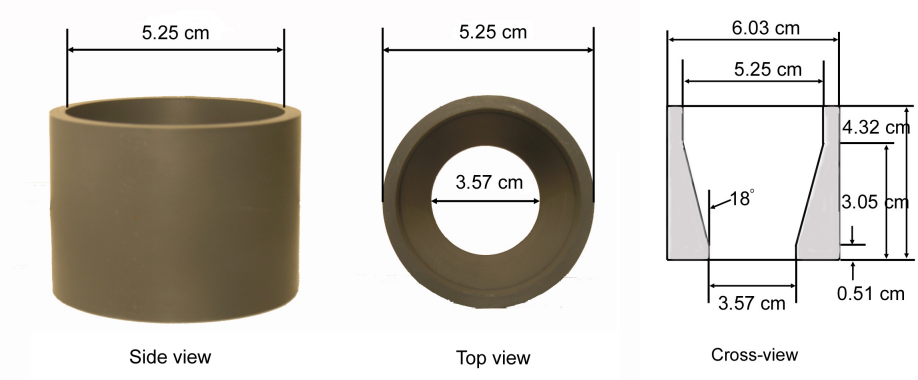

Figure 3.6: Photograph of the circular jet nozzle

to 5.08 cm (2") flexible rubber coupling, thereby connecting the mixing "Y" with the flow conditioner in the case of the circular jet. Referring to Figure 3.5, a second 5.08 cm (2") to 5.08 cm (2") flexible rubber coupling (B) is attached to the bottom of the flow conditioner and holds the nozzle. A photograph of the nozzle is shown in Figure 3.6. The coordinate system associated with this nozzle is presented in Figure 3.5. The origin is located at the center of the nozzle exit with the x-axis along the flow direction. The y- and z-axes are within the plan of the nozzle exit. The nozzle contracts from a circular cross section of $\phi_i = 5.25$ cm (2.067") diameter to an exit cross section of $\phi_e = 3.57$ cm (1.404") diameter. The three-dimensional contraction is presented in Figure 3.6. By removing the rubber boot (B) and the associated 3.57 cm (1.404") exit ID circular nozzle, the flow conditioner is mounted by itself without any nozzle on the flow loop; in that case, a 5.25 cm (2.067") diameter circular jet can be produced.

3.1.4 Flow Conditioner and Nozzle Design for an Annular Jet - Confinement Options and Components

The flow conditioner and nozzle designs follow the aforementioned recommendations. The flow conditioner includes a perforated plate, a honeycomb section, and a fine-mesh screen; a boundary-layer cutter is placed at the nozzle exit. A photograph and a schematic diagram of the flow conditioner and nozzle assembly are shown in Figure

3.7. The list of the different flow conditioner and nozzle sections is provided in Table 3.6, while the list of the flow conditioner components is presented in Table 3.7.

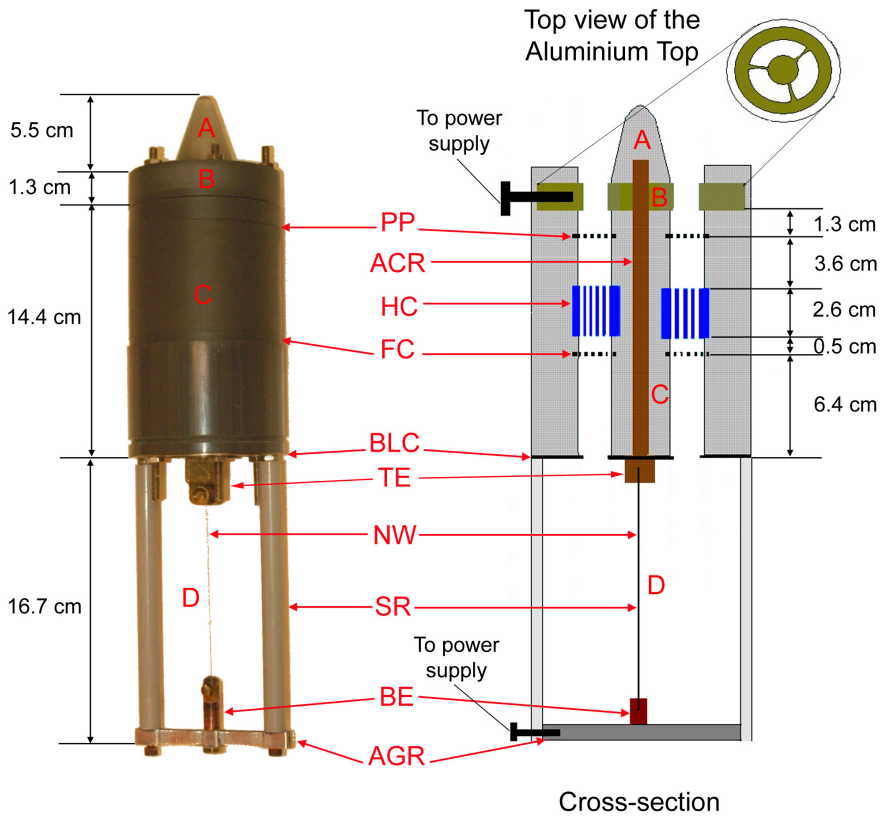

Figure 3.7: Photograph of the flow conditioner assemblies with the attached nozzle for the small annular jet

Annular jets with an outside diameter of $\varphi_{e,o} = 5.18$ cm and an inside diameter of $\varphi_{e,i} = 4.0$ cm are produced. The coordinate system associated with this nozzle is the same as that associated with the circular jet. The air compressor also supplies the tube injecting air at 2 psig (0.138 bar) into the annular jet to prevent it from collapsing. Referring to Figure 3.8, this line has a valve (Q) and a pressure gauge (R) to control the air pressure. A detailed list of the air line components is provided in Table 3.8.

The enclosure surrounding the annular jet is designed to allow experiments to be conducted with three different boundary conditions (see Figure 3.9).

Table 3.6: Detailed list of flow conditioner and nozzle sections for the small annular jet

Label	Description	Material	Dimensions (length)
A	Flow diverter	PVC	5.5 cm
B	Aluminium ring section	Aluminium	1.3 cm
C	Flow conditioner	PVC	14.4 cm
D	Discharging section		16.7 cm

Table 3.7: Detailed list of flow conditioner components for the small annular jet

Label	Component type	Description
PP	Perforated plate	50% open area with 4.8 mm staggered holes
ACR	Aluminum conducting rod	2.2 cm dia., 17 cm long
HC	Honeycomb	3.2 mm dia. $\times$ 25.4 mm circular cells
FC	Fine screen	37.1% open area, 0.33 mm wire dia. w/ cell width 0.51 mm
BLC	Aluminum boundary layer cutter	5.2 m OD, 4.0 cm inner dia.
TE	Top brass electrode	3.6 cm long
NW	Nichrome wire	0.44 mm wire dia., 11.5 cm long
SR	PVC spacer rod	15.6 cm long
BE	Bottom brass electrode	3.0 cm long
AGR	Aluminum grounding square rod	9.5 cm wide, 1 cm long and thick

Table 3.8: Detailed list of the small-scale experimental loop components

Label	Description	Manufacturer	Model
Q	Manual valve	NUPRO CO.	
R	Process pressure gauge 0-15 psig	USG / Solfrunt	33001

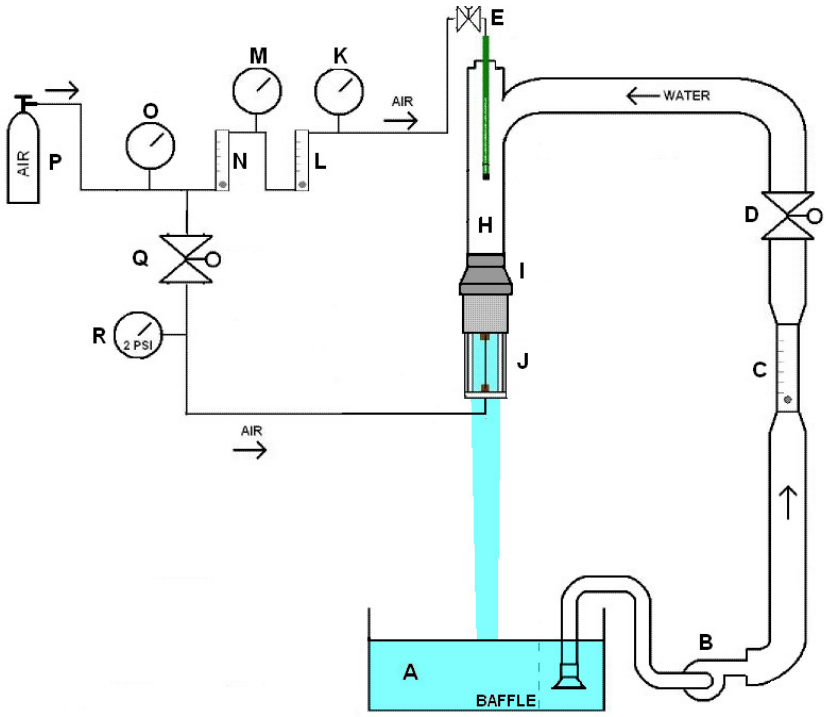

Figure 3.8: Schematic of the small-scale experimental facility adapted for the annular jet

1. The first boundary condition (unconfined shocks) pertains to the case where no shield is placed around the jet, thereby allowing the shock wave produced by an exploding wire placed along the center of the jet to freely expand.

2. The second boundary condition (radially-confined shocks) pertains to the case where the polycarbonate shield (A) surrounding the jet axially extends only to the level corresponding to bottom of the exploding wire. This geometry allows the shock waves produced by the exploding wire to be radially confined, while allowing ambient air to axially enter and exit the shielded region as pressure changes due to the reflection and expansion of the shock waves from/toward the 10.0 cm ID polycarbonate shield.

3. The third boundary condition (radially-and-axially confined shocks) pertains to the case where a cylindrical polycarbonate shield (A and B, 9.5 cm ID) is placed

along the entire length of the annular jet extending from the top of the flow conditioner to a point approximately 5.0 cm below the free surface of the water reservoir. This geometry allows the shock waves produced by the exploding wire to be confined within the polycarbonate shield while allowing the two-phase jet to enter and leave the enclosed volume unimpeded.

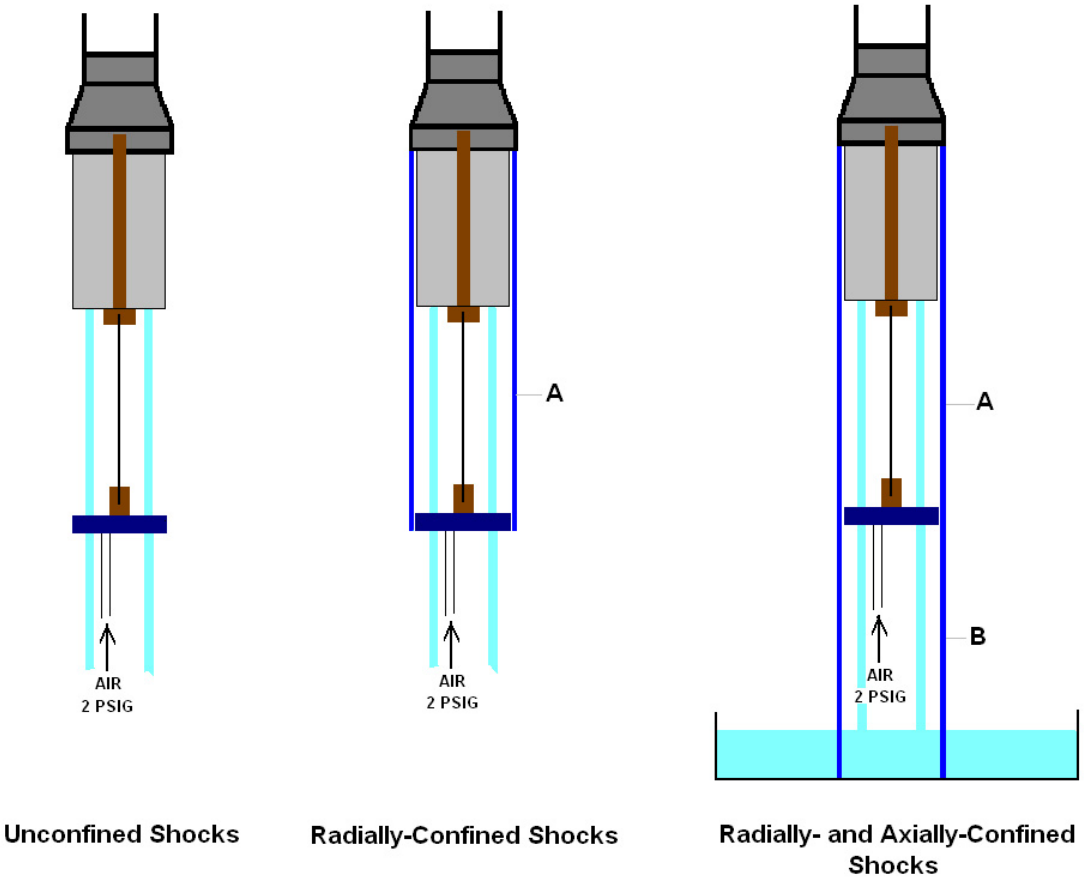

Figure 3.9: Schematic diagram of the three system boundary conditions

3.2 Large-Scale Experimental Loop

3.2.1 Large-Scale Loop Components

In order to quantify scale effects on jet behavior and shock attenuation, a larger flow loop with a larger annular nozzle and flow conditioner has been constructed. The large-scale experimental flow loop occupies two floors and spans a total height of

approximately 5.5 m. The upper part of the flow loop contains the open test section, while the lower part contains the main circulation pump and storage tanks. The overall schematic of the test loop is shown in Figure 3.10. The main components of the flow loop are identified by letters; a detailed list of these components is given in Table 3.9.

Referring to Figure 3.10, the recirculating flow loop is driven by a three-phase centrifugal pump (A). Water is pumped up through 7.62 cm (3") PVC pipe over the entire apparatus height of approximately 5.5 m above the pump (A). A flow meter (C) above the pump measures the flow rate in the test section. A flexible rubber coupling (E) connects the 7.62 cm PVC pipe to the 15.24 cm diameter flange of the flow conditioner (F). The water passes through the flow conditioner inlet, then exits the flow conditioner/nozzle where the flow has an outside diameter of 15.2 cm and an inside diameter of 12.7 cm. Earlier experiments showed that excitation of the flow by the pump is minimal (Durbin, 2005). Water issues into ambient air from the nozzle exit, forming the annular jet in the open test section, and falls about 1.9 m before collecting in the upper 1.5 m^3 receiving tank (H). Two 5.08 cm (2") PVC pipes drain the water to the lower 1.23 m^3 supply tank (L); the flow through these pipes is controlled by a ball and a butterfly valve (J and K, respectively). A sump pump (I) is connected to a 5.08 cm (2") PVC pipe leading to the bottom supply tank (L). A float switch activates the sump pump when the water level in the upper tank reaches two-thirds of the tank volume to provide additional drainage to the bottom tank required at the highest Reynolds number. The flow to the test section is controlled by a bypass butterfly valve (B). When valve (B) is fully open, all the flow is recirculated at a flow rate of 0.79 m^3/min from the tank (L) through a monofilament polyester mesh filter (M) placed across the inlet to pump (A). This filter traps debris, thereby minimizing blockage of the flow conditioner. By partially closing valve (B), a portion of the flow is redirected to the open test section, with the remainder passing

through the recirculation loop. The overflow tank (Q) is connected to the bottom supply tank by a length of 5.08 cm (2") PVC pipe. Ball valves (N), (O), and (P) allow drainage of the entire flow loop through a drain in the laboratory floor; (N) and (P) allow the bottom supply tank to be drained separately from the overflow tank. A 20 kW chiller (R) maintains the temperature of the water at a constant value of approximately 24^{o}C. The chiller pulls water from the overflow tank (Q) through an ordinary garden hose and discharges the chilled water to the bottom supply tank (L). A water level alarm sounds when the bottom supply (L) tank is approximately 10 cm from overflowing.

Filtered air is supplied to the test loop by an air regulator (S) connected to a regulated house line. The gas supply line includes two flow meters (U and W) connected in series. Pressure gauges (V and X) are placed at the exit of each flow meter. The gas supply line terminates in a stainless steel porous tube (D) positioned along the axis of the 7.62 cm (3") pump discharge water line to ensure uniformity of mixing. The porous tube has an outer diameter of 3.24 cm (1.276") and an inner diameter of 2.37 cm (0.935"); it is 91.44 cm long and plugged. An air shut-off valve (Y) is placed upstream of the porous tube.

3.2.2 Flow Conditioner and Nozzle Design for the Annular Jet - Confinement and Components

The flow conditioner has been adapted to the new dimensions of the nozzle, while retaining the same components (perforated plate, honeycomb, thin screen, boundary layer cutter, aluminum rod and electrodes). A photograph and a schematic diagram of the flow conditioner and nozzle assembly for the large annular jets are shown in Figure 3.11. The lists of the different flow conditioner and nozzle sections, and the flow conditioner components are provided in Table 3.10 and 3.11, respectively. Annular jets with an outside diameter of 15.2 cm and an inside diameter of 12.7 cm are produced. The coordinate system associated with this nozzle is the same as that

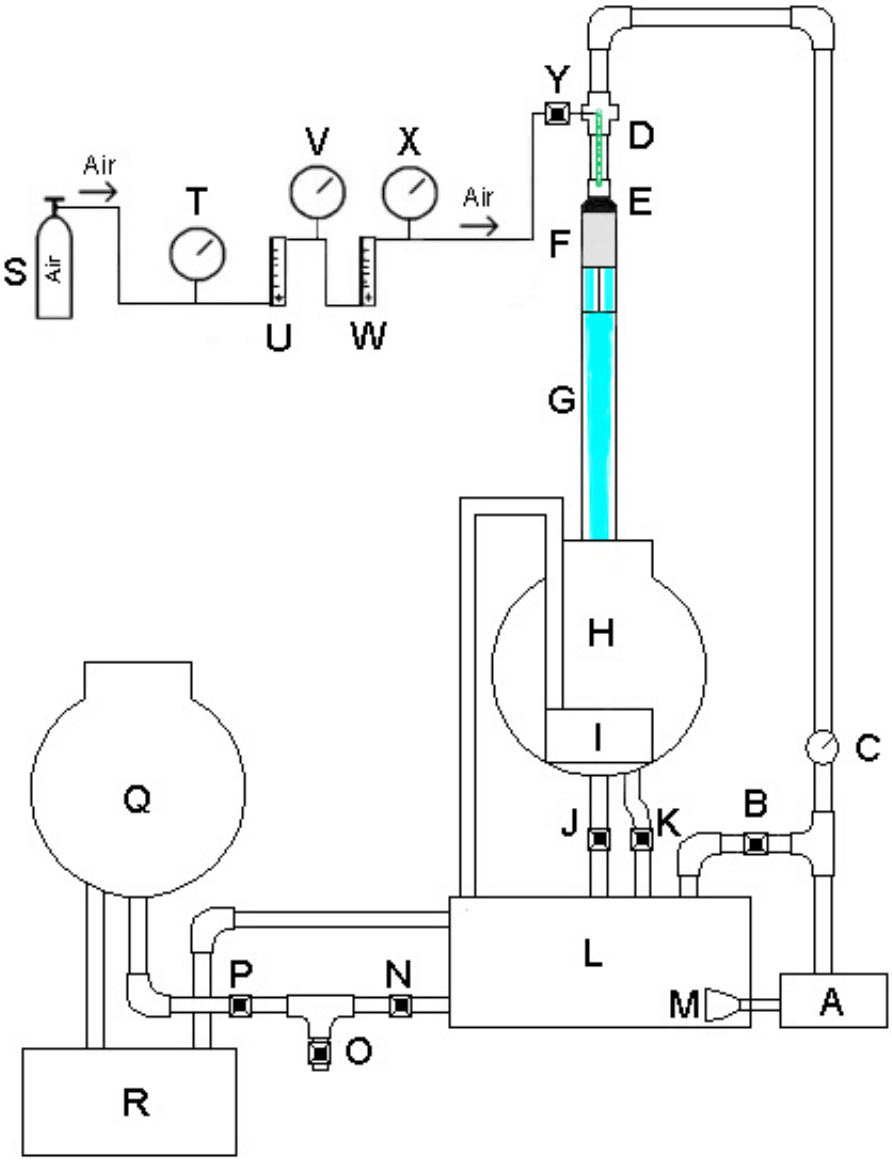

Figure 3.10: Schematic of the large-scale experimental facility

Table 3.9: Detailed list of the large-scale experimental loop components

Label	Description	Manufacturer	Model
A	Recirculating pump with 7.5 HP (5.62 kW), 3465 RPM Motor	TEEL	6406291A
B	Bypass Valve, PVC, 7.62 cm, 10.3 bar	SPEARS	
C	Flow meter, 0.04-0.4 m^3/min, 13.8 bar	SEE-FLO	3223-12T2
D	0.914 cm long stainless steel porous tube with stainless steel plug, 2.54cm (1") pipe size, 3.34cm (1.315") ID		
E	Flexible rubber coupling, 10.16 cm to 15.24 cm connection	Mc Master	
F	Flow conditioner and nozzle	In house construction	
G	20 cm ID, 2.2 m long polycarbonate shield		
H	Upper receiving tank, 1.5 m^3 capacity		
I	Sump pump with 0.3 kW, 1700 RPM	TEEL	4RK65
J	Ball valve, bronze, 5.08 cm, 12.1 bar	MILWAUKEE	
K	Butterfly valve, bronze, 5.08 cm, 10.3 bar	GRINNELL	
L	Bottom supply tank, 1.23 m^3 capacity		
M	Filter Monofilament polyester mesh, 45.7 × 45.7 mesh, 0.037 cm opening	Mc MASTER	9218T65
N,O	Ball valve, PVC, 5.08 cm, 10.3bar	WATERWHIZ	
P	Ball valve, PVC, 5.08 cm	HAYNARD	
Q	Bottom overflow tank, 1.5 m^3 capacity		
R	20 kW Chiller	AFFINITY	FAA-050D
S	Compressed air regulator	WILKERSON	R26-04-000 0874
T	Industrial all stainless steel process pressure gauge, 6.35 cm , 0-60 psig	WIKA	232.53
U	Air rotameter, 0-44 l/min at STP	BROOKS	1355-01C1AAA
V	Pressure gauge, 0-60 psig	ASHCROFT	
W	Air rotameter, 0-4.8l/min at STP	BROOKS	1355-01C1AAA
X	Process pressure gauge, 0-15 psig	WEISS INSTRUMENTS	NF4UGY1 NON-FILLED
Y	Solid brass 3-way diverter valve	WHITEY	B-45XF8

associated with the small annular jet. Only one boundary condition has been used (radially and axially confined shocks) for experiments using the large annular jets; a cylindrical polycarbonate shield (20.0 cm ID) is placed along the entire length of the annular jet extending from the top of the flow conditioner to a point approximately 30 cm below the entrance of the upper receiving tank.

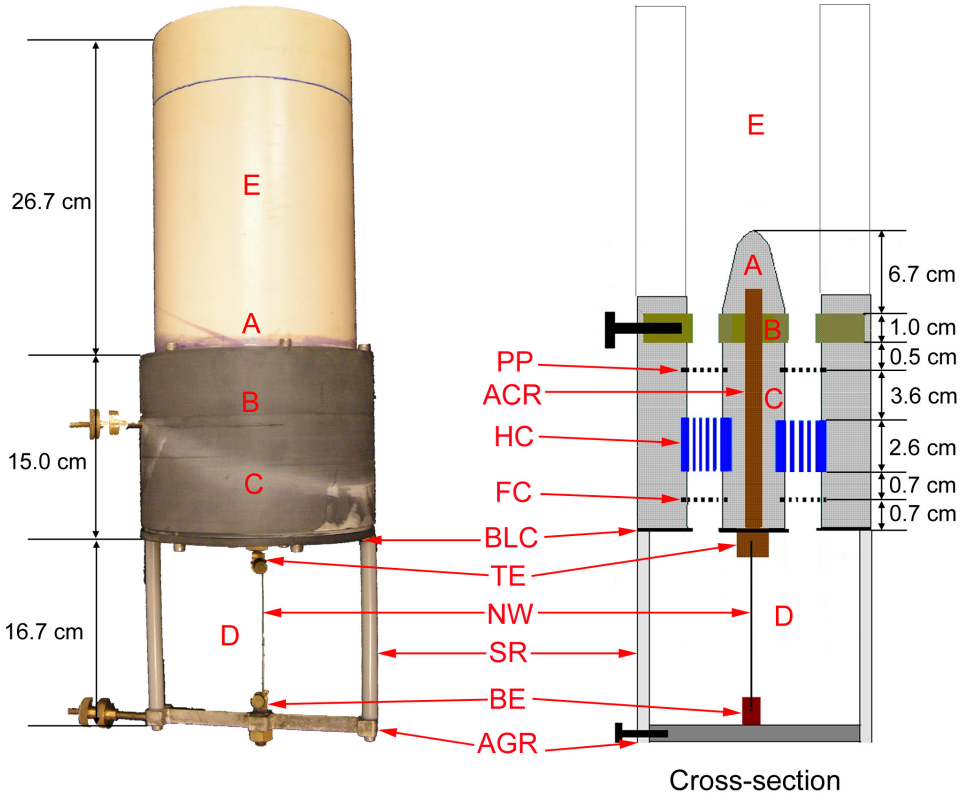

Figure 3.11: Photograph of the flow conditioner assemblies with the attached nozzle for the large annular jet

3.3 Settings of the Small- and the Large-Scale Experimental Loops

3.3.1 Setting the Superficial Liquid Velocity and Gas Void Fraction

- For the Small-Scale Experimental Loop:

Prior to each experimental run, the flow conditioning sections are examined for any debris collected from prior experiments. Any debris is removed using jets of water and

Table 3.10: Detailed list of flow conditioner and nozzle sections for the small annular jet

Label	Description	Material	Dimensions (length)
A	Flow diverter	PVC	6.7 cm
B	Aluminium ring section	Aluminium	1.0 cm
C	Flow conditioner	PVC	15.0 cm
D	Discharging section		16.7 cm
E	15.24 cm (6") PVC pipe		26.7 cm

Table 3.11: Detailed list of flow conditioner components for the small annular jet

Label	Component type	Description
PP	Perforated plate	50% open area with 4.8 mm staggered holes
ACR	Aluminum conducting rod	2.2 cm dia., 12 cm long
HC	Honeycomb	3.2 mm dia. $\times$ 25.4 mm circular cells
FC	Fine screen	37.1% open area, 0.33 mm wire dia. w/ cell width 0.51 mm
BLC	Aluminum boundary layer cutter	15.2 m OD, 12.7 cm ID
TE	Top brass electrode	3.3 cm long
NW	Nichrome wire	0.44 mm wire dia., 11.5 cm long
SR	PVC spacer rod	15.6 cm long
BE	Bottom brass electrode	2.0 cm long
AGR	Aluminum grounding square rod	20 cm wide, 1.2 m long, and 2.5 cm thick

compressed air with the flow conditioner removed from the test section. Referring to Figure 3.1, the reservoir is emptied every week, and the water reservoir (A) is filled with nearly 400 liters of deionized water so that the pump inlet (B) is fully submerged. For experiments with radially-and-axially confined shocks, the water level in the reservoir should be higher than the shield bottom without submerging the lower pressure transducer. Both the water and air isolation valves (respectively D, and E) are closed. The nozzle and associated flow conditioner (J) are attached to the 5.08 cm (2") water supply line (H) immediately following the mixing "Y". If necessary, a new Ni-chrome wire is installed between the electrodes; the appropriate shield is then attached. The liquid control valve (D) is then slowly opened until the desired liquid flow rate (i.e., the desired liquid superficial velocity at the nozzle exit) is reached (C). The gas flow rate is then gradually increased until the desired volume fraction is achieved. This is accomplished by adjusting the pressure regulator (O) to produce a supply pressure of 30 psig (2.068 bar) (pressure gauge M), opening the on/off ball valve at the top of the porous tube (E), and adjusting the gas rotameter needle valve (L and/or N) to obtain the required gas flow rate. The average one-dimensional homogeneous void fraction is the ratio between the volumetric flow rate of the gas and the total (liquid plus gas) volumetric flow rate. Appropriate density corrections are applied to the gas flow meter readings depending on the supply pressure (M or K). Care is taken to remain within the calibrated ranges of the flow meters and pressure gauges. The settings of the rotameter are calculated according the Equations 3.5, 3.6, and 3.7. We defined the following variables:

P_M = Pressure at the pressure gauge (M) [psig]

$\dot{V}_{l,e}$ = Liquid flow rate (C) at the nozzle exit [l/min]

α_e = Desired void fraction within the jet at the nozzle exit [-].

$\dot{V}_{g,e}$ = Air flow rate in water at the nozzle exit [l/min]

$\dot{V}_{g,P_M}$ = Air flow rate at pressure P_M [l/min]

The homogeneous void fraction is defined in Equation 3.5. The relation between the pressure, and the flow rate at the pressure gauge (M), and at the nozzle exit are given in Equation 3.6. The air flow rate adjusted with the rotameters (L and/or N) is given by Equation 3.7.

$$\alpha_e = \frac{\dot{V}_{g,e}}{\dot{V}_{g,e} + \dot{V}_{l,e}} \tag{3.5}$$

$$\dot{V}_{g,e} = \dot{V}_{g,P_M} \cdot \sqrt{\frac{P_M + P_{atm}}{P_{atm}}} \tag{3.6}$$

$$\dot{V}_{g,P_M} = \frac{\frac{\alpha_e}{1-\alpha_e} \cdot \dot{V}_{l,e}}{\sqrt{\frac{P_M + P_{atm}}{P_{atm}}}} \tag{3.7}$$

Referring to Figure 3.8, in order to prevent the annular jet from collapsing, a slight positive pressure is maintained in the center of the jet by adjusting the control valve (Q) to produce an air by-pass pressure (pressure gauge R) of 2 psig (0.1384 bar). A constant air bypass pressure (2 psig) is used for all experiments (regardless of void fraction or superficial velocity) including those for single-phase (liquid) jets. Once the desired liquid and gas volumetric flow rates are reached, the system is allowed to operate continuously in a steady-state.

- For the Large-Scale Experimental Loop:

Debris inside the annular flow conditioner are removed using jets of water and compressed air. Referring to Figure 3.10, the reservoirs (H, L, and Q) are emptied every week, and the bottom supply tank (L) is filled with nearly 2.6 m^3 of deionized water. A new Ni-chrome wire is installed between the electrodes; the polycarbonate shield is then attached to the annular flow conditioner. The water valves (J, K, N, and P) are open; the water valves (B and O) as well as the air valve (Y) are closed. The chiller is turned on and allowed to maintain the water temperature to 24^{o}C. The recirculating pump (A) is turned on. The liquid control valve (B) is then slowly opened until

the desired liquid flow rate (i.e., the desired liquid superficial velocity at the nozzle exit) is reached (C). The gas flow rate is then gradually increased according to the aforementioned method until the desired equilibrium void fraction is achieved. This is accomplished by adjusting the pressure regulator (S) to produce a supply pressure of 30 psig (2.068 bar) (pressure gauge T), opening the on/off ball valve (Y), and adjusting the gas rotameter needle valve (U and/or W) to obtain the required gas flow rate. Appropriate density corrections are applied to the gas flow meter readings depending on the supply pressure (V or X). Care is taken to remain within the calibrated ranges of the flow meters and pressure gauges. Once the desired liquid and gas volumetric flow rates are reached, the system is allowed to operate continuously in a steady-state.

3.3.2 Photographs of Two-phase Jets

The jets are photographed using a progressive scanning full frame shutter camera (Pulnix Model # TM-9701), attached to a personal computer and controlled by PX500 PIV software. The camera is focused on the mid-plane of the jet, and is positioned so that the nozzle edge (exit plane) and at least ten nozzle thicknesses/diameters can be viewed. Two or three halogen lights are strategically placed to indirectly reflect off a white backdrop in order to allow clear imaging of the two-phase regime within the jets. This minimizes the reflection of the light off the front of the flow as well as preventing the bright spots that occur when the light is placed directly behind the flow. The computer software is then used to capture and record a series of 30 images within a second. In the case of annular jets, a series of 1000 images is recorded within a second.

3.4 Measurements of Void Fraction and Slip Ratio Distribution

3.4.1 Instrumentation for Void Fraction Measurements

- Gamma-Ray Densitometer and Counter:

A 45 mCi Americium 241 (Am-241) sealed source is used as the radiation source in the Gamma-Ray Densitometer. Referring to Figure 3.12, the source is exposed when its shutter is opened by pulling the lock pin, lifting the shutter until the magnet on the top contacts the limit switch, and inserting again the lock pin into the upper hole. A warning light is connected to the limit switch and flashes whenever the magnet on the top of the shutter contacts with the limit switch. The Am-241 sealed source is mounted on a rubber-lined rigid clamp attached to a horizontal movement adjuster, allowing the source to be easily positioned onto the 19.6 cm rigid clamp. Four mounting brackets are bolted on the Am-241 sealed source, thereby providing a brace to hold a gamma-ray radiation detector in place (see Figure 3.13). The largest mounting bracket of the densitometer is fastened onto a vertical movement adjuster (NRC Model 370) via a mounting plate. The Am-241 sealed source is adjusted on the rigid clamp with the horizontal movement adjuster, so that the source beam (5 mm diameter) can be positioned on the x-axis passing by the center of the nozzle exit 4.0 cm away from the center of the nozzle. The Am-241 sealed source can only be moved vertically along the x-axis. A gamma-ray radiation detector is clamped to two mounting brackets 7.8 cm opposite from the source hole. The gamma-ray radiation detector is connected to electrical power associated to a bias voltage supply, an amplifier and timing single-channel analyzer (SCA), and a timer and counter. The list of the ORTEC radiation instruments is provided in Table 3.12. A schematic diagram of the radiation instrumentation assembly and the nozzle is shown in Figure 3.14.

- Container:

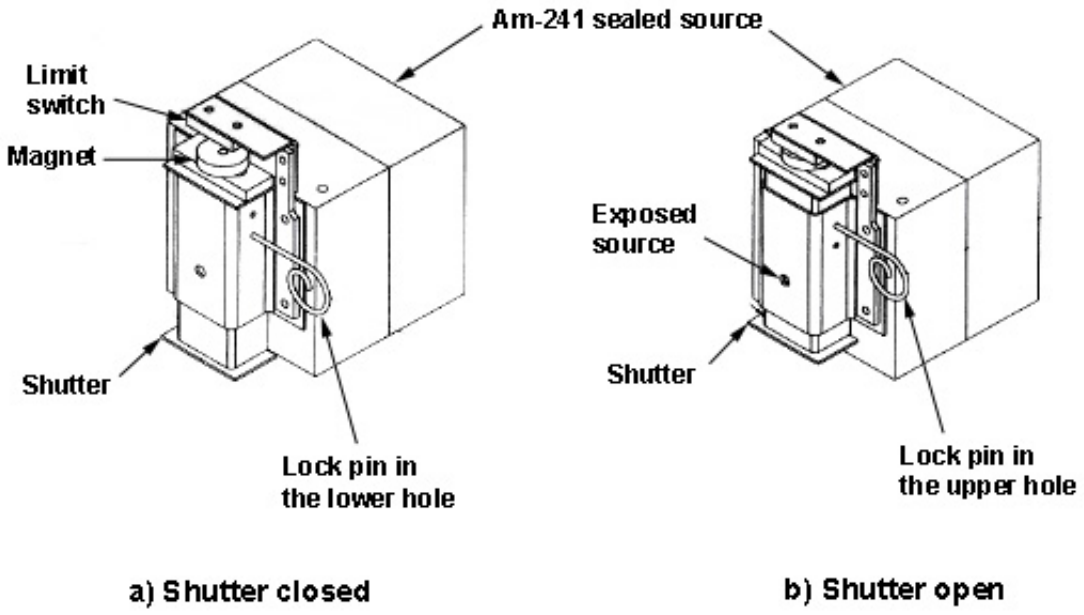

Figure 3.12: Schematic diagram of the Am-241 sealed source shown in a) with shutter closed, and b) with shutter open

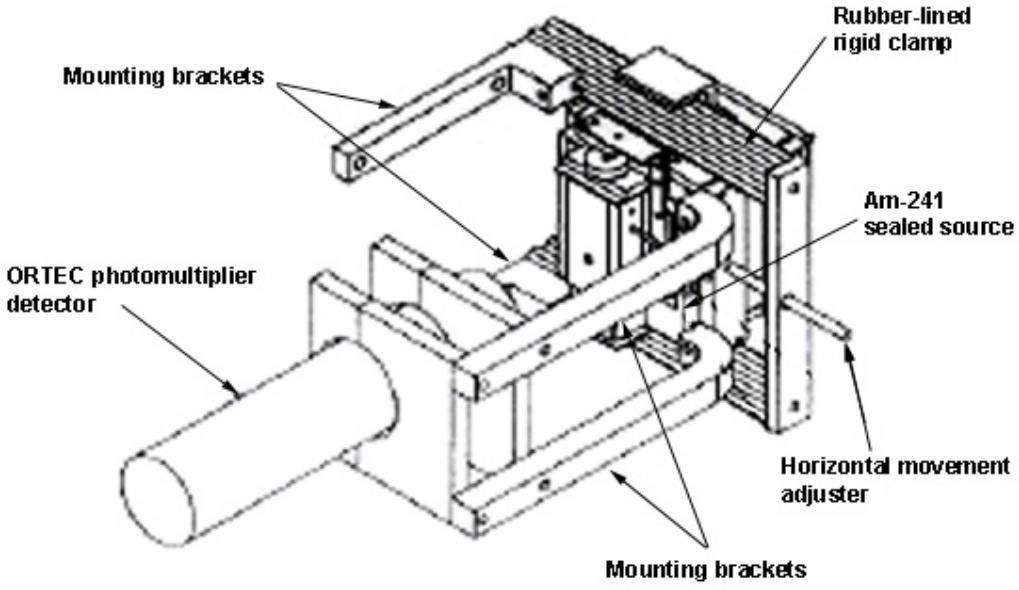

Figure 3.13: Schematic diagram of the Am-241 sealed source/detector assembly

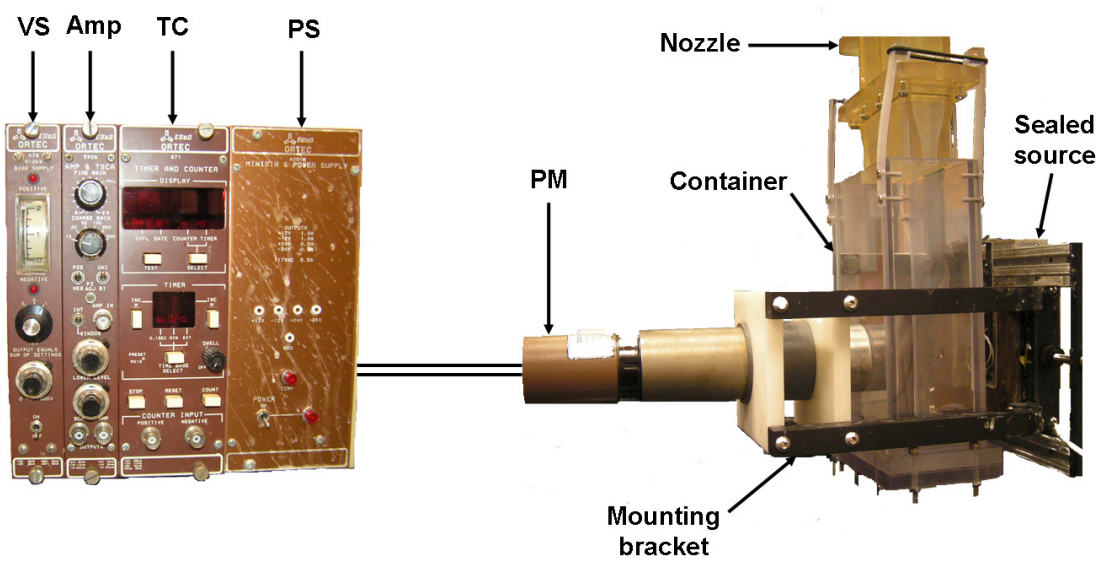

Figure 3.14: Schematic diagram of the radiation instrumentation assembly

Table 3.12: Detailed list of the ORTEC radiation instruments

Label	Description	Manufacturer	Model
PM	Photomultiplier base with preamp detector	ORTEC	276
PS	Minibin and power supply	EG&G ORTEC	401M
VS	2-kV bias voltage supply	EG&G ORTEC	478
Amp	Amplifier and timing single-channel analyzer	EG&G ORTEC	590A
TC	Timer and counter	EG&G ORTEC	871

A container is used to hold water for the densitometer calibration process. A rectangular container of inner dimensions $w_C = 12$ cm $\times$ $\delta_C = 6.5$ cm $\times$ $h_C = 24$ cm is constructed from acrylic plastic. The top of the container is open, while the bottom has a removable rectangular plate than can seal the container. The container is used for the air/water calibration of the densitometer as well as for running plunging jet experiments. It is directly clamped on the nozzle of the studied jet, thereby maintaining a constant position during the experimental gamma-ray counting; the top of the container is positioned at the same elevation as the nozzle exit.

- Jet Thickness Tester:

The jet thickness tester is a rectangular frame of inner dimensions 19.1 cm $\times$ 6.35 cm made from 0.953 cm (3/8") square aluminum bar stock (see Figure 3.15). One of the smaller sides is mounted to the vertical movement adjuster via the same mounting plate that is used to mount the gamma-ray densitometer. One very fine thread screw (1.9 mm diameter) is mounted on each of the larger sides corresponding to the centerline of the jet. A Lufkin depth micrometer is used in order to measure the distance from the screw-head to the side of the jet thickness tester.

3.4.2 Void Fraction and Slip Ratio Measurement Procedures

- Use of the densitometer:

Prior to any manipulation of the Am-241 sealed source, the user must receive a training on radiation safety and equipment from the Office of Radiological Safety. A Geiger survey count and a wipe test for leakage or contamination must be conducted. During any manipulation of the Am-241 sealed source, the user must always carry a dosimeter which measures the radiation exposure. The gamma-ray densitometer is set up according to pre-defined specifications (Kern, 2007). The list of the settings on the gamma-ray densitometer is provided in Table 3.13. Calibration of the gamma-ray

Table 3.13: Settings of the ORTEC radiation instruments

2 kV bias voltage supply	Amplifier and timing single-channel analyzer
Positive 1.316 kV	Fine gain = 1.07 Coarse gain = 10 Positive input pulses from the preamplifier Unipolar output shape Integral single discriminator threshold Analyzer window width = 8.02 Lower level = 2.58

densitometer have to be performed every day before and after conducting a experimental trial. The calibration process accounts for the change in physical properties such as room temperature and relative humidity. Experiments to measure void fraction and slip ratio distributions are performed on the small-scale experimental loop with planar and circular jets. Referring to Figure 3.1, the nozzle and associated flow conditioner (J) are attached to the 5.08 cm (2") water supply line (H) immediately following the mixing "Y" via the rubber boot (I). The gamma-ray densitometer is fastened onto the vertical movement adjuster, so that the source beam is positioned on the x-axis passing by the center of the nozzle exit. The gamma-ray radiation detector is connected to electrical power. The rectangular container is clamped to the nozzle between the detector and source and filled with deionized water. The bias voltage supply and the power supply are then turned on. The timer and the counter are stopped and reset to count for five minutes. In 2006, Brian Kern (Kern, 2007) concluded that a five minute counting time for the calibration of the gamma-ray densitometer is statistically sufficient. The shutter on the Am-241 sealed source is safely opened by pulling the lock pin, lifting the shutter until the magnet on the top contacts the limit switch, and inserting the lock pin into the upper hole (see Figure 3.12). The counter is started, and the number of counts after five minutes, denoted I_l is recorded. The counter is then reset to zero. The calibration with water is repeated five times.

The shutter on the Am-241 sealed source is then closed by removing the lock pin from the upper hole, pulling down the shutter, and inserting the lock pin into the lower hole (see Figure 3.12). The water-filled container is emptied, cleaned and dried. The bottom of the container is then removed. Again the gamma-ray densitometer is used for five minutes and the number of counts, denoted I_g is recorded. This process is also repeated five times. This process is repeated every day at the end of the experimental trial. The ten calibration values of I_l and I_g are averaged for each experimental trial $I_{l,avg}$ and $I_{g,avg}$, respectively; the averaged values $I_{l,avg}$ and $I_{g,avg}$ are used to calculate the void fraction in the experimental trial. The gamma-ray densitometer is now calibrated and ready to use for void fraction distribution measurements.

The desired liquid and gas volumetric flow rates are reached according to the procedure described in Section 3.3; the system is then allowed to operate continuously in a steady-state. The densitometer is then used for five minutes and the number of counts at the desired x-location, denoted as $I_{2-phase}(x)$ is recorded. Experiments are repeated at different locations, for different void fractions and liquid superficial velocities. At the end of the test run, the gamma-ray densitometer is calibrated according to the aforementioned process.

- Measurement of the jet thickness:

Once the counts $I_{2-phase}$(x) are recorded for different locations, void fractions, and liquid superficial velocities, the gamma-ray densitometer is removed from the vertical movement rail. The jet thickness tester is then fastened onto the vertical movement rail. The tester is designed to measure the thickness of the jet on its centerline and at the various x-locations where the densitometer measurements were taken. Using to aforementioned method, the liquid control valve is turned on and the desired water and air flows are set (see Section 3.3). The screws are turned towards the jet until a wake is formed from touching it. The screws are then turned away, until the wake is at its faintest. Using a depth micrometer, the distances from the screw head to the

side of the apparatus $L_{j,1}(x)$ and $L_{j,2}(x)$ are measured (see Figure 3.15). The jet is then turned off and the screws are allowed to touch each other. Again, the distances from the screw head to the side of the apparatus $L_{s,1}(x)$ and $L_{s,2}(x)$are measured. The jet thickness is then $\delta_{jet}(x) = [L_{j,1}(x) + L_{j,2}(x)$ - $L_{s,1}(x)$ - $L_{s,2}(x)]$. The tester is then moved to the next x-location.

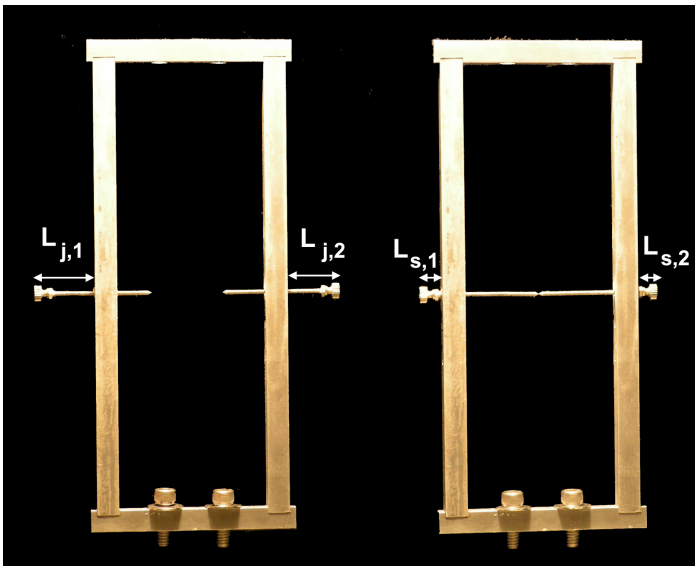

Figure 3.15: Photograph of the jet thickness tester

- Measurement of the jet width:

As mentioned above, the jets are photographed using a progressive scanning full frame shutter camera. The pictures are scaled by measuring the number of pixels on the nozzle exit and comparing it to the known nozzle width. The width of the jet, denoted $w(x)$ is then calculated with the same method at the different x-locations.

3.5 Measurements of Shock Attenuation

3.5.1 Instrumentation

- Exploding wire:

Experiments on shock attenuation are conducted using annular two-phase (water/air) jets (see Sections 3.1.4 and 3.2.2). A shock wave is produced by exploding the Ni-chrome wire placed along the center of the jet immediately after the nozzle exit (see Figures 3.7 and 3.11). The wire is clamped between two electrodes connected to a high-energy, low-impedance, capacitive discharge pulser (Slapshot Model 6KS manufactured by Plasma Research Corp, Oakland, CA). The Slapshot pulser can store up to 6 kJ at a maximum charge of 2400 volts. Since the output impedance is about 0.1 Ω, currents of several thousand amps can be produced in low impedance loads. The output voltage (up to 2400 volts) and the output current (determined by the load impedance) are set by the user from 200 volts to full scale with a panel meter controller that also indicates the charge status of the pulser at all times. This provides the means to control the initial shock strength produced by the exploding wire.

- Pressure transducers:

Piezoelectric quartz crystals transducers purchased from PCB Piezotronics, Inc. are used to measuring the transient dynamic pressure history outside the annular jet. A photograph show the transducers in Figure 3.16. A list of the transducers with their characteristics is presented in Table 3.14. The transducers (A) and (B) are used on

Table 3.14: Detailed list of pressure transducers and their characteristics

Label	Transducer model	Measurement range	Diameter	Length	Sensitivity
A	102A07	$0 - 50$ psig	0.95 cm	3.73 cm	100.4 mV/psi
B	HE102A06	$0 - 500$ psig	0.95 cm	3.76 cm	10.50 mV/psi
C	106B	$0 - 8.3$ psig	1.10 cm	3.99 cm	298.5 mV/psi

the small-scale flow loop, while the transducer (C) is mounted on the large-scale flow loop. Experiments run on the small-scale flow loop are conducted using three different confinements (see Section 3.1.4). For experiments with either radially-confined or

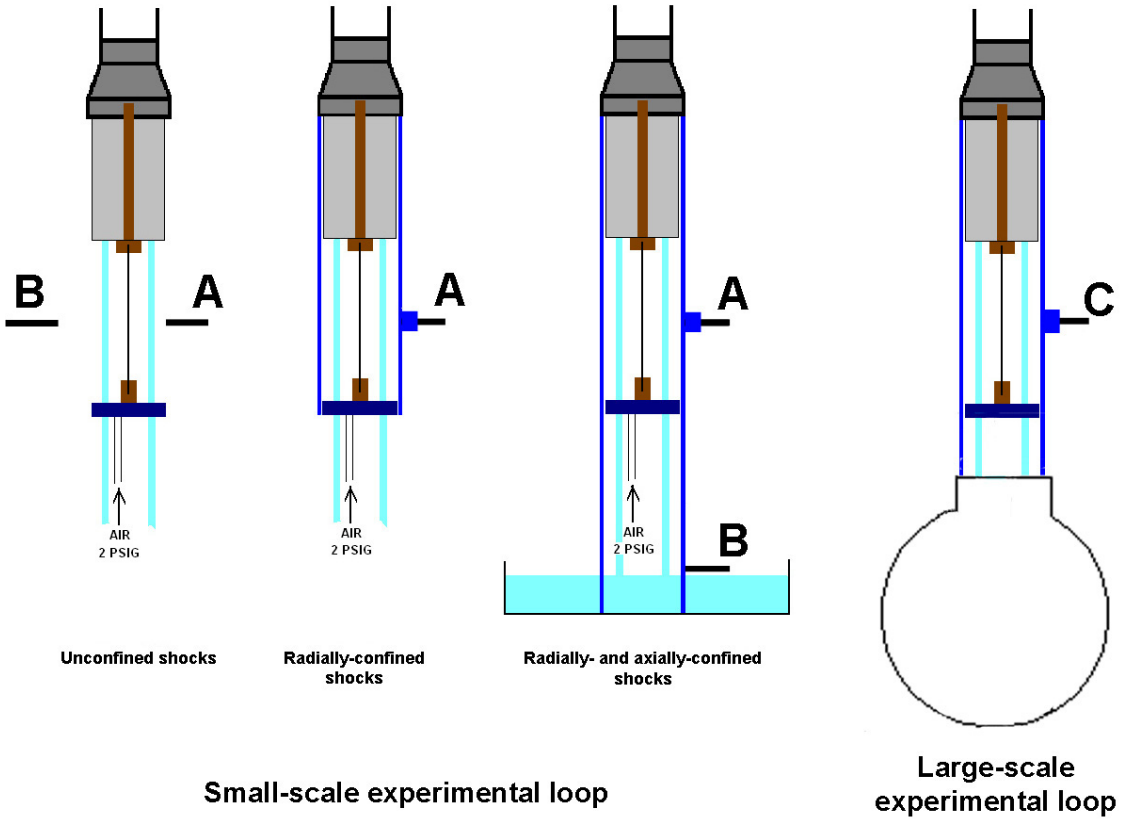

Figure 3.16: Schematic diagram of the position of the transducers

radially-and-axially-confined shocks, the pressure transducer (A) is mounted within a re-enforced 2.7 cm thick segment of the 3.2 mm thick polycarbonate shield wall so that its surface is flush with the shield's inner surface (10.0 cm ID) at an elevation corresponding to the mid elevation of the exploding wire (7.5 cm below the jet entrance point). The same transducer (A) is used for experiments with unconfined shocks by rigidly mounting it at a point 5.0 cm away from the jet axis at the mid elevation of the exploding wire, while the second pressure transducer (B) is mounted at a point 50 cm away from the jet axis at the mid elevation of the exploding wire, facing the transducer (A). For experiments with radially-and-axially-confined shocks, the same pressure (B) is mounted within the shield wall at an elevation immediately above the free surface in the water reservoir (100 cm below the jet entrance point). Its electrical connection is insulated from water with electrical tape. Experiments run on the large-scale flow loop are only conducted using a radially-and-axially confined shock. The pressure transducer (C) is mounted within a re-enforced 2.2 cm thick segment of the 3.2 mm thick polycarbonate shield wall so that its surface is flush with the shield's inner surface (19.3 cm ID) at an elevation corresponding to the mid elevation of the exploding wire (8.7 cm below the jet entrance point).

- Charge Amplifiers:

Each transducer is connected by a low-noise coaxial cable to its dedicated amplifier. Amplifiers (Kistler Instrument Corporation, Model 5004) are used to amplify the voltage signals from the pressure transducer. Twelve capacitor settings are provided to select the pressure range of interest, three resistor settings to choose a low-frequency cut-off for measurements, and a ten-turn dial to adjust the transducer sensitivity. Each amplifier's transducer sensitivity dial is set to its respective transducer sensitivity value (as given in Table 3.14). The amplifier output is limited to +/- 10 Volts. When this limit is exceeded, a flashing indicator light provides indication that the output is saturated.

Transient pressure signals from the amplifier outputs are digitized and stored using a digital LeCroy 9400 oscilloscope with two identical input channels. The top pressure transducer signal is used to trigger the scope. The oscilloscope is interfaced with a host computer through a GPIB (IEEE-488) port. Waves acquired by the oscilloscope are stored as PRN format files readable by Excel using interface software provided by National Instruments (NI-488.2^{TM}).

3.5.2 Shock Attenuation Test Procedures

Prior to the conduct of an experiment, the capacitor bank of the Slapshot pulser needs to be charged to about 5% of full charge capacity for 30-45 minutes on the clamp mode. Following that period, the Slapshot pulser is turned off and placed in the normal mode. Once the desired liquid and gas volumetric flow rates are reached according to the procedure described in Section 3.3, the system is allowed to operate continuously in a steady-state fashion to establish the desired initial conditions prior to exploding the wire and initiating the shock wave. The charge amplifiers are reset, and the oscilloscope is set to the trigger mode for channels 1 and 2 (scales are usually set at 1.5 V/div and 20 ms/div). The Slapshot pulser is turned on. When the capacitors are charged to the desired initial condition (typically 40% or 50% of full scale), the Slapshot pulser is triggered, thereby exploding the wire. The data acquired by the oscilloscope are transmitted through the GPIB card to the computer and stored for later analysis by Excel. The Slapshot and the experimental loop are turned off, and a new wire is installed in preparation for the next experiment.

CHAPTER IV

EXPERIMENTAL RESULTS AND DISCUSSION

In this chapter, the experimental results obtained in this investigation are presented. Flow visualization results and bubble size distributions are presented in Section 4.1. Void fraction measurements and the corresponding slip ratios are presented in Section 4.2. Section 4.3 presents experimental results for shock attenuation in single- and two-phase jets.

4.1 Interfacial Structures

4.1.1 Flow Visualizations

Flows out of four different nozzles at different flow conditioners are observed. Each nozzle is tested at three different liquid superficial velocities, with a wide range of gas flow rates (i.e., void fractions). A total of 66 test conditions are documented; the corresponding liquid superficial velocities $j_{l,e}$ at the nozzle exit, the liquid superficial velocities $j_{l,h}$ within the honeycomb section, the Reynolds numbers Re_l, and the exit homogeneous void fractions α_e are given in Table 4.1.

Table 4.1: Detailed list of flow visualization experiments for planar, circular, and annular jets

Test #	Nozzle	$j_{l,e}$ (m/s)	$j_{l,h}$ (m/s)	Re_l	α_e (%)
1	Planar	1.26	0.42	2.38×10^4	0.00
2	Planar	1.26	0.42	2.38×10^4	1.00
3	Planar	1.26	0.42	2.38×10^4	2.50
4	Planar	1.26	0.42	2.38×10^4	5.00
5	Planar	1.26	0.42	2.38×10^4	9.90
6	Planar	1.26	0.42	2.38×10^4	25.00
7	Planar	2.52	0.84	4.77×10^4	0.00

continued on next page

continued from previous page

Test #	Nozzle	$j_{l,e}$ (m/s)	$j_{l,h}$ (m/s)	Re_l	α_e (%)
8	Planar	2.52	0.84	4.77×10^4	1.00
9	Planar	2.52	0.84	4.77×10^4	2.50
10	Planar	2.52	0.84	4.77×10^4	5.00
11	Planar	2.52	0.84	4.77×10^4	10.20
12	Planar	2.52	0.84	4.77×10^4	15.00
13	Planar	4.92	1.64	9.31×10^4	0.00
14	Planar	4.92	1.64	9.31×10^4	1.00
15	Planar	4.92	1.64	9.31×10^4	2.60
16	Planar	4.92	1.64	9.31×10^4	5.00
17	Planar	4.92	1.64	9.31×10^4	7.50
18	Planar	4.92	1.64	9.31×10^4	9.90
19	3.6 cm ID circular	1.26	0.58	4.68×10^4	0.00
20	3.6 cm ID circular	1.26	0.58	4.68×10^4	1.00
21	3.6 cm ID circular	1.26	0.58	4.68×10^4	2.50
22	3.6 cm ID circular	1.26	0.58	4.68×10^4	5.00
23	3.6 cm ID circular	1.26	0.58	4.68×10^4	10.00
24	3.6 cm ID circular	1.26	0.58	4.68×10^4	25.00
25	3.6 cm ID circular	2.52	1.17	9.36×10^4	0.00
26	3.6 cm ID circular	2.52	1.17	9.36×10^4	1.00
27	3.6 cm ID circular	2.52	1.17	9.36×10^4	2.50
28	3.6 cm ID circular	2.52	1.17	9.36×10^4	5.00
29	3.6 cm ID circular	2.52	1.17	9.36×10^4	10.00
30	3.6 cm ID circular	2.52	1.17	9.36×10^4	15.00
31	3.6 cm ID circular	4.73	2.19	1.76×10^5	0.00
32	3.6 cm ID circular	4.73	2.19	1.76×10^5	1.00
33	3.6 cm ID circular	4.73	2.19	1.76×10^5	2.50
34	3.6 cm ID circular	4.73	2.19	1.76×10^5	5.00
35	3.6 cm ID circular	4.73	2.19	1.76×10^5	7.50
36	3.6 cm ID circular	4.73	2.19	1.76×10^5	10.00
37	5.3 cm ID circular	0.63	0.63	4.68×10^4	0.00
38	5.3 cm ID circular	0.63	0.63	4.68×10^4	1.00
39	5.3 cm ID circular	0.63	0.63	4.68×10^4	2.50
40	5.3 cm ID circular	0.63	0.63	4.68×10^4	5.00
41	5.3 cm ID circular	0.63	0.63	4.68×10^4	10.00
42	5.3 cm ID circular	0.63	0.63	4.68×10^4	25.00
43	5.3 cm ID circular	1.26	1.26	9.36×10^4	0.00
44	5.3 cm ID circular	1.26	1.26	9.36×10^4	1.00
45	5.3 cm ID circular	1.26	1.26	9.36×10^4	2.50
46	5.3 cm ID circular	1.26	1.26	9.36×10^4	5.00
47	5.3 cm ID circular	1.26	1.26	9.36×10^4	10.00

continued on next page

continued from previous page					
Test #	Nozzle	$j_{l,e}$ (m/s)	$j_{l,h}$ (m/s)	Re_l	α_e (%)
48	5.3 cm ID circular	1.26	1.26	9.36×10^4	15.00
49	5.3 cm ID circular	2.37	2.37	1.76×10^5	0.00
50	5.3 cm ID circular	2.37	2.37	1.76×10^5	1.00
51	5.3 cm ID circular	2.37	2.37	1.76×10^5	2.50
52	5.3 cm ID circular	2.37	2.37	1.76×10^5	5.00
53	5.3 cm ID circular	2.37	2.37	1.76×10^5	7.50
54	5.3 cm ID circular	2.37	2.37	1.76×10^5	10.00
55	4.0 cm ID annular	1.00	1.00	1.23×10^4	0.00
56	4.0 cm ID annular	1.00	1.00	1.23×10^4	1.00
57	4.0 cm ID annular	1.00	1.00	1.23×10^4	5.00
58	4.0 cm ID annular	1.00	1.00	1.23×10^4	10.00
59	4.0 cm ID annular	2.00	2.00	2.45×10^4	0.00
60	4.0 cm ID annular	2.00	2.00	2.45×10^4	1.00
61	4.0 cm ID annular	2.00	2.00	2.45×10^4	5.00
62	4.0 cm ID annular	2.00	2.00	2.45×10^4	10.00
63	4.0 cm ID annular	4.00	4.00	4.90×10^4	0.00
64	4.0 cm ID annular	4.00	4.00	4.90×10^4	1.00
65	4.0 cm ID annular	4.00	4.00	4.90×10^4	5.00
66	4.0 cm ID annular	4.00	4.00	4.90×10^4	10.00

Figures 4.1 through 4.3 show the photographs for experiments conducted using the planar jet. Figure 4.1 corresponds to the case with a 1.26 m/s liquid superficial velocity at the nozzle exit. At that liquid flow rate, the superficial liquid velocity within the 3.2 mm diameter honeycomb cells of the flow conditioner is three times lower than the velocity at the nozzle exit (i.e., nearly 0.42 m/s). Experimental data for two-phase flow within small-diameter tubes (Fukano and Kariyasaki, 1993) suggest that the two-phase flow with a liquid superficial velocity less than 0.54 m/s within the honeycomb tubes can be intermittent (i.e., slug flow) over the entire void fraction range of interest (see Figure 4.4). This means that the diameter of the gas "bubbles" entering the calming section ahead of the nozzle is slightly larger than 3.2 mm. Nevertheless, homogeneous flow is formed within the calming section, the nozzle, and the jet (see Figure 4.1). It should be noted that the jet thickness ($\sim$ 1 cm) is significantly larger than the bubble diameter so that multiple bubble images are projected in the two-dimensional image.

Figure 4.4 presents the flow regime map developed by Fukano and Kariyasaki for downward flow in small tubes with 1.0-5.0 mm diameter (Fukano and Kariyasaki, 1993). Figure 4.5 shows the different test conditions examined in this study for the planar, circular, and annular jets (Table 4.1) superimposed on the bubbly/slug transition given by Fukano and Kariyasaki (Fukano and Kariyasaki, 1993). The transition line in Figure 4.5 is plotted as a function of the homogeneous void fraction and the superficial liquid velocity within the honeycomb; it corresponds to the transition line shown in Figure 4.4.

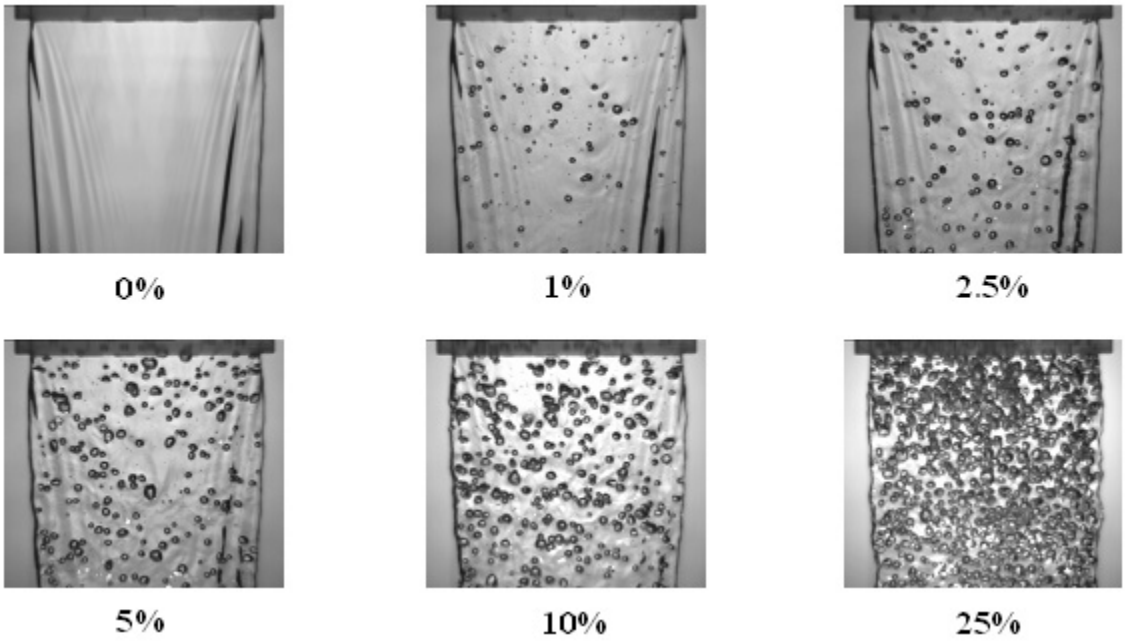

Figure 4.1: Near-field behavior of two-phase planar jets with different exit homogenous void fractions (initial liquid superficial velocity = 1.26 m/s, $Re_l = 2.38 \times 10^4$)

Figures 4.2 and 4.3 show similar photographs at higher liquid velocities, 2.52 and 4.92 m/s respectively. At these higher velocities, the flow regime within the 3.2 mm diameter honeycomb cells becomes bubbly (see Figure 4.5), so that smaller gas bubbles ($\sim$ 2 mm, dictated by the Taylor length scale) are produced. Again, homogeneous flow is formed within the calming section, the nozzle, and the jet (see Figures 4.2 and 4.3).

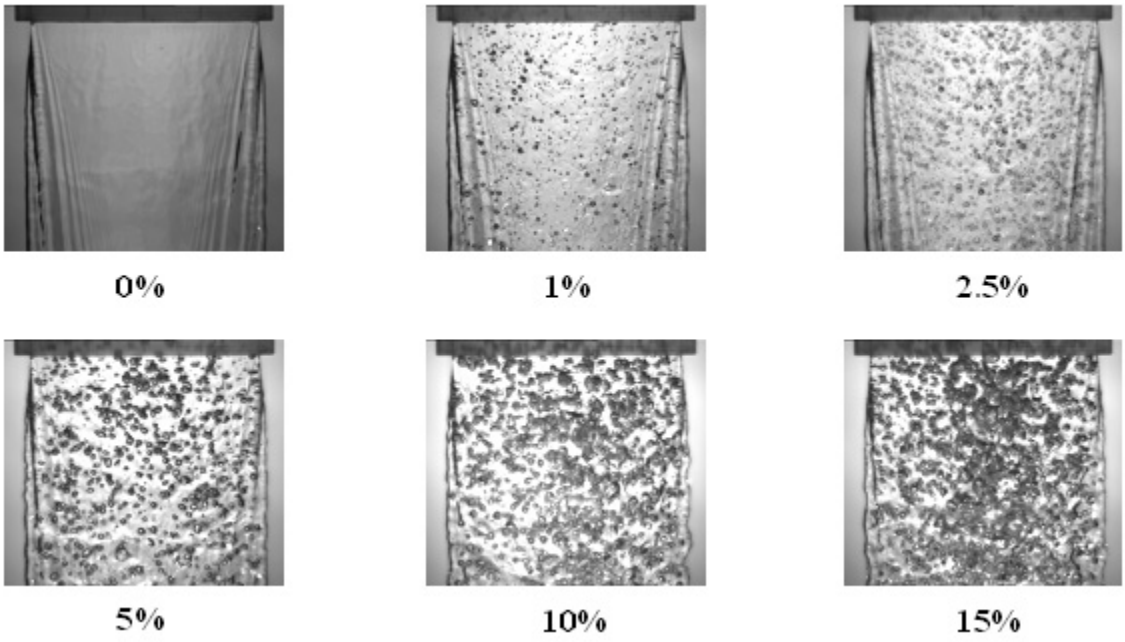

Figure 4.2: Near-field behavior of two-phase planar jets with different exit homogenous void fractions (initial liquid superficial velocity = 2.52 m/s, $Re_l = 4.77 \times 10^4$)

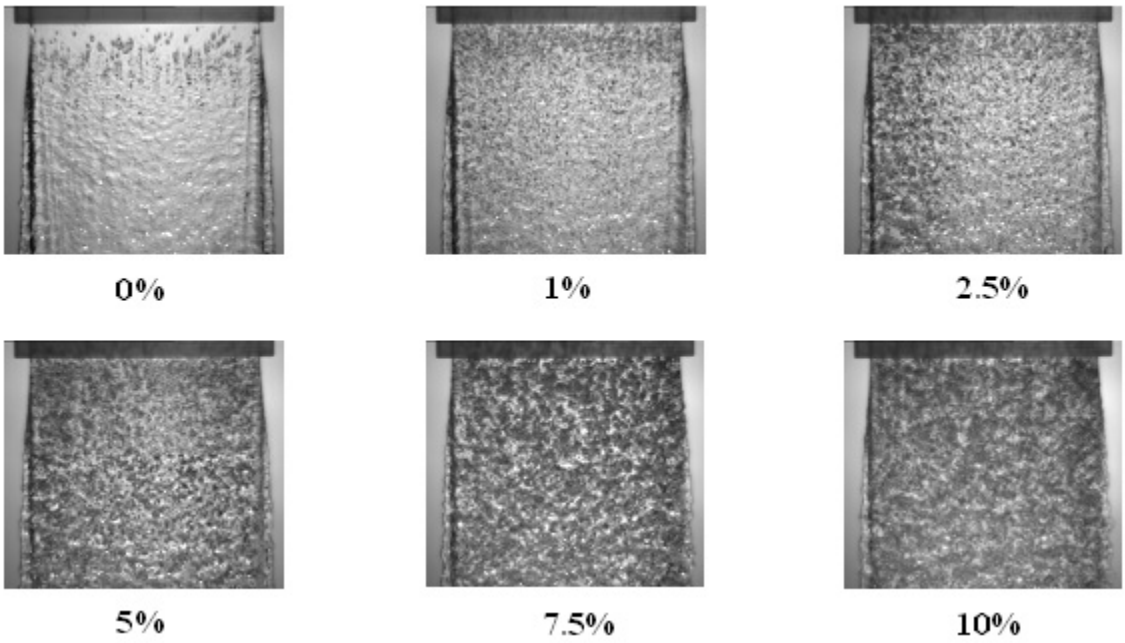

Figure 4.3: Near-field behavior of two-phase planar jets with different exit homogenous void fractions (initial liquid superficial velocity = 4.92 m/s, $Re_l = 9.31 \times 10^4$)

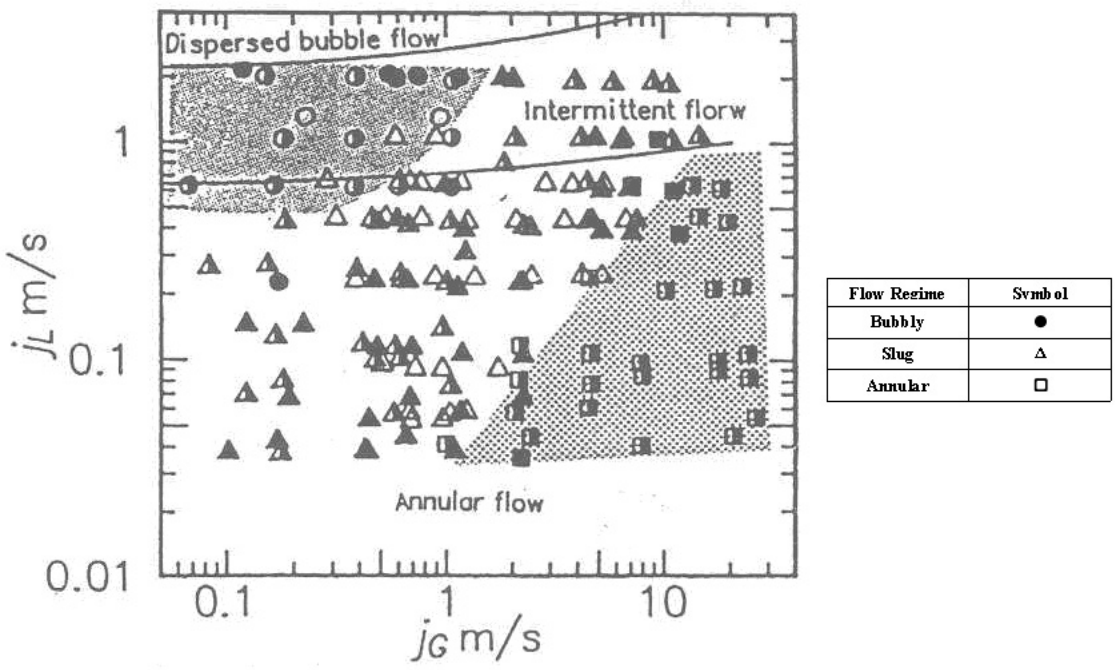

Figure 4.4: Two-phase flow regime transitions for downward flow in small tubes with 1.0-5.0 mm diameter (Fukano and Kariyasaki) (Fukano and Kariyasaki, 1993)

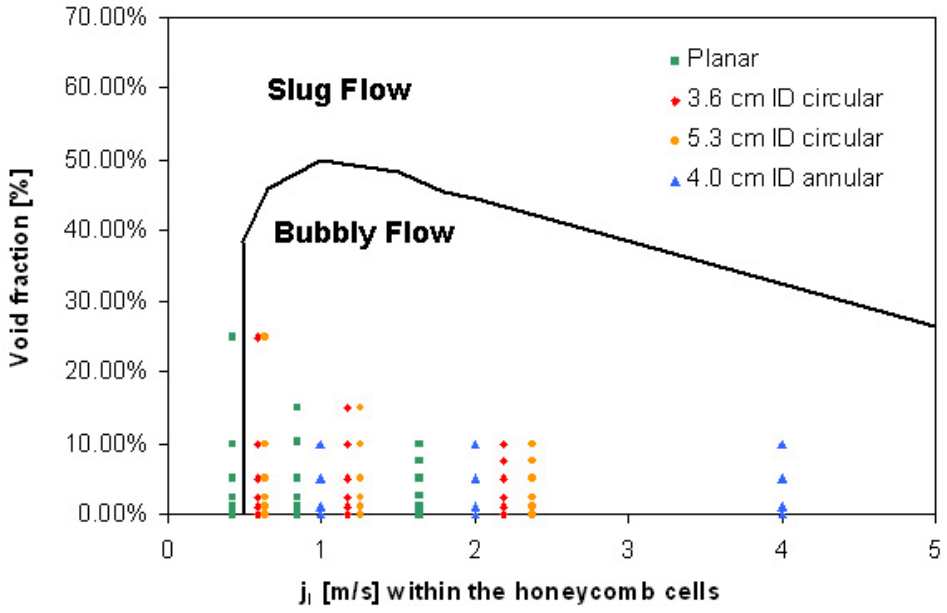

Figure 4.5: Test conditions for the planar, circular, and annular jets superimposed on the flow regime of Fukano and Kariyasaki (Fukano and Kariyasaki, 1993)

The liquid/gas planar jet changes geometry downstream of the imposed rectangular exit condition. The jet width decreases slightly along the flow direction due to surface tension forces and gravitational acceleration of the flow. The face of the jet is nearly flat with protrusions along the edges growing along the x-axis. The inner protrusions are wake structures emanating from the corners of the nozzle. The fluctuations increase in a linear manner with downstream distance.

At low jet velocities and exit homogenous void fractions, the jets appear "glassy" with little surface disturbance. At higher exit homogenous void fractions, the jet surface becomes more rippled because of increased turbulence and, more importantly, because of gas bubbles randomly crossing the jet surface. The density of drops due to turbulent breakup at the jet free surface increases as the distance from the nozzle x increases; there are more drops near the source of breakup, i.e., the jet surface. Nevertheless, the majority of the gas bubbles remain "contained" within the jet in the near-field. Unlike ion-beam and laser-driven systems, the surface smoothness of the jets and the hydrodynamic source term (i.e., droplets generated by turbulent breakup and/or gas bubbles "breaking through" the liquid surface) in a Z-pinch reactor will not interfere with either beam or target delivery. The important consideration here is that the majority of the gas remains contained within the jets as they flow towards the bottom of the reactor cavity, so that the two-phase jet can adequately attenuate the shock wave produced by rapid energy deposition of the target debris and x-rays.

At relatively low jet velocities, "small" bubbles are distributed over the entire jet width, while the "larger" bubbles tend to be concentrated in the center region (see Figure 4.2). Sun *et al.* (Sun et al., 2005) showed in 2005 that the "larger" bubbles have a larger average velocity than the "small" bubbles, and this causes the "small" bubbles in the wake of the "larger" bubbles to move faster than the ones outside of the wake. The bubble concentration in the jet center increases the population near the jet

center, which enhances the bubble coalescence resulting in the formation of "larger" bubbles (Hibiki et al., 2003). The bubble diffusion in the transverse direction is clearly demonstrated, due to the effects of turbulence, void concentration, and lateral lift force. No stable slug bubble can exist, since the width of the test section is much larger than the maximum cap bubble limit that is about 100 mm for air-water flow under atmospheric pressure and 20^{o}C temperature conditions (Sun et al., 2005). However, careful observation of the bubble repartition within the jets suggests that off-centered peaks are likely to exist (see Figure 4.1).

Hibiki (Hibiki et al., 2003) suggested that the bubble shape deformed by the turbulence and the velocity gradient in the liquid phase might change the velocity field surrounding the bubbles with a change in the pressure field. This change may force the bubbles to migrate toward the free surface, in an attempt to avoid the fast moving liquid in the central part of the jet (Hibiki et al., 2003). At higher jet velocities, the coalescence and disintegration mechanisms due to turbulence become more important, leading to smaller and more homogeneous bubbles (see Figure 4.3).

Results similar to those presented above for the other three nozzles are presented in Appendix A. Figures A.1 through A.3 show the photographs for the 3.57 cm diameter circular jets, while Figures A.4 through A.6 show the photographs for the 5.25 cm diameter circular jets. Figures A.7 through A.9 show the photographs for the 4.00 cm ID annular jets. The same behavior is observed as previously described for the planar jets. At low velocities and void fractions, the jet is highly stable; the jet surface is smooth and steady. At higher velocities, the jet remains stable and the surface relatively smooth despite the increased surface ripple resulting from higher turbulence, particularly at elevated exit homogenous void fractions, where the gas randomly crosses the jet surface as it proceeds downstream. At high velocities and void fractions (above 25 %), the jets become unstable, i.e. pulsating or oscillatory, due to the formation of slug flow within the honeycomb section of the flow conditioner.

The above described data show that coherent stable two-phase jets at homogeneous void fractions up to 25 % can be formed with standard nozzle and flow conditioner designs. The choice of optimum operating conditions (jet velocity and average void fraction) for the Z-Pinch reactor represents a trade-off between mechanical response and vacuum pumping requirements.

4.1.2 Bubble Size Measurement

The 10 cm × 1 cm planar jet provides an effective setup for flow visualization and measurement of bubble size distribution. The motion of the bubbles is nearly 2D due to the large aspect ratio and the influence of overlap on the bubble image analysis is minimal. Additionally, by using a planar jet to measure the bubble size, image distortion due to curvature is eliminated. The 2D picture shapes of the bubbles are approximated by spheroids (Majumder et al., 2006) whose maximum and minimum axes are computed from visual measurements. The third dimension is calculated with the assumption that the bubbles are symmetric around the minimum axis (Majumder et al., 2006). From the known values of maximum and minimum axes, $d_{b,max}$ and $d_{b,min}$ respectively, an equivalent spherical bubble diameter $d_{b,s}$ is calculated by the following equation (Couvert et al., 1999):

$$d_{b,s} = \sqrt[3]{d_{b,max}^2 \cdot d_{b,min}} \tag{4.1}$$

A program *bubble.m* is written in $MATLAB^{®}$ to display pictures, calculate the size of a pixel, and measure the equivalent spherical bubble diameters for 40 different bubbles distributed over nearly 12 cm downward the nozzle exit (see Appendix B). Referring to Table 4.1, the diameters of 40 bubbles are calculated for test numbers 2 through 6, 8 through 12, and 14 through 18 (i.e, 600 bubbles). Ishii and Zuber (Ishii and Zuber, 1979) defined the maximum distorted bubble limit $D_{d,max}$ to determine the limit between spherical/distorted bubbles and cap/Taylor bubbles. $D_{d,max}$ is equal

to four times the characteristic Laplace length scale:

$$D_{d,max} = 4 \cdot \sqrt{\frac{\sigma}{g \cdot (\rho_l - \rho_g)}} \tag{4.2}$$

where σ, ρ_l, and ρ_g are the surface tension between the liquid and the gas phases, the density of the liquid and the gas, respectively. For an air-water flow at atmospheric pressure and room temperature (295 K), the maximum distorted bubble size is estimated to be 10.9 mm. The structure and design of the flow conditioner make it impossible to form cap bubbles within the 20 cm long test section of the two-phase jet. Therefore, the maximum measured diameters are much smaller than 10 mm. The number density of "larger" bubbles seems to decrease along the flow direction. This is due to generation of "small" bubbles due to turbulence. However, the size distribution along the x-axis appears to be rather uniform, as noted by Sun (Sun et al., 2005). Therefore, the 40 different measured bubbles can be spread over $\sim$ 12 cm downstream of the nozzle exit. The bubble size distribution is obtained by sorting the equivalent diameters of bubbles into different uniform classes of 0.1 mm.

Figures 4.6 to 4.10 present the bubble size distributions for a jet with initial liquid superficial velocity equal to 1.26 m/s and a homogeneous exit void fraction between 1% and 25%. As the initial void fraction increases for a given jet velocity, the overall bubble diameters also increase, remaining below the limit fixed by Ishii (see Equation 4.2). At low jet velocity, due to the relatively low turbulence, bubble breakup is negligible. Therefore, the coalescence process leading to "larger bubbles" becomes predominant, due to bubble-bubble collision induced by liquid turbulence, and the higher rate of bubble-bubble collision at elevated void fractions.

At higher jet velocities, the breakup mechanism due to bubble-turbulent eddy collision is considered. As the void fraction increases, the rate of bubble-bubble collision increases; the coalescence process is still present within the jet, leading to "larger bubbles" with larger void fractions, but the breakup mechanism due to the turbulent eddies contained within the liquid phase prevent the bubbles from growing

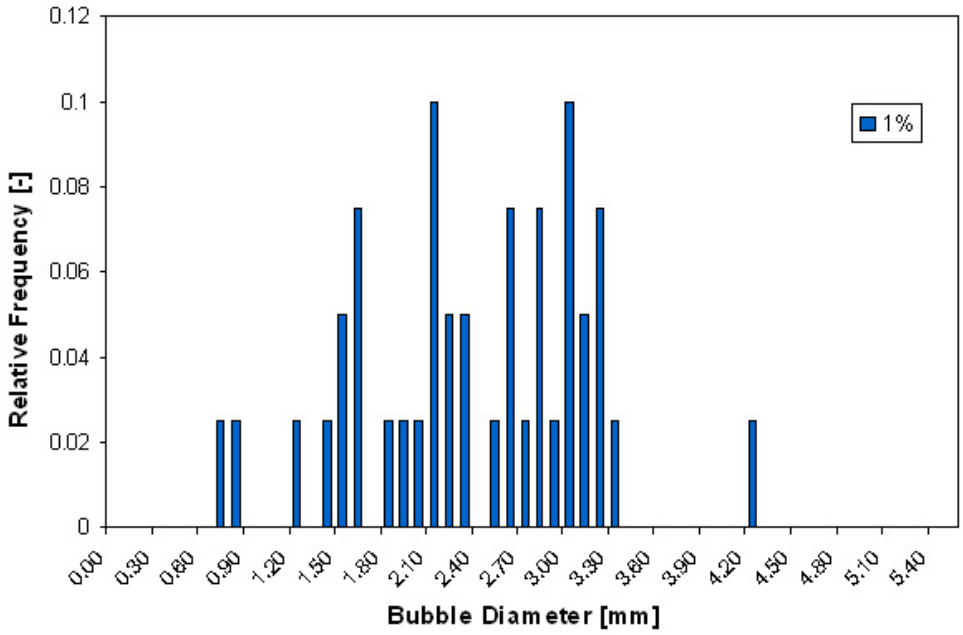

Figure 4.6: Bubble size distribution within a planar jet (initial liquid superficial velocity = 1.26 m/s, initial homogenous void fraction = 1%, $Re_l = 2.38 \times 10^4$)

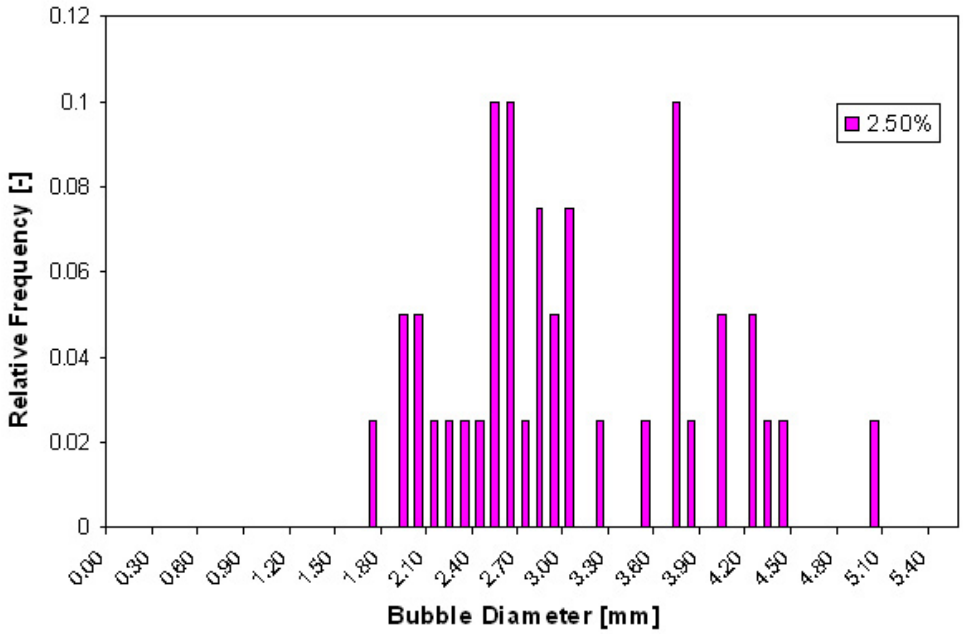

Figure 4.7: Bubble size distribution within a planar jet (initial liquid superficial velocity = 1.26 m/s, initial homogenous void fraction = 2.5%, $Re_l = 2.38 \times 10^4$)

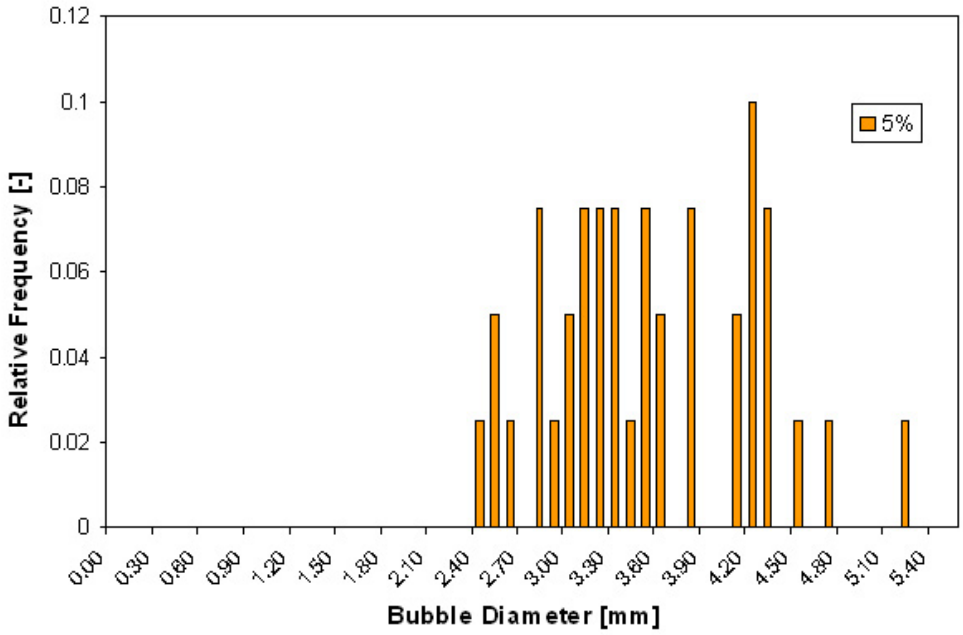

Figure 4.8: Bubble size distribution within a planar jet (initial liquid superficial velocity = 1.26 m/s, initial homogenous void fraction = 5%, $Re_l = 2.38 \times 10^4$)

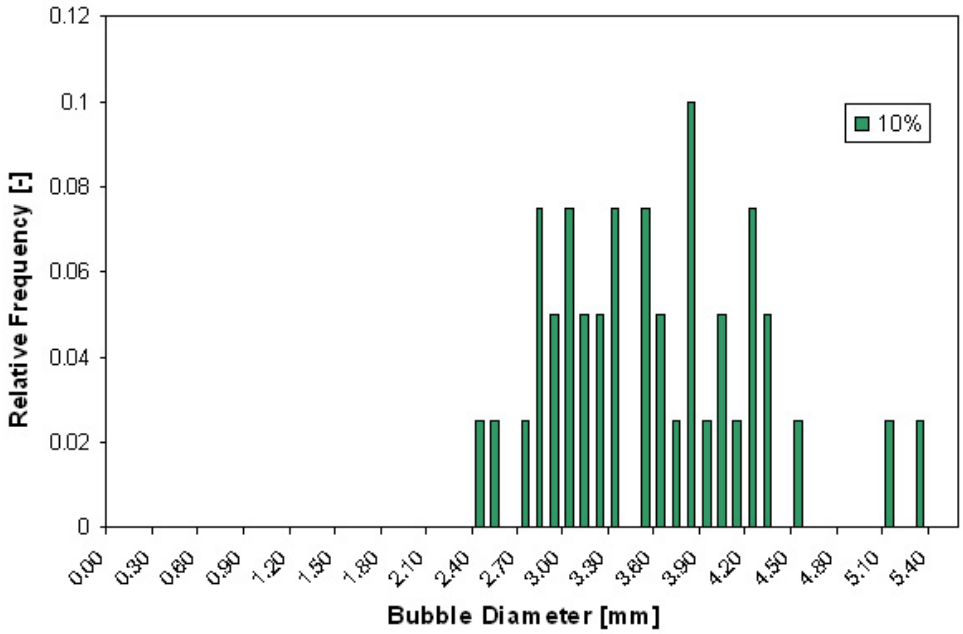

Figure 4.9: Bubble size distribution within a planar jet (initial liquid superficial velocity = 1.26 m/s, initial homogenous void fraction = 10%, $Re_l = 2.38 \times 10^4$)

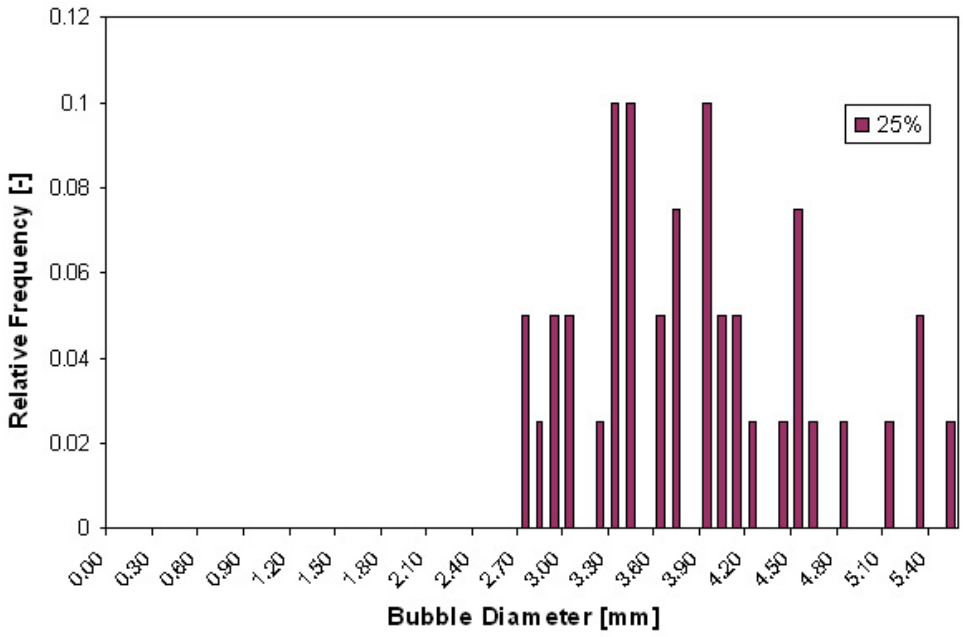

Figure 4.10: Bubble size distribution within a planar jet (initial liquid superficial velocity = 1.26 m/s, initial homogenous void fraction = 25%, $Re_l = 2.38 \times 10^4$)

as much as they do at low jet velocities. Therefore, at high jet velocities, the bubble size distributions are considerably narrower (see Appendix C for the bubble diameter distributions of each different test).

At high jet velocities and relatively low void fractions, the bubble shapes are easily distinguishable, and the bubble size distribution is nearly normal. For low velocities and low void fractions, the bubble size distribution does not properly follow a normal distribution; this result may be influenced by the relatively small sample size (40 measured bubbles), which is limited by the number of bubbles within the viewing section. For high velocities and high void fractions, the large number of bubbles within the viewing section makes it difficult to distinguish individual bubbles, particularly those with small diameters. Figure 4.11 shows the size distribution (i.e., the relative frequency for each group within a range of 0.1 mm) versus the bubble diameter. The density profiles for each test condition and their fitted normal distributions are displayed in Appendix C.

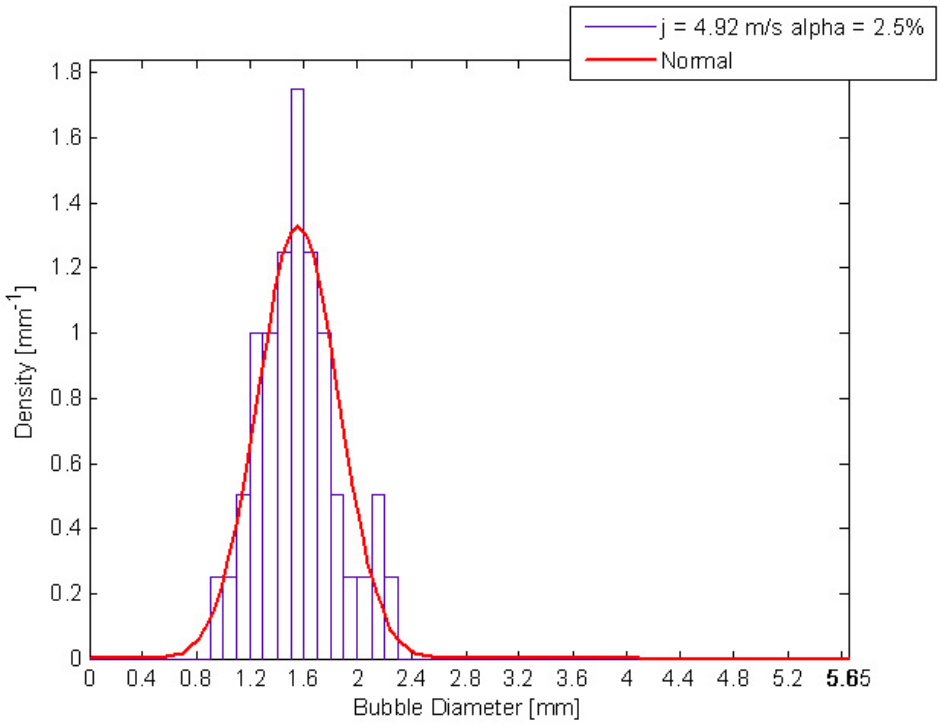

Figure 4.11: Bubble size density within a planar jet (initial liquid superficial velocity = 4.92 m/s, $Re_l = 9.31 \times 10^4$, initial void fraction = 2.5%) and fitted normal distribution

4.1.3 Correlations of the Sauter Diameter

The Sauter mean bubble diameter d_{Sauter} is defined as the volume-to-surface mean bubble diameter (Couvert et al., 1999):

$$d_{Sauter} = \frac{\sum_{i=1}^{N} \left(N_i \cdot {d_{b,s,i}}^3 \right)}{\sum_{i=1}^{N} \left(N_i \cdot {d_{b,s,i}}^2 \right)} \tag{4.3}$$

where N_i is the number of bubbles of diameter $d_{b,s,i}$. In this study N is equal to 40. Figure 4.12 shows the variation of the Sauter diameter with the initial value of the homogenous void fraction and liquid jet velocity. These data show that the bubble size decreases with increasing liquid superficial velocity. This is due to bubble breakup; the momentum transfer of liquid jet increases with increasing the liquid flow rate. Also the rate of coalescence increases as the gas flow rate increases which enhances bubble-bubble interactions. As the probability of coalescence increases with increase in the superficial gas velocity, the Sauter mean bubble diameter increases.

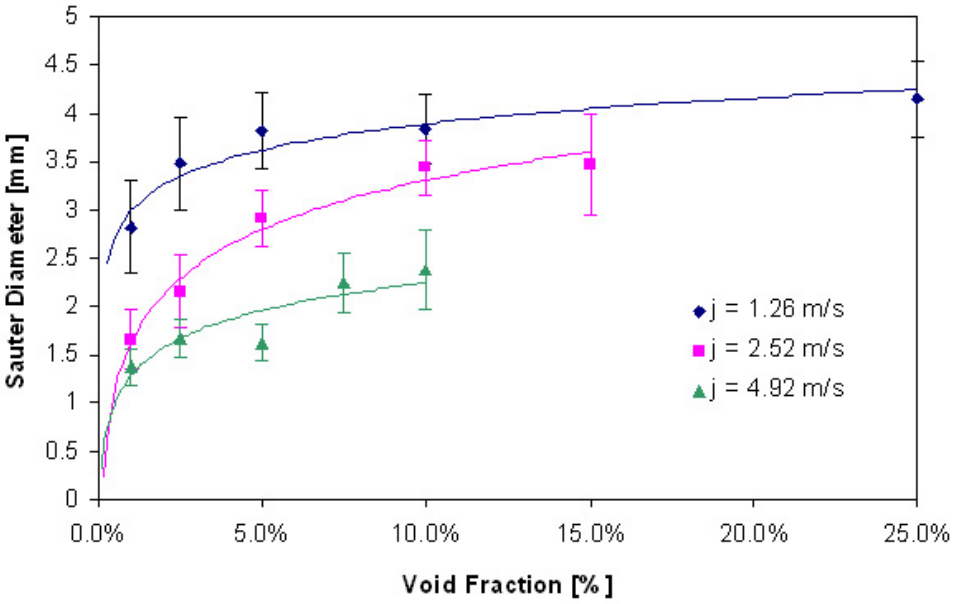

Figure 4.12: Variation of the Sauter mean bubble diameter with initial homogeneous void fraction for $j_{l,e}$ = 1.26, 2.52, and 4.92 m/s, Re_l = 2.38 $\times$ 10^4, 4.77 $\times$ 10^4, 9.31 $\times$ 10^4

In addition to bubble interaction rates, bubble coalescence and breakup rates may

also be governed by the bubble coalescence and breakup efficiencies, respectively. According to Hibiki *et al.* (Hibiki et al., 2003), the bubble coalescence and breakup efficiencies, respectively, are decreasing and increasing functions of the Weber number. A correlation is proposed in Equation 4.11; the dimensionless Sauter mean bubble diameter (i.e, the Sauter diameter over the Laplace length scale) is expressed as a function of the Reynolds, the Weber, and the Froude numbers in order to take into account the turbulence effects, the bubble coalescence and breakup efficiencies, and the buoyancy effects, respectively (see also Section 4.2.3 for further explanation of the correlation structure). The Laplace length scale $D_{Laplace}$, the Reynolds number Re_l, the Weber number We_l, and the Froude number Fr_l are defined according Equations 4.5, 4.6, 4.7, and 4.8. $D_{h,planar}$ represents the hydraulic diameter of the planar nozzle and is equal to 1.818 cm. The bubble rise velocity U_{rise} is defined in Section 4.2.3 (see Equation 4.47) and its physical interpretation are given in Paragraph 4.2.3. The dimensionless number $j^*_{g,e}$ is defined in Equation 4.9, while C_0, a, and b are constants.

$$\frac{d_{Sauter}}{D_{Laplace}} = C_0 \cdot \left(\frac{Re_l \cdot We_l}{Fr_l} \right)^a \cdot \left(j^*_{g,e} \right)^b \tag{4.4}$$

$$D_{Laplace} = \sqrt{\frac{\sigma}{g \cdot (\rho_l - \rho_g)}} \tag{4.5}$$

$$Re_l = \frac{j_{l,e} \cdot D_{h,planar}}{\nu_l} \tag{4.6}$$

$$We_l = \frac{\rho_l \cdot (j_{l,e})^2 \cdot D_{h,planar}}{\sigma} \tag{4.7}$$

$$Fr_l = \frac{j_{l,e}}{\sqrt{g \cdot D_{h,planar}}} \tag{4.8}$$

$$j^*_{g,e} = \frac{j_{g,e}}{U_{rise}} \tag{4.9}$$

The recommended values for C_0, a, and b are provided in Equation 4.10. The coefficients of multiple determination for this correlation are $R^2 = 96\%$. This correlation is valid for bubbly flow within planar jets for the following parameters 1.26 m/s $\leq$

$j_{l,e} \leq 4.92$ m/s and $1\% \leq \alpha_e \leq 25\%$. Note that the probability that the coefficients C_0, a, b, and c have a different value is null or nearly null.

$$\frac{d_{Sauter}}{D_{Laplace}} = 137 \cdot \left(\frac{Re_l \cdot We_l}{Fr_l} \right)^{-0.282} \cdot \left(j_g^* \right)^{0.145} \tag{4.10}$$

Figure 4.13 present the dimensionless experimental data versus the results obtained from the proposed correlation 4.10. The dashed lines show plus or minus 20% of the correlation. The data points with their associated errors bars are within the +/- 20% section; the errors on the experimental data are examined in Appendix F.

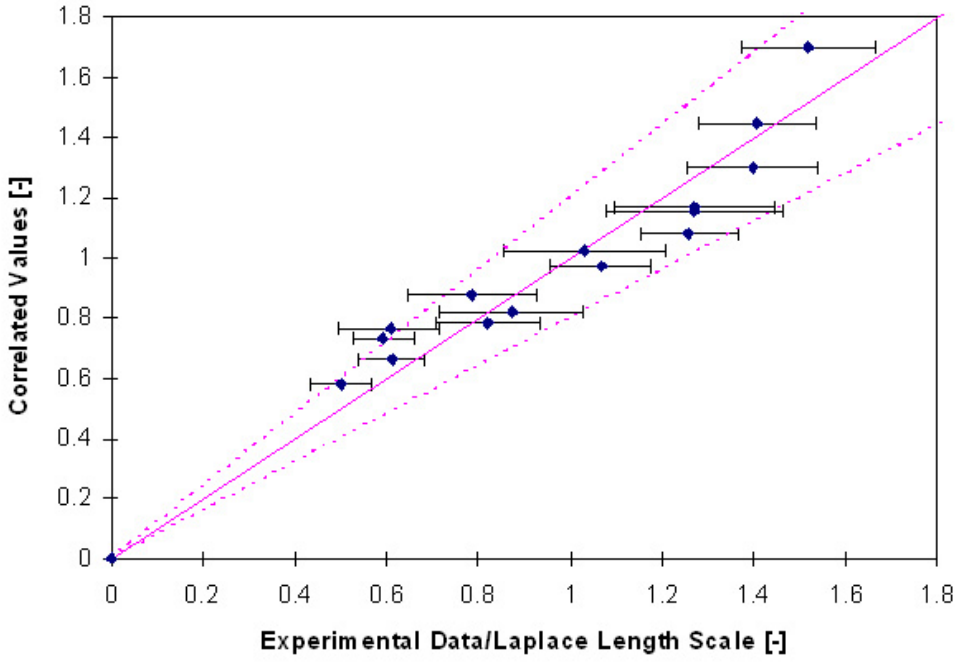

Figure 4.13: Dimensionless experimental Sauter mean bubble diameter versus the results obtained from the proposed correlation 4.10

Majumder *et al.* (Majumder et al., 2006) developed an empirical correlation to predict the bubble size in a bubble column. It was found experimentally that the bubble size depends on different operating variables: fluid flow rate, nozzle diameter, and axial location in the column. Applying Rayleigh's method of dimensional

analysis, the Sauter mean bubble diameter is expressed as:

$$\frac{d_{Sauter}}{D_{h,planar}} = 1.48\times10^{-2}\cdot\left(\frac{x}{D_{h,planar}}\right)^{1.09}\cdot\left(\frac{j_{g,e}}{j_{l,e}}\right)^{-1.388}\cdot(Fr_g)^{-0.759}\cdot(Re_l)^{0.449}\cdot(Su_l)^{-0.303} \tag{4.11}$$

where x represents the height in the bubble column at which bubbles are measured. In this case, it is assumed that x equals 5 cm (mid-way along the test region). The liquid Reynolds number Re_l was previously defined in Equation 4.6, while the gas Froude number Fr_g is defined in Equation 4.12. The liquid Suratman number based on nozzle diameter Su_l is defined in Equation 4.13 as the ratio of surface tension forces to viscous forces.

$$Fr_g = \frac{g\cdot D_{h,planar}}{{j_{g,e}}^2} \tag{4.12}$$

$$Su_l = \frac{D_{h,planar}\cdot\sigma\cdot\rho_l}{{\mu_l}^2} \tag{4.13}$$

Figure 4.14 present the dimensionless experimental data versus the results obtained

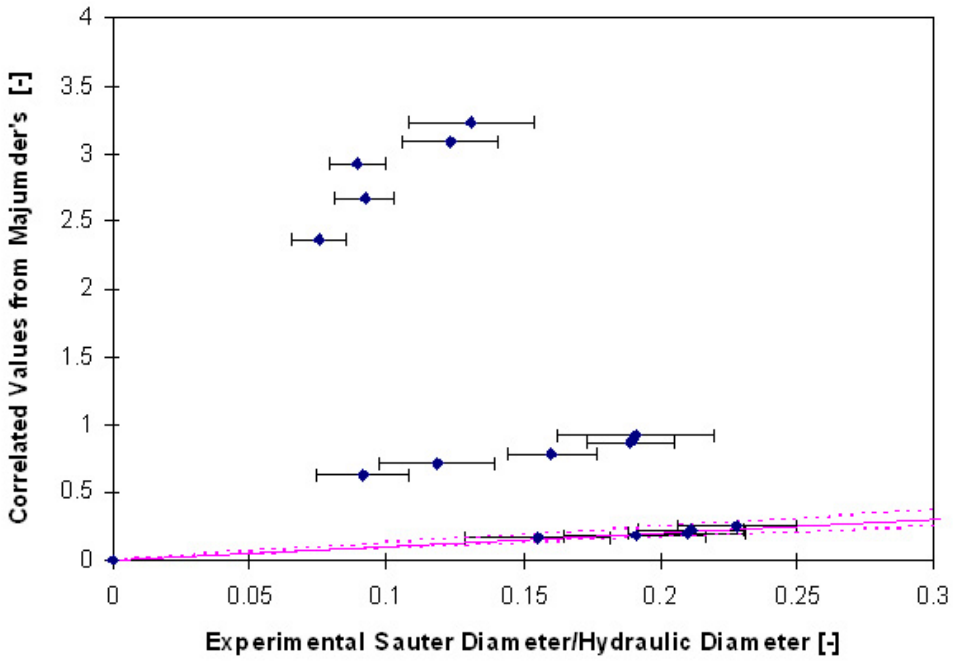

Figure 4.14: Dimensionless experimental Sauter mean bubble diameter versus the correlated values obtained from the Majumder's correlation 4.11

from the Majumder's correlation 4.11. The dashed lines show plus or minus 20% of

the correlation. The data points $j_{l,e}$ = 1.26 m/s for with their associated errors bars are within the +/- 20% section. For $j_{l,e}$ = 2.52 m/s and 4.92 m/s, the correlation developed by Majumder *et al.* (Majumder et al., 2006) clearly overestimates the Sauter mean bubble diameter for free planar jets.

4.2 Void Fraction and Slip Ratio Distribution Measurements

A detailed list of the test conditions for the void fraction and slip ratio distribution measurements is provided in Table 4.2. For each test condition, the local jet void fraction and thickness are measured along the jet centerline at 14 different x-locations, every centimeter from x = 2.9 cm to x = 15.9 cm from the nozzle exit; the lowest x-value (2.9 cm) is dictated by physical limitations of the positioner. The gamma-ray densitometer and radiation detection station are used in order to measure the number of radiation counts for a total of 420 experiments (30 × 14).

4.2.1 Void Fraction

Kern (Kern, 2007) demonstrated that, if two different types of slab materials are used, and if the gamma-rays are kept at a fixed energy (mono-energetic), the difference in the number of gamma-particles detected can be solely attributed to the type of slab material. Therefore, in this experiment, measurements can be taken with the desired two-phase flow, and repeated with ambient air as well as pure liquid water. By comparing the number of counts measured with each respective medium, Stahl and von Rohr (Stahl and von Rohr, 2004) came up with an expression to determine the void fraction of the two-phase flow; the averaged void fraction across the container $\alpha_C(x)$ is given by:

$$\alpha_C(x) = \frac{\ln\left(\frac{I_{2-phase}(x)}{I_{l,avg}}\right)}{\ln\left(\frac{I_{g,avg}}{I_{l,avg}}\right)} \tag{4.14}$$

Table 4.2: Detailed list of test conditions for void fraction and slip ratio distribution measurements

Test #	Nozzle	$j_{l,e}$ (m/s)	Re_l	α_e (%)
1	Planar	1.0	1.89×10^4	0.0
2	Planar	1.0	1.89×10^4	1.0
3	Planar	2.0	3.78×10^4	0.00
4	Planar	2.0	3.78×10^4	1.0
5	Planar	2.0	3.78×10^4	2.50
6	Planar	2.0	3.78×10^4	5.00
7	Planar	3.0	5.68×10^4	0.00
8	Planar	3.0	5.68×10^4	1.00
9	Planar	3.0	5.68×10^4	2.50
10	Planar	3.0	5.68×10^4	5.00
11	Planar	4.0	7.57×10^4	0.00
12	Planar	4.0	7.57×10^4	1.00
13	Planar	4.0	7.57×10^4	2.50
14	Planar	4.0	7.57×10^4	5.00
15	Planar	4.0	7.57×10^4	10.00
16	3.6 cm ID circular	1.0	3.72×10^4	0.00
17	3.6 cm ID circular	1.0	3.72×10^4	1.00
18	3.6 cm ID circular	1.0	3.72×10^4	2.50
19	3.6 cm ID circular	2.0	7.43×10^4	0.00
20	3.6 cm ID circular	2.0	7.43×10^4	1.00
21	3.6 cm ID circular	2.0	7.43×10^4	2.50
22	3.6 cm ID circular	2.0	7.43×10^4	5.00
23	3.6 cm ID circular	3.0	1.11×10^5	0.00
24	3.6 cm ID circular	3.0	1.11×10^5	1.00
25	3.6 cm ID circular	3.0	1.11×10^5	2.50
26	3.6 cm ID circular	3.0	1.11×10^5	5.00
27	3.6 cm ID circular	3.0	1.11×10^5	10.00
28	3.6 cm ID circular	4.0	1.49×10^5	0.00
29	3.6 cm ID circular	4.0	1.49×10^5	1.00
30	3.6 cm ID circular	4.0	1.49×10^5	2.50
31	3.6 cm ID circular	4.0	1.49×10^5	5.00
32	3.6 cm ID circular	4.0	1.49×10^5	10.00
33	3.6 cm ID circular	4.0	1.49×10^5	15.00

The error associated with the void fraction is calculated from Equation 4.14 and is given in Equation 4.15. The details of the calculation are provided in Appendix F (see Section F.2.2). The terms $U_{I_{l,avg}}$ and $U_{I_{g,avg}}$ are given in Section F.2.1. The term $U_{I_{2-phase}(x)}$ is assumed to be equal to the maximum of $U_{I_{l,avg}}$ and $U_{I_{g,avg}}$. Therefore, the error on the void fraction across the container is maximized.

$$U_{\alpha_C(x)} = \sqrt{\left[U_{I_{2-phase}(x)} \cdot \frac{\partial \alpha_C(x)}{\partial I_{2-phase}(x)}\right]^2 + \left[U_{I_{l,avg}} \cdot \frac{\partial \alpha_C(x)}{\partial I_{l,avg}}\right]^2 + \left[U_{I_{g,avg}} \cdot \frac{\partial \alpha_C(x)}{\partial I_{g,avg}}\right]^2} \tag{4.15}$$

The collapsed liquid thickness of the jet $\delta_{CLT}(x)$ is determined using the Equation 4.16 where δ_C is the inner length of the container cross section.

$$\delta_{CLT}(x) = \delta_C \cdot (1 - \alpha_C(x)) \tag{4.16}$$

The error associated with the collapsed liquid thickness of the jet is calculated from Equation 4.16 and is given in Equation 4.17. Details of the calculation are provided in Appendix F (see Section F.2.3). U_{δ_C} is assumed to be 7.62×10^{-4} m.

$$U_{\delta_{CLT}(x)} = \sqrt{\left[U_{\delta_C} \cdot (1 - \alpha_C(x))\right]^2 + \left[U_{\alpha_C(x)} \cdot \delta_C\right]^2} \tag{4.17}$$

Figures 4.15 and 4.16 show the collapsed liquid thickness of the planar and circular jets, respectively, at a superficial liquid velocity of 3 m/s at the nozzle exit; the corresponding Reynolds number values are $Re_l = 5.68 \times 10^4$ and 1.11×10^5 respectively. The profiles shown are acquired at average homogeneous exit void fractions α_e, of 0% (♦), 1% (■), 2.5% (▲), 5% (•), and 10% (∗). The collapsed liquid thickness with a void fraction $\alpha_e = 10\%$ is only presented for the circular geometry; the high turbulence at $\alpha_e = 10\%$ due to the introduction of bubbles within the planar liquid jet does not allow accurate measurements of the actual jet thickness. The error bars are calculated using Equations 4.15 and 4.17. The uncertainties for the collapsed liquid thickness in the case of the planar and the circular geometries are on the order of 1 - 2 $\times$ 10^{-4} m and 4 - 5 $\times$ 10^{-4} m, respectively (i.e., $U_{\delta_{CLT}(x)} < 2.3\%$). The solid

lines represent curve fittings for each test condition ($R^2 > 95\%$ in all cases); they are within the error bars.

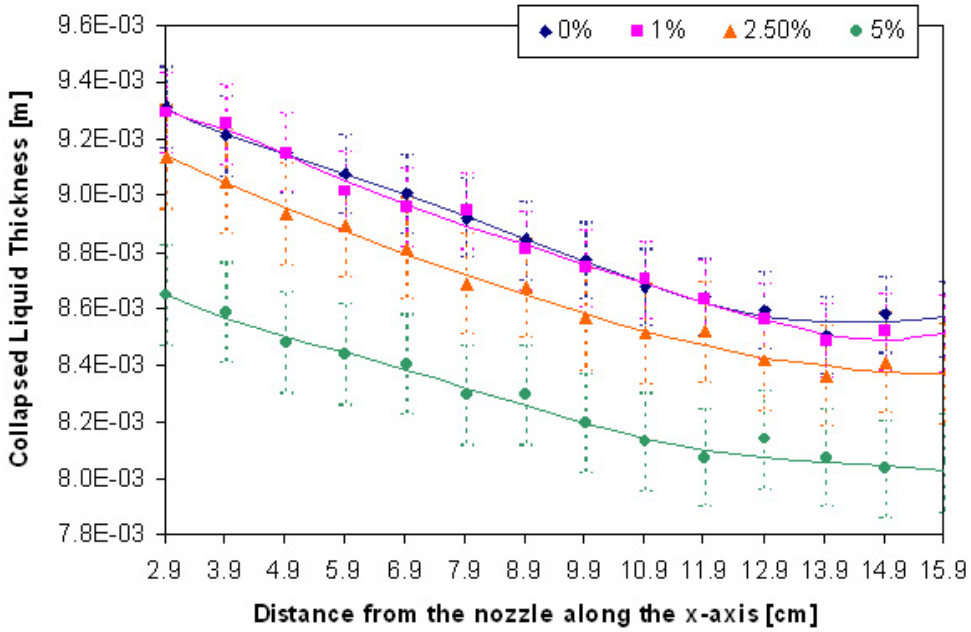

Figure 4.15: Collapsed liquid thickness profile along the x-axis for a planar jet (initial liquid superficial velocity = 3.0 m/s, $Re_l = 5.68 \times 10^4$)

It should be noted that an increase in the the initial superficial liquid velocity and void fractions results in a decrease in the slope of the collapsed liquid thickness profiles along the x-axis (Figures 4.17 and 4.18). The profiles shown also include the case with $\alpha_e = 15\%$ (□) for the circular geometry. At low velocities, the jet tends to narrow on its centerline; at high velocities, the free surface of the jet remains nearly unchanged along the x-axis. The contours of the free surface are weakly dependent on the void fraction, and mainly dependent on the initial liquid velocity and the distance along the x-axis from the nozzle exit.

The jet thickness $\delta_{jet}(x)$ is measured and curve-fitted in a manner similar to that used for the collapsed liquid thickness ($R^2 > 95\%$ in all cases); the void fraction of the jet $\alpha_{jet}(x)$ is then simply obtained from Equation 4.18.

$$\alpha_{jet}(x) = 1 - \frac{\delta_{CLT}(x)}{\delta_{jet}(x)} \tag{4.18}$$

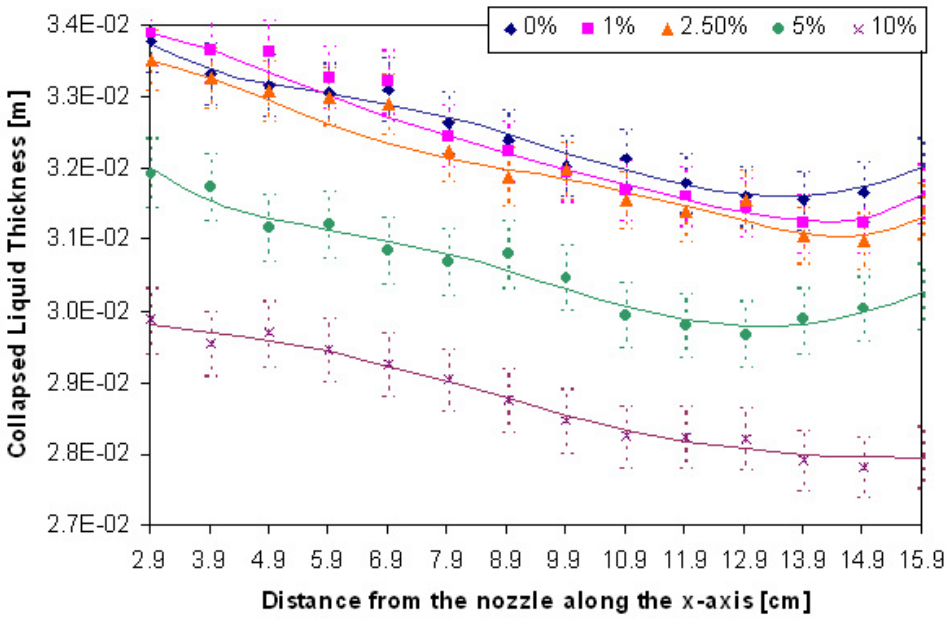

Figure 4.16: Collapsed liquid thickness profile along the x-axis for a circular jet (initial liquid superficial velocity = 3.0 m/s, $Re_l = 1.11 \times 10^5$)

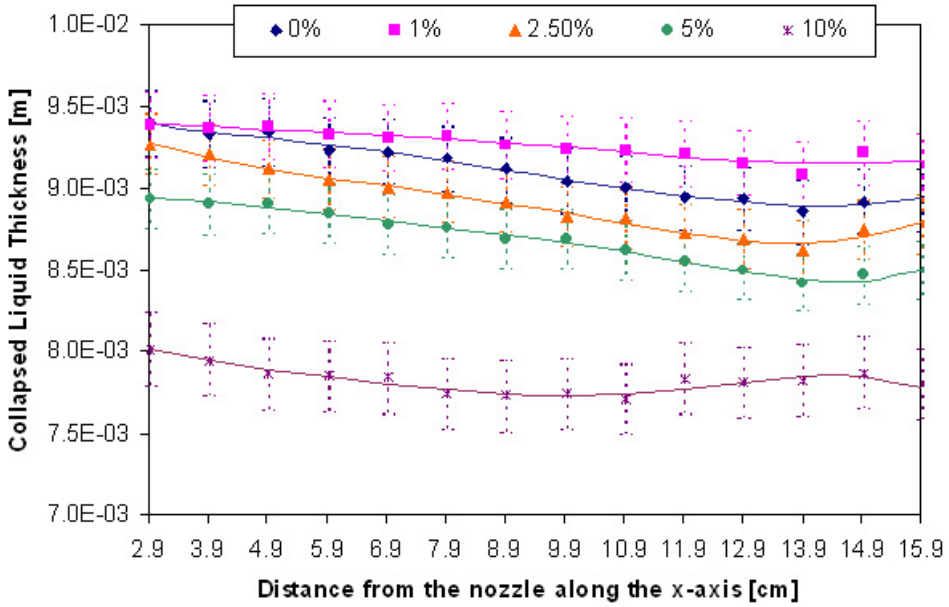

Figure 4.17: Collapsed liquid thickness profile along the x-axis for a planar jet (initial liquid superficial velocity = 4.0 m/s, $Re_l = 7.57 \times 10^4$)

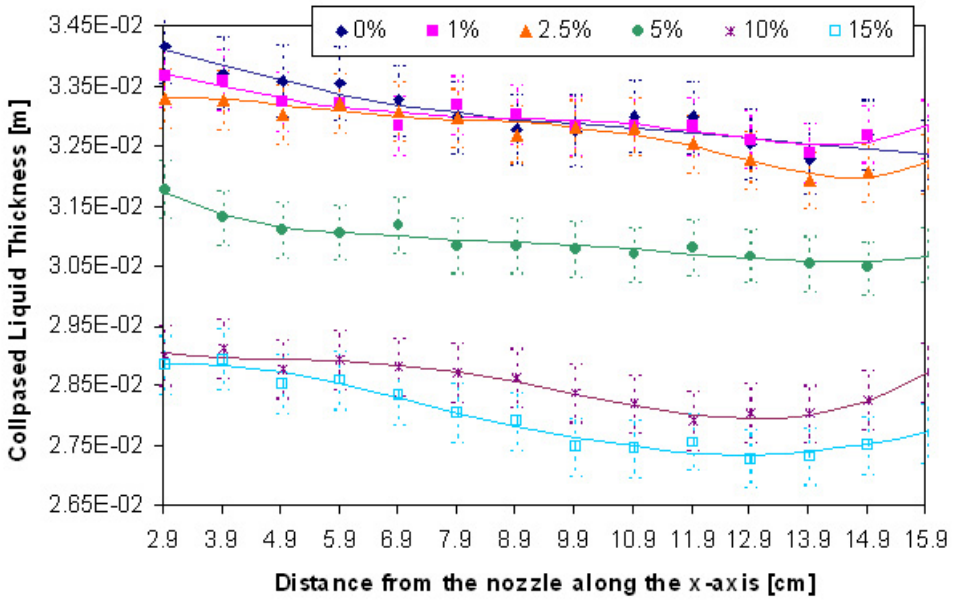

Figure 4.18: Collapsed liquid thickness profile along the x-axis for a circular jet (initial liquid superficial velocity = 4.0 m/s, $Re_l = 1.49 \times 10^5$)

The error associated with the jet thickness is calculated from Equation 4.18 and is given in Equation 4.19; details of the calculation are provided in Appendix F (see Section F.2.4). The error $U_{\delta_{jet}(x)}$ is assumed to be constant and equal to $U_{\delta_{jet}(x)} = 6.35 \times 10^{-5}$ m, which corresponds to the precision of the depth micrometer.

$$U_{\alpha_{jet}(x)} = \sqrt{\left[U_{\delta_{CLT}(x)} \cdot \frac{-1}{\delta_{jet}(x)}\right]^2 + \left[U_{\delta_{jet}(x)} \cdot \frac{\delta_{CLT}(x)}{\delta_{jet}^2(x)}\right]^2} \tag{4.19}$$

Figures 4.19 and 4.20 show the 1-D void fraction distribution within a planar and a circular jet at a superficial liquid exit velocity of 3 m/s which corresponds to a Reynolds number of 5.68×10^4 and 1.11×10^5, respectively. The 1-D void fraction distribution is plotted against the ratio of distance x from the nozzle over the nozzle hydraulic diameter. For the planar jet, the hydraulic diameter D_h equals 1.818 cm, while for the circular jet, the hydraulic diameter D_h equals the inner diameter of the circular nozzle, i.e. 3.57 cm. The profiles shown are acquired at homogeneous exit void fractions of α_e = 0% (♦), 1% (■), 2.5% (▲), 5% (•), and 10% (∗). The points are calculated from the experimental measured points, while the solid lines are

obtained by curve fitting the collapsed liquid and jet thicknesses. The errors on the void fraction measurements are presented in Appendix F (see Section F.2.4); they are on the same order for both the planar and the circular jets. The errors are calculated using Equation 4.19. The errors for void fraction in the case of the planar and the circular geometries are on the order of 1.50 - 2.58% and 1.18 - 5.37%, respectively. The first value measured for the void fraction (at x = 2.9 cm) is close to the average homogeneous void fraction at the nozzle exit α_e. It can also be noted that the void fraction within the free jet increases with the distance x from the nozzle for the planar jet, as well as for the circular jet. The bubbles tend to migrate to low velocity regions, and they are subject to buoyancy effects, which tend to slow them down. The liquid accelerates downward due to the gravitational forces. Therefore, since the gas velocity decreases and the liquid velocity increases along the flow direction, the local void fraction increases and the slip ratio decreases as the jet proceeds away from the nozzle exit. The entire analysis method is also applied to the case where α_e = 0%. The resulting void fraction values are nearly zero; the estimated void fraction becomes negative when the collapsed liquid thickness is greater than the measured jet thickness. The void fraction profiles for all experiments performed in this investigation are presented in Appendix D.

Table 4.3 provides the ratio between the void fraction values at x = 15.9 cm and x = 2.9 cm for different initial superficial liquid velocity $j_{l,e}$ and void fraction α_e in the case of the planar jet. The increase in void fraction with the distance x from the nozzle $\alpha_{jet}(x)$ is greater for low initial superficial liquid velocity ($j_{l,e} \sim 2$ m/s) and void fraction ($\alpha_e \sim 1\%$) rather than for relatively high initial superficial liquid velocity ($j_{l,e} \sim 4$ m/s) and void fractions ($\alpha_e \sim 5\%$).

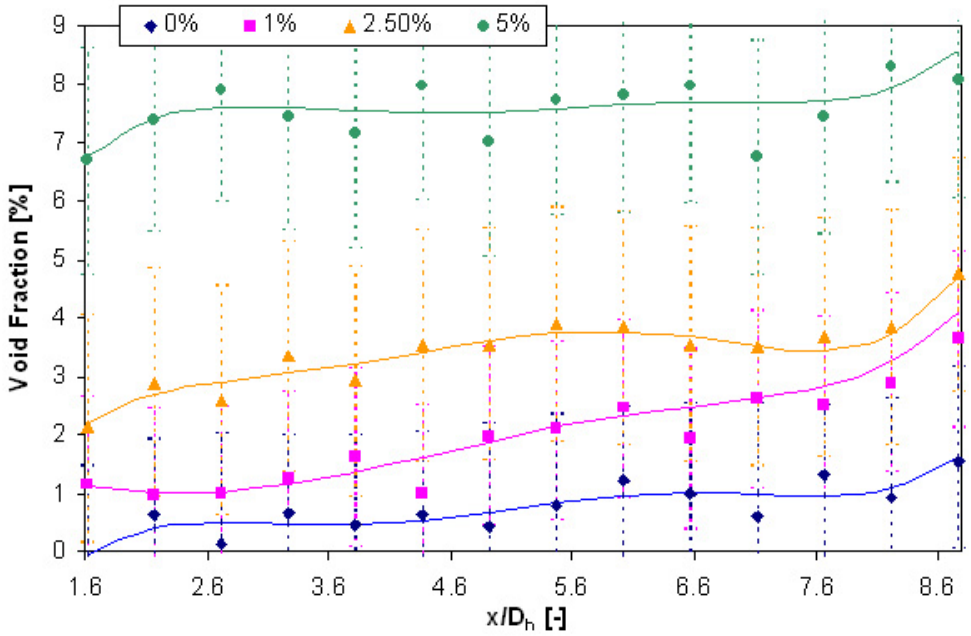

Figure 4.19: Void fraction distribution along the dimensionless x-axis for a planar jet (initial liquid superficial velocity = 3.0 m/s, $Re_l = 5.68 \times 10^4$)

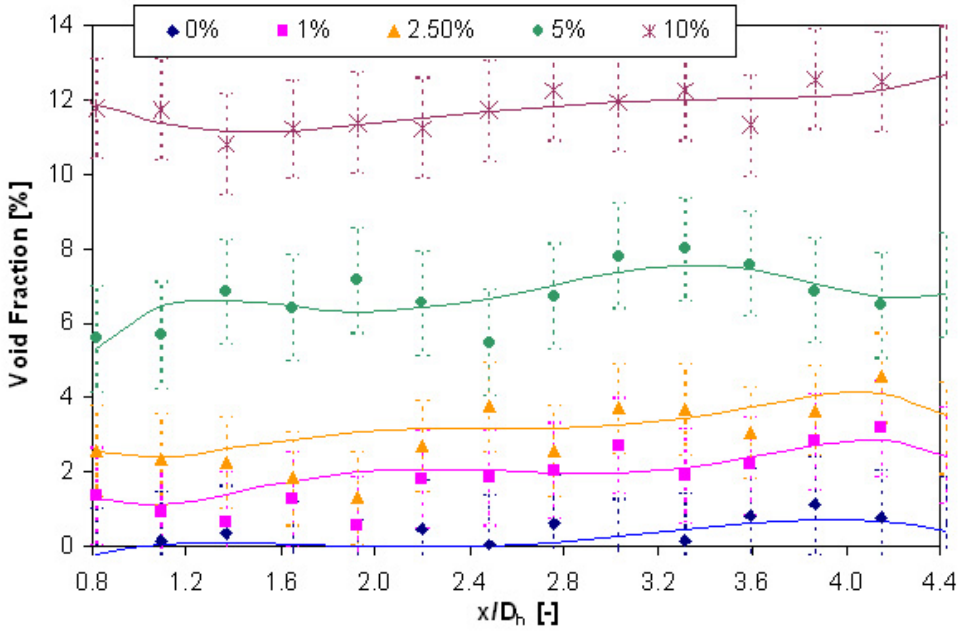

Figure 4.20: Void fraction distribution along the dimensionless x-axis for a circular jet (initial liquid superficial velocity = 3.0 m/s, $Re_l = 1.11 \times 10^5$)

Table 4.3: Ratios of $\alpha_{jet}(x = 15.9\ cm)$ over $\alpha_{jet}(x = 2.9\ cm)$ for 2 m/s $\leq j_{l,e} \leq$ 4 m/s and 1% $\leq \alpha_e \leq$ 5% in the case of the planar jet

	$j_{l,e}$ = 2 m/s	$j_{l,e}$ = 3 m/s	$j_{l,e}$ = 4 m/s
α_e = 1%	4.2	4	2
α_e = 2.5%	2.4	2	1.67
α_e = 5%	1.55	1.31	1.33

4.2.2 Slip Ratio

The slip ratio is defined in Equation 4.20 as the ratio of gas and liquid phase velocities, U_g and U_l, respectively.

$$S(x) = \frac{U_g}{U_l} \tag{4.20}$$

The phase velocity of a specific phase (gas or liquid) is defined as the ratio of the phase volume flow rate at the nozzle exit $\dot{V}_{g-or-l,e}$ over the area occupied by the phase. The phase volume flow rate at the nozzle exit $\dot{V}_{g-or-l,e}$ can be expressed as a function of the superficial velocity at the nozzle exit $j_{g-or-l,e}$. Equations 4.21 and 4.22 provide the relationship between the superficial velocity and the volume flow rate for the gas phase in the case of the planar jet and the circular jet, respectively . Equations 4.23 and 4.24 provide the relationship between the superficial velocity and the volume flow rate for the liquid phase in the case of the planar jet and the circular jet, respectively .

$$j_{g,e} = \frac{\dot{V}_{g,e}}{\delta_e \cdot w_e} = \alpha_e \cdot \frac{\dot{V}_{g,e} + \dot{V}_{l,e}}{\delta_e \cdot w_e} \tag{4.21}$$

$$j_{g,e} = \frac{\dot{V}_{g,e}}{\pi/4 \cdot \phi_e^2} = \alpha_e \cdot \frac{\dot{V}_{g,e} + \dot{V}_{l,e}}{\pi/4 \cdot \phi_e^2} \tag{4.22}$$

$$j_{l,e} = \frac{\dot{V}_{l,e}}{\delta_e \cdot w_e} = (1 - \alpha_e) \cdot \frac{\dot{V}_{g,e} + \dot{V}_{l,e}}{\delta_e \cdot w_e} \tag{4.23}$$

$$j_{l,e} = \frac{\dot{V}_{l,e}}{\pi/4 \cdot \phi_e^2} = (1 - \alpha_e) \cdot \frac{\dot{V}_{g,e} + \dot{V}_{l,e}}{\pi/4 \cdot \phi_e^2} \tag{4.24}$$

Equations 4.25 and 4.26 provide the definition of the phase velocity as a function of the superficial velocity for the gas phase in the case of the planar jet and the

circular jet, respectively; the corresponding definitions for the liquid phase are given by Equations 4.27 and 4.28.

$$U_g(x) = \frac{\delta_e \cdot w_e \cdot j_{g,e}}{\delta(x) \cdot w(x) \cdot \alpha_{jet}(x)} \tag{4.25}$$

$$U_g(x) = \frac{\pi/4 \cdot \phi_e^2 \cdot j_{g,e}}{\pi/4 \cdot [\phi(x)]^2 \cdot \alpha_{jet}(x)} \tag{4.26}$$

$$U_l(x) = \frac{\delta_e \cdot w_e \cdot j_{l,e}}{\delta(x) \cdot w(x) \cdot (1 - \alpha_{jet}(x))} \tag{4.27}$$

$$U_l(x) = \frac{\pi/4 \cdot \phi_e^2 \cdot j_{l,e}}{\pi/4 \cdot [\phi(x)]^2 \cdot (1 - \alpha_{jet}(x))} \tag{4.28}$$

Simplified expressions for the slip ratio are provided in Equations 4.29 and 4.30.

$$S(x) = \frac{j_{g,e} \cdot (1 - \alpha_{jet}(x))}{j_{l,e} \cdot \alpha_{jet}(x)} \tag{4.29}$$

$$S(x) = \frac{\alpha_e}{\alpha_{jet}(x)} \cdot \frac{1 - \alpha_{jet}(x)}{1 - \alpha_e} \tag{4.30}$$

The error associated with the slip ratio is calculated from Equation 4.30 and is given by Equation 4.31; details of the error calculation are provided in Appendix F (see Section F.2.5).

$$U_{S(x)} = \sqrt{\left[U_{\alpha_{jet}(x)} \cdot \frac{\alpha_e}{(1 - \alpha_e) \cdot (\alpha_{jet}(x))^2}\right]^2} = \left|U_{\alpha_{jet}(x)} \cdot \frac{\alpha_e}{(1 - \alpha_e) \cdot (\alpha_{jet}(x))^2}\right| \tag{4.31}$$

Figures 4.21 and 4.22 show variations of the slip ratio with non-dimensional distance along the flow direction for a planar and a circular jet, respectively. These data pertain to Reynolds number values of 5.68×10^4 and 1.11×10^5, i.e., a superficial liquid velocity of 3 m/s at the nozzle exit. The profiles shown are acquired at $\alpha_e =$ 0% (♦), 1% (■), 2.5% (▲), 5% (•), and 10% (∗). The points and the solid lines are calculated from the curve fitted values of the jet thicknesses, since the fitting curves are within the error bars. The error is calculated using Equation 4.31, and is on the order of 0.3 and 0.25 for the planar and the circular jets, respectively. Since the liquid accelerates downward while the gas decelerates due to the buoyancy effect, the void

fraction increases with the distance x from the nozzle and the slip ratio decreases. The geometry of the jet does not seem to affect the distribution trend; the slip ratio distributions have the same trends for both planar and circular jets when the initial void fraction α_e varies. It should also be noted that, at low void fraction ($\alpha_e \sim 1\%$), the slip ratio can decrease to values as low as 0.3 - 0.4, 15 cm from the nozzle exit. The different slip ratio profiles for all experiments performed in this investigation are presented in Appendix D.

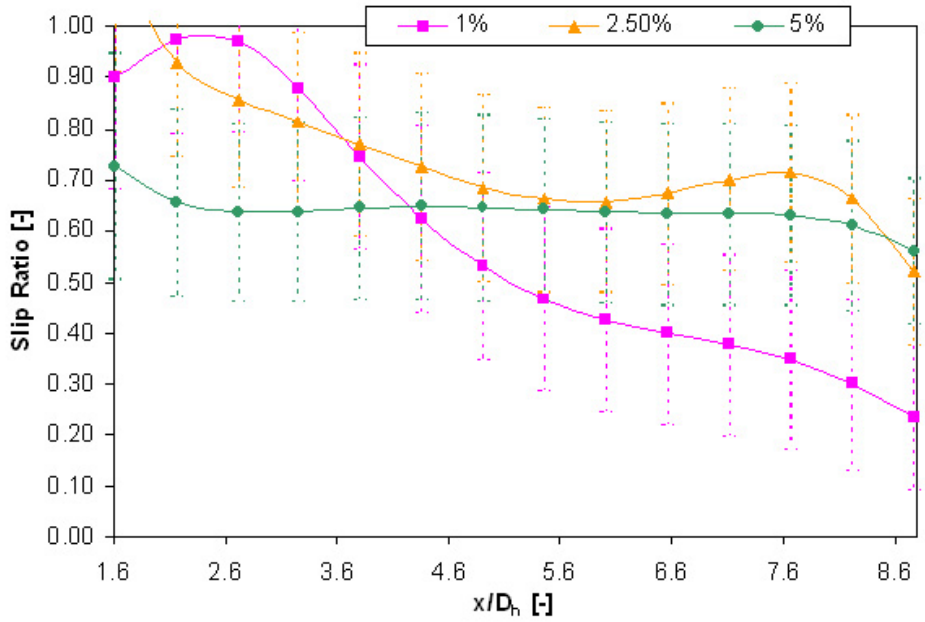

Figure 4.21: Slip ratio distribution along the dimensionless x-axis for a planar jet (initial liquid superficial velocity = 3.0 m/s, $Re_l = 5.68 \times 10^4$)

Figure 4.23 shows the slip ratio distribution for a planar jet with a constant initial void fraction ($\alpha_e = 1\%$) at different liquid flow rates. The profiles shown are acquired at $j_{l,e}$ = 0% (♦), 1 m/s (■), 2 m/s (▲), 3 m/s (•), and 4 m/s (∗). At low void fractions ($\alpha_e \sim 1\%$), the slip ratio at the end of the test region (15.9 centimeters downstream the nozzle exit) increases as the superficial liquid velocity increases (see Figure 4.23). This is caused by the increased downward drag on the gas at higher liquid velocity versus the upward buoyancy force which is unaffected by the liquid

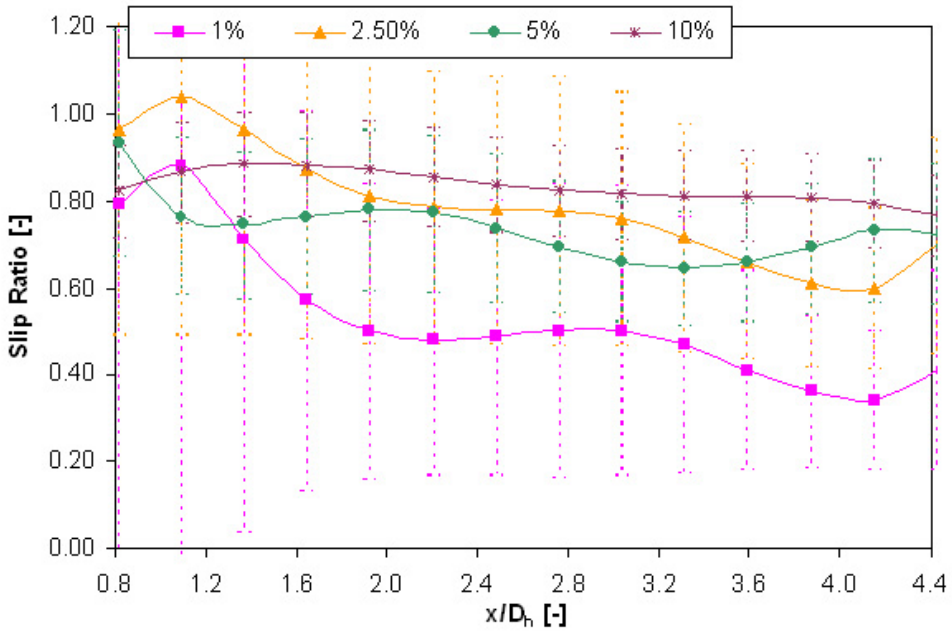

Figure 4.22: Slip ratio distribution along the dimensionless x-axis for a circular jet (initial liquid superficial velocity = 3.0 m/s, $Re_l = 1.11 \times 10^5$)

velocity. Buoyancy effects dominate at low initial superficial liquid velocity ($j_{l,e} = 1$ m/s); at x = 2.9 cm, the slip ratio for $j_{l,e} = 1$ m/s is already around 0.2. At relatively high void fractions ($\alpha_e \sim 5\%$), the differences in slip ratio are weakly dependent on the initial superficial liquid velocity $j_{l,e}$.

4.2.3 Comparison with Empirical Correlations

Todreas and Kazimi (Todreas and Kazimi, 1990) present a general approach to obtain the void fraction; this method was suggested by Zuber and Findlay (Zuber and Findlay, 1965) by considering the effective drift velocity of the vapor in the channel. It physically represents the velocity at which the gas passes through a unit area (normal to the channel axis) that is already traveling with the flow at a velocity j. Equation 4.32 expresses the void fraction at the nozzle exit α_e as a function of the quality x, the mass flux of the mixture G, and the effective drift velocity of the gas V_{gj}.

$$\alpha_e = \frac{1}{C_0 \cdot \left(1 + \frac{1-x}{x} \cdot \frac{\rho_l}{\rho_g}\right) + \frac{V_{gj} \cdot \rho_g}{x \cdot G}} \tag{4.32}$$

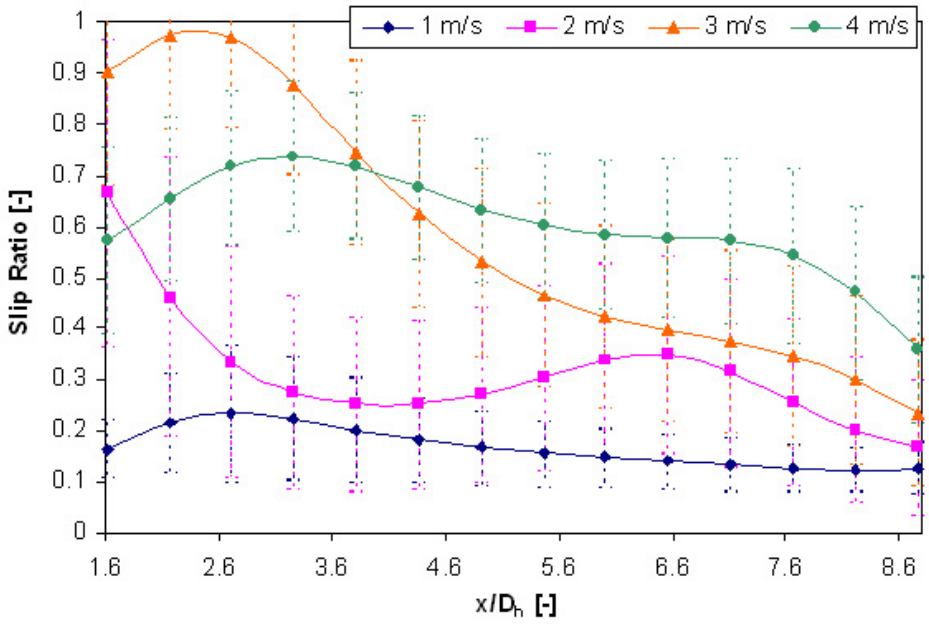

Figure 4.23: Slip ratio distribution within a planar jet for $\alpha_e = 1\%$ and 1 m/s $\leq j_{l,e} \leq$ 4 m/s, $1.89 \times 10^4 \leq Re_l \leq 7.57 \times 10^4$

The flow quality x is defined in Equation 4.33 as the ratio between the gas mass flow and the total mass flow.

$$x = \frac{\dot{m}_g}{\dot{m}_g + \dot{m}_l} \tag{4.33}$$

For uniform void fraction in the flow area, $C_0 = 1$. Zuber and Findlay (Zuber and Findlay, 1965) suggested that C_0 and V_{gj} are functions of the flow regime; $C_0 = 1.2$ for bubbly and slug flow, and $C_0 = 0$ for near zero void fraction and 1.0 for high void fraction. The drift velocity V_{gj} for the bubbly and slug flow regimes is given by:

$$V_{gj} = \left(1 - \frac{\beta}{C_0}\right)^n \cdot V_\infty \tag{4.34}$$

For small bubbles ($D_{bubble} < 0.54$ cm), $n = 3$ and V_∞ is given by Equation 4.35, where μ_l is the dynamic viscosity of the liquid, β is the homogeneous equilibrium void fraction. Here β is assumed to be equal to the 1-D void fraction at the nozzle exit α_e.

$$V_\infty = \frac{g \cdot (\rho_l - \rho_g) \cdot D_{bubble}^2}{18 \cdot \mu_l} \tag{4.35}$$

When the local slip (or drift) is small, Armand and Treschev (Armand and Treschev, 1947) suggested that:

$$\frac{1}{C_0} = 0.833 + 0.05 \cdot \ln(10 \cdot p) \tag{4.36}$$

where p is in MPa. Bankoff (Bankoff, 1960) suggested that:

$$\frac{1}{C_0} = 0.71 + 0.0001 \cdot p \tag{4.37}$$

where p is in psi. Dix (Dix, 1971) suggested a general expression for C_0 for all flow regimes, given by:

$$C_0 = \beta \cdot \left[1 + \left(\frac{1}{\beta} - 1\right)^b\right] \tag{4.38}$$

where:

$$b = \left(\frac{\rho_g}{\rho_l}\right)^{0.1} \tag{4.39}$$

If p is assumed to be equal to P_{atm} = 14.7 psi = 101.1 kPa, C_0 for Armand and Treschev's correlation and Bankoff's correlation is equal to 1.2 and 1.4, respectively. The advantage of Dix' correlation is that it provides a value for C_0 which varies with β or the homogeneous equilibrium 1-D void fraction at the nozzle exit α_e. For the Dix correlation, C_0 varies between 0.1 and 0.5. The Laplace length's scale, as presented in Equation 4.46, suggests that $D_{bubble} \approx 2.7$ mm. Figures 4.24 and 4.25 present the ratio between the void fraction values predicted by the Dix correlation and α_e, versus the dimensionless experimental data at x = 2.9 cm (i.e, the ratio between $\alpha_{jet}(x = 2.9cm)$ and α_e). The upper and lower values obtained from the Dix correlation correspond to a bubble diameter D_{bubble} of 2 and 3 mm, respectively. The test conditions excluded from on Figures 4.24 and 4.25 ($j_{l,e}$ = 1 m/s and α_e = 1% for the planar jet; $j_{l,e}$ = 1 m/s and α_e = 1%, 2.5%; and $j_{l,e}$ = 2 m/s and α_e = 1% for the circular jet) are underpredicted by Dix' correlation for a bubble diameter D_{bubble} equal to 2 or 3 mm. Therefore, in these cases, a better fit would be obtained if the bubble diameter is lower than 2 mm. The data suggest that increasing the initial void fraction α_e results in a larger bubble size (see Section 4.1.2). Since the void fraction increases with the

distance x from the nozzle, the Dix correlation can provide a reasonable estimate for the minimum void fraction within the jet.

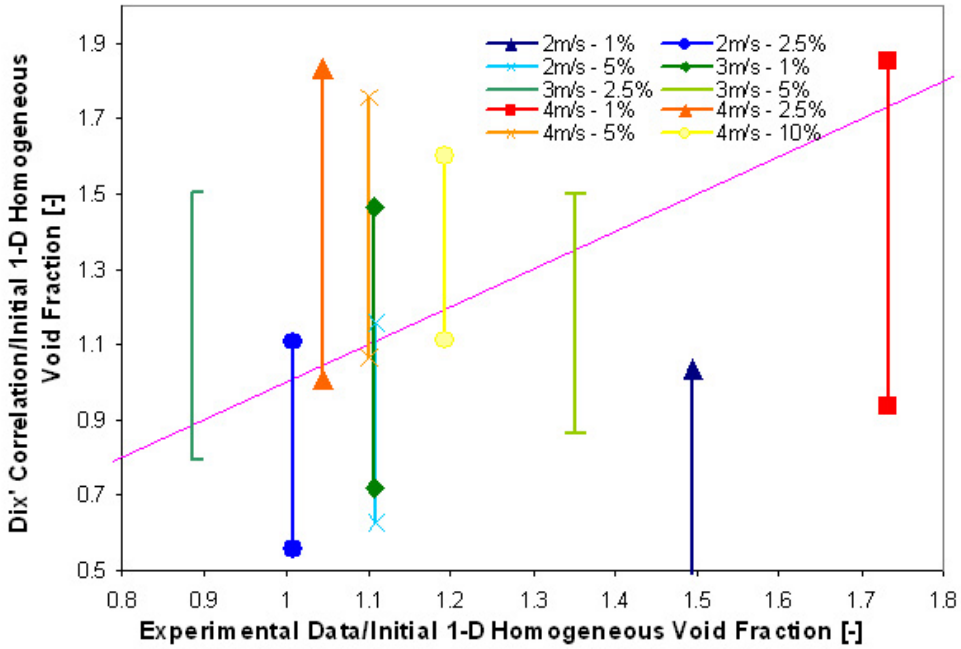

Figure 4.24: Dimensionless values predicted with Dix' correlation versus dimensionless experimental data at x = 2.9 cm for the planar jet

Kern (Kern, 2007) recommends a correlation for the void fraction for the 1 cm × 10 cm planar jet as a function of the Reynolds number *Re*, the Weber number *We*, and the Froude number *Fr*. The suggested form of the empirical correlation is given by Equation 4.40 with the dimensionless numbers defined in Equations 4.41, 4.42, 4.43, and 4.44. The parameters ν_l, ρ_l, and σ are respectively the kinematic viscosity of the liquid, the density of the liquid, and the surface tension between the gas and the liquid determined at the room temperature T_{room} = 295 K = 22°C, while C_0, a, b, c, and d are constants.

$$\frac{\alpha_{jet}(x)}{\alpha_e} = C_0 \cdot [Re_l(x)]^a \cdot [We_l(x)]^b \cdot [Fr_l(x)]^c \cdot [L^*(x)]^d \tag{4.40}$$

$$Re_l(x) = \frac{j_l(x) \cdot \delta_{jet}(x)}{\nu_l} \tag{4.41}$$

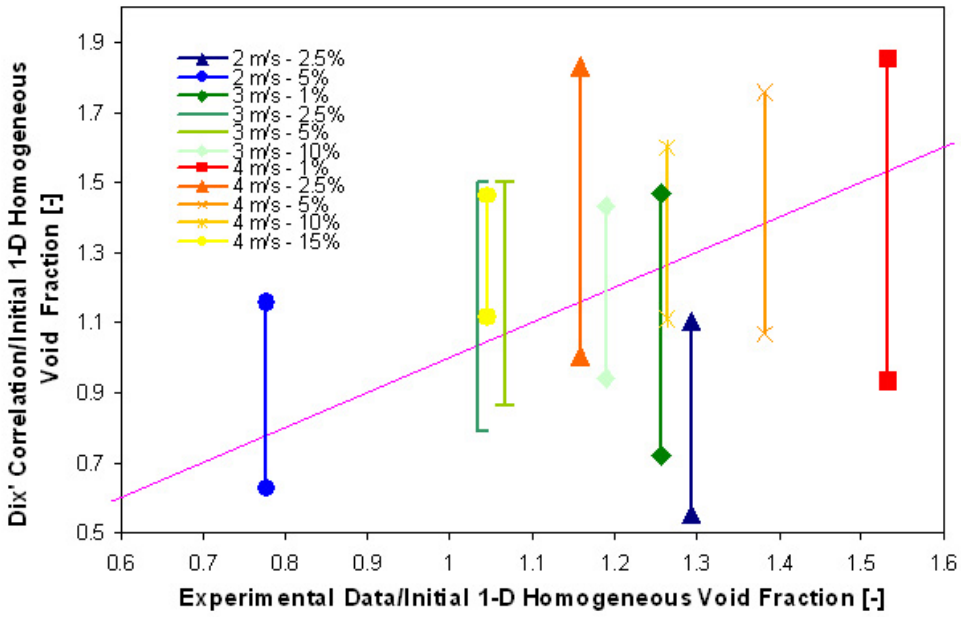

Figure 4.25: Dimensionless values predicted with Dix' correlation versus dimensionless experimental data at x = 2.9 cm for the circular jet

$$We_l(x) = \frac{\rho_l \cdot [j_l(x)]^2 \cdot \delta_{jet}(x)}{\sigma} \tag{4.42}$$

$$Fr_l(x) = \frac{j_l(x)}{\sqrt{g \cdot \delta_{jet}(x)}} \tag{4.43}$$

$$L^*(x) = \frac{x}{\delta_e} \tag{4.44}$$

Kern (Kern, 2007) bases his correlation either on the superficial liquid velocity $j_l(x)$ or on the phase liquid velocity $U_l(x)$. As it is shown in Equation 4.27, $U_l(x)$ is dependent on $\alpha_{jet}(x)$; therefore, any correlations in this study will be based on the superficial liquid velocity $j_l(x)$ so that the left-hand side of the Equation 4.40 is independent of the right-hand side, as it is presented in Equations 4.40, 4.41, 4.42, 4.43, and 4.44. Kern (Kern, 2007) recommends the values $C_0 = 1.300 \times 10^{-5}$, $a = 1.4080$, $b = -0.1891$, $c = -0.839$, and $d = 0.1180$ for the 1 cm × 10 cm planar jet and a room temperature $T_{room} = 295$ K $= 22^o$C. The coefficient of multiple determination for this correlation is $R^2 = 95\%$. This correlation is valid for bubbly flow within planar jets within the following parameter ranges: 4 m/s $\leq j_{l,e} \leq$ 4.79 m/s and 9% $\leq \alpha_e \leq$

16.7%.

Experimental data in the range of application of Kern's correlation are compared against values predicted by the correlation. Referring to Table 4.2, only test #15 respects the conditions of application ($j_{l,e} = 4$ m/s and $\alpha_e = 10\%$). Figure 4.26 compares and shows poor agreement between the experimental data and the results obtained from Kern's correlation. The coefficient of multiple determination for this case is $R^2 = 46\%$.

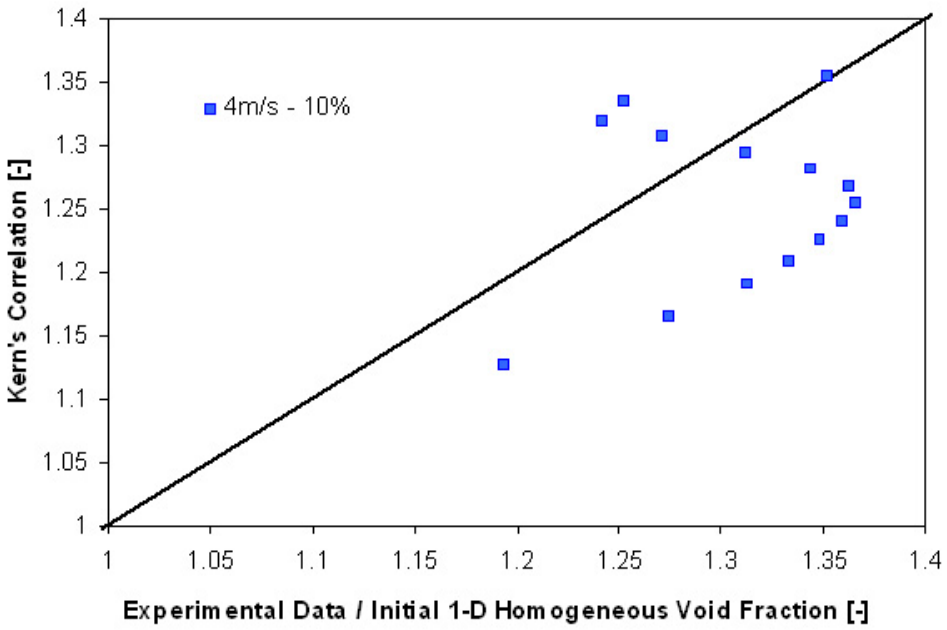

Figure 4.26: Experimental data versus results obtained from Kern's correlation for $j_{l,e} = 4$ m/s, $Re_l = 7.57 \times 10^4$, and $\alpha_e = 10\%$

The Kern correlation has been modified in order to make it applicable to both planar and circular bubbly jets, and to expand the parameter ranges to include 1 m/s $\leq j_{l,e} \leq$ 4.0 m/s and 1% $\leq \alpha_e \leq$ 15%. Since the same fluid (incompressible water at $T_{room} = 295$ K $= 22^o$C and P_{atm}) is used in all the tests, the dimensionless numbers Re_l, We_l, and Fr_l are combined together under the same exponent so that the inertia forces only appear once. A new parameter representing the ratio between the superficial gas velocity $j_g(x)$ and the bubble rise velocity U_{rise} has been included.

Equation 4.45 provides the balance of gravitational and drag forces acting on a bubble rising in a liquid. $D_{Laplace}$, ρ_l, ρ_g, and C_D are the diameter of the bubble, the density of the liquid, the density of the gas, and the drag coefficient, respectively, determined at the room temperature $T_{room} = 295$ K $= 22^oC$. The diameter of the bubble $D_{Laplace}$ is determined according to the Laplace's length scale, provided in Equation 4.46. The drag coefficient C_D is determined using Schlichting's method (Incropera and DeWitt, 2002) correlating the drag coefficient to the Reynolds number for a sphere. The drag coefficient is assumed to be constant and equal to 0.45 for the range of the Reynolds number in this study ($1.89 \times 10^4 \leq Re_l \leq 1.49 \times 10^5$). The expression for the bubble rise velocity U_{rise} is given in Equation 4.47.

$$\left(\frac{4}{3}\cdot\pi\cdot\left(\frac{D_{Laplace}}{2}\right)^3\right)\cdot(\rho_l-\rho_g)\cdot g = C_D\cdot\left(\frac{\pi}{4}\cdot D_{Laplace}^2\right)\cdot\frac{1}{2}\cdot\rho_g\cdot U_{rise} \tag{4.45}$$

$$D_{Laplace} = \sqrt{\frac{\sigma}{g\cdot(\rho_l-\rho_g)}} \tag{4.46}$$

$$U_{rise} = \sqrt{\frac{4}{3}\cdot D_{Laplace}\cdot\frac{\rho_l-\rho_g}{\rho_g}\cdot\frac{g}{C_D}} \tag{4.47}$$

The improved correlation is presented in Equation 4.48; C_0, a, b, and c are constants. The Reynolds number $Re_l(x)$, the Weber number $We_l(x)$, the Froude number $Fr_l(x)$, and $L^*(x)$ are defined in Equations 4.41, 4.42, 4.43, and 4.44, respectively. The dimensionless number $j_g^*(x)$ is defined in Equation 4.49.

$$\frac{\alpha_{jet}(x)}{\alpha_e} = C_0\cdot\left[\frac{Re(x)\cdot We(x)}{Fr(x)}\right]^a\cdot\left[j_g^*(x)\right]^b\cdot\left[L^*(x)\right]^c \tag{4.48}$$

$$j_g^*(x) = \frac{j_g(x)}{U_{rise}} \tag{4.49}$$

The recommended values for C_0, a, b, and c are provided in Table 4.4 for the planar and circular jets. The coefficients of multiple determination for this correlation are $R^2 = 87\%$ and 86%, respectively for the planar and the circular jets. This correlation is valid for bubbly flow within planar and circular free jets within the following

Table 4.4: Values recommended for C_0, a, b, and c in the proposed correlation (Equation 4.48), respectively for the planar and the circular jets

	C_0	a	b	c
Planar	19.0	-0.343	-0.352	0.525
3.6 cm ID circular	305	-0.329	-0.141	0.329

parameter ranges: 1.0 m/s $\leq j_{l,e} \leq$ 4.0 m/s and 1% $\leq \alpha_e \leq$ 15%. The probability that the coefficients C_0, a, b, and c have different values is nearly null.

Figures 4.27 and 4.28 present the dimensionless experimental data versus the results obtained from the proposed correlation 4.48 for the planar and the circular geometries, respectively. Note that the experimental data for the tests run at $j_{l,e} =$ 2 m/s are not presented in Figure 4.28; at $j_{l,e} = 2$ m/s, the jets are in the transition regime, and therefore, while being stable, the jets have strong surface waves, which prevent accurate measurements of the thickness, and hence, the local void fraction. The errors for void fraction in the case of the planar and the circular geometries are on the order of 1.50 - 2.58% and 1.18 - 5.37%, respectively. The correlation matches the main trends indicated in the previous paragraphs. The void fraction within the free jet increases with increasing distance from the nozzle exit for both the planar jet and the circular jet. The increase in void fraction with the distance x from the nozzle $\alpha_{jet}(x)$ is greater for low initial superficial liquid velocity ($j_{l,e} \sim 2$ m/s) and void fraction ($\alpha_e \sim 1\%$) rather than for relatively high initial superficial liquid velocity ($j_{l,e} \sim 4$ m/s) and void fraction ($\alpha_e \sim 5\%$). This is caused by the increased downward drag on the gas at higher liquid velocity versus the upward buoyancy force which is unaffected by the liquid velocity.

4.3 Shock Attenuation with Two-Phase Annular Jets

4.3.1 Repeatability between Experiments

Experiments have been conducted to quantify the extent by which two-phase jets can attenuate a shock wave. The pressure history at the enclosure wall is recorded as the

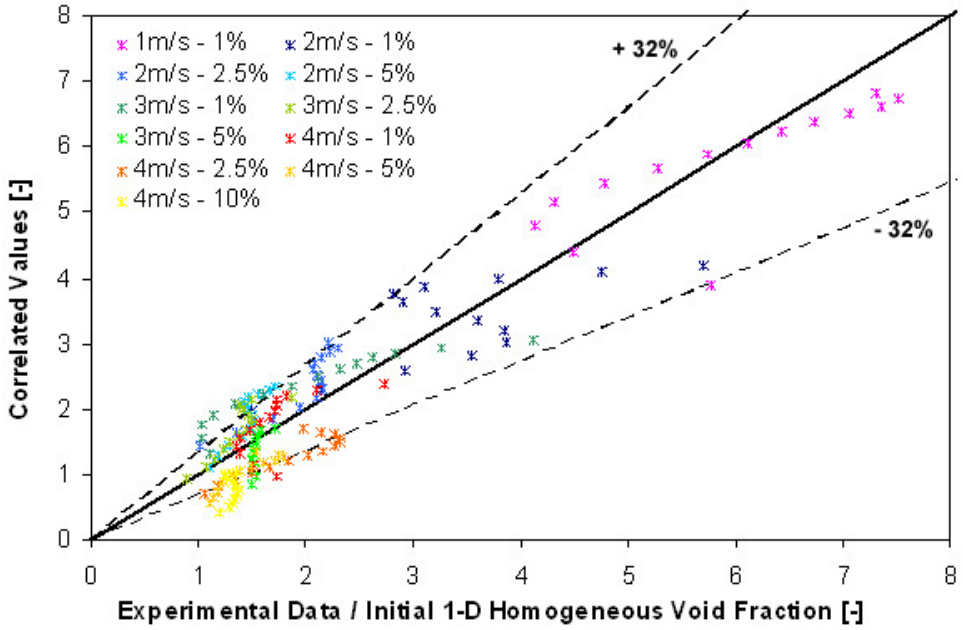

Figure 4.27: Comparison of the dimensionless experimental data (∗) and the data obtained from the proposed correlation (-) in the case of the planar jet

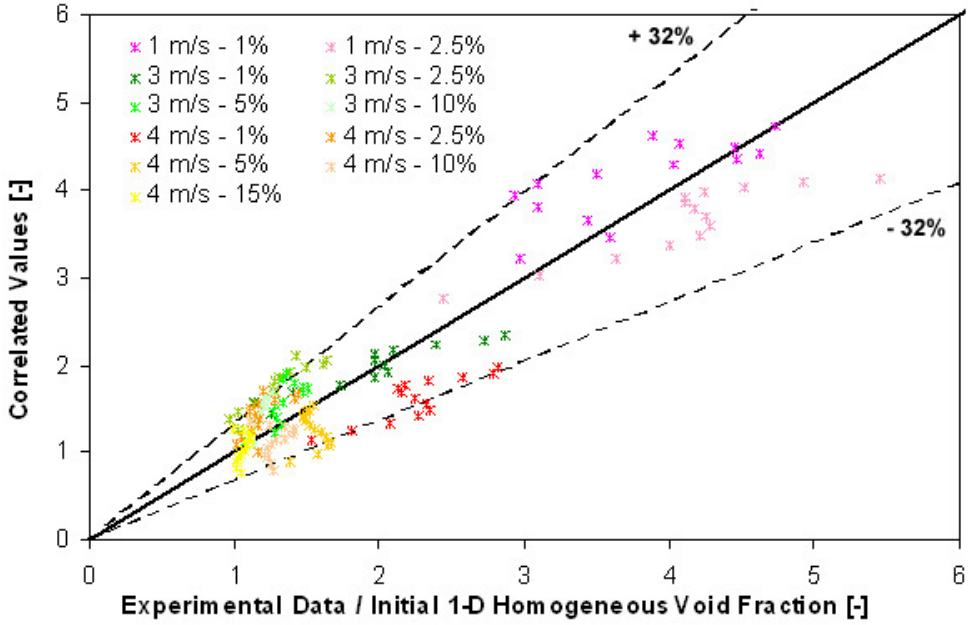

Figure 4.28: Comparison of the dimensionless experimental data (∗) and the data obtained from the proposed correlation (-) in the case of the circular jet

shock wave propagates through the attenuating two-phase medium. Experiments are conducted on the small-scale experimental loop using the 5.18 cm OD and 4.0 cm ID annular jet. Experiments are conducted at three different liquid superficial velocities $j_{l,e}$ of 1.0, 2.0, and 4.0 m/s, with different homogeneous void fractions at the nozzle exit α_e (0 to 10%), using three different boundary conditions. The maximum void fraction of 10% is limited by the ability to maintain a stable, thin (6.0 mm thick), annular jet at higher void fractions. A total of 738 experiments at 39 different test conditions have been performed. Detailed listing of the test conditions for annular jet experiments is provided in Table 4.5. The shock type refers to the boundary condition used in the experiment (# 1 for unconfined shocks, # 2 for radially-confined shocks, and # 3 for radially- and axially-confined shocks). The transducer # 1 refers to the $0 - 50$ psig pressure transducer, while the transducer # 2 refers to the $0 - 500$ psig pressure transducer. For each combination of test conditions, the experiment is repeated between 10 and 24 times, except for test condition # 20 (see Table 4.5), where the input energy of 2.1 kJ was too low to produce a sufficiently strong shock to propagate through the liquid jet. Figure 4.29 shows the transient pressure histories for six experiments conducted without a jet present in the enclosure; the experiments are conducted using the radial-and-axial confinement boundary configuration with pulser input energy of 2.4 kJ (referring to Table 4.5 test # 21). The pressure signal captured by the transducer at the bottom of the confinement tube is shown. The data show a high degree of repeatability between experiments; differences in the measured peak pressures for each set of 10 to 24 repeated experiments are less than 6%.

The shock wave produced by the exploding wire propagates radially and axially, and reflects from the enclosure boundaries (i.e., tube walls and liquid free surface at the bottom of the enclosure). The shock wave eventually dissipates as the mechanical energy is converted into thermal energy within the medium (air). The initial shock

Table 4.5: Detailed list of test conditions for small-scale annular jet experiments

Test #	Shock Type	Shock Strength (kJ)	$j_{l,e}$ (m/s)	Re_l	α_e (%)	Transducers used	# of experiments for given conditions
1	1	2.4	Air Only	0	-	1 and 2	10
2	1	2.4	2	2.45×10^4	0.00	1 and 2	20
3	1	2.4	2	2.45×10^4	1.00	1 and 2	20
4	1	2.4	2	2.45×10^4	10.00	1 and 2	20
5	1	2.7	2	2.45×10^4	10.00	1 and 2	20
6	1	3.0	2	2.45×10^4	10.00	1 and 2	20
7	2	2.4	Air Only	0	-	1	12
8	2	2.4	1	1.23×10^4	0.00	1	12
9	2	2.4	1	1.23×10^4	1.00	1	12
10	2	2.4	1	1.23×10^4	5.00	1	12
11	2	2.4	2	2.45×10^4	0.00	1	12
12	2	2.4	2	2.45×10^4	1.00	1	12
13	2	2.4	2	2.45×10^4	5.00	1	12
14	2	2.4	4	4.90×10^4	0.00	1	12
15	2	2.4	4	4.90×10^4	1.00	1	12
16	2	2.4	4	4.90×10^4	5.00	1	12
17	2	2.7	2	2.45×10^4	5.00	1	12
18	2	3.0	2	2.45×10^4	5.00	1	12
19	3	2.1	Air only	0	-	1 and 2	24
20	3	2.1	2	2.45×10^4	0.00	1 and 2	4
21	3	2.4	Air only	0	-	1 and 2	24
22	3	2.4	1	1.23×10^4	0.00	1 and 2	24
23	3	2.4	1	1.23×10^4	1.00	1 and 2	24
24	3	2.4	1	1.23×10^4	5.00	1 and 2	24
25	3	2.4	1	1.23×10^4	10.00	1 and 2	24
26	3	2.4	2	2.45×10^4	0.00	1 and 2	24
27	3	2.4	2	2.45×10^4	1.00	1 and 2	24
28	3	2.4	2	2.45×10^4	5.00	1 and 2	24
29	3	2.4	2	2.45×10^4	10.00	1 and 2	24
30	3	2.4	4	4.90×10^4	0.00	1 and 2	24
31	3	2.4	4	4.90×10^4	1.00	1 and 2	24
32	3	2.4	4	4.90×10^4	5.00	1 and 2	24
33	3	2.4	4	4.90×10^4	10.00	1 and 2	24
34	3	2.7	Air only	0	-	1 and 2	24
35	3	2.7	2	2.45×10^4	0.00	1 and 2	24
36	3	2.7	2	2.45×10^4	5.00	1 and 2	24
37	3	3.0	Air only	0	-	1 and 2	24
38	3	3.0	2	2.45×10^4	0.00	1 and 2	24
39	3	3.0	2	2.45×10^4	5.00	1 and 2	24

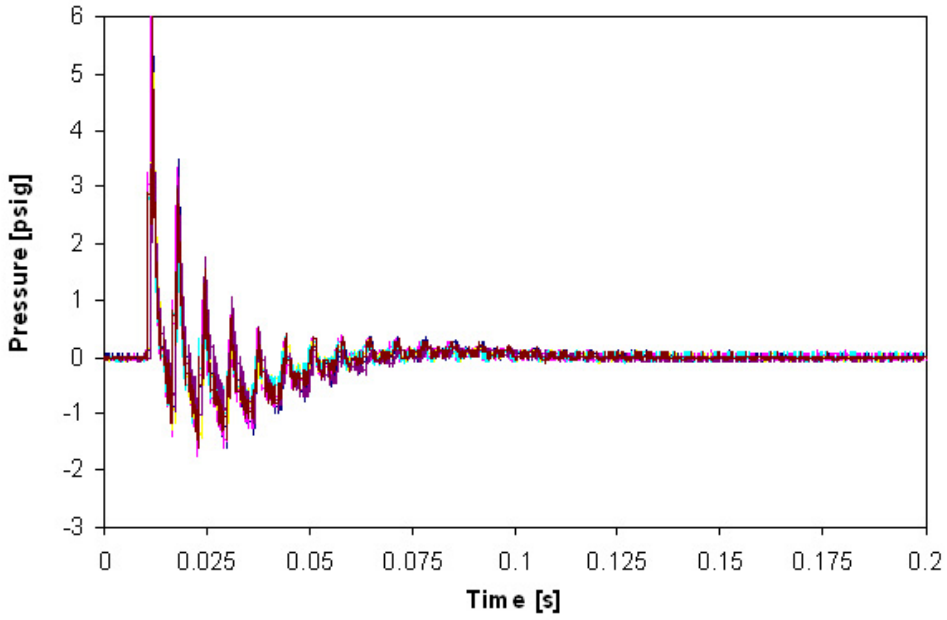

Figure 4.29: Transient pressure history at the bottom transducer location for six different air-only experiments with radially- and axially-confined shocks (pulser input energy of 2.4 kJ)

speed for"air-only" experiments can be estimated using the system geometry (distance, L, between the exploding wire mid-point and the transducer location), along with the initial shock travel time (time, t, between pulser trigger and arrival of first peak at the transducer location). The air within the enclosure can be treated as an ideal gas; hence, the corresponding Mach number, M, can be calculated using the relation:

$$M = f(t) = \frac{\frac{L}{t}}{\sqrt{\gamma \cdot R_{air} \cdot T_{room}}} \tag{4.50}$$

where γ is the specific heat ratio ($\gamma = 1.4$), R_{air} is the gas constant for air, and T is the gas temperature (assumed to be equal to the ambient temperature, $T_{room} = 295$ K $= 22^{o}$C). The uncertainty in the computed value of the Mach number is estimated using a Taylor expansion:

$$\Delta f = f(t + \Delta t) - f(t) \approx f'(t) \cdot \Delta t \tag{4.51}$$

$$\Delta f = -\frac{L}{t^2} \cdot \frac{\triangle t}{\sqrt{\gamma \cdot R_{air} \cdot T_{room}}} \tag{4.52}$$

Figure 4.30 shows the calculated Mach number values for twelve "air-only" experiments (including the six shown in Figure 4.29); the experiments correspond to the radial-and-axial confinement geometry with pulser input energy of 2.4 kJ. The data show that the shock wave produced by the exploding wire propagates at an initial Mach number of nearly 4.0. Differences in the estimated Mach number values (+/- 5%) are within the computed uncertainties, thereby showing a high degree of repeatability between experiments. Hence, the data presented in the following figures correspond to single experiments.

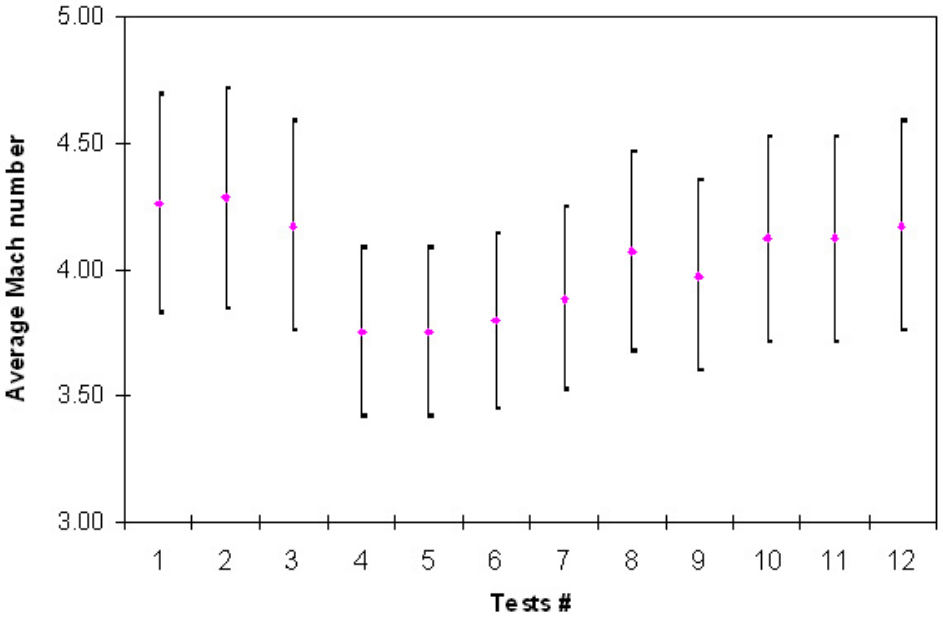

Figure 4.30: Estimated Mach number values for 12 different "air-only" experiments with radially- and axially-confined shocks (pulser input energy of 2.4 kJ)

The "air-only" experiments provide a simple set of test conditions (ideal gas within a well-defined geometry and sensor locations) against which predictions of shock attenuation models can be compared without concern about the model's ability to correctly account for two-phase effects. These results provide the basis for estimating the initial conditions (i.e., the initial shock speed for a given pulser energy input) necessary for modeling shock propagation when a single or two-phase jet is present

within the enclosure.

4.3.2 Effects of Void Fraction and Pulser Input Energy on Shock Attenuation

Figure 4.31 shows typical data for the transient pressure histories obtained for experiments on shock attenuation through either a single-phase (liquid water) jet or a two-phase (water-air) jet with a void fraction of 1% or 10%. For all three cases, the superficial liquid velocity of the jets is 2 m/s. The experiments are conducted using the unconfined boundary condition with pulser input energy of 2.4 kJ. This data shows that two-phase jets attenuate the pressure pulse by a greater extent than a single-phase jet with the same geometry and superficial velocity, as evidenced by the lower magnitude of the pressure pulse. The data also suggest that beyond a relatively moderate value of the void fraction ($\sim$ 1%), further increase in the jet void fraction does not result in a commensurate attenuation of the pressure pulse. The shift in the arrival time of the pressure peak to the transducer location indicates significant slowing down of the shock within the two-phase medium versus the corresponding case of a single-phase (liquid) jet. Figure 4.32 shows the effect of pulser input energy on the resulting pressure history. The data pertain to a two-phase (water-air) annular jet with a superficial liquid velocity of 2.0 m/s and a void fraction of 10%. The experiments are conducted using the unconfined boundary condition with pulser input energy of 2.4, 2.7, and 3.0 kJ. As expected, an increase in the pulser input energy produces a stronger initial shock, which increases the pressure pulse amplitude before and after its attenuation by the jet. The shift in arrival time of the peak to the transducer location reflects the increase in initial shock speed as the pulser input energy is increased.

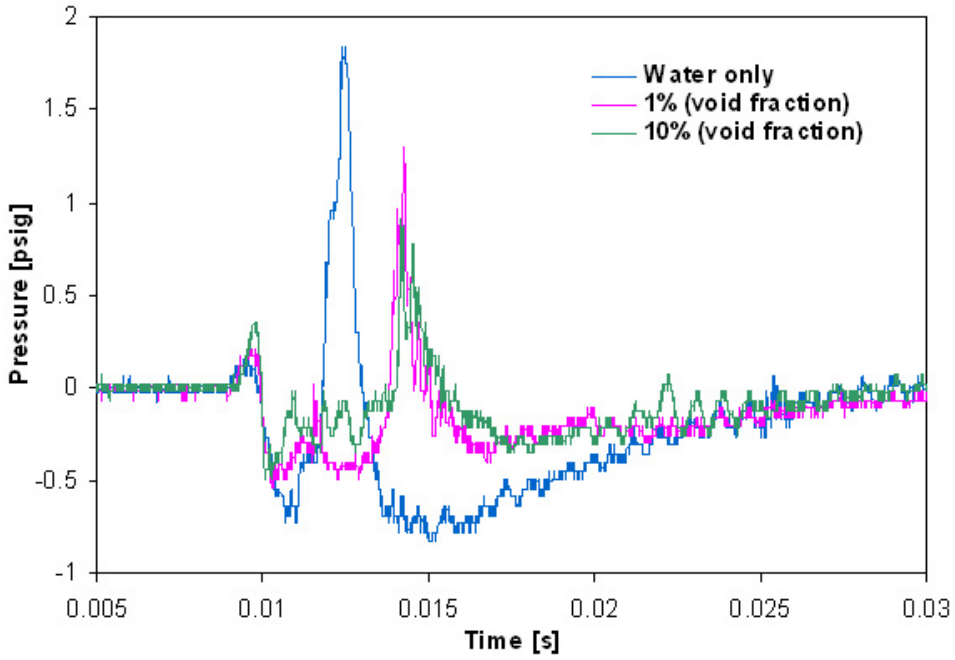

Figure 4.31: Transient pressure histories for unconfined shocks attenuated by either a single-phase (water) jet or a two-phase (water-air) jet (initial liquid superficial velocity = 2 m/s, $Re_l = 2.45 \times 10^4$)

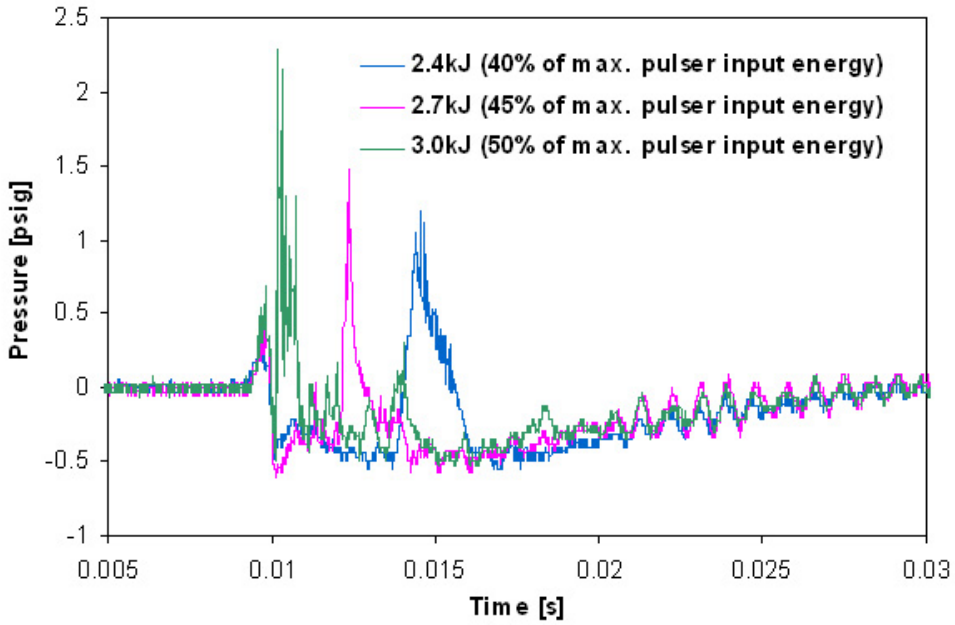

Figure 4.32: Effect of pulser input energy on the pressure history for unconfined shocks attenuated by a two-phase jet (initial liquid superficial velocity = 2 m/s, Re_l = 2.45 × 10^4, and initial void fraction = 10%)

4.3.3 Scale Effects

In order to quantify scale effects (i.e., the ratio between jet thickness/length scale and gas bubble diameter) on jet behavior and shock attenuation, the larger flow loop with the larger annular nozzle and flow conditioner is used. Annular jets with an outside diameter of 15.2 cm and an inside diameter of 12.7 cm are produced. Experiments are conducted for different pulser input energies, jet velocities and void fractions. In this case, only one boundary condition is considered (radially- and axially-confined shocks). The test conditions are selected to match the jet Reynolds numbers of the small-scale experiment; at nozzle exit velocities of 1, 2, and 4 m/s, the corresponding Reynolds numbers for the smaller nozzle are 1.23×10^4, 2.45×10^4, and 4.90×10^4, respectively. The same Reynolds numbers can be obtained when the larger nozzle is operated at water velocities of 0.47, 0.93, and 1.86 m/s. Experiments are conducted for an intermediate liquid flow rate corresponding to superficial liquid velocity of 0.93 m/s, with different void fractions between 0% and 10%. A total of 132 experiments at 15 different test conditions have been performed; Table 4.6 provides a detailed list of the test conditions. For each combination of test conditions, the experiment is repeated 10 times. Figures 4.33 and 4.34 show the pressure histories obtained using the large-scale and the small-scale test facilities at different void fractions. All experiments are conducted at the same Reynolds number for the water phase (Re_l $= 2.45 \times 10^4$). For both the small-scale and large-scale experiments, the extent of shock attenuation clearly increases with void fraction. However, the shapes of the pressure histories are different, because of differences in confinement size (i.e., transit time) and/or pulser energy input (i.e., initial shock strength). The tests on the large-scale experiment are performed using 3.0 kJ pulser energy input (Figure 4.33), while the tests performed on the small-scale experiment are conducted using 2.4 kJ pulser energy input (Figure 4.34).

Table 4.6: Detailed list of test conditions for large-scale annular jet experiments

Test #	Shock Strength (kJ)	$j_{l,e}$ (m/s)	Re_l	α_e (%)	# of experiments for given conditions
1	2.4	Air Only	0	-	10
2	2.4	0.93	2.45×10^4	0.00	10
3	2.4	0.93	2.45×10^4	1.00	10
4	2.4	0.93	2.45×10^4	5.00	2
5	2.4	0.93	2.45×10^4	10.00	0
6	3.0	Air Only	0	-	10
7	3.0	0.93	2.45×10^4	0.00	10
8	3.0	0.93	2.45×10^4	1.00	10
9	3.0	0.93	2.45×10^4	5.00	10
10	3.0	0.93	2.45×10^4	10.00	10
11	3.6	Air Only	0	-	10
12	3.6	0.93	2.45×10^4	0.00	10
13	3.6	0.93	2.45×10^4	1.00	10
14	3.6	0.93	2.45×10^4	5.00	10
15	3.6	0.93	2.45×10^4	10.00	10

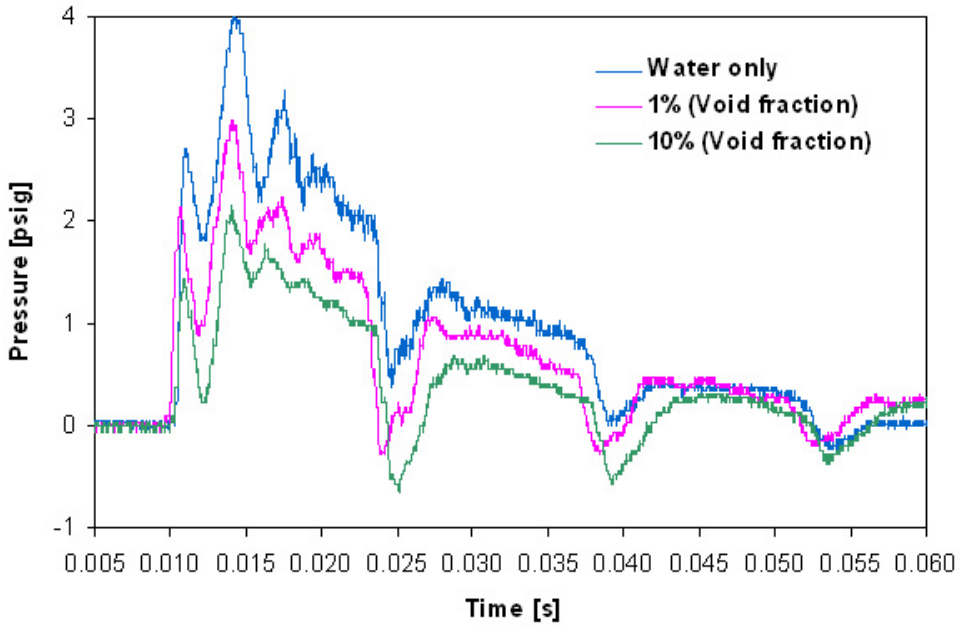

Figure 4.33: Transient pressure histories for shocks attenuated by either a single phase water jet or a two-phase jet (initial liquid superficial velocity = 0.94 m/s, Re_l = 2.45×10^4) on large-scale experiment

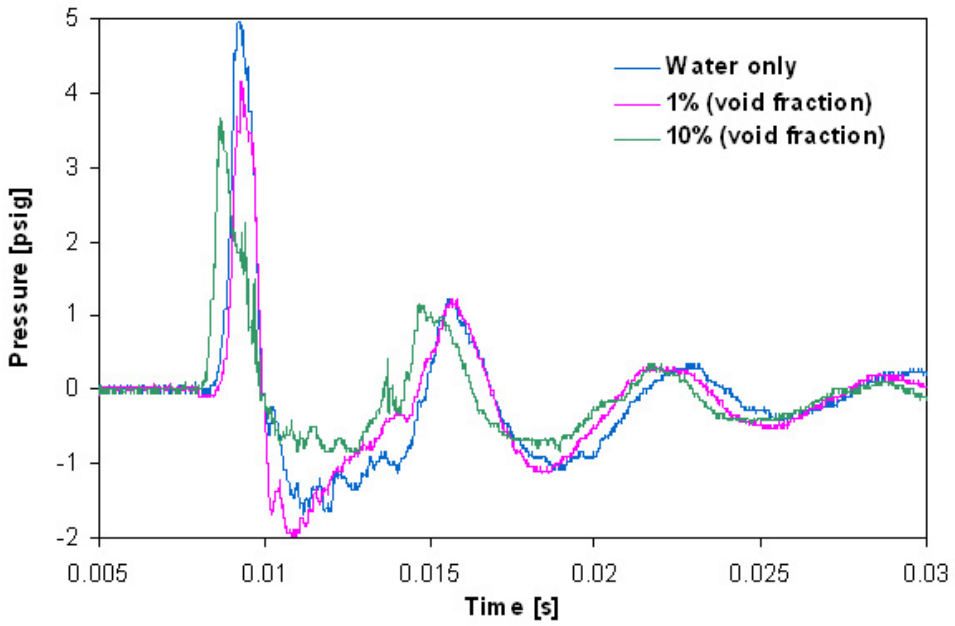

Figure 4.34: Transient pressure histories for shocks attenuated by either a single-phase water jet or a two-phase jet (initial liquid superficial velocity = 2 m/s, $Re_l = 2.45 \times 10^4$) on small-scale experiment

A complete listing of the pressure history data for all shock attenuation experiments is given in Appendix E. These data can be used to validate future models for shock attenuation in two-phase jets.

CHAPTER V

NUMERICAL MODELING

In this chapter, the behavior and geometry of single- and two-phase free jets are simulated using the $FLUENT^{®}$ CFD code. Section 5.1 deals with the description of the mesh and the model options used for single-phase jets, while Section 5.2 contains the two-phase modeling options and results.

5.1 Single-Phase Jet Modeling

5.1.1 Problem Description and Meshing

The characteristics, geometry, and behavior of a free, planar, vertical, single-phase jet flowing downward are simulated using the commercial Computational Fluid Dynamics (CFD) software $FLUENT^{®}$ Release 6.2.16. The initial cross section of the jet (at the nozzle exit) is 1.0 cm $\times$ 10.0 cm. Among commercial CFD software products, $FLUENT^{®}$ has the largest array of industrially tested capabilities - some $1,000$ physical models. These models are robust, with associated features to accelerate convergence. The models allow simulations involving incompressible or compressible flow and heat transfer, species transport, chemical mixing and reaction (combustion), rotating reference frames, radiation and conjugate heat transfer, dispersed phase trajectories, multiphase flows, aeroacoustics, dynamic meshing, and turbulence models. $GAMBIT^{®}$ Release 2.2.30, $FLUENT^{®}$'s companion preprocessor, is used to create the computational grids ($FLUENT^{®}$, 2004).

Prior to modeling the flow within and through the planar nozzle, $FLUENT^{®}$ must be given a mesh which defines the numerical domain that includes the nozzle and the free jet of interest. For the following simulations, the mesh is created in 3D within $GAMBIT^{®}$. The geometry of the nozzle is imported as an IGES file created using

I-DEAS 8.0 CAD software. Since the geometry is symmetric about the y- and z-axes, only a quarter of the nozzle is included in the computation domain. A rectangular domain is attached to the bottom of the nozzle and meshed; its dimensions are 16 cm (x) × 1 cm (y) × 5.5 cm (z). This domain will contain the predicted free jet. A simple hexahedral mesh consisting of 656,000 elements is created. The grid increments used for this mesh are $\Delta x = 1$ mm, $\Delta y = 0.25$ mm, and $\Delta z = 0.5$ mm in the x-, y-, and z-directions, respectively. Figure 5.1 show the four meshed quadrants of the nozzle with their attached rectangular domains. The type of boundary condition for each face is then specified (see Figure 5.1 for the name of each face). The mesh volume is specified as being liquid. Other meshes and grid increments have been tested (e.g., $\Delta x = 2$ mm, or $\Delta z = 0.25$ mm).

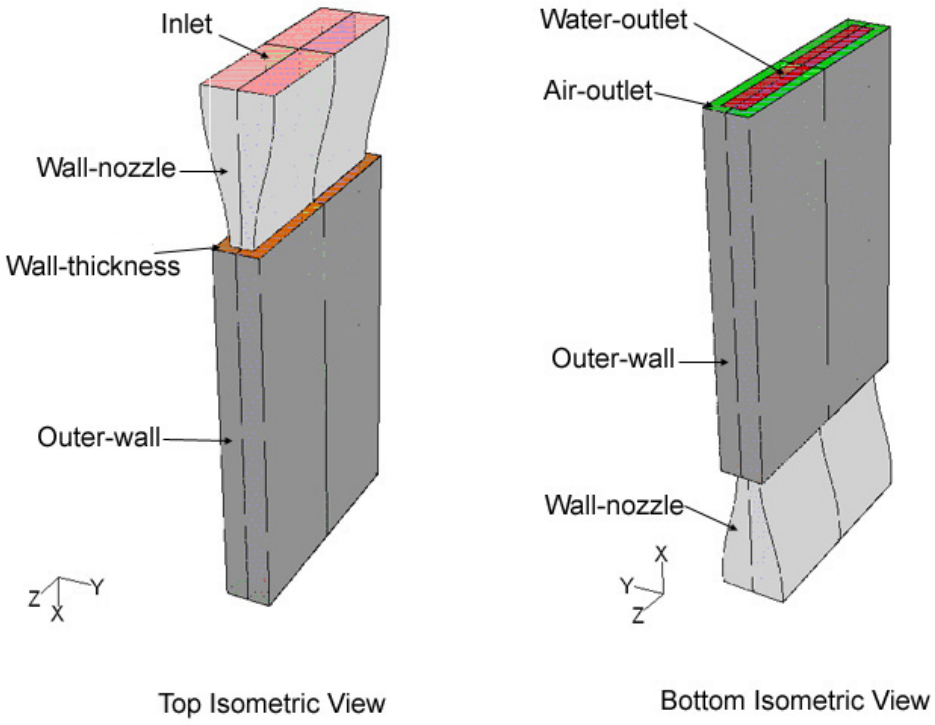

Figure 5.1: Top and bottom isometric views of the numerical domain, plotted with its symmetric about the y- and z-axes.

5.1.2 Conclusions on Single-Phase Jet Modeling

The model selection and parametric analysis presented in Appendix G allowed the optimization of single-phase jet modeling (see Sections G.1.1 and G.1.2). The optimum chosen parameters are the *VOF-Implicit* formulation, the *realizable* k-ϵ turbulence model, the *second-order* discretization scheme for the volume fraction equation, and *PISO* as the pressure-velocity coupling scheme. The mesh is built with the mesh size $\Delta x = 1$ mm, $\Delta y = 0.25$ mm, and $\Delta z = 0.5$ mm for the x-, y-, and z-directions, respectively. The detailed list of the boundary conditions and their different parameters is given in Table 5.1. The backflow volume fraction of air across the "Water-Outlet" is set to 0. The time step is $\Delta t = 0.8$ ms.

Table 5.1: Detailed list of the boundary conditions and their parameters

Name	Mixture	Water	Air
Inlet	***Velocity-Inlet*** - Velocity specification method: magnitude, normal to the boundary - Velocity magnitude: 1 m/s - Turbulence specification method: intensity and hydraulic diameter - Turbulence Intensity: 4.18% - Hydraulic diameter: 4.62 cm		Volume fraction: 0

continued on next page

continued from previous page

Name	Mixture	Water	Air
Air-Outlet	***Pressure-Outlet*** - Gauge pressure: 0 Pa - Backflow direction specification method: normal to the boundary - Turbulence specification method: intensity and hydraulic diameter - Turbulence intensity: 5.00% - Hydraulic diameter: 1.10 cm		Backflow volume: 1
Water-Outlet	***Pressure-Outlet*** - Gauge Pressure: 0 Pa - Backflow direction specification method: normal to the boundary - Turbulence specification method: intensity and hydraulic diameter - Turbulence intensity: 4.82% - Hydraulic diameter: 1.48 cm		Backflow volume: 0
Wall-Nozzle	***Wall*** - Shear condition: no slip		
Wall-Thickness	***Wall*** - Shear condition: no slip		
Outer-Wall	***Wall*** - Shear condition: specified stress (0,0,0)		

The jet thicknesses in the y-direction and the jet widths in the z-direction are simulated by the code for different liquid superficial velocities at the nozzle exit ($j_{l,e}$ = 1, 2, 3, and 4 m/s) and nozzle geometries (δ_e = 1 cm $\times$ w_e = 10 cm planar nozzle and ϕ_e = 3.57 cm diameter circular nozzle). Variations of the experimental and predicted values of jet thickness and width for the rectangular jet are shown in Figures 5.2 and 5.3, while those of jet diameter for the circular jet are shown in Figure 5.4; the predicted curves are plotted in pink while the experimental values are plotted in green. The errors on the experimental values are 0.127 mm and 0.225 mm for the thickness and the width, and correspond to the errors due to the depth micrometer and the pixel size, respectively.

Figures 5.2 and 5.3 show the evolution along the x-axis of the planar jet thickness and width, respectively. The pink-plotted predicted curves in Figures 5.2 and 5.3 are the water isosurfaces $\alpha_{water} = 0.6$ and $\alpha_{water} = 0.8$, respectively. Referring to Figure 5.2, experimental and predicted values show excellent agreement for 2 m/s $\leq j_{l,e} \leq$ 4 m/s and 4 cm $\leq x \leq$ 13 cm; differences are within the errors bars. The predicted values deviate from the experimental data for 14 cm $\leq x \leq$ 16 cm. For the case $j_{l,e}$ = 1 m/s, deviations between experimental and predicted values are primarily due to the partial convergence of the code in this case; improvement can be made on the code by reducing the time step, turning the *geometric reconstruction* scheme back on after calculating a solution with the implicit scheme, or running the case without any turbulence model for example.

Figure 5.3 shows excellent agreement between experimental and predicted values for 2 m/s $\leq j_{l,e} \leq$ 4 m/s and 4 cm $\leq x \leq$ 13 cm; differences are within the errors bars. For the case $j_{l,e} = 1$ m/s, deviations between experimental and predicted values are similar to those noted in Figure 5.2.

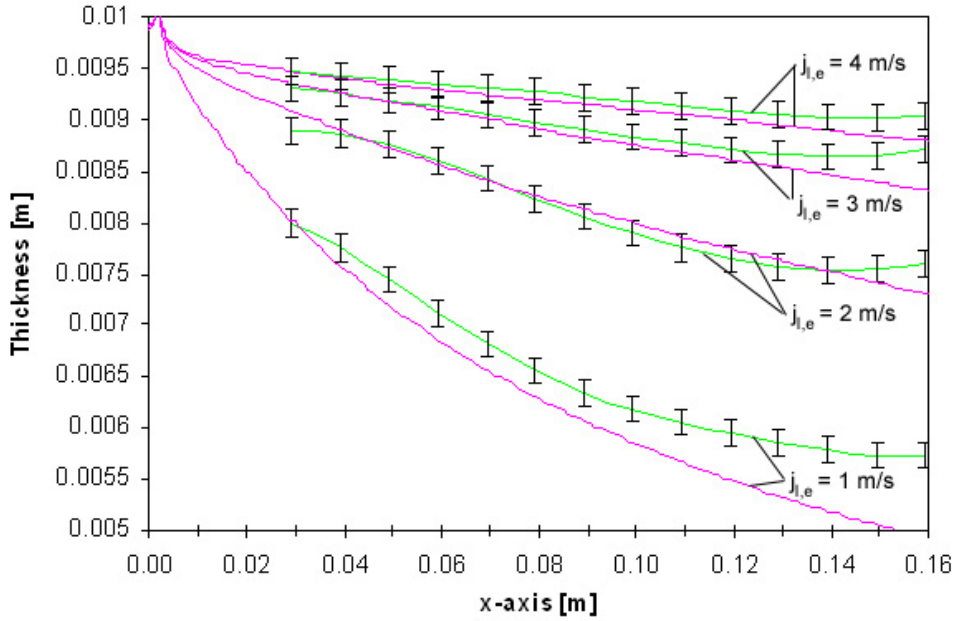

Figure 5.2: Comparison of the jet thicknesses (y-direction) along the x-axis, between experimental (green) and predicted values (pink) for 1 m/s $\leq j_{l,e} \leq$ 4 m/s, 1.89 $\times$ $10^4 \leq Re_l \leq 7.57 \times 10^4$

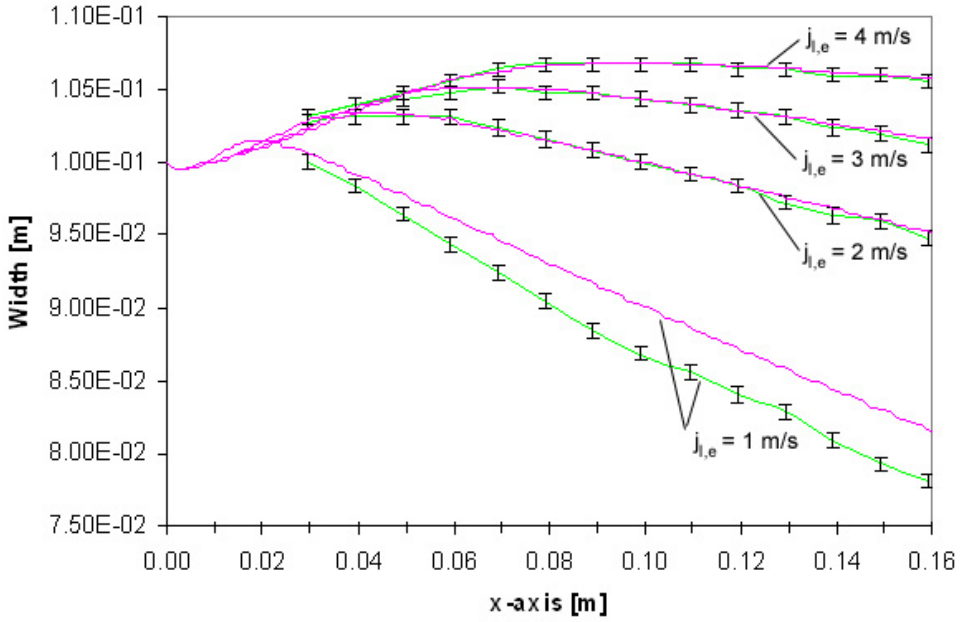

Figure 5.3: Comparison of the jet widths (z-direction) along the x-axis, along the x-axis, between experimental (green) and predicted values (pink) for 1 m/s $\leq j_{l,e} \leq$ 4 m/s, 1.89 $\times$ $10^4 \leq Re_l \leq 7.57 \times 10^4$

Figure 5.4 shows the evolution along the x-axis of the circular jet diameter. The pink-plotted predicted curve corresponds to the water isosurface $\alpha_{water} = 0.9$. Experimental and predicted values show excellent agreement for 3 m/s $\leq j_{l,e} \leq$ 4 m/s and 3 cm $\leq x \leq$ 14 cm; differences are within the errors bars. For the case $j_{l,e} = 1$ m/s, deviations between experimental and predicted values are again primarily due to the partial convergence of the code in this case. For the case $j_{l,e} = 2$ m/s, the disagreement noticed on this graph is probably related to the experimentally-observed "transient" behavior of the jet; at this velocity, the jet is very unstable with strong oscillatory waves on the free surface.

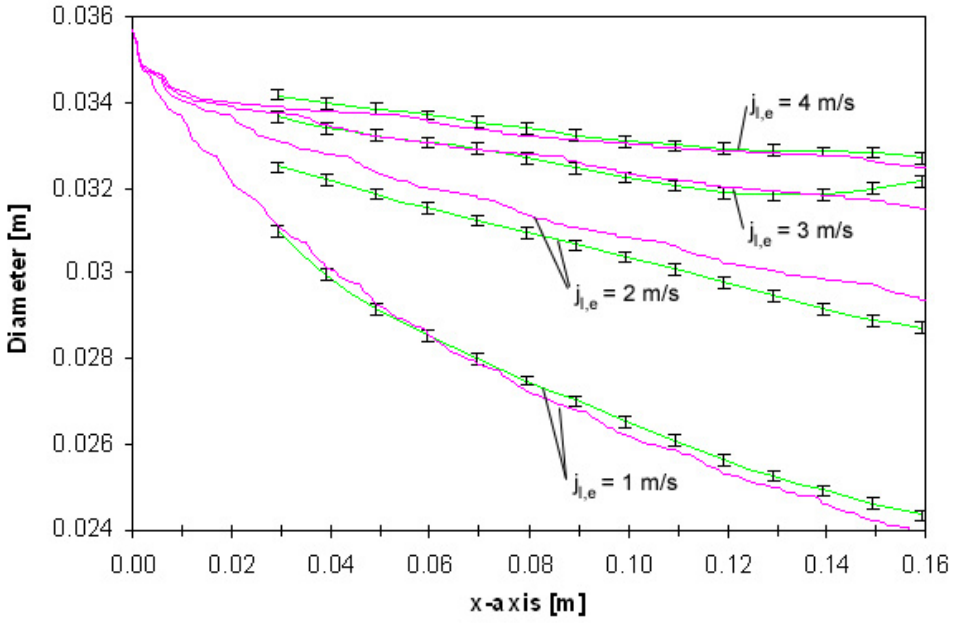

Figure 5.4: Comparison of the jet diameters along the x-axis, between experimental (green) and predicted values (pink) for 1 m/s $\leq j_{l,e} \leq$ 4 m/s, $3.71 \times 10^4 \leq Re_l \leq 1.47 \times 10^5$

5.2 Two-Phase Jet Modeling

5.2.1 Two-Phase Modeling in *FLUENT*®

FLUENT® has also been used to predict the characteristics and the behavior of a two-phase (gas-liquid) vertical jet. The main difficulty here is to select an appropriate

multiphase model to simulate this complex problem since two flow types are involved: (a) free surface flow; and (b) two-phase bubbly flow with discrete gaseous bubbles in a continuous liquid. The selected two-phase jet models are presented and detailed in Appendix G (see Section G.2).

5.2.2 Parametric Analysis and Conclusions on Two-Phase Jet Modeling

Again, in order to assess the $FLUENT$® model's ability to predict the contours of a two-phase jet, a baseline case is created; it simulates a planar jet with a liquid superficial velocity at the nozzle exit $j_{l,e} = 3$ m/s and an exit homogeneous void fraction $\alpha_e = 5\%$. The chosen parameters are the *VOF-Implicit* formulation, the *realizable k-ϵ* turbulence model, the *second-order* discretization scheme for the volume fraction equation, *PISO* as the pressure-velocity coupling scheme, and the *discrete phase* model to simulate the air bubbles. The mesh is built with the mesh size $\Delta x =$ 1 mm, $\Delta y = 0.25$ mm, and $\Delta z = 0.5$ mm for the x-, y-, and z-directions, respectively. The backflow volume fraction of air across the "Water-Outlet" is set to 0. The time step is $\Delta t = 1$ ms. The code is run first for a single phase jet (*VOF* model) until it fully converges. The injections of discrete particles are then created and the *discrete phase* model is turned on.

The *droplet collisions* model leads to large roundoff errors for particle diameters above 0.5 mm. The collision model assumes that the frequency of collisions is much less than the particle time step. If the particle time step is too large, then the results may be time-step-dependent ($FLUENT$®, 2004). Additionally, the model is most applicable for low-Weber-number collisions where collisions result in bouncing and coalescence. According to $FLUENT$®'s documentation ($FLUENT$®, 2004), above a Weber number of about 100, the outcome of collision could be shattering. With a particle diameter equal to or less than 0.5 mm, the code can run without leading to errors. Therefore, the diameter of particles used for each injection is assumed to be

0.5 mm; in reality, this diameter is the order of one millimeter.

The effect of the *interaction with continuous phase* option is also investigated. This option makes the code and, more precisely, the turbulence dissipation rate ϵ diverge. It quickly leads to an extremely unstable jet, which explains the general divergence of the code. Reducing the under-relaxation factor for particles/droplets to improve the stability of coupled calculations does not help and leads to errors.

Finally, the code is run without the option of *interaction with continuous phase*. Therefore, the contours of the water phase calculated with the *VOF* model are not affected by the injection of particles. Figure 5.5 shows the planar nozzle outline, the contours of the water phase determined in Section 5.1.2, the particle diameters with coalescence and breakup processes enabled, and their locations after 100 ms. Particles are injected with a diameter equal to 0.5 mm; few of them coalesce to reach 0.9 mm or break up into much smaller bubbles, but most of them stay in the range 0.3-0.6 mm. This confirms the fact that the particle diameters at the nozzle inlet must be the order of 1-3 mm (i.e., the order of the values found experimentally). The nozzle contraction along the y-dimension gives rise to very small particles which tend to disappear within the free jet along the x-axis, while large particles are created within the nozzle. Figure 5.5 also shows the water volume fraction associated with each particle. Red particles are inside the jet and the blue ones represent those that have escaped or collapsed on the free surface.

Figure 5.6 compares the velocity magnitude of the water phase and those of the particles; the ratio of the air and water velocities is the slip ratio. At a given location, the particle velocity equals or is slightly higher than the water velocity. The corresponding slip ratio is equal to or more than 1. Therefore, based on these calculations, it is concluded that the code cannot correctly model the variation of the slip ratio within the free jet along the x-axis.

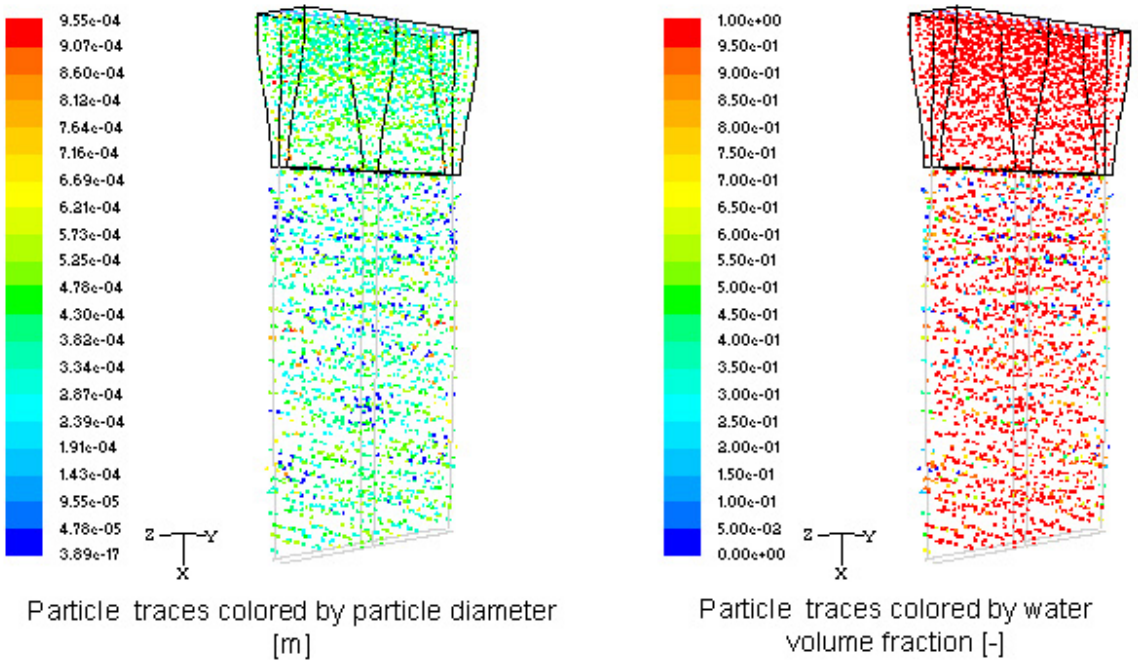

Figure 5.5: Particle distribution within the numerical domain for a planar jet with a liquid superficial velocity at the nozzle exit $j_{l,e} = 3$ m/s ($Re_l = 5.68 \times 10^4$) and an exit homogeneous void fraction $\alpha_e = 5\%$. Particles are colored by their diameter on the left and by the water volume fraction on the right

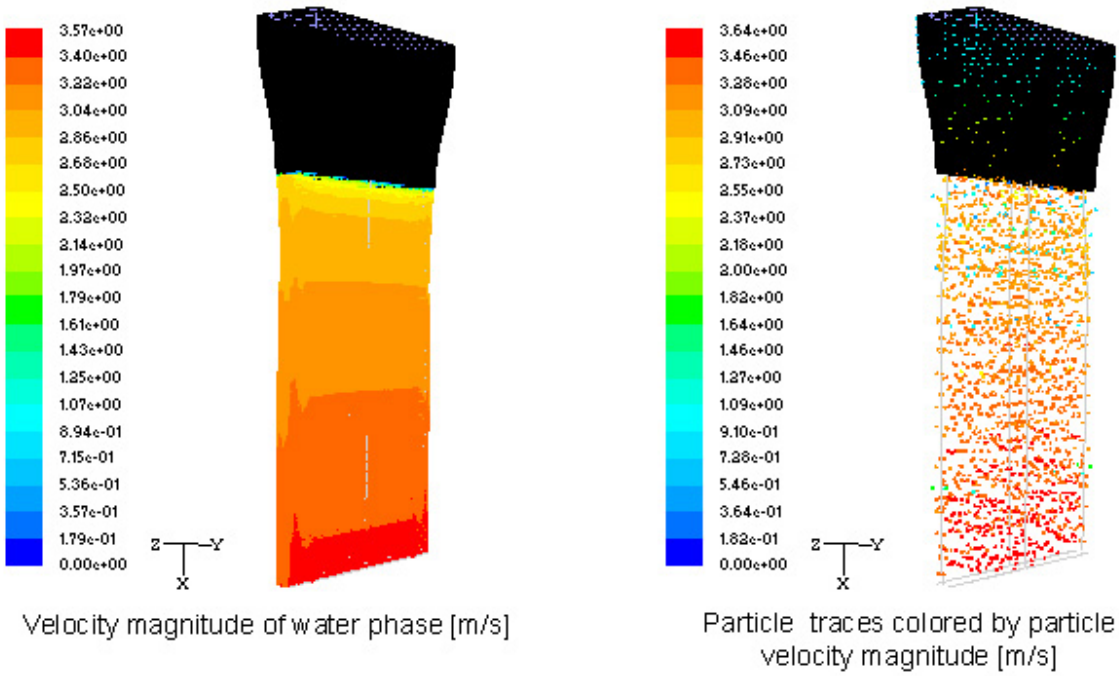

Figure 5.6: Comparison between the velocity magnitude of the water phase (left) and those of the particles

CHAPTER VI

CONCLUSIONS AND RECOMMENDATIONS

The purpose of this investigation was to examine the possibility of using compressible liquid/gas jets as a means of protecting the Z-Pinch IFE reactor cavity walls from the target photons, ions, and neutrons, thereby limiting and mitigating the mechanical consequences of rapid energy deposition within the jets in a high-yield, low repetition rate, Z-Pinch IFE reactor system. Two different scale experimental test facilities were constructed with the general goal of producing steady, two-phase, (liquid/gas) jets with controllable velocities and gas void fractions. The jets were formed by allowing a homogeneous mixture of liquid and gas with the appropriate volumetric flow rates and flow regime (either single-phase liquid or bubbly two-phase flow) to flow through a flow conditioner and converging nozzle before being discharged into the ambient air. The open-loop test facility was instrumented to allow the liquid superficial velocity at the nozzle exit and the homogeneous equilibrium (one-dimensional) gas void fraction within the jet to be measured and controlled. Different jet cross sections, viz. rectangular, circular, and annular, were produced.

Planar, circular, and annular jets were examined over wide ranges of liquid velocities and void fractions. Experiments were conducted to examine the effect of void fraction and nozzle design on the stability and behavior of a two-phase jet discharging into an open cavity. Additionally for planar jets, bubble size distributions were studied within the discharging jet. For rectangular and circular jets, the actual void fraction and slip ratio distributions were measured. For annular jets, an exploding wire placed along the axis was used to produce a shock wave. Attenuation of the shock by the surrounding annular jet was measured by recording the pressure history

at the enclosure wall as the shock wave propagated through the attenuating jet. Experiments were conducted using two different-size jets and three different enclosures at various liquid velocities, void fractions, and initial shock strength.

In addition, a state-of-art, two-phase, CFD code, such as $FLUENT^{®}$, was used to model the experimental jets. The experimental data were compared against predictions of the numerical two-fluid model.

6.1 Conclusions

6.1.1 Interfacial Structures

- Flow Visualizations:

The data obtained in this investigation show that stable, coherent, vertical two-phase jets with a wide range of initial superficial liquid velocities ($j_{l,e} \leq 4.92$ m/s) and average homogeneous void fraction ($\alpha_e \leq 25\%$) can be formed with standard nozzle and flow conditioner designs. The choice of optimum operating conditions (jet velocity and average void fraction) for the Z-Pinch reactor represents a trade-off between mechanical response and vacuum pumping requirements.

The vertical liquid/gas jets change geometry downstream of the imposed nozzle exit conditions. The jet width (diameter) decreases slightly along the flow direction due to surface tension forces and gravitational acceleration of the flow. The surface of the jets is nearly smooth with protrusions along the edges growing linearly along the x-axis. At low jet velocities and void fractions, the jets appear "glassy" with little surface disturbance. At low liquid flow rates, two-phase flow can be intermittent in theory; nevertheless, the design of the calming section and the nozzle allows homogeneous flow to be formed. "Small" bubbles are distributed over the entire jet width/diameter, while the "larger" bubbles tend to be concentrated in the center region. However, careful observation of the bubble redistribution within the jets suggests that off-centered peaks are likely to exists. Turbulence, void concentration, and

lateral lift force allow bubble diffusion in the transverse direction. The bubble concentration in the jet center enhances the bubble coalescence resulting in the formation of "larger" bubbles. "Small" bubbles tend to migrate toward the free surface, in an attempt to avoid the fast moving liquid in the central part of the jet.

At higher void fractions and velocities, the jet surface becomes more rippled because of increased turbulence and, more importantly, because of gas bubbles randomly crossing the jet surface. However, the majority of the gas bubbles remain "contained" within the jet in the near-field, so that the two-phase jet can adequately attenuate the shock wave produced by rapid energy deposition of the target debris and x-rays. "Smaller" gas bubbles (dictated by the Taylor length scale) are produced; homogeneous flow is formed within the calming section and the nozzle. Additionally, the coalescence and disintegration mechanisms due to turbulence become more important, leading to smaller and more homogeneous bubbles.

- Bubble Size Measurement:

The planar jet provides an effective setup for flow visualization and measurement of bubble size distribution; the motion of the bubbles is nearly two dimensional due to the large aspect ratio; image distortion due to curvature is eliminated. As the initial void fraction increases for a given jet velocity, the overall bubble diameters also increase, remaining below the limit identified by Ishii (Ishii and Zuber, 1979).

At low jet velocity, due to the relatively low turbulence, bubble breakup is negligible. The coalescence process leading to "larger bubbles" becomes dominant, due to bubble-bubble collision induced by liquid turbulence, and the higher rate of bubble-bubble collision at elevated void fractions.

At higher jet velocities, the breakup mechanism due to bubble-turbulent eddy collision becomes significant. As the void fraction increases, the coalescence process is still present within the jet, leading to "larger bubbles" with larger void fractions, but the breakup mechanism due to the turbulent eddies within the liquid phase prevent

the bubbles from growing as much as they do at low jet velocities. Therefore, the bubble size distributions become considerably narrower as the jet velocity increases. At high jet velocities and relatively low void fractions, the bubble size distribution is nearly normal.

- Correlations of the Sauter Diameter:

The average bubble size decreases with increasing liquid superficial velocity. As the gas flow rate increases, the Sauter mean bubble diameter increases since the probability of coalescence increases with increasing void fraction.

A correlation has been proposed to predict the Sauter mean bubble diameter; the dimensionless Sauter mean bubble diameter (i.e, the Sauter diameter divided by the Laplace length scale) is expressed as a function of the Reynolds, the Weber, and the Froude numbers in order to take into account the turbulence effects, the bubble coalescence and breakup efficiencies, and the buoyancy effects, respectively. The correlation is valid for bubbly flow within planar jets for the following parameter ranges: 1.26 m/s $\leq j_{l,e} \leq$ 4.92 m/s and 1% $\leq \alpha_e \leq$ 25%.

6.1.2 Void Fractions and Slip Ratio Distribution Measurements

The local jet void fraction and thickness were measured along the jet centerline at 14 different x-locations away from the nozzle exit. A gamma-ray densitometer was used to determine the collapsed jet thickness. The collapsed liquid thickness and the actual jet thickness of the jet were measured and used to determine the average void fraction along the centerline of the jet. The resulting void fractions were used to estimate the local slip ratios. A total of 420 experiments were conducted.

- Void Fraction:

The measured void fraction at the nearest position to the nozzle exit (x = 2.9 cm) is nearly equal to the average homogeneous void fraction at the nozzle exit. The void

fraction along the free jet centerline increases as the jet flows downward away from the nozzle. The migration of bubbles to low velocity regions and the buoyancy effects slow them down. Since the gas velocity decreases and the liquid velocity increases along the flow direction, the volume of the gas increases compared to the volume of the liquid and the slip ratio decreases. As the slip ratio decreases along the flow direction, the void fraction increases. The increase in void fraction with the distance x from the nozzle is greater for low initial superficial liquid velocity ($j_{l,e} \sim 2$ m/s) and void fraction ($\alpha_e \sim 1\%$) compared to jets with relatively high initial superficial liquid velocity ($j_{l,e} \sim 4$ m/s) and void fractions ($\alpha_e \sim 5\%$).

- Slip Ratio:

The slip ratio is defined as the ratio of gas and liquid phase velocities and can be expressed as a function of the homogeneous void fraction. Since the void fraction increases with the distance x from the nozzle, the slip ratio decreases; the liquid accelerates downward, while the gas decelerates due to buoyancy. The geometry of the jet does not seem to affect the distribution trend. At low void fraction ($\alpha_e \sim 1\%$), the slip ratio can decrease to values as low as 0.3 - 0.4, 15 cm from the nozzle exit.

At low void fractions ($\alpha_e \sim 1\%$), the slip ratio at the end of the test region (15.9 centimeters downstream of the nozzle exit) increases as the superficial liquid velocity decreases. This is caused by the increased downward drag on the gas at higher liquid velocity versus the upward buoyancy force which is unaffected by the liquid velocity. Buoyancy effects dominate at low initial superficial liquid velocity ($j_{l,e} = 1$ m/s). At relatively high void fractions ($\alpha_e \sim 5\%$), the differences in slip ratio are weakly dependent on the initial superficial liquid velocity.

- Comparison with Empirical Correlations:

The Dix correlation (Dix, 1971) was used to predict the void fraction at x = 2.9 cm and the average bubble diameter. Since the void fraction increases with the

distance x from the nozzle, the Dix correlation can provide a reasonable estimate for the minimum void fraction within the jet. Poor agreement was obtained between the experimental data and the results obtained from Kern's correlation (Kern, 2007). The Kern correlation was modified in order to make it applicable to both planar and circular bubbly jets, and to expand the parameter ranges to include 1 m/s $\leq j_{l,e} \leq$ 4.0 m/s and 1% $\leq \alpha_e \leq$ 15%. A new parameter representing the ratio between the superficial gas velocity and the bubble rise velocity has been included. The correlation matches the main trends observed in the experiments.

6.1.3 Shock Attenuation with Two-Phase Annular Jets

- Repeatability between Experiments:

Experiments were conducted to quantify the extent by which two-phase jets can attenuate a shock wave. The pressure history at the enclosure wall is recorded as the shock wave propagates through the attenuating two-phase medium. A total of 738 experiments were conducted on the small-scale experimental loop using the 5.18 cm OD and 4.0 cm ID annular jet, at three different liquid superficial velocities, with different homogeneous void fractions at the nozzle exit, using three different boundary conditions. The data show a high degree of repeatability between experiments; differences in the measured peak pressures are less than 6%.

The shock wave produced by the exploding wire propagates radially and axially, and reflects from the enclosure boundaries. The shock wave eventually dissipates as the mechanical energy is converted into thermal energy within the medium (air). The initial shock speed for"air-only" experiments was estimated: the data showed that shock wave produced by the exploding wire propagates at an initial Mach number of nearly 4.0.

The "air-only" experiments provide a simple set of test conditions (ideal gas within a well-defined geometry and sensor locations) against which predictions of shock attenuation models can be compared without concern about the model's ability to correctly account for two-phase effects. These results provide the basis for estimating the initial conditions (i.e., the initial shock speed for a given pulser energy input) necessary for modeling shock propagation when a single or two-phase jet is present within the enclosure.

- Effects of Void Fraction and Pulser Input Energy on Shock Attenuation:

The data show that two-phase jets attenuate the pressure pulse by a greater extent than a single-phase jet with the same geometry and superficial velocity, as evidenced by the lower magnitude of the pressure pulse. They also suggest that beyond a relatively moderate value of the void fraction ($\sim 1\%$), further increase in the jet void fraction does not result in a commensurate attenuation of the pressure pulse.

As expected, an increase in the pulser input energy produces a stronger initial shock, which increases the pressure pulse amplitude before and after its attenuation by the jet.

- Scale Effects:

In order to quantify scale effects on jet behavior and shock attenuation, a larger flow loop with the larger annular nozzle and flow conditioner was used. A total of 132 experiments were conducted for different pulser input energies, jet velocities and void fractions. The test conditions were selected to match the jet Reynolds numbers of the small-scale experiment.

For both the small-scale and large-scale experiments, the extent of shock attenuation clearly increases with void fraction. However, the shapes of the pressure histories are different, because of differences in confinement size (i.e., transit time) and/or pulser energy input (i.e., initial shock strength).

6.1.4 Numerical Modeling

- Single-Phase Jet Modeling:

The behavior and characteristics of a vertical planar single-phase jet were simulating using a commercial computational Fluid Dynamics (CFD) software $FLUENT^{®}$ Release 6.2.16.

In order to assess the model's ability to predict the contours of a single-phase jet, different parameters of the code were varied in order to optimize the simulation. Simulated contours of the jet were compared with the experimental results obtained in this investigation. The effects of the mesh size, the time step Δt, the backflow volume fraction of air across the outlet, the turbulence model, and the controls and discretization schemes were examined. Based on the results of parametric analysis, an optimum model has been selected; the optimum model includes the *VOF-Implicit* formulation, the *realizable k-ϵ* turbulence model, the *second-order* discretization scheme for the volume fraction equation, and *PISO* as the pressure-velocity coupling scheme. The mesh was shown to be fine enough for the simulation to be independent from the mesh grid.

The calculated water isosurfaces $\alpha_{water} = 0.6$ and $\alpha_{water} = 0.8$ show excellent agreement with the experimentally measured thickness and width values, respectively. For the circular jet, the experimental diameter values show excellent agreement with the water isosurface $\alpha_{water} = 0.9$. In both cases, differences are within the estimated measurement errors. At low jet velocities, deviations between experimental and predicted values are primarily due to partial convergence of the code; improvement can be made on the code by reducing the time step, activating the *geometric reconstruction* scheme after calculating a solution with the implicit scheme, or running the problem without any turbulence model.

- Two-Phase Jet Modeling:

$FLUENT$® has also been used to predict the behavior and characteristics of a two-phase (gas-liquid) planar vertical jet. For the prediction of a coupled two-phase flow, the code is run first for a single phase jet (*VOF* model) until it fully converges. The injections of discrete particles are then created and the *discrete phase* model is initiated. For each discrete-phase iteration, $FLUENT$® computes the particle/droplet trajectories and updates the interphase exchange of momentum, heat, and mass in each control volume. The model options selected include the *VOF-Implicit* formulation, the *realizable* k-ϵ turbulence model, the *second-order* discretization scheme for the volume fraction equation, *PISO* as the pressure-velocity coupling scheme, and the *discrete phase* model to simulate the air bubbles.

The results show that the *droplet collisions* model leads to large roundoff errors for particle diameters above 0.5 mm, and that collision leads to fragmentation. The effect of including the *interaction with continuous phase* option was also investigated. It quickly leads to an extremely unstable jet, which explains the general divergence of the code.

When the code is run without the *interaction with continuous phase* option, the contours of the water phase calculated with the *VOF* model are not affected by the injection of particles. The bubble diameter range predicted by the code does not match the experimentally measured values. Additionally, the predicted slip ratio is nearly equal to or larger than unity, which is considerably different than the experimental observations. Therefore, it is concluded that the $FLUENT$® code cannot adequately predict the behavior and characteristics of two-phase free jets.

6.2 Contributions

The work presented in this thesis is the first in the open literature to study and understand the stability and behavior of two-phase (gas/liquid) vertical jets with different geometries, as well as to quantify the extent by which these jets can attenuate

shock waves in a Z-Pinch IFE reactor. The main contributions of this doctoral thesis are:

1. Characterization of the parameter ranges over which stable, coherent, two-phase jets can be maintained for IFE applications. The choice of optimum operating conditions (jet velocity and average void fraction) for the Z-Pinch reactor represents a trade-off between mechanical response and vacuum pumping requirements. Coherent stable two-phase jets at homogeneous void fractions up to 25 % can be formed with standard nozzle and flow conditioner designs.

2. Statistical quantification of bubble size within free, vertical, planar, two-phase (gas/liquid) jets as a function of liquid velocity and void fractions. A correlation was proposed to predict the average bubble size within a vertical planar jet.

3. Measurement of void fraction and slip ratio distributions within vertical, planar or circular, two-phase jets. Quantitative data were acquired as a function of downstream distance for a variety of different liquid velocities, void fractions, and nozzle geometries. A correlation was proposed to estimate the minimum void fraction within the jet and to predict the slip ratio distribution as a function of downstream distance.

4. Measurement of the effects of two-phase jet void fraction on shock attenuation. Quantitative data were obtained for the extent by which two-phase (gas/liquid) jets can attenuate shock waves for different liquid velocities, void fractions, shock strength, and annulus dimensions.

5. Establishment of guidelines to model vertical jets in a state-of-the-art CFD code. It is shown that the $FLUENT^{®}$ code cannot adequately model the behavior and characteristics of two-phase free jets.

6.3 Recommendations

This doctoral thesis represents an extensive effort to study the behavior of two-phase (gas/liquid) vertical jets with different geometries, as well as to quantify the extent by which these jets can attenuate shock waves in a Z-Pinch IFE reactor. Based on the experience gained in this study, the following recommendations for future research are made below.

1. A more precise technique to measure the jet thickness would reduce the experimental error in void fraction and slip ratio measurements. This technique should also allow measurement of the jet thickness for an annular two-phase (gas/liquid) jet in order to be able to measure the void fraction and slip ratio distribution within an annular jet.

2. The local jet void fraction was measured along the jet centerline; the measurement locations were dictated by physical limitations of the positioner. Expansion of the measurement zone along the centerline ($x \leq 2.9$ cm and $x \geq 15.9$ cm) and off-centerline ($x \neq 0$) would be useful to confirm that off-centered peaks are likely to exist, as suggested by careful observation of the bubble repartition within the jets.

3. Experiments with radially- and axially-confined shocks should be conducted on the small-scale experiment for an intermediate liquid flow rate corresponding to superficial liquid velocity of 2 m/s, with different void fractions between 0% and 10%, and a 3.0 kJ pulser energy input. Such data would help in interpreting the differences in shape of the observed pressure histories in the two facilities with different size jets.

4. Experiments on the large-scale apparatus should be extended using flows with the Reynolds numbers 1.23×10^4 and 4.90×10^4 in order to completely match the experiments performed on the small-scale apparatus.

5. A parametric study should be performed to investigate the effects of the jet thickness (or aspect ratio) and the shock Mach number in order to allow reactor system designers to optimize the shock attenuation.

6. Measurement of bubble sizes and distributions before and after the flow conditioner would be useful in optimizing the input conditions for particle injection in the $FLUENT^{®}$ model.

7. Improvements of the $FLUENT^{®}$ code and its models named *droplet collisions* and *interaction with continuous phase* (i.e, the interaction between the injected particles and the continuous phase) should be developed to permit reasonable prediction of the structure of two-phase (gas/liquid) jets. This step would be necessary for the practical implementation of a code allowing reactor system designers to quantify the effectiveness of two-phase jets in mitigating the consequences of shock waves in high yield IFE reactor systems.

APPENDIX A

FLOW VISUALIZATION

In this Appendix, photographs of the two-phase circular and annular jets examined in this investigation are presented. Sections A.1, A.2, and A.3 contain pictures for the 3.57 cm diameter circular jet, 5.25 cm diameter circular jet, and 4.0 cm I.D. annular jet, respectively. The 48 corresponding test conditions are documented; values of the liquid superficial velocities $j_{l,e}$ at the nozzle exit, the liquid superficial velocities $j_{l,h}$ within the honeycomb section, the Reynolds numbers Re_l, and the exit homogeneous void fractions α_e are given in Table 4.1 for test numbers 19 through 66.

A.1 Photographs for the 3.57 *cm diameter circular jets*

In this section, photographs of the circular single- and two-phase jets with 3.57 cm initial diameter are presented. Figures A.1, A.2, and A.3 correspond to cases with initial liquid superficial velocities of 1.26, 2.52, and 4.73 m/s, respectively. For each value of the superficial liquid velocity, jets with different values of the initial homogeneous void fraction are shown.

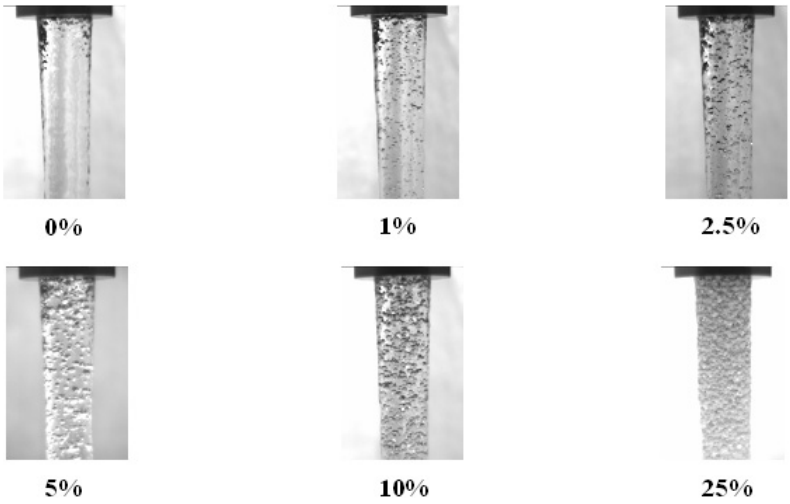

Figure A.1: Near-field behavior of two-phase circular jets with different void fractions (initial diameter = 3.57 cm and initial liquid superficial velocity = 1.26 m/s, $Re_l = 4.68 \times 10^4$)

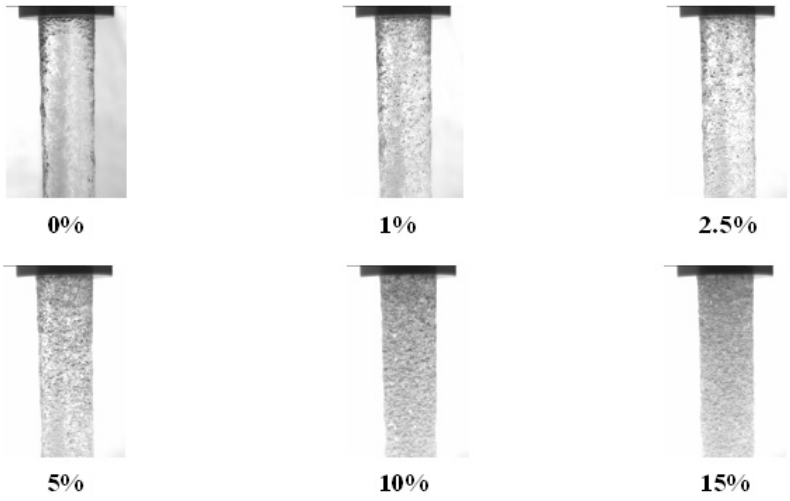

Figure A.2: Near-field behavior of two-phase circular jets with different void fractions (initial diameter = 3.57 cm and initial liquid superficial velocity = 2.52 m/s, $Re_l = 9.36 \times 10^4$)

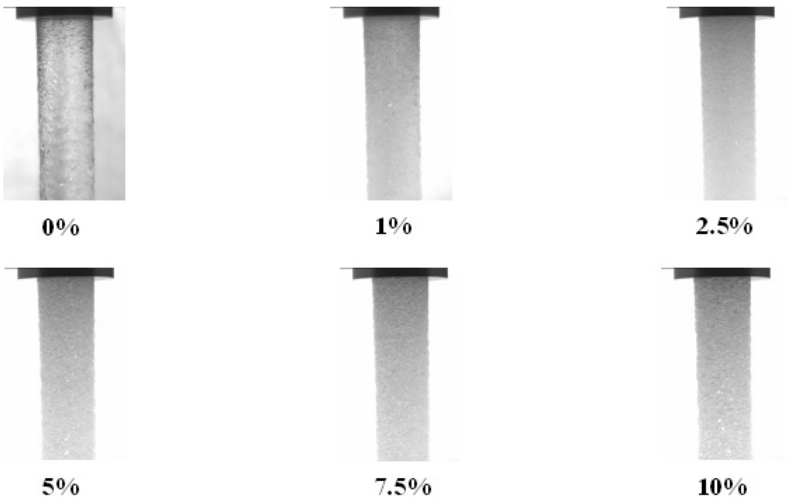

Figure A.3: Near-field behavior of two-phase circular jets with different void fractions (initial diameter = 3.57 cm and initial liquid superficial velocity = 4.73 m/s, $Re_l = 1.76 \times 10^5$)

A.2 Photographs for the 5.25 *cm diameter circular jets*

In this section, photographs of the circular single- and two-phase jets with 5.25 cm initial diameter are presented. Figures A.4, A.5, and A.6 correspond to cases with initial liquid superficial velocities of 0.63, 1.26, and 2.37 m/s, respectively. For each value of the superficial liquid velocity, jets with different values of the initial homogeneous void fraction are shown.

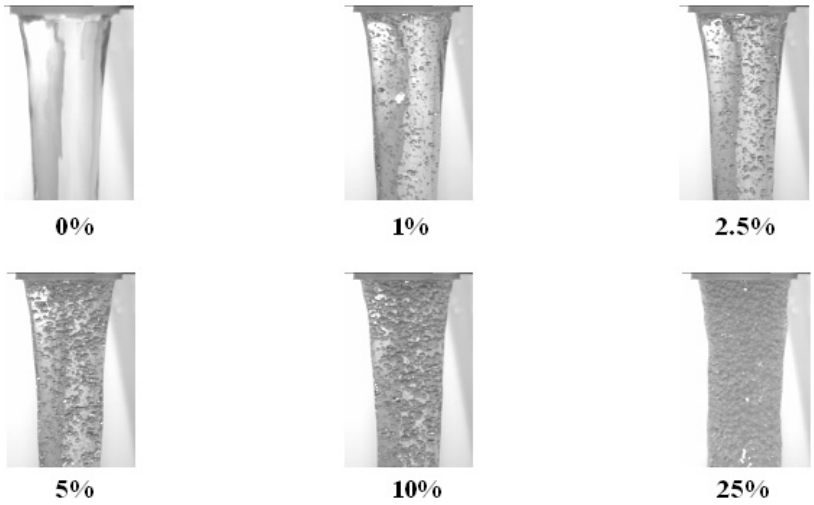

Figure A.4: Near-field behavior of two-phase circular jets with different void fractions (initial diameter = 5.25 cm and initial liquid superficial velocity = 0.63 m/s, $Re_l = 4.68 \times 10^4$)

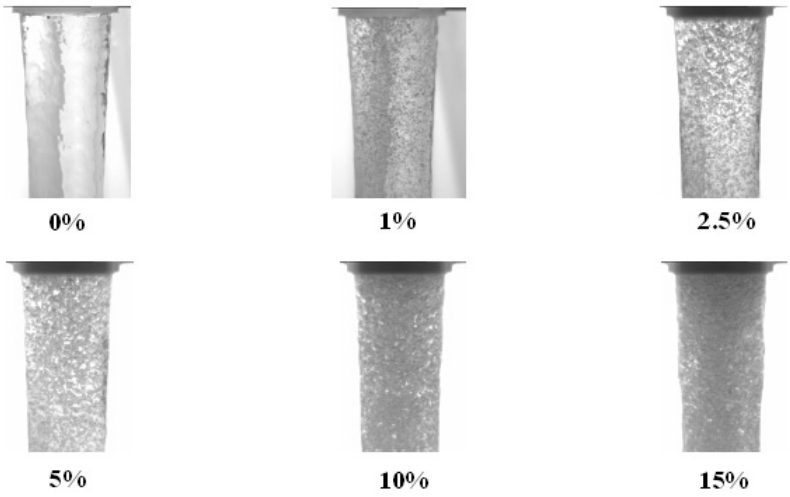

Figure A.5: Near-field behavior of two-phase circular jets with different void fractions (initial diameter = 5.25 cm and initial liquid superficial velocity = 1.26 m/s, $Re_l = 9.36 \times 10^4$)

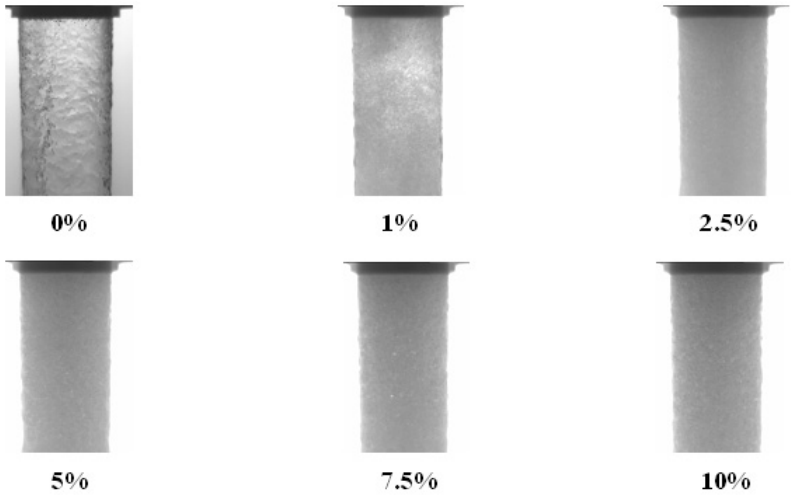

Figure A.6: Near-field behavior of two-phase circular jets with different void fractions (initial diameter = 5.25 cm and initial liquid superficial velocity = 2.37 m/s, $Re_l = 1.76 \times 10^5$)

A.3 Photographs for the 4.00 *cm ID annular jets*

In this section, photographs of the annular single- and two-phase jets with initial ID of 4.00 cm are presented. Figures A.7, A.8, and A.9 correspond to cases with initial liquid superficial velocities of 1.00, 2.00, and 4.00 m/s, respectively. For each value of the superficial liquid velocity, jets with different values of the initial homogeneous void fraction are shown.

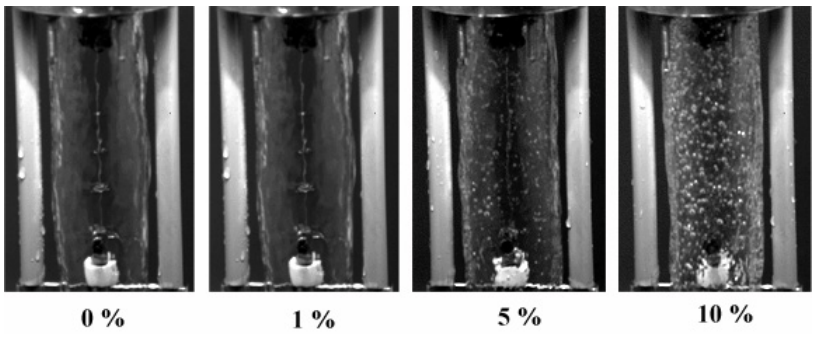

Figure A.7: Near-field behavior of two-phase annular jets with different void fractions (initial liquid superficial velocity = 1.0 m/s, , $Re_l = 1.23 \times 10^4$)

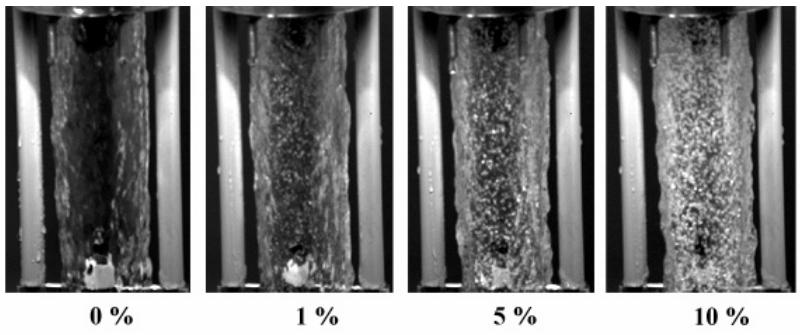

Figure A.8: Near-field behavior of two-phase annular jets with different void fractions (initial liquid superficial velocity = 2.0 m/s, $Re_l = 2.45 \times 10^4$)

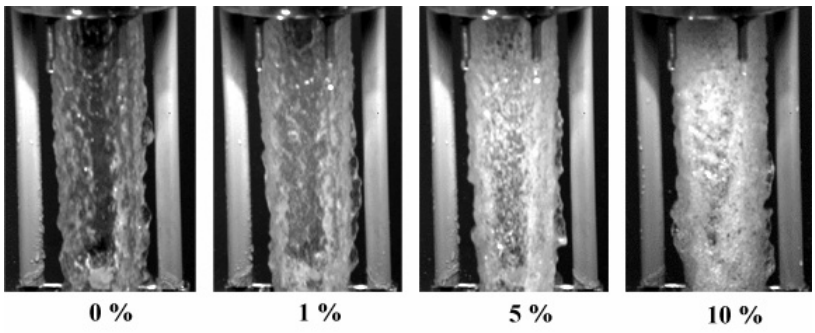

Figure A.9: Near-field behavior of two-phase annular jets with different void fractions (initial liquid superficial velocity = 4.0 m/s, $Re_l = 4.90 \times 10^4$)

APPENDIX B

BUBBLE.M *MATLAB*® PROGRAM LISTING

In this Appendix, the *bubble.m MATLAB*® program is listed. The program is used to to display photographs of the planar two-phase jets, calculate the size of a pixel, and measure the equivalent spherical bubble diameters for 40 different bubbles distributed over nearly 12 cm downward the nozzle exit.

B.1 Program Listing

```
clear all
% Read image file from work directory: e.g "25%, 20 gpm005.
    bmp" here.
im = imread('25%, 20 gpm005.bmp');
%Creation of a dummy index which counts the number of
    measured bubble
i=1;
%Size of a pixel in mm, knowing that the inner width of the
    planar nozzle is 10 cm
imagesc(im); colormap(gray)
[S_x,S_y] = ginput(2)
pixel_size = 100/abs(S_x(2)-S_x(1));
bubble_size(1,1) = pixel_size;
% 40 buubles are measured
while i <= 40
    % Display image
```

```
    imagesc(im); colormap(gray)
    % Use ginput to select corner points of a rectangular
       region by pointing and clicking the mouse twice
    p = ginput(2);
    % Get the x and y corner coordinates as integers
    sp(1) = min(floor(p(1)), floor(p(2))); %xmin
    sp(2) = min(floor(p(3)), floor(p(4))); %ymin
    sp(3) = max(ceil(p(1)), ceil(p(2)));   %xmax
    sp(4) = max(ceil(p(3)), ceil(p(4)));   %ymax
    % Index into the original image to create the new image
    MM = im(sp(2):sp(4), sp(1): sp(3) ,:);
    % Display the subsetted image with appropriate axis ratio
    imagesc(MM); colormap(gray)
    %Pick the coordinates of 4 points out of the image
    [x,y] = ginput(4)
    %Diameter of the bubble in mm
    d_max=max(abs(x(2)-x(1),abs(y(3)-y(4)));
    d_min=min(abs(x(2)-x(1),abs(y(3)-y(4)));
    bubble_size(i+1,1) = pixel_size*((d_max)^2*(d_min))^(1/3)
       ;
    i=i+1;
end
%write the 40 measured diameters in an excel file named "
   bubble_size" in the work directory
xlswrite('bubble_size', bubble_size)
```

APPENDIX C

BUBBLE DIAMETER DENSITIES AND FITTED NORMAL DISTRIBUTIONS

In this Appendix, bubble size distributions within the two-phase planar jets examined in this investigation are presented. Sections C.1, C.2, and C.3 contain graphs of the bubble diameter densities and their associated fitted normal distributions for planar jets with initial liquid superficial velocities of 1.26, 2.52, and 4.92 m/s, respectively. The bubble diameter density corresponds to the relative frequency for each group within a range of 0.1 mm; it is plotted versus the bubble diameter. The fitted normal distribution function is defined as:

$$f(x|\mu,\sigma) = \frac{1}{\sigma \cdot \sqrt{2 \cdot \pi}} \cdot \exp^{\frac{-(x-\mu)^2}{2 \cdot \sigma^2}} \tag{C.1}$$

The corresponding 18 test conditions are documented; values of the liquid superficial velocities $j_{l,e}$ at the nozzle exit, the liquid superficial velocities $j_{l,h}$ within the honeycomb section, the Reynolds numbers Re_l, and the exit homogeneous void fractions α_e are given in Table 4.1 for test numbers 1 through 18.

C.1 Planar Jets with an Initial Liquid Superficial Velocity of $j_{l,e} = 1.26 m/s$

In this section, bubble size distributions for the two-phase planar jets with an initial liquid superficial velocity of $j_{l,e} = 1.26$ m/ are presented. Figures C.1, C.2, C.3, C.4, and C.5 correspond to cases with initial homogeneous void fractions of 1, 2.5, 5, 10, and 25%, respectively. Each subsection contains the density profile, the fitted normal distribution as well as its characteristics.

C.1.1 Jet with an Initial Homogeneous Void Fraction of $\alpha_e = 1\%$

	Estimate	Standard Error
μ:	2.415	0.118622
σ:	0.750231	0.0854967

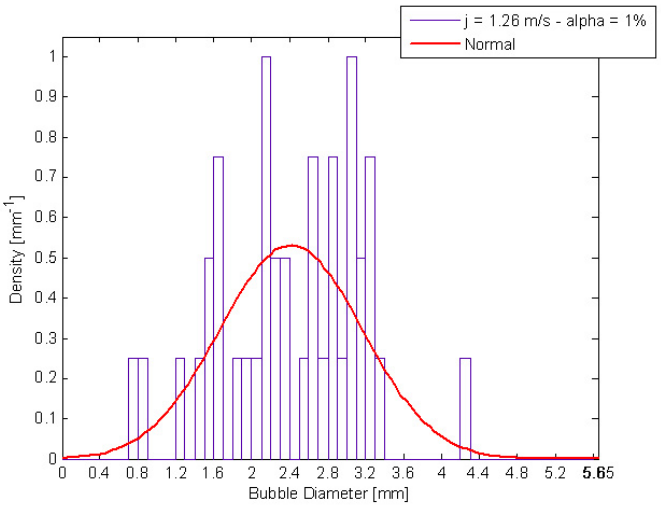

Figure C.1: Bubble size density within a planar jet (initial liquid superficial velocity = 1.26 m/s, $Re_l = 2.38 \times 10^4$, and initial void fraction = 1%) and fitted normal distribution

C.1.2 Jet with an Initial Homogeneous Void Fraction of $\alpha_e = 2.5\%$

	Estimate	Standard Error
μ:	3.055	0.12835
σ:	0.811757	0.0925082

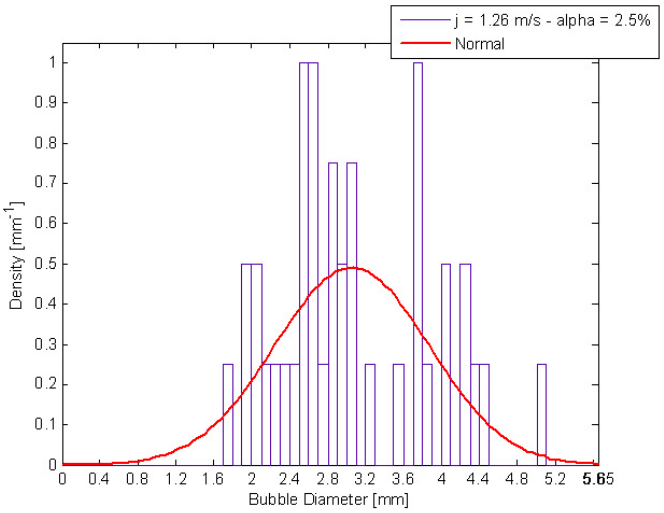

Figure C.2: Bubble size density within a planar jet (initial liquid superficial velocity = 1.26 m/s, $Re_l = 2.38 \times 10^4$, and initial void fraction = 2.5%) and fitted normal distribution

C.1.3 Jet with an Initial Homogeneous Void Fraction of $\alpha_e = 5\%$

	Estimate	Standard Error
μ:	3.5725	0.105702
σ:	0.668518	0.0761847

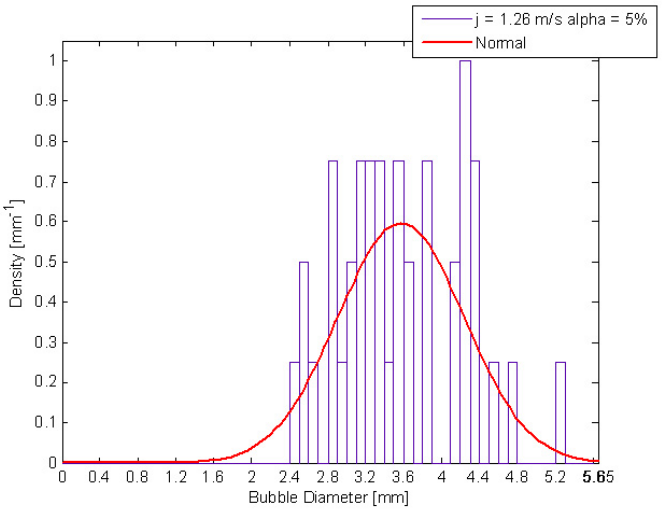

Figure C.3: Bubble size density within a planar jet (initial liquid superficial velocity = 1.26 m/s, $Re_l = 2.38 \times 10^4$, and initial void fraction = 5%) and fitted normal distribution

C.1.4 Jet with an Initial Homogeneous Void Fraction of $\alpha_e = 10\%$

	Estimate	Standard Error
μ:	3.6	0.105308
σ:	0.666025	0.0759006

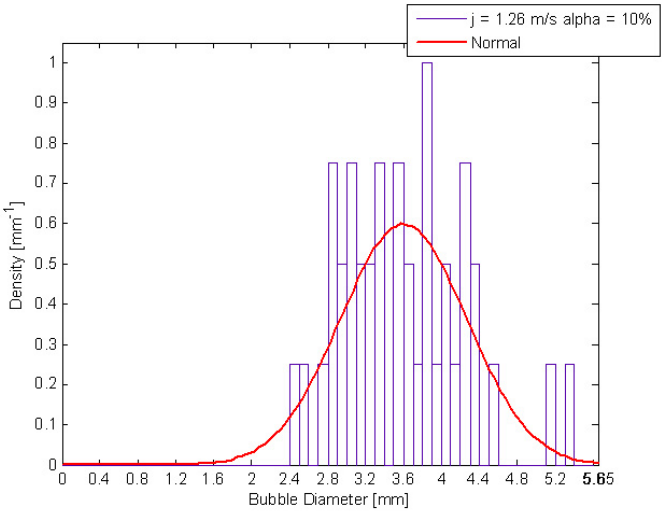

Figure C.4: Bubble size density within a planar jet (initial liquid superficial velocity = 1.26 m/s, $Re_l = 2.38 \times 10^4$, and initial void fraction = 10%) and fitted normal distribution

C.1.5 Jet with an Initial Homogeneous Void Fraction of $\alpha_e = 25\%$

	Estimate	Standard Error
μ:	3.87	0.117189
σ:	0.74117	0.0844642

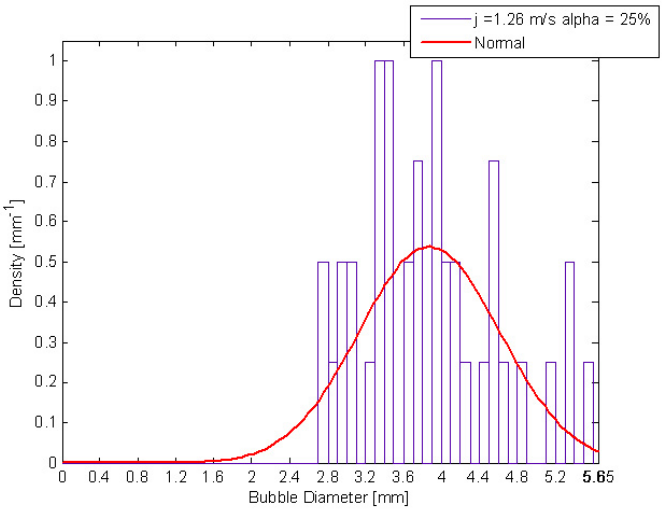

Figure C.5: Bubble size density within a planar jet (initial liquid superficial velocity = 1.26 m/s, $Re_l = 2.38 \times 10^4$, and initial void fraction = 25%) and fitted normal distribution

C.2 Planar Jets with an Initial Liquid Superficial Velocity of $j_{l,e} = 2.52$ m/s

In this section, bubble size distributions for the two-phase planar jets with an initial liquid superficial velocity of $j_{l,e} = 2.52$ m/ are presented. Figures C.6, C.7, C.8, C.9, and C.10 correspond to cases with initial homogeneous void fractions of 1, 2.5, 5, 10, and 15%, respectively. Each subsection contains the density profile, the fitted normal distribution as well as its characteristics.

C.2.1 Jet with an Initial Homogeneous Void Fraction of $\alpha_e = 1\%$

	Estimate	Standard Error
μ:	1.44	0.0631238
σ:	0.39923	0.0454965

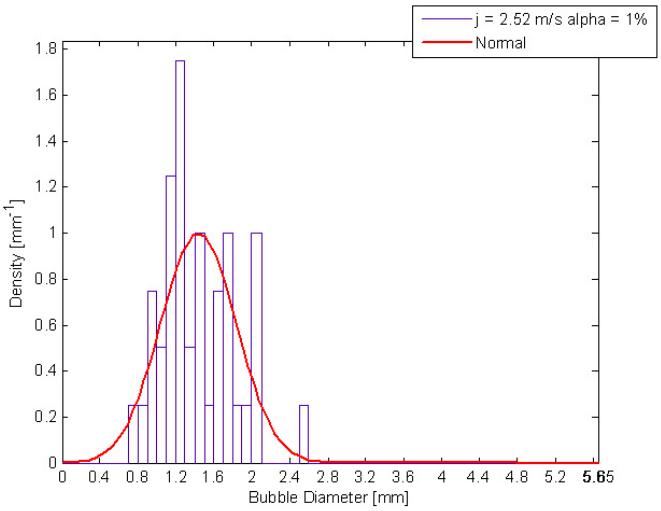

Figure C.6: Bubble size density within a planar jet (initial liquid superficial velocity = 2.52 m/s, $Re_l = 4.77 \times 10^4$, and initial void fraction = 1%) and fitted normal distribution

C.2.2 Jet with an Initial Homogeneous Void Fraction of $\alpha_e = 2.5\%$

	Estimate	Standard Error
μ:	1.9325	0.0852513
σ:	0.539177	0.0614449

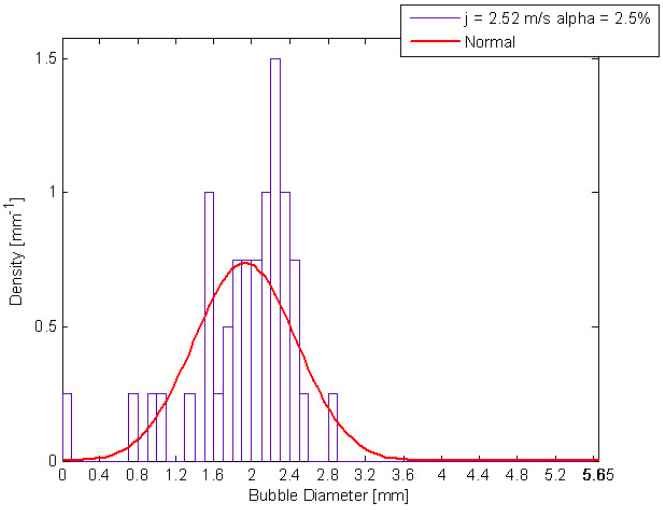

Figure C.7: Bubble size density within a planar jet (initial liquid superficial velocity = 2.52 m/s, $Re_l = 4.77 \times 10^4$, and initial void fraction = 2.5%) and fitted normal distribution

C.2.3 Jet with an Initial Homogeneous Void Fraction of $\alpha_e = 5\%$

	Estimate	Standard Error
μ:	2.7225	0.0812552
σ:	0.513903	0.0585647

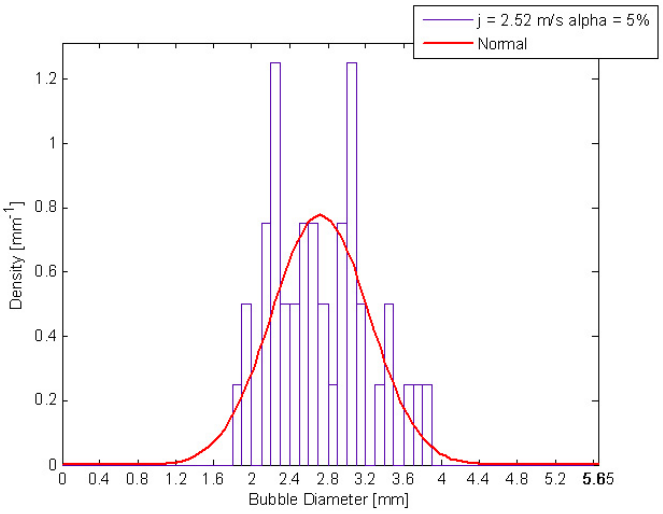

Figure C.8: Bubble size density within a planar jet (initial liquid superficial velocity = 2.52 m/s, $Re_l = 4.77 \times 10^4$, and initial void fraction = 5%) and fitted normal distribution

C.2.4 Jet with an Initial Homogeneous Void Fraction of $\alpha_e = 10\%$

	Estimate	Standard Error
μ:	3.2675	0.08495
σ:	0.537271	0.0612277

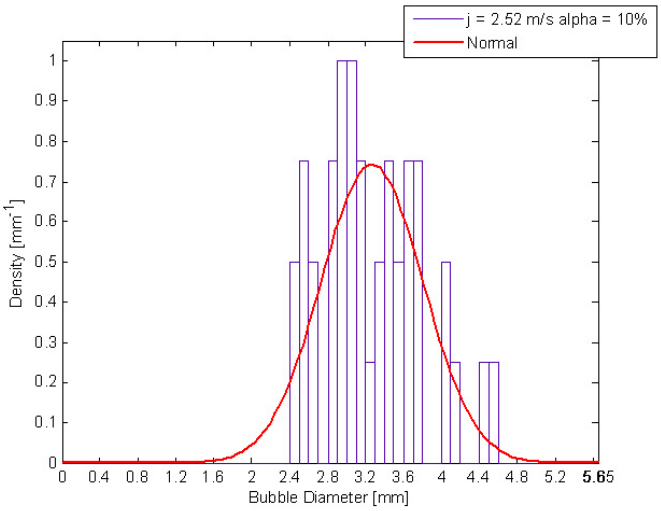

Figure C.9: Bubble size density within a planar jet (initial liquid superficial velocity = 2.52 m/s, $Re_l = 4.77 \times 10^4$, and initial void fraction = 10%) and fitted normal distribution

C.2.5 Jet with an Initial Homogeneous Void Fraction of $\alpha_e = 15\%$

	Estimate	Standard Error
μ:	3.0875	0.126069
σ:	0.797331	0.0908643

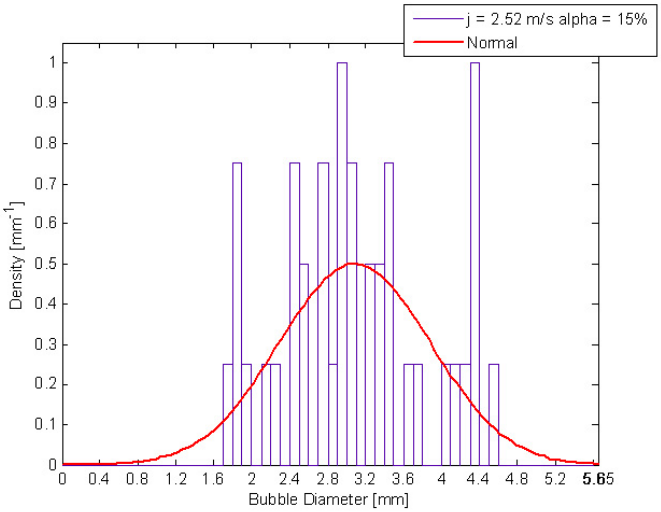

Figure C.10: Bubble size density within a planar jet (initial liquid superficial velocity = 2.52 m/s, $Re_l = 4.77 \times 10^4$, and initial void fraction = 15%) and fitted normal distribution

C.3 Planar Jets with an Initial Liquid Superficial Velocity of $j_{l,e} = 4.92$ m/s

In this section, bubble size distributions for the two-phase planar jets with an initial liquid superficial velocity of $j_{l,e} = 4.92$ m/ are presented. Figures C.11, 4.11, C.13, C.14, and C.15 correspond to cases with initial homogeneous void fractions of 1, 2.5, 5, 7.5, and 10%, respectively. Each subsection contains the density profile, the fitted normal distribution as well as its characteristics.

C.3.1 Jet with an Initial Homogeneous Void Fraction of $\alpha_e = 1\%$

	Estimate	Standard Error
μ:	1.2575	0.0410421
σ:	0.259573	0.0295811

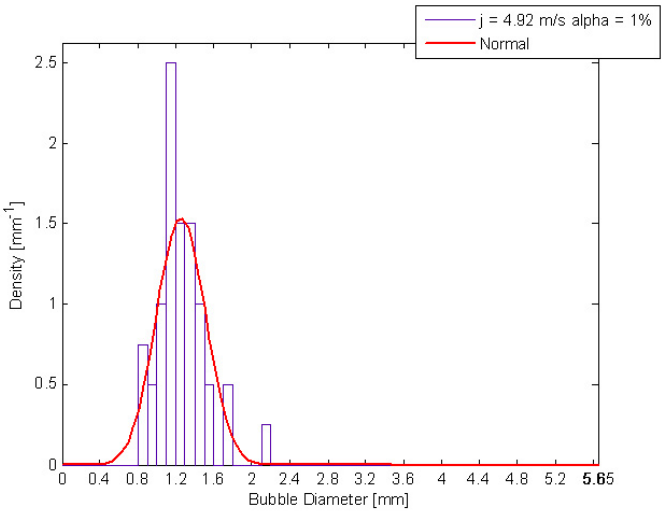

Figure C.11: Bubble size density within a planar jet (initial liquid superficial velocity = 4.92 m/s, $Re_l = 9.31 \times 10^4$, and initial void fraction = 1%) and fitted normal distribution

C.3.2 Jet with an Initial Homogeneous Void Fraction of $\alpha_e = 2.5\%$

	Estimate	Standard Error
μ:	1.5575	0.047419
σ:	0.299904	0.0341772

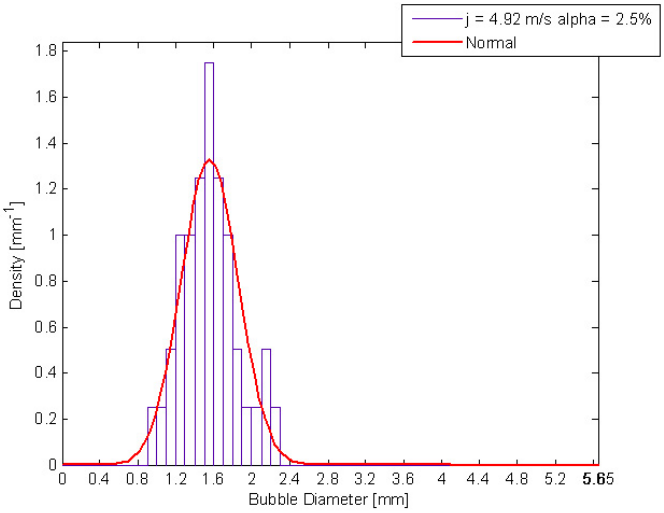

Figure C.12: Bubble size density within a planar jet (initial liquid superficial velocity = 4.92 m/s, $Re_l = 9.31 \times 10^4$, and initial void fraction = 2.5%) and fitted normal distribution

C.3.3 Jet with an Initial Homogeneous Void Fraction of $\alpha_e = 5\%$

	Estimate	Standard Error
μ:	1.5475	0.0383117
σ:	0.242305	0.0276132

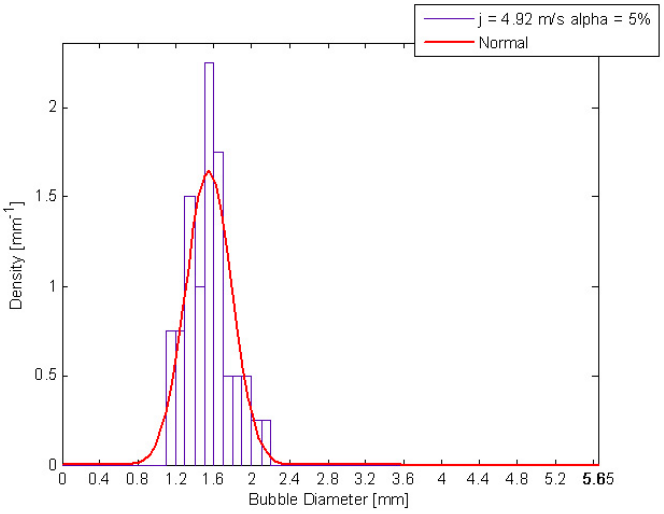

Figure C.13: Bubble size density within a planar jet (initial liquid superficial velocity = 4.92 m/s, $Re_l = 9.31 \times 10^4$, and initial void fraction = 5%) and fitted normal distribution

C.3.4 Jet with an Initial Homogeneous Void Fraction of $\alpha_e = 7.5\%$

	Estimate	Standard Error
μ:	1.955	0.0791744
σ:	0.500743	0.057065

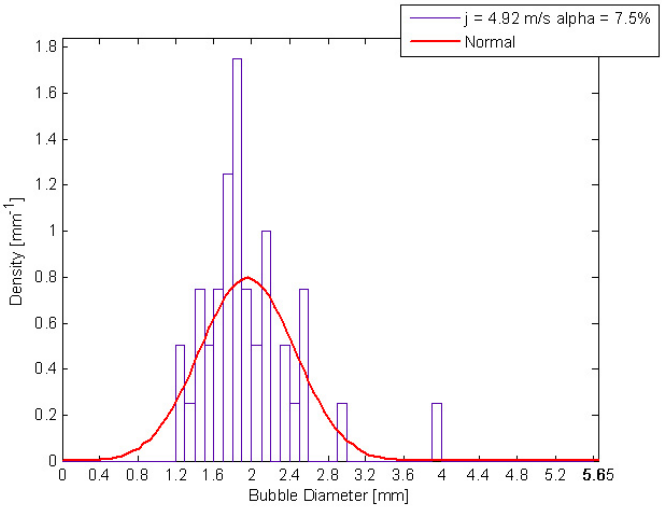

Figure C.14: Bubble size density within a planar jet (initial liquid superficial velocity = 4.92 m/s, $Re_l = 9.31 \times 10^4$, and initial void fraction = 7.5%) and fitted normal distribution

C.3.5 Jet with an Initial Homogeneous Void Fraction of $\alpha_e = 10\%$

	Estimate	Standard Error
μ:	1.965	0.0984202
σ:	0.622464	0.0709364

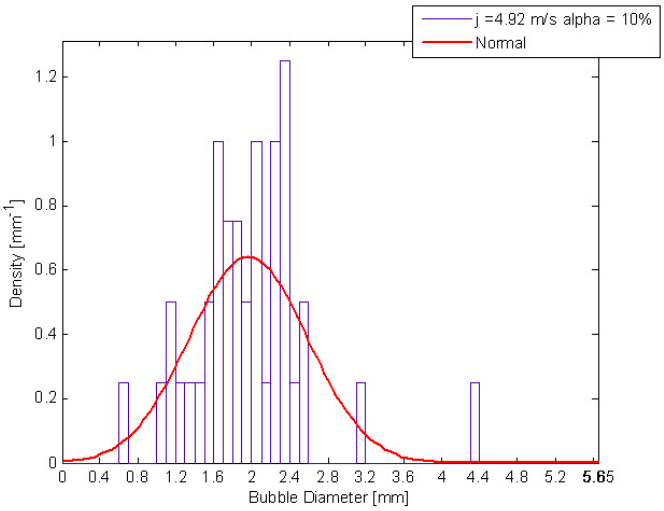

Figure C.15: Bubble size density within a planar jet (initial liquid superficial velocity = 4.92 m/s, $Re_l = 9.31 \times 10^4$, and initial void fraction = 10%) and fitted normal distribution

APPENDIX D

EXPERIMENTAL VALUES OF VOID FRACTION AND SLIP RATIO

In this Appendix, void fraction and slip ratio distributions along the jet centerline of the two-phase planar and circular jets examined in this investigation are presented. A detailed list of the test conditions for the void fraction and slip ratio distribution measurements is provided in Table 4.2. The absorption of gamma-particles were measured with the desired two-phase flow, and repeated with ambient air as well as pure liquid water. By comparing the number of counts measured with each respective medium, the averaged void fraction of the two-phase flow could be measured. The slip ratio was expressed as a function of the void fraction (see Sections 4.2.1 and 4.2.2). Details of the uncertainty calculation are provided in Appendix F. Sections D.1 and D.2 contain the experimental data plotted against the ratio between the distance x from the nozzle exit and the nozzle hydraulic diameter, for the 10 cm $\times$ 1 cm planar jet and 3.57 cm diameter circular jet, respectively.

D.1 Void Fraction and Slip Ratio Distributions for Planar Jets

In this section, void fraction and slip ratio distributions along the jet centerline of two-phase 10 cm $\times$ 1 cm planar jets are presented. Sections D.1.1, D.1.2, D.1.3, and D.1.4 correspond to cases with initial liquid superficial velocities of 1.0, 2.0, 3.0 and 4.0 m/s, respectively. For each value of the superficial liquid velocity, void fraction and slip ratio distributions are shown for different values of the initial homogeneous void fraction. For the void fraction distributions, the points are calculated from

the experimental measured points, while the solid lines are obtained by curve fitting the collapsed liquid and jet thicknesses. For the slip ratio distributions, the points and the solid lines are calculated from the curve fitted values of the jet thicknesses, since the fitting curves are within the error bars. The entire analysis method is also applied to the case where $\alpha_e = 0\%$. The resulting void fraction values are nearly zero; the estimated void fraction values for $\alpha_e = 0\%$ correspond to sources of errors (see Appendix F for error analysis). The corresponding slip ratio values are not shown since they are equal to zero.

D.1.1 Planar Jets with $j_{l,e} = 1.0$ m/s

Figures D.1 and D.2 show the void fraction and slip ratio distribution for 10 cm × 1 cm planar jets with with initial liquid superficial velocities of 1.0 m/s.

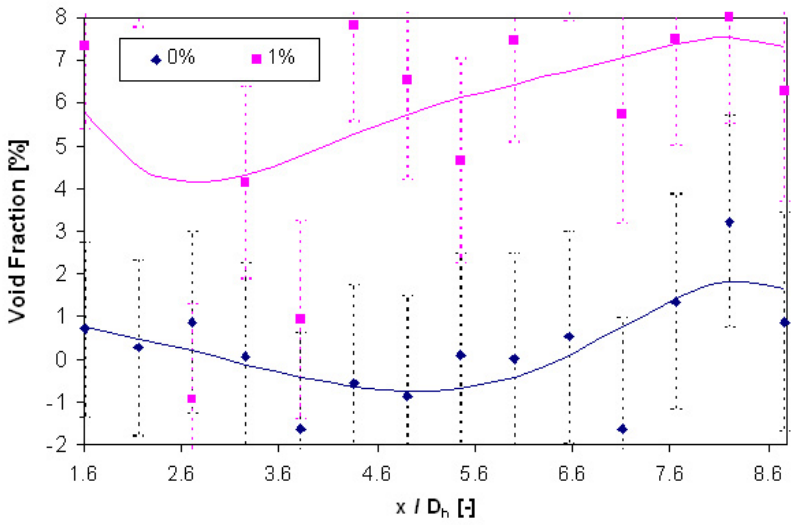

Figure D.1: Measured void fraction distribution along the dimensionless x-axis for a planar jet (initial liquid superficial velocity = 1.0 m/s, $Re_l = 1.89 \times 10^4$)

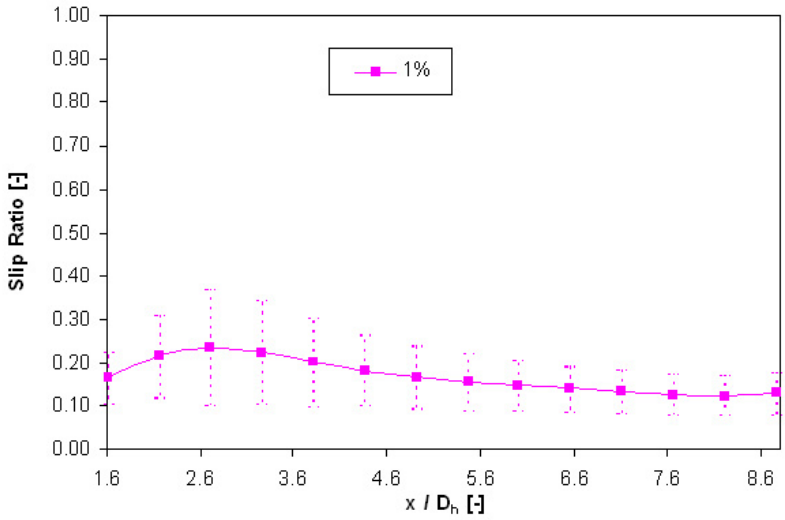

Figure D.2: Calculated slip ratio distribution along the dimensionless x-axis for a planar jet (initial liquid superficial velocity = 1.0 m/s, $Re_l = 1.89 \times 10^4$)

D.1.2 Planar Jets with $j_{l,e} = 2.0$ m/s

Figures D.3 and D.4 show the void fraction and slip ratio distribution for 10 cm × 1 cm planar jets with with initial liquid superficial velocities of 2.0 m/s.

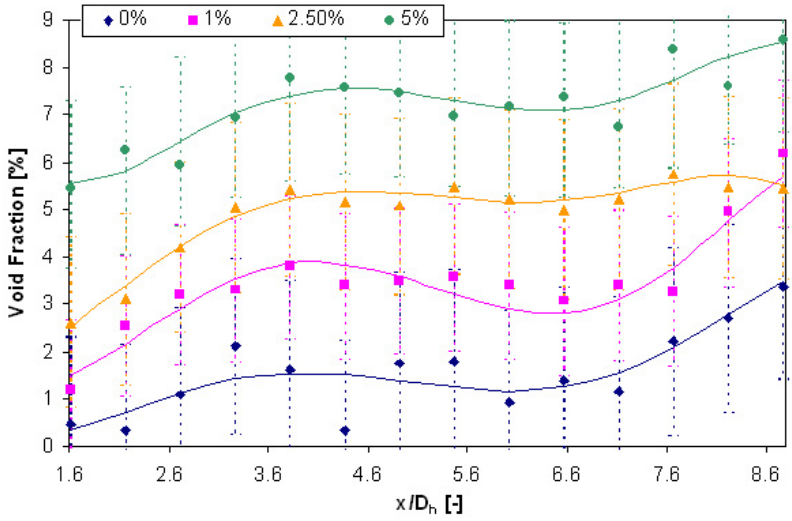

Figure D.3: Measured void fraction distribution along the dimensionless x-axis for a planar jet (initial liquid superficial velocity = 2.0 m/s, $Re_l = 3.78 \times 10^4$)

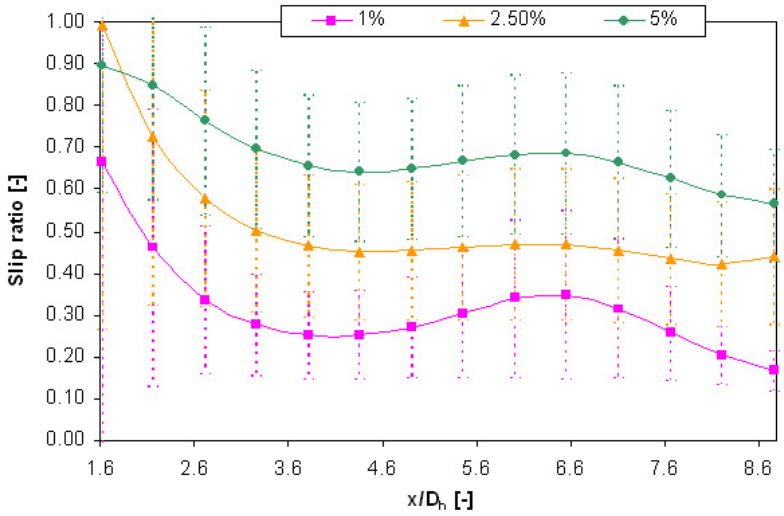

Figure D.4: Calculated slip ratio distribution along the dimensionless x-axis for a planar jet (initial liquid superficial velocity = 2.0 m/s, $Re_l = 3.78 \times 10^4$)

D.1.3 Planar Jets with $j_{l,e} = 3.0$ m/s

Figures D.5 and D.6 show the void fraction and slip ratio distribution for 10 cm × 1 cm planar jets with with initial liquid superficial velocities of 3.0 m/s.

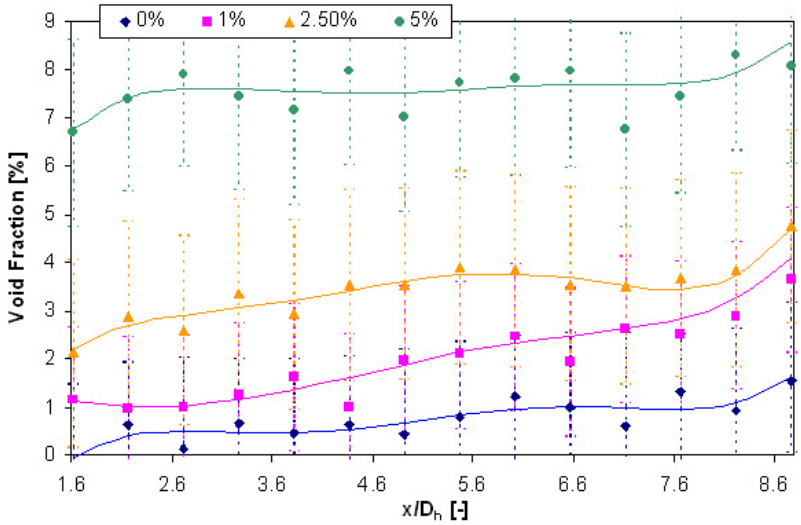

Figure D.5: Measured void fraction distribution along the dimensionless x-axis for a planar jet (initial liquid superficial velocity = 3.0 m/s, $Re_l = 5.67 \times 10^4$)

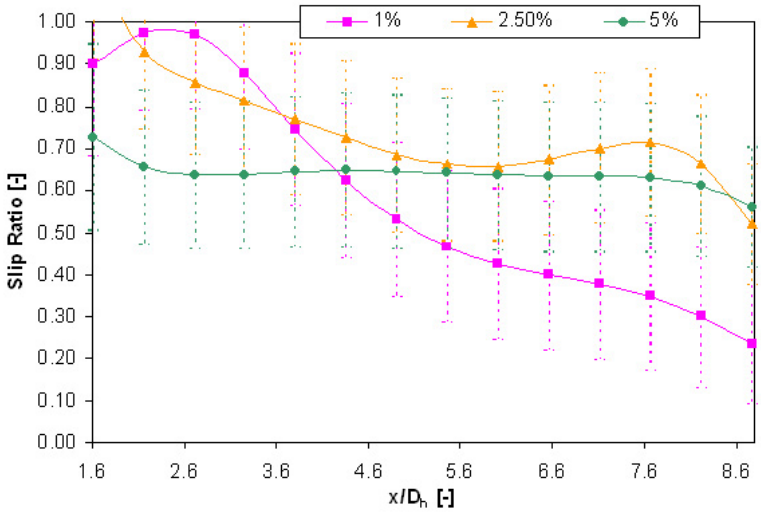

Figure D.6: Calculated slip ratio distribution along the dimensionless x-axis for a planar jet (initial liquid superficial velocity = 3.0 m/s, $Re_l = 5.67 \times 10^4$)

D.1.4 Planar Jets with $j_{l,e} = 4.0$ m/s

Figures D.7 and D.8 show the void fraction and slip ratio distribution for 10 cm × 1 cm planar jets with with initial liquid superficial velocities of 4.0 m/s.

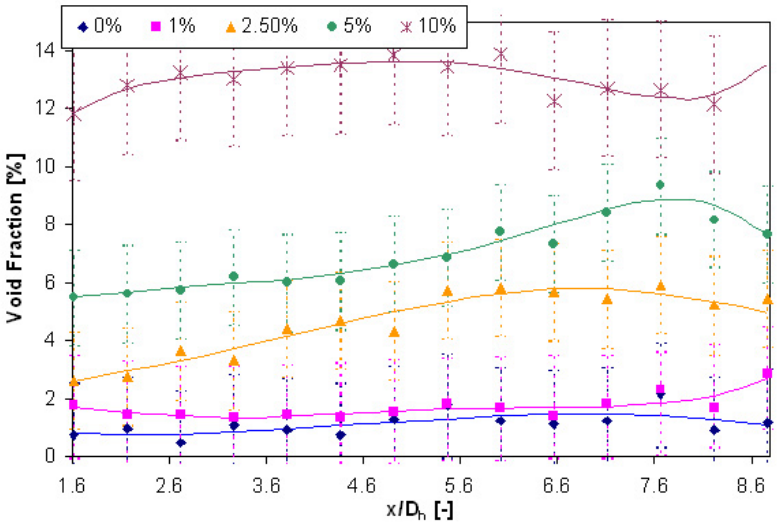

Figure D.7: Measured void fraction distribution along the dimensionless x-axis for a planar jet (initial liquid superficial velocity = 4.0 m/s, $Re_l = 7.57 \times 10^4$)

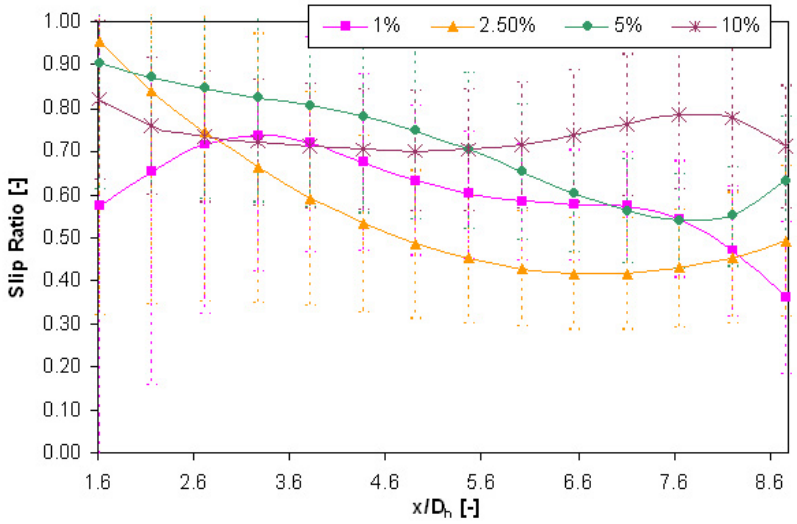

Figure D.8: Calculated slip ratio distribution along the dimensionless x-axis for a planar jet (initial liquid superficial velocity = 4.0 m/s, $Re_l = 7.57 \times 10^4$)

D.2 Void Fraction and Slip Ratio Distributions for Circular Jets

In this section, void fraction and slip ratio distributions along the jet centerline of two-phase 3.57 cm diameter circular jets are presented. Sections D.2.1, D.2.2, D.2.3, and D.2.4 correspond to cases with initial liquid superficial velocities of 1.0, 2.0, 3.0 and 4.0 m/s, respectively. For each value of the superficial liquid velocity, void fraction and slip ratio distributions are shown for different values of the initial homogeneous void fraction. For the void fraction distributions, the points are calculated from the experimental measured points, while the solid lines are obtained by curve fitting the collapsed liquid and jet thicknesses. For the slip ratio distributions, the points and the solid lines are calculated from the curve fitted values of the jet thicknesses, since the fitting curves are within the error bars. The entire analysis method is also applied to the case where $\alpha_e = 0\%$. The resulting void fraction values are nearly zero; the estimated void fraction values for $\alpha_e = 0\%$ correspond to sources of errors (see Appendix F for error analysis). The corresponding slip ratio values are not shown since they are equal to zero.

D.2.1 Circular Jets with $j_{l,e} = 1.0$ m/s

Figures D.9 and D.10 show the void fraction and slip ratio distribution for 3.57 cm diameter circular jets with with initial liquid superficial velocities of 1.0 m/s.

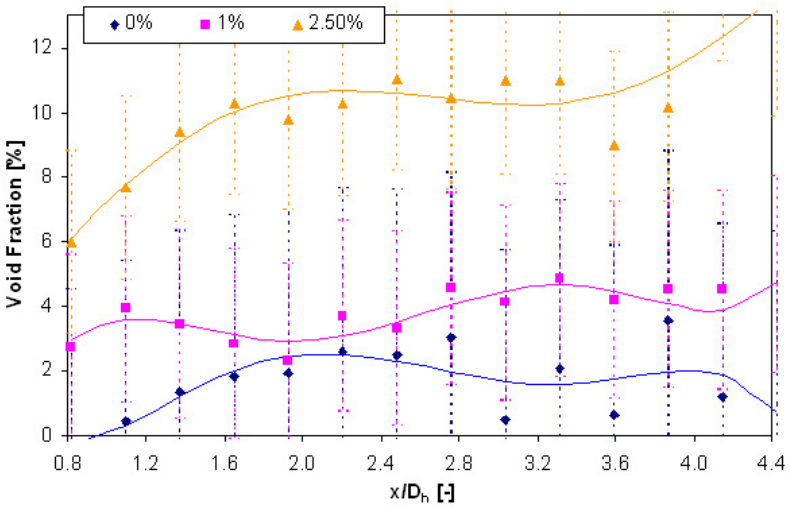

Figure D.9: Measured void fraction distribution along the dimensionless x-axis for a circular jet (initial liquid superficial velocity = 1.0 m/s, $Re_l = 3.72 \times 10^4$)

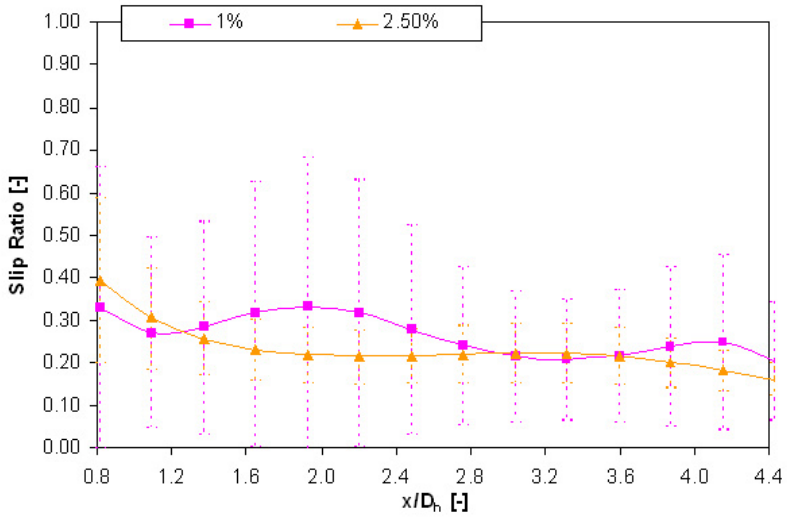

Figure D.10: Calculated slip ratio distribution along the dimensionless x-axis for a circular jet (initial liquid superficial velocity = 1.0 m/s, $Re_l = 3.72 \times 10^4$)

D.2.2 Circular Jets with $j_{l,e}$ = 2.0 m/s

Figures D.11 and D.12 show the void fraction and slip ratio distribution for 3.57 cm diameter circular jets with with initial liquid superficial velocities of 2.0 m/s. At $j_{l,e}$ = 2 m/s, the jets are in the transition regime, and therefore, while being stable, the jets have strong surface waves, which prevent accurate measurements of the thickness, and hence, the local void fraction, and lead to unreasonable data.

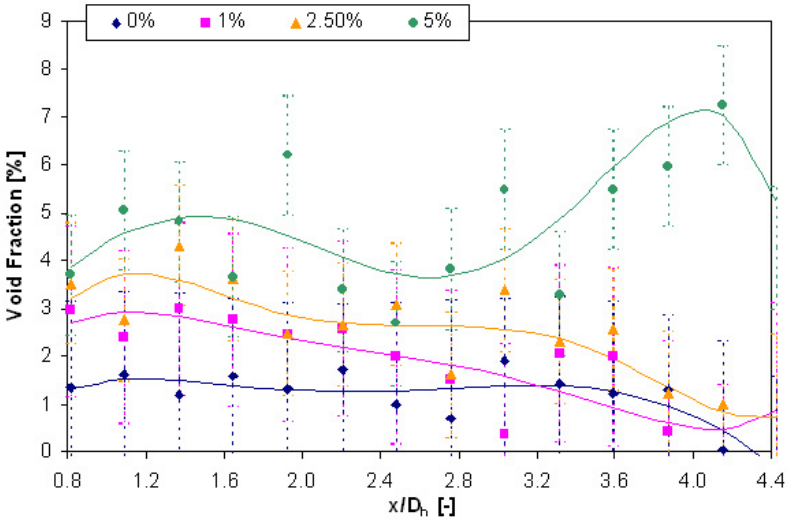

Figure D.11: Measured void fraction distribution along the dimensionless x-axis for a circular jet (initial liquid superficial velocity = 2.0 m/s, $Re_l = 7.43 \times 10^4$)

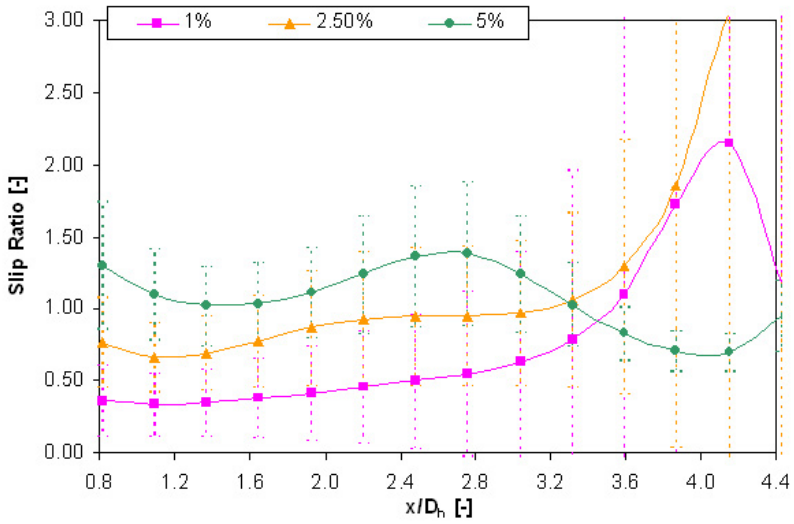

Figure D.12: Calculated slip ratio distribution along the dimensionless x-axis for a circular jet (initial liquid superficial velocity = 2.0 m/s, $Re_l = 7.43 \times 10^4$)

D.2.3 Circular Jets with $j_{l,e} = 3.0$ m/s

Figures D.13 and D.14 show the void fraction and slip ratio distribution for 3.57 cm diameter circular jets with with initial liquid superficial velocities of 3.0 m/s.

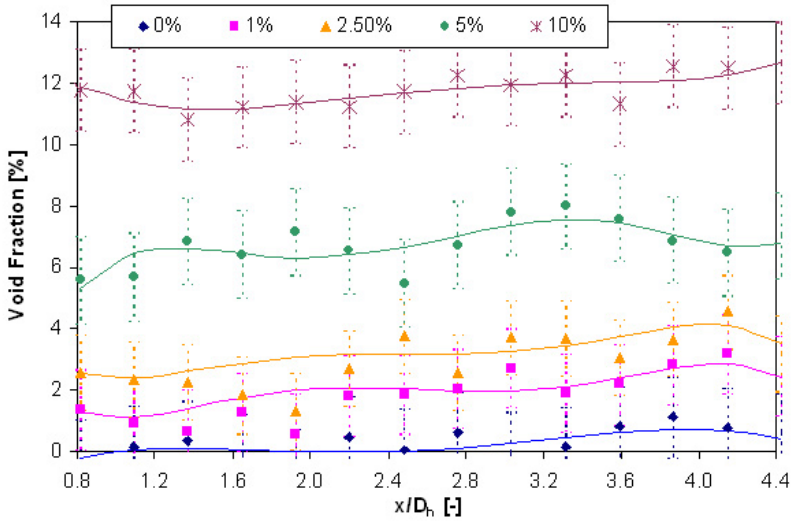

Figure D.13: Measured void fraction distribution along the dimensionless x-axis for a circular jet (initial liquid superficial velocity = 3.0 m/s, $Re_l = 1.11 \times 10^5$)

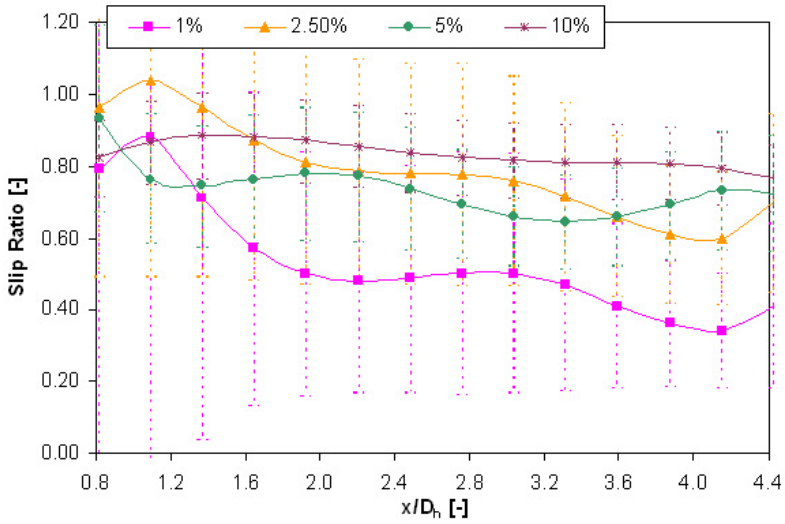

Figure D.14: Calculated slip ratio distribution along the dimensionless x-axis for a circular jet (initial liquid superficial velocity = 3.0 m/s, $Re_l = 1.11 \times 10^5$)

D.2.4 Circular Jets with $j_{l,e} = 4.0$ m/s

Figures D.15 and D.16 show the void fraction and slip ratio distribution for 3.57 cm diameter circular jets with with initial liquid superficial velocities of 4.0 m/s.

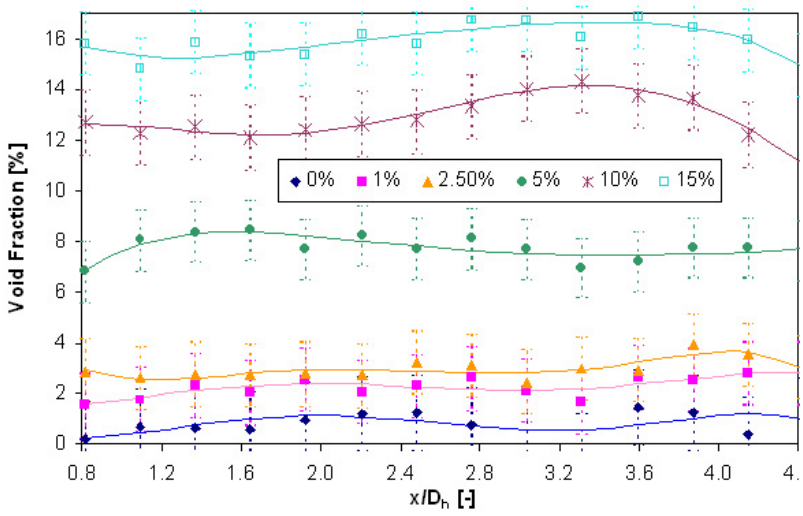

Figure D.15: Measured void fraction distribution along the dimensionless x-axis for a circular jet (initial liquid superficial velocity = 4.0 m/s, $Re_l = 1.47 \times 10^5$)

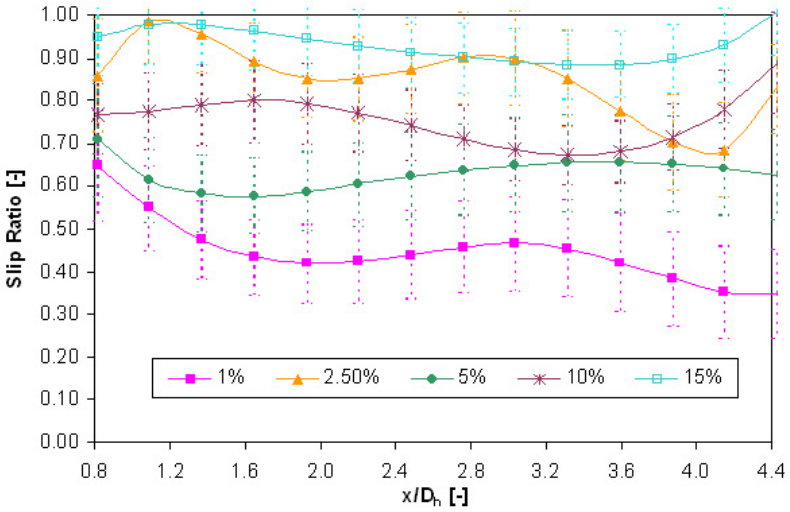

Figure D.16: Calculated slip ratio distribution along the dimensionless x-axis for a circular jet (initial liquid superficial velocity = 4.0 m/s, $Re_l = 1.47 \times 10^5$)

APPENDIX E

PRESSURE HISTORY DATA FOR SHOCK ATTENUATION EXPERIMENTS

In this Appendix, characteristics of the pressure histories recorded at the enclosure wall for the shock attenuation experiments with two-phase annular jets (see Section 4.3), are presented. Sections E.1 and E.2 contain tables giving amplitude and time of the first few pressure pulses of the pressure histories recorded for small- and large-scale annular jet experiments, respectively. Complete data are available on DVD in the Thermal-Hydraulic Laboratory at Georgia Tech.

E.1 Detailed Listing of Pressure Histories for Small-Scale Annular Jet Experiments

In this section, characteristics of the pressure histories recorded for the small-scale annular jet experiments (see Table 4.5), are presented. Sections E.1.1, E.1.2, and E.1.3 correspond to experiments with unconfined, radially-confined, and radially- and axially-confined shocks, respectively. For each type of boundary condition, characteristics of pressure histories with different values of the shock strength, superficial liquid velocity, and initial homogeneous void fraction are given.

E.1.1 Attenuation of Unconfined Shocks

In this subsection, characteristics of the pressure histories recorded for small-scale annular jet experiments conducted with unconfined shocks (boundary condition # 1 in Table 4.5) are given. Referring to Table 4.5, the amplitudes and locations of the first four pressure pulses for test numbers 1 through 6 are presented in Tables E.2 through E.7, respectively. For each combination of test conditions, the experiment

is repeated 20 times, except for test condition # 1 (see Table 4.5). Ten experiments are recorded transducer # 1, while the other ten are recorded with transducer # 2. Since the experiments recorded with transducer # 2 are extremely noisy, only those recorded with transducer # 1 are shown here. For test condition # 1, five experiments recorded with transducer # 1 are presented.

The pressure histories for small-scale annular jet experiments conducted with unconfined shocks have the same general trend as that shown in Figure E.1. The time location t_0 corresponds to the initial time of the experiment, i.e. the time at which the oscilloscope detects a significant change in pressure and is triggered by the first channel. The amplitudes and time locations of the first four pressure pulses (A_1 through A_4 and t_1 through t_4, respectively) are noted in Figure E.1 and reported in a table for each combination of test conditions, as it is shown in Table E.1. For this set of experiments, the pressure amplitude after the fourth pulse is negligible.

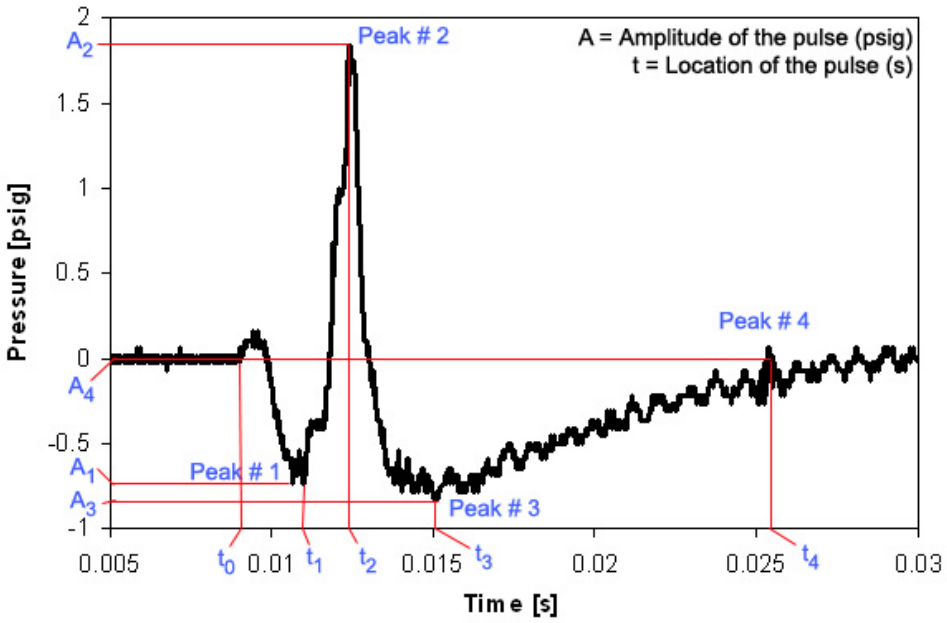

Figure E.1: Figure example for data related to small-scale annular jet experiments conducted with unconfined shocks

Table E.1: Table example for data related to small-scale annular jet experiments conducted with unconfined shocks

			Peaks			
Run	Transducer	t_0	#1	#2	#3	#4
Test #	Transducer used	Initial time (s)	Amplitude of the pulse (psig) Location of the pulse (s)			
Test	1	t_0	A_1 t_1	A_2 t_2	A_3 t_3	A_4 t_4

Table E.2: Detailed list of pressure pulse characteristics for Test #1 of Table 4.5

			Peaks			
Run	Transducer	t_0	#1	#2	#3	#4
1	1	9.99E-03	-3.15E-01 1.03E-02	2.22 1.05E-02	-2.99 1.74E-02	0.00 3.00E-02
2	1	1.00E-02	-1.16 1.05E-02	1.98 1.05E-02	-2.52 1.67E-02	0.00 3.12E-02
3	1	1.00E-02	-3.24E-01 1.04E-02	2.68 1.05E-02	-1.82 1.67E-02	0.00 2.86E-02
4	1	1.00E-02	-3.67E-01 1.04E-02	2.96 1.05E-02	-2.05 1.74E-02	0.00 2.93E-02
5	1	1.01E-02	-3.03E-02 1.01E-02	3.30 1.01E-02	-2.00 1.64E-02	0.00 2.83E-02

Table E.3: Detailed list of pressure pulse characteristics for Test #2 of Table 4.5

			Peaks			
Run	Transducer	t_0	#1	#2	#3	#4
1	1	9.26E-03	-5.54E-01 1.03E-02	8.52E-01 1.27E-02	-6.48E-01 1.49E-02	0.00 2.53E-02
2	1	9.13E-03	-5.59E-01 1.07E-02	1.50 1.21E-02	-6.53E-01 1.47E-02	0.00 2.25E-02
3	1	9.45E-03	-8.24E-01 1.20E-02	2.07E-01 6.40E-02	-2.15E-01 1.39E-01	0.00 2.00E-01
4	1	9.08E-03	-5.74E-01 1.08E-02	3.64E-01 1.18E-02	-6.67E-01 1.42E-02	0.00 2.53E-02
5	1	9.26E-03	-7.32E-01 1.07E-02	1.85 1.24E-02	-8.25E-01 1.50E-02	0.00 2.53E-02
6	1	9.23E-03	-6.08E-01 1.10E-02	7.51E-01 1.27E-02	-6.08E-01 1.58E-02	0.00 2.51E-02
7	1	9.11E-03	-5.19E-01 1.04E-02	1.12 1.29E-02	-5.66E-01 1.60E-02	0.00 2.78E-02
8	1	9.22E-03	-8.01E-01 1.36E-02	1.83E-01 3.18E-02	-1.92E-01 1.36E-01	0.00 2.00E-01

continued on next page

continued from previous page

			Peaks			
Run	Transducer	t_0	#1	#2	#3	#4
9	1		-4.78E-01	1.21	-5.25E-01	0.00
		9.04E-03	1.03E-02	1.25E-02	1.48E-02	2.71E-02
10	1		-7.45E-01	7.08E-01	-9.33E-01	0.00
		9.26E-03	1.17E-02	1.33E-02	1.50E-02	2.63E-02

Table E.4: Detailed list of pressure pulse characteristics for Test #3 of Table 4.5

			Peaks			
Run	Transducer	t_0	#1	#2	#3	#4
1	1		-4.48E-01	1.38	-4.01E-01	0.00
		9.39E-03	1.03E-02	1.09E-02	1.15E-02	1.30E-02
2	1		-4.88E-01	7.31E-01	-4.41E-01	0.00
		9.29E-03	1.03E-02	1.31E-02	1.49E-02	2.72E-02
3	1		-5.33E-01	6.39E-01	-8.14E-01	0.00
		9.25E-03	1.04E-02	1.18E-02	1.24E-02	2.66E-02
4	1		-6.20E-01	6.08	-4.80E-01	0.00
		9.24E-03	1.01E-02	1.27E-02	1.81E-02	3.26E-02
5	1		-4.20E-01	1.83	-5.14E-01	0.00
		9.22E-03	1.03E-02	1.32E-02	1.35E-02	1.36E-02
6	1		-5.47E-01	2.64	-7.34E-01	0.00
		9.33E-03	1.02E-02	1.19E-02	1.46E-02	2.80E-02
7	1		-4.88E-01	6.07	-6.76E-01	0.00
		9.26E-03	1.03E-02	1.13E-02	1.33E-02	2.98E-02
8	1		-4.52E-01	6.06	-5.93E-01	0.00
		9.34E-03	1.03E-02	1.11E-02	1.28E-02	2.74E-02
9	1		-4.67E-01	3.75	-5.61E-01	0.00
		9.30E-03	1.01E-02	1.03E-02	1.05E-02	1.06E-02
10	1		-5.36E-01	1.29	-3.95E-01	0.00
		9.38E-03	1.02E-02	1.43E-02	1.67E-02	3.12E-02

Table E.5: Detailed list of pressure pulse characteristics for Test #4 of Table 4.5

			Peaks			
Run	Transducer	t_0	#1	#2	#3	#4
1	1		3.95E-02	3.68E-01	-5.70E-01	0.00
		9.33E-03	9.33E-03	9.66E-03	1.60E-02	2.65E-02
2	1		-5.42E-01	1.19	-5.42E-01	0.00
		9.38E-03	1.29E-02	1.46E-02	1.68E-02	2.73E-02
3	1		-4.29E-01	1.31	-3.82E-01	0.00
		9.36E-03	1.02E-02	1.43E-02	1.80E-02	2.73E-02
4	1		-4.26E-01	1.31	-3.80E-01	0.00
		9.40E-03	1.02E-02	1.59E-02	1.82E-02	2.38E-02
5	1		-3.73E-01	3.80	-2.79E-01	0.00

continued on next page

continued from previous page

			Peaks			
Run	Transducer	t_0	#1	#2	#3	#4
		9.30E-03	1.01E-02	1.50E-02	1.76E-02	2.38E-02
6	1		-4.45E-01	9.15E-01	-4.45E-01	0.00
		9.39E-03	1.01E-02	1.40E-02	1.75E-02	2.39E-02
7	1		-4.91E-01	9.15E-01	-3.50E-01	0.00
		9.38E-03	1.01E-02	1.41E-02	1.74E-02	2.21E-02
8	1		-5.03E-01	2.31	-5.03E-01	0.00
		9.38E-03	1.01E-02	1.41E-02	1.61E-02	2.73E-02
9	1		-4.72E-01	1.54	-3.31E-01	0.00
		9.34E-03	1.02E-02	1.45E-02	2.00E-02	3.50E-02
10	1		-4.35E-01	3.27	-4.82E-01	0.00
		9.39E-03	1.01E-02	1.42E-02	1.86E-02	2.11E-02

Table E.6: Detailed list of pressure pulse characteristics for Test #5 of Table 4.5

			Peaks			
Run	Transducer	t_0	#1	#2	#3	#4
1	1		3.95E-02	5.08E-01	-5.23E-01	0.00
		9.45E-03	9.45E-03	9.77E-03	1.01E-02	1.06E-02
2	1		-4.61E-01	1.37	-5.55E-01	0.00
		9.46E-03	1.02E-02	1.38E-02	1.61E-02	2.66E-02
3	1		5.70E-02	4.32E-01	-5.52E-01	0.00
		9.39E-03	9.39E-03	9.71E-03	1.41E-02	2.31E-02
4	1		-5.53E-01	1.65	-6.00E-01	0.00
		9.52E-03	1.02E-02	1.43E-02	1.71E-02	2.75E-02
5	1		-5.46E-01	1.56	-4.99E-01	0.00
		9.46E-03	1.22E-02	1.46E-02	1.77E-02	2.74E-02
6	1		-5.29E-01	5.49E-01	-4.36E-01	0.00
		9.47E-03	1.01E-02	1.29E-02	1.43E-02	2.21E-02
7	1		-4.96E-01	9.10E-01	-5.43E-01	0.00
		9.46E-03	1.01E-02	1.39E-02	1.62E-02	2.38E-02
8	1		-5.11E-01	2.02	-6.05E-01	0.00
		9.42E-03	1.01E-02	1.20E-02	1.48E-02	2.31E-02
9	1		-6.14E-01	1.64	-5.67E-01	0.00
		9.41E-03	1.01E-02	1.24E-02	1.42E-02	2.31E-02
10	1		-6.14E-01	1.64	-5.67E-01	0.00
		9.41E-03	1.01E-02	1.24E-02	1.42E-02	2.31E-02

Table E.7: Detailed list of pressure pulse characteristics for Test #6 of Table 4.5

			Peaks			
Run	Transducer	t_0	#1	#2	#3	#4
1	1		-5.45E-01	1.24	-6.86E-01	0.00
		9.52E-03	1.01E-02	1.32E-02	1.61E-02	2.57E-02
2	1		-4.92E-01	2.27	-5.39E-01	0.00

continued on next page

continued from previous page						
			Peaks			
Run	Transducer	t_0	#1	#2	#3	#4
		9.45E-03	1.01E-02	1.02E-02	1.51E-02	2.39E-02
3	1		-6.80E-01	5.09	-7.74E-01	0.00
		9.48E-03	1.17E-02	1.39E-02	1.63E-02	2.65E-02
4	1		-8.32E-01	2.68	-1.02	0.00
		9.44E-03	1.23E-02	1.41E-02	1.61E-02	2.66E-02
5	1		-6.01E-01	1.46	-6.95E-01	0.00
		9.46E-03	1.16E-02	1.39E-02	1.63E-02	2.66E-02
6	1		-5.45E-01	1.24	-6.86E-01	0.00
		9.52E-03	1.01E-02	1.32E-02	1.61E-02	2.57E-02
7	1		-9.69E-01	3.16	-1.11	0.00
		9.46E-03	1.22E-02	1.36E-02	1.55E-02	2.58E-02
8	1		7.72E-02	5.46E-01	-7.67E-01	0.00
		1.05E-02	1.05E-02	1.08E-02	1.45E-02	2.49E-02
9	1		-5.48E-01	5.83	-7.82E-01	0.00
		1.05E-02	1.12E-02	1.36E-02	1.61E-02	2.86E-02
10	1		5.24E-02	5.68E-01	-8.85E-01	0.00
		9.49E-03	9.49E-03	9.78E-03	1.62E-02	2.57E-02

E.1.2 Attenuation of Radially-Confined Shocks

In this subsection, characteristics of the pressure histories recorded for small-scale annular jet experiments conducted with radially-confined shocks (boundary condition # 2 in Table 4.5) are given. Referring to Table 4.5, the amplitudes, locations, and durations of the first three pressure pulses for test numbers 7 through 16 are presented in Tables E.9 through E.18, respectively. For each combination of test conditions, the experiment is repeated 12 times and recorded with transducer # 1. The data for test conditions # 17 and 18 are not presented here; the strong shocks experienced in these tests resulted in chaotic pressure histories at the enclosure wall.

The pressure histories for small-scale annular jet experiments conducted with radially-confined shocks have the same general trend as that shown in Figure E.2. The time t_0 corresponds to the initial time of the experiment, i.e. the time at which the oscilloscope detects a significant change in pressure and is triggered by the first channel. The amplitudes, time locations, and durations of the first three pressure pulses (A_1 through A_3, t_1 through t_3, and D_1 through D_3, respectively) are noted in

Figure E.2 and reported in a table for each combination of test conditions, as it is shown in Table E.8.

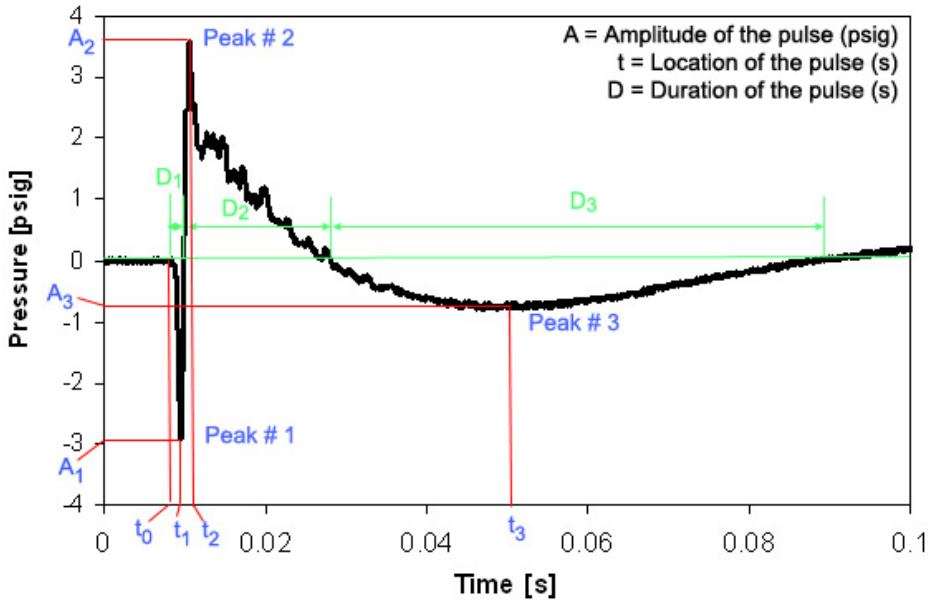

Figure E.2: Figure example for data related to small-scale annular jet experiments conducted with radially-confined shocks

Table E.8: Table example for data related to small-scale annular jet experiments conducted with radially-confined shocks

			Peaks		
Run	Transducer	t_0	#1	#2	#3
Test #	Transducer used	Initial time (s)	Amplitude of the pulse (psig) Location of the pulse (s) Duration of the pulse (s)		
Test	1	t_0	A_1 t_1 D_1	A_2 t_2 D_2	A_3 t_3 D_3

Table E.9: Detailed list of pressure pulse characteristics for Test #7 of Table 4.5

			Peaks		
Run	Transducer	t_0	#1	#2	#3
1	1	9.26E-03	-3.72 9.36E-03	2.70 1.06E-02	-6.27E-01 5.80E-02

continued on next page

continued from previous page

			Peaks		
Run	Transducer	t_0	#1	#2	#3
			6.48E-04	2.01E-02	6.93E-02
2	1	9.31E-03	-4.09	2.90	-5.24E-01
			9.42E-03	1.08E-02	5.05E-02
			6.88E-04	1.98E-02	6.92E-02
3	1	9.14E-03	-5.24	2.83	-8.31E-01
			9.26E-03	1.06E-02	5.04E-02
			6.80E-04	1.99E-02	6.82E-02
4	1	9.34E-03	-3.45	2.55	-5.88E-01
			9.62E-03	1.07E-02	6.14E-02
			6.56E-04	2.06E-02	7.13E-02
5	1	9.14E-03	-3.35	2.51	-4.91E-01
			9.23E-03	1.05E-02	5.51E-02
			8.56E-04	2.00E-02	7.19E-02
6	1	9.30E-03	-3.47	2.90	-5.19E-01
			9.39E-03	1.07E-02	5.48E-02
			7.04E-04	1.96E-02	7.34E-02
7	1	9.27E-03	-3.29	2.62	-5.68E-01
			9.46E-03	1.08E-02	6.32E-02
			7.20E-04	2.07E-02	7.35E-02
8	1	1.04E-02	-2.04	2.13	-6.34E-01
			1.05E-02	1.41E-02	6.67E-02
			6.96E-04	1.98E-02	5.67E-02
9	1	9.91E-03	-3.68	2.60	-5.83E-01
			1.03E-02	1.14E-02	5.75E-02
			6.80E-04	2.01E-02	6.92E-02
10	1	9.28E-03	-3.62	2.99	-3.58E-02
			9.42E-03	1.28E-02	9.55E-02
			7.20E-04	8.55E-02	8.00E-06
11	1	9.26E-03	-3.83	3.07	-6.85E-01
			9.33E-03	1.28E-02	4.67E-02
			6.64E-04	1.94E-02	6.81E-02
12	1	9.20E-03	-3.29	2.94	-5.25E-01
			9.39E-03	1.06E-02	5.04E-02
			7.36E-04	1.97E-02	7.31E-02

Table E.10: Detailed list of pressure pulse characteristics for Test #8 of Table 4.5

			Peaks		
Run	Transducer	t_0	#1	#2	#3
1	1	8.64E-03	-3.37	3.07	-6.82E-01
			9.46E-03	1.06E-02	4.81E-02
			1.34E-03	1.94E-02	5.46E-02
2	1	8.66E-03	-3.41	2.78	-4.69E-01
			9.48E-03	1.06E-02	4.95E-02

continued on next page

continued from previous page

			Peaks		
Run	Transducer	t_0	#1	#2	#3
			1.34E-03	1.87E-02	5.84E-02
3	1	8.63E-03	-3.91	2.71	-6.61E-01
			9.48E-03	1.06E-02	5.96E-02
			1.35E-03	2.24E-02	6.15E-02
4	1	8.67E-03	-3.39	3.36	-6.07E-01
			9.50E-03	1.06E-02	4.66E-02
			1.31E-03	1.88E-02	5.97E-02
5	1	8.58E-03	-3.97	3.09	-5.63E-01
			9.47E-03	1.06E-02	5.93E-02
			1.40E-03	1.86E-02	6.46E-02
6	1	8.61E-03	-3.71	2.85	-6.81E-01
			9.50E-03	1.06E-02	3.57E-02
			1.37E-03	2.30E-02	5.87E-02
7	1	8.62E-03	-4.02	2.76	-2.27E-02
			9.38E-03	1.04E-02	8.06E-02
			1.36E-03	7.06E-02	1.60E-05
8	1	8.66E-03	-3.38	3.12	-7.86E-01
			9.48E-03	1.05E-02	5.40E-02
			1.31E-03	1.91E-02	5.82E-02
9	1	8.62E-03	-3.50	2.75	-6.27E-01
			9.45E-03	1.05E-02	5.46E-02
			1.35E-03	1.97E-02	6.18E-02
10	1	8.68E-03	-3.50	2.82	-5.28E-01
			9.49E-03	1.04E-02	5.47E-02
			1.30E-03	1.87E-02	5.81E-02
11	1	8.53E-03	-3.81	2.84	-7.20E-01
			9.49E-03	1.04E-02	5.45E-02
			1.46E-03	2.05E-02	6.12E-02
12	1	8.62E-03	-3.51	2.52	-7.27E-01
			9.53E-03	1.06E-02	5.27E-02
			1.37E-03	1.96E-02	5.95E-02

Table E.11: Detailed list of pressure pulse characteristics for Test #9 of Table 4.5

			Peaks		
Run	Transducer	t_0	#1	#2	#3
1	1	8.64E-03	-4.55	1.73	-2.40E-01
			9.53E-03	1.03E-02	4.28E-02
			1.34E-03	2.03E-02	5.36E-02
2	1	8.98E-03	-4.36	4.69	-9.28E-02
			9.57E-03	1.55E-02	5.08E-02
			1.01E-03	4.08E-02	3.16E-03
			-5.02	2.15	-2.86E-01

continued on next page

continued from previous page

			Peaks		
Run	Transducer	t_0	#1	#2	#3
3	1	8.57E-03	9.41E-03	1.05E-02	5.05E-02
			1.40E-03	2.06E-02	5.44E-02
4	1	9.02E-03	-4.32	2.66	-3.82E-01
			9.61E-03	1.03E-02	4.40E-02
			9.68E-04	1.91E-02	5.66E-02
5	1	8.67E-03	-4.60	2.43	-3.80E-01
			9.47E-03	1.03E-02	4.54E-02
			1.31E-03	1.93E-02	5.58E-02
6	1	8.46E-03	-4.55	1.79	-1.92E-01
			9.33E-03	9.97E-03	4.32E-02
			1.44E-03	1.93E-02	4.60E-02
7	1	8.54E-03	-6.02	6.02	-2.56E-01
			9.42E-03	1.48E-02	4.85E-02
			1.44E-03	2.75E-02	4.19E-02
8	1	8.64E-03	-5.75	4.56	-5.00E-01
			9.50E-03	1.05E-02	5.05E-02
			1.34E-03	1.96E-02	5.65E-02
9	1	8.54E-03	-4.60	2.02	-1.96E-01
			9.39E-03	1.15E-02	5.01E-02
			1.45E-03	2.38E-02	4.28E-02
10	1	8.74E-03	-4.04	3.04	-2.41E-01
			9.53E-03	1.03E-02	4.15E-02
			1.24E-03	1.88E-02	5.08E-02
11	1	8.60E-03	-4.22	4.41	-1.87E-01
			9.43E-03	1.16E-02	4.39E-02
			1.38E-03	2.34E-02	3.85E-02
12	1	8.50E-03	-4.55	2.86	-1.87E-01
			9.40E-03	1.12E-02	4.37E-02
			1.49E-03	1.88E-02	2.85E-02

Table E.12: Detailed list of pressure pulse characteristics for Test #10 of Table 4.5

			Peaks		
Run	Transducer	t_0	#1	#2	#3
1	1	8.98E-03	-4.64	3.79	-1.36E-01
			9.60E-03	1.19E-02	4.04E-02
			9.92E-04	1.92E-02	3.22E-02
2	1	8.91E-03	-4.18	1.49	-1.98E-01
			9.60E-03	1.02E-02	4.44E-02
			1.06E-03	1.97E-02	5.03E-02
3	1	8.98E-03	-4.60	2.05	-1.99E-01
			9.54E-03	1.02E-02	5.58E-02
			9.92E-04	2.25E-02	4.46E-02

continued on next page

continued from previous page

			Peaks		
Run	Transducer	t_0	#1	#2	#3
4	1	8.98E-03	-5.27 9.59E-03 1.02E-03	1.76 1.02E-02 2.04E-02	-2.12E-01 5.02E-02 4.97E-02
5	1	8.94E-03	-4.71 9.60E-03 1.04E-03	1.71 1.02E-02 1.91E-02	-2.14E-01 4.66E-02 4.66E-02
6	1	8.37E-03	-8.46E-02 8.38E-03 3.04E-04	4.26 9.61E-03 1.97E-02	-1.31E-01 4.41E-02 2.50E-02
7	1	8.88E-03	-6.00 9.51E-03 1.09E-03	2.58 1.09E-02 1.90E-02	-6.06E-01 3.89E-02 4.72E-02
8	1	8.91E-03	-4.60 9.55E-03 1.06E-03	1.45 1.09E-02 1.94E-02	-2.39E-01 4.59E-02 5.32E-02
9	1	8.52E-03	-4.68 9.38E-03 1.42E-03	2.48 1.08E-02 2.37E-02	-1.37E-01 3.56E-02 1.99E-02
10	1	8.94E-03	-4.79 9.59E-03 1.04E-03	2.96 1.19E-02 1.94E-02	-2.45E-01 5.27E-02 5.26E-02
11	1	8.79E-03	-4.50 9.58E-03 1.18E-03	2.16 1.29E-02 1.88E-02	-1.42E-01 4.37E-02 3.93E-02
12	1	8.94E-03	-4.73 9.54E-03 1.00E-03	1.83 1.02E-02 2.27E-02	-2.29E-01 4.41E-02 4.49E-02

Table E.13: Detailed list of pressure pulse characteristics for Test #11 of Table 4.5

			Peaks		
Run	Transducer	t_0	#1	#2	#3
1	1	8.70E-03	-3.08 9.55E-03 1.27E-03	3.95 1.06E-02 2.03E-02	-6.08E-01 4.89E-02 5.72E-02
2	1	8.66E-03	-2.91 9.50E-03 1.32E-03	3.31 1.05E-02 1.89E-02	-6.59E-01 5.05E-02 5.86E-02
3	1	8.69E-03	-3.10 9.50E-03 1.30E-03	3.68 1.05E-02 2.11E-02	-6.36E-01 5.31E-02 5.86E-02
4	1	8.70E-03	-3.29 9.51E-03	3.68 1.05E-02	-6.98E-01 5.50E-02

continued on next page

continued from previous page

			Peaks		
Run	Transducer	t_0	#1	#2	#3
			1.28E-03	1.96E-02	5.75E-02
5	1	8.55E-03	-3.31	3.97	-4.03E-01
			9.60E-03	1.04E-02	5.01E-02
			1.43E-03	2.44E-02	5.47E-02
6	1	8.66E-03	-3.08	3.76	-7.71E-01
			9.49E-03	1.06E-02	5.33E-02
			1.32E-03	1.90E-02	5.80E-02
7	1	8.51E-03	-2.41	3.62	-8.80E-01
			9.56E-03	1.06E-02	5.13E-02
			1.46E-03	2.00E-02	5.96E-02
8	1	8.34E-03	-1.66E-01	3.27	-6.78E-01
			8.45E-03	9.52E-03	5.46E-02
			3.36E-04	2.24E-02	5.59E-02
9	1	8.65E-03	-2.95	3.61	-1.65E-02
			9.54E-03	1.05E-02	8.70E-02
			1.33E-03	7.70E-02	8.00E-06
10	1	8.62E-03	-3.28	3.16	-5.61E-01
			9.49E-03	1.05E-02	5.06E-02
			1.36E-03	2.12E-02	5.60E-02
11	1	8.74E-03	-2.89	3.26	-6.10E-01
			9.58E-03	1.05E-02	4.84E-02
			1.24E-03	1.88E-02	5.59E-02
12	1	8.38E-03	-3.23	3.87	-6.65E-01
			9.51E-03	1.05E-02	5.10E-02
			1.61E-03	2.05E-02	5.70E-02

Table E.14: Detailed list of pressure pulse characteristics for Test #12 of Table 4.5

			Peaks		
Run	Transducer	t_0	#1	#2	#3
1	1	8.79E-03	-3.63	3.40	-1.97E-01
			9.60E-03	1.04E-02	5.87E-02
			1.19E-03	2.64E-02	5.07E-02
2	1	8.70E-03	-3.42	1.98	-3.28E-01
			9.53E-03	1.04E-02	4.92E-02
			1.29E-03	2.03E-02	5.34E-02
3	1	8.75E-03	-3.26	2.89	-3.56E-01
			9.56E-03	1.04E-02	5.30E-02
			1.23E-03	2.26E-02	5.63E-02
4	1	8.70E-03	-4.01	2.68	-3.50E-01
			9.50E-03	1.04E-02	5.52E-02
			1.28E-03	2.01E-02	5.65E-02
			-4.01	2.81	-3.81E-01

continued on next page

continued from previous page

			Peaks		
Run	Transducer	t_0	#1	#2	#3
5	1	8.70E-03	9.48E-03	1.03E-02	5.21E-02
			1.28E-03	1.87E-02	5.82E-02
6	1	8.75E-03	-3.94	2.34	-3.75E-01
			9.55E-03	1.03E-02	4.82E-02
			1.23E-03	1.99E-02	5.43E-02
7	1	8.78E-03	-2.00	2.15	-1.27E-01
			9.49E-03	1.04E-02	4.68E-02
			1.20E-03	1.88E-02	5.32E-02
8	1	8.61E-03	-4.02	2.96	-3.36E-01
			9.45E-03	1.17E-02	4.81E-02
			1.38E-03	2.02E-02	5.24E-02
9	1	8.67E-03	-3.77	2.51	-3.29E-01
			9.53E-03	1.05E-02	4.43E-02
			1.31E-03	1.91E-02	5.08E-02
10	1	8.69E-03	-3.46	3.01	-2.41E-01
			9.54E-03	1.04E-02	4.62E-02
			1.30E-03	2.19E-02	5.26E-02
11	1	8.78E-03	-3.02	3.54	-2.08E-01
			9.57E-03	1.04E-02	5.73E-02
			1.20E-03	1.89E-02	4.99E-02
12	1	8.70E-03	-3.97	2.97	-3.13E-01
			9.54E-03	1.06E-02	5.53E-02
			1.29E-03	2.00E-02	5.41E-02

Table E.15: Detailed list of pressure pulse characteristics for Test #13 of Table 4.5

			Peaks		
Run	Transducer	t_0	#1	#2	#3
1	1	8.64E-03	-4.21	2.01	-2.29E-01
			9.46E-03	1.08E-02	4.66E-02
			1.33E-03	1.87E-02	3.52E-02
2	1	8.67E-03	-3.65	1.56	-2.73E-01
			9.48E-03	1.10E-02	4.23E-02
			1.27E-03	1.94E-02	4.40E-02
3	1	8.60E-03	-3.21	1.71	-2.11E-01
			9.46E-03	1.24E-02	4.06E-02
			1.36E-03	2.06E-02	4.90E-02
4	1	8.62E-03	-3.85	2.40	-2.39E-01
			9.36E-03	1.01E-02	4.21E-02
			1.24E-03	1.88E-02	4.87E-02
5	1	8.69E-03	-4.02	1.84	-2.26E-01
			9.53E-03	1.03E-02	4.12E-02
			1.29E-03	1.88E-02	4.41E-02

continued on next page

continued from previous page

			Peaks		
Run	Transducer	t_0	#1	#2	#3
6	1	8.80E-03	-4.00 9.62E-03 1.20E-03	1.62 1.02E-02 1.94E-02	-1.58E-01 3.90E-02 4.07E-02
7	1	8.74E-03	-4.61 9.54E-03 1.24E-03	2.97 1.52E-02 1.88E-02	-2.04E-01 4.16E-02 3.94E-02
8	1	8.80E-03	-3.78 9.56E-03 1.17E-03	4.85 1.12E-02 2.54E-02	-2.13E-01 4.72E-02 4.20E-02
9	1	8.84E-03	-3.68 9.58E-03 1.14E-03	1.61 1.02E-02 6.05E-02	-2.76E-02 7.05E-02 8.00E-06
10	1	8.76E-03	-3.45 9.49E-03 1.20E-03	1.85 1.11E-02 1.92E-02	-2.59E-01 4.08E-02 4.54E-02
11	1	8.86E-03	-2.30 9.55E-03 1.12E-03	2.87 1.30E-02 1.90E-02	-1.00E-01 4.10E-02 2.67E-02
12	1	8.71E-03	-3.99 9.50E-03 1.26E-03	2.11 1.10E-02 1.88E-02	-2.40E-01 3.98E-02 4.75E-02

Table E.16: Detailed list of pressure pulse characteristics for Test #14 of Table 4.5

			Peaks		
Run	Transducer	t_0	#1	#2	#3
1	1	8.82E-03	-3.85 9.58E-03 1.16E-03	3.28 1.04E-02 7.22E-02	-2.88E-02 8.22E-02 8.00E-06
2	1	8.71E-03	-3.23 9.62E-03 1.28E-03	3.33 1.04E-02 1.93E-02	-4.83E-01 5.02E-02 5.54E-02
3	1	8.69E-03	-3.07 9.57E-03 1.30E-03	2.65 1.03E-02 1.93E-02	-4.09E-01 3.92E-02 5.44E-02
4	1	8.74E-03	-3.34 9.58E-03 1.24E-03	3.04 1.04E-02 7.03E-02	-5.51E-02 8.03E-02 8.00E-06
5	1	8.80E-03	-3.26 9.57E-03 1.18E-03	3.34 1.04E-02 7.38E-02	-3.74E-02 8.38E-02 8.00E-06
6	1	8.80E-03	-3.44 9.62E-03	3.37 1.04E-02	-2.45E-02 8.22E-02

continued on next page

continued from previous page

			Peaks		
Run	Transducer	t_0	#1	#2	#3
			1.19E-03	7.22E-02	8.00E-06
7	1	8.80E-03	-4.00	3.97	-2.88E-02
			9.45E-03	1.03E-02	8.34E-02
			1.19E-03	7.34E-02	8.00E-06
8	1	8.81E-03	-4.00	3.53	-4.96E-01
			9.49E-03	1.07E-02	4.63E-02
			1.18E-03	1.89E-02	5.62E-02
9	1	1.00E-02	-1.51	3.95	-6.46E-01
			1.04E-02	1.21E-02	5.63E-02
			9.92E-04	2.36E-02	5.89E-02
10	1	8.85E-03	-4.02	3.64	-1.84E-02
			9.52E-03	1.04E-02	8.04E-02
			1.14E-03	7.04E-02	8.00E-06
11	1	8.78E-03	-3.86	3.96	-4.29E-02
			9.58E-03	1.04E-02	8.21E-02
			1.21E-03	7.21E-02	8.00E-06
12	1	8.73E-03	-4.02	3.95	-4.87E-01
			9.56E-03	1.03E-02	4.40E-02
			1.26E-03	1.88E-02	5.19E-02

Table E.17: Detailed list of pressure pulse characteristics for Test #15 of Table 4.5

			Peaks		
Run	Transducer	t_0	#1	#2	#3
1	1	8.84E-03	-6.01	6.01	-4.31E-01
			9.49E-03	1.05E-02	4.64E-02
			1.15E-03	1.89E-02	5.11E-02
2	1	8.72E-03	-6.04	5.71	-8.36E-02
			9.46E-03	1.13E-02	8.00E-02
			1.27E-03	7.00E-02	8.00E-06
3	1	8.78E-03	-4.84	4.72	-5.26E-01
			9.54E-03	1.04E-02	4.80E-02
			1.21E-03	1.89E-02	5.54E-02
4	1	8.77E-03	-5.73	4.49	-6.64E-01
			9.61E-03	1.03E-02	5.13E-02
			1.22E-03	1.88E-02	5.57E-02
5	1	8.82E-03	-6.00	4.92	-5.15E-02
			9.54E-03	1.08E-02	8.33E-02
			1.17E-03	7.33E-02	8.00E-06
6	1	8.72E-03	-5.99	4.79	-4.57E-01
			9.50E-03	1.03E-02	4.69E-02
			1.27E-03	1.90E-02	5.03E-02
			-5.26	5.20	-3.35E-01

continued on next page

continued from previous page

			Peaks		
Run	Transducer	t_0	#1	#2	#3
7	1	8.67E-03	9.58E-03	1.05E-02	4.97E-02
			1.31E-03	1.87E-02	5.52E-02
8	1	8.78E-03	-5.99	4.36	-8.82E-02
			9.50E-03	1.03E-02	7.97E-02
			1.21E-03	6.97E-02	8.00E-06
9	1	8.82E-03	-6.02	4.43	-6.80E-02
			9.50E-03	1.09E-02	8.09E-02
			1.18E-03	7.10E-02	8.00E-06
10	1	8.80E-03	-6.03	5.13	-7.81E-02
			9.50E-03	1.08E-02	7.97E-02
			1.18E-03	6.97E-02	8.00E-06
11	1	8.78E-03	-6.03	6.03	-3.58E-01
			9.46E-03	1.03E-02	3.95E-02
			1.21E-03	1.95E-02	4.72E-02
12	1	8.74E-03	-5.08	4.67	-4.84E-01
			9.59E-03	1.03E-02	4.37E-02
			1.24E-03	1.88E-02	5.47E-02

Table E.18: Detailed list of pressure pulse characteristics for Test #16 of Table 4.5

			Peaks		
Run	Transducer	t_0	#1	#2	#3
1	1	8.91E-03	-3.29	2.38	-3.39E-01
			9.61E-03	1.09E-02	4.10E-02
			1.07E-03	1.96E-02	5.00E-02
2	1	8.84E-03	-3.52	2.15	-2.42E-01
			9.53E-03	1.06E-02	3.94E-02
			1.14E-03	1.89E-02	4.77E-02
3	1	8.87E-03	-3.40	2.22	-3.10E-01
			9.53E-03	1.07E-02	4.00E-02
			1.10E-03	1.89E-02	4.79E-02
4	1	8.92E-03	-3.53	2.00	-2.93E-01
			9.52E-03	1.07E-02	4.15E-02
			1.06E-03	1.90E-02	4.89E-02
5	1	8.81E-03	-3.87	1.48	-2.16E-01
			9.46E-03	1.02E-02	3.93E-02
			1.14E-03	1.91E-02	4.30E-02
6	1	8.87E-03	-3.40	2.22	-3.10E-01
			9.53E-03	1.07E-02	4.00E-02
			1.10E-03	1.89E-02	4.79E-02
7	1	8.88E-03	-3.93	4.59	-2.74E-01
			9.58E-03	1.24E-02	4.68E-02
			1.10E-03	2.08E-02	4.50E-02

continued on next page

continued from previous page					
			Peaks		
Run	Transducer	t_0	#1	#2	#3
8	1	8.86E-03	-3.77 9.43E-03 1.10E-03	2.37 1.05E-02 1.95E-02	-3.49E-01 3.61E-02 4.73E-02
9	1	8.63E-03	-3.55 9.25E-03 1.33E-03	1.98 1.06E-02 1.88E-02	-2.23E-01 3.65E-02 4.25E-02
10	1	8.80E-03	-3.67 9.39E-03 1.18E-03	2.24 1.06E-02 1.90E-02	-2.92E-01 4.85E-02 4.77E-02
11	1	8.84E-03	-3.72 9.61E-03 1.14E-03	2.33 1.08E-02 1.90E-02	-3.92E-01 4.90E-02 5.23E-02
12	1	8.91E-03	-3.94 9.55E-03 1.06E-03	2.20 1.02E-02 1.91E-02	-2.88E-01 4.66E-02 4.83E-02

E.1.3 Attenuation of Radially- and Axially-Confined Shocks

In this subsection, characteristics of the pressure histories recorded for small-scale annular jet experiments conducted with radially- and axially-confined shocks (boundary condition # 3 in Table 4.5) are given. Referring to Table 4.5, the amplitudes, locations, and durations of the first five pressure pulses for test numbers 19 through 39 are presented in Tables E.20 through E.39, respectively. For each combination of test conditions, the experiment is repeated 24 times, except for test condition # 20 (see Table 4.5), where the input energy of 2.1 kJ was too low to produce a sufficiently strong shock to propagate through the liquid jet; 12 experiments are recorded with the transducer # 1, while the 12 others are recorded with the transducer # 2.

The pressure histories for small-scale annular jet experiments conducted with radially- and axially-confined shocks have the same general trend as that shown in Figure E.3. The time location t_0 corresponds to the initial time of the experiment, i.e. the time at which the oscilloscope detects a significant change in pressure and is triggered by the first channel. The amplitudes, time locations, and durations of the

first five pressure pulses (A_1 through A_5, t_1 through t_5, and D_1 through D_5, respectively) are noted in Figure E.3 and reported in a table for each combination of test conditions, as it is shown in Table E.19.

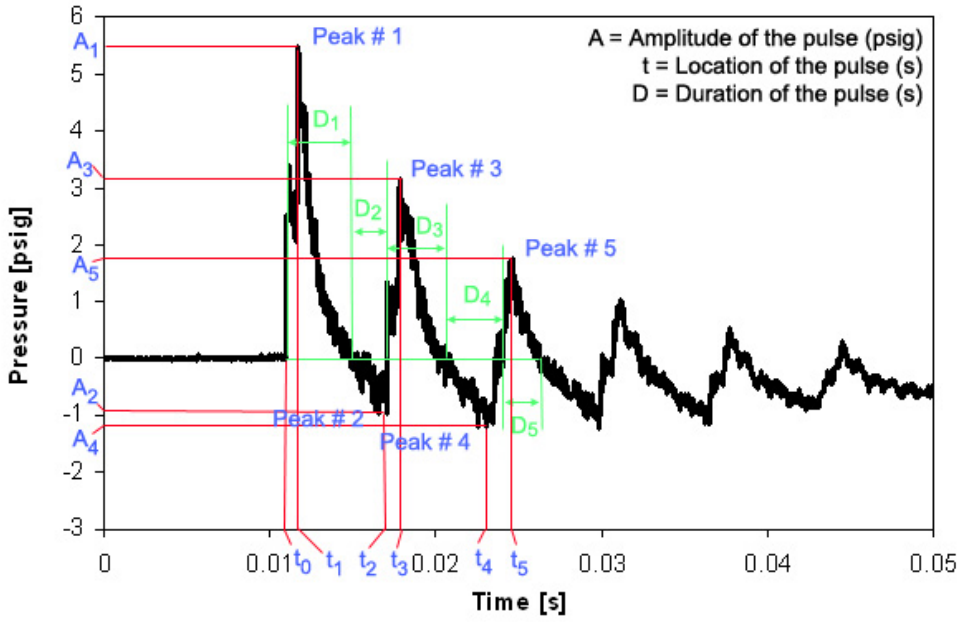

Figure E.3: Figure example for data related to small-scale annular jet experiments conducted with radially- and axially-confined shocks

Table E.19: Table example for data related to small-scale annular jet experiments conducted with radially- and axially-confined shocks

			Peaks				
Run	T.	t_0	#1	#2	#3	#4	#5
Test #	Transducer used	Initial time (s)	Amplitude of the pulse (psig) Location of the pulse (s) Duration of the pulse (s)				
Test	Transducer used	t_0	A_1 t_1 D_1	A_2 t_2 D_2	A_3 t_3 D_3	A_4 t_4 D_4	A_5 t_5 D_5

Table E.20: Detailed list of pressure pulse characteristics for Test #19 of Table 4.5

			Peaks				
Run	T.	t_0	#1	#2	#3	#4	#5
			1.98	-8.97E-01	1.51	-9.31E-01	8.97E-01
continued on next page							

continued from previous page

			Peaks				
Run	T.	t_0	#1	#2	#3	#4	#5
1	1	1.01E-02	1.05E-02	1.58E-02	1.62E-02	1.80E-02	2.22E-02
			1.66E-03	4.07E-03	1.40E-03	4.48E-03	1.54E-03
1	2	1.27E-02	2.58	-2.79E-01	5.61E-01	-1.64	6.08E-01
			1.31E-02	1.52E-02	1.70E-02	1.92E-02	2.31E-02
			2.43E-03	1.26E-03	2.38E-03	1.82E-03	4.25E-03
2	1	1.03E-02	2.78	-1.11	9.02E-01	-1.35	7.14E-01
			1.06E-02	1.41E-02	1.63E-02	1.82E-02	2.24E-02
			1.42E-03	4.31E-03	9.44E-04	5.05E-03	1.06E-03
2	2	1.29E-02	2.67	-4.20E-01	5.14E-01	-1.55	5.14E-01
			1.33E-02	1.53E-02	1.71E-02	1.92E-02	2.11E-02
			2.14E-03	1.54E-03	2.38E-03	1.74E-03	2.94E-03
3	1	1.02E-02	2.17	-1.75	1.28	-1.07	9.03E-01
			1.05E-02	1.58E-02	1.62E-02	1.79E-02	2.22E-02
			1.66E-03	4.06E-03	1.17E-03	4.85E-03	1.14E-03
3	2	1.26E-02	2.59	-4.57E-01	1.65	-5.97E-01	1.04
			1.31E-02	1.70E-02	1.91E-02	2.12E-02	2.51E-02
			2.18E-03	4.04E-03	1.74E-03	4.31E-03	1.26E-03
4	1	1.03E-02	1.92	-9.33E-01	1.59	-9.42E-01	1.12
			1.07E-02	1.59E-02	1.63E-02	1.84E-02	2.26E-02
			1.82E-03	3.91E-03	1.29E-03	4.71E-03	1.44E-03
4	2	1.27E-02	2.63	-5.07E-01	2.26E-01	-3.67E-01	1.56
			1.33E-02	1.71E-02	1.77E-02	1.87E-02	1.92E-02
			3.70E-03	1.26E-03	7.60E-04	5.04E-04	1.79E-03
5	1	1.03E-02	2.38	-1.14	1.21	-1.09	9.26E-01
			1.06E-02	1.41E-02	1.65E-02	1.82E-02	2.23E-02
			1.82E-03	3.93E-03	1.09E-03	4.80E-03	1.22E-03
5	2	1.28E-02	2.40	-3.20E-01	4.14E-01	-1.51	5.07E-01
			1.32E-02	1.52E-02	1.71E-02	1.93E-02	2.13E-02
			2.15E-03	1.58E-03	2.36E-03	1.74E-03	4.34E-03
6	1	1.03E-02	1.94	-8.24E-01	1.43	-8.70E-01	1.00
			1.07E-02	1.47E-02	1.64E-02	2.01E-02	2.25E-02
			1.68E-03	4.04E-03	1.34E-03	4.73E-03	1.40E-03
6	2	1.29E-02	2.87	-2.28E-01	6.03E-01	-1.65	6.50E-01
			1.34E-02	1.58E-02	1.89E-02	1.93E-02	2.32E-02
			2.74E-03	8.16E-04	2.52E-03	1.97E-03	4.18E-03
7	1	1.00E-02	2.26	-1.16	1.05	-1.25	7.18E-01
			1.02E-02	1.48E-02	1.63E-02	1.80E-02	2.22E-02
			1.48E-03	4.30E-03	9.28E-04	5.25E-03	7.60E-04
7	2	1.25E-02	2.47	-4.81E-01	1.53	-5.28E-01	9.72E-01
			1.31E-02	1.69E-02	1.90E-02	2.11E-02	2.51E-02
			2.74E-03	3.42E-03	1.76E-03	4.31E-03	1.25E-03
8	1	1.01E-02	2.35	-1.02	1.13	-1.21	7.10E-01
			1.04E-02	1.52E-02	1.62E-02	1.80E-02	2.21E-02

continued on next page

continued from previous page							
			Peaks				
Run	T.	t_0	#1	#2	#3	#4	#5
			2.22E-03	3.63E-03	1.03E-03	5.01E-03	9.84E-04
8	2	1.26E-02	2.51	-3.51E-01	4.92E-01	-1.48	5.39E-01
			1.31E-02	1.54E-02	1.69E-02	1.91E-02	2.11E-02
			2.24E-03	1.42E-03	2.54E-03	1.76E-03	4.32E-03
9	1	1.00E-02	2.48	-1.08	1.07	-1.22	8.39E-01
			1.04E-02	1.25E-02	1.61E-02	1.79E-02	2.21E-02
			2.20E-03	3.58E-03	9.60E-04	5.07E-03	9.68E-04
9	2	1.25E-02	2.73	-2.68E-01	5.50E-01	-1.75	5.97E-01
			1.31E-02	1.62E-02	1.85E-02	1.91E-02	2.30E-02
			3.28E-03	5.20E-04	2.34E-03	1.74E-03	3.80E-03
10	1	8.96E-03	2.44	-6.97E-01	8.37E-01	-1.37	9.31E-01
			9.26E-03	1.12E-02	1.39E-02	1.50E-02	1.67E-02
			1.84E-03	7.52E-04	2.98E-03	1.49E-03	4.51E-03
10	2	1.13E-02	2.55	-3.56E-01	5.43E-01	-1.57	5.43E-01
			1.19E-02	1.40E-02	1.58E-02	1.79E-02	2.00E-02
			2.24E-03	1.38E-03	2.62E-03	1.78E-03	4.26E-03
11	1	1.01E-02	1.94	-1.61	1.57	-1.01	1.10
			1.05E-02	1.58E-02	1.62E-02	1.80E-02	2.22E-02
			2.23E-03	3.50E-03	1.50E-03	4.52E-03	1.55E-03
11	2	1.26E-02	3.07	-5.82E-01	1.95	-7.22E-01	1.20
			1.33E-02	1.69E-02	1.91E-02	2.30E-02	2.53E-02
			2.54E-03	3.61E-03	1.91E-03	4.20E-03	1.60E-03
12	1	1.01E-02	2.29	-9.88E-01	1.36	-1.17	1.07
			1.04E-02	1.41E-02	1.61E-02	2.17E-02	2.22E-02
			1.81E-03	3.92E-03	1.14E-03	4.78E-03	1.22E-03
12	2	1.26E-02	2.60	-4.45E-01	3.51E-01	-1.52	5.85E-01
			1.31E-02	1.69E-02	1.85E-02	1.90E-02	2.13E-02
			3.10E-03	2.42E-03	6.16E-04	1.86E-03	3.66E-03

Table E.21: Detailed list of pressure pulse characteristics for Test #21 of Table 4.5

			Peaks				
Run	T.	t_0	#1	#2	#3	#4	#5
1	1	8.34E-03	5.36	-1.86	3.25	-1.86	1.61
			8.69E-03	1.25E-02	1.46E-02	1.89E-02	2.12E-02
			2.05E-03	3.94E-03	1.66E-03	4.66E-03	1.89E-03
1	2	1.09E-02	5.92	-1.26	2.87	-1.40	1.56
			1.17E-02	1.69E-02	1.80E-02	2.33E-02	2.46E-02
			4.29E-03	1.93E-03	2.86E-03	4.12E-03	1.62E-03
2	1	8.15E-03	4.42	-1.79	4.56	-1.53	2.45
			8.62E-03	1.41E-02	1.43E-02	2.02E-02	2.06E-02
			2.38E-03	3.65E-03	2.54E-03	3.70E-03	2.77E-03
			6.01	-8.34E-01	1.21	-3.43	1.44
continued on next page							

continued from previous page

			Peaks				
Run	T.	t_0	#1	#2	#3	#4	#5
2	2	1.08E-02	1.16E-02	1.53E-02	1.68E-02	1.78E-02	2.32E-02
			4.04E-03	8.88E-04	1.15E-03	3.36E-03	3.65E-03
3	1	8.34E-03	5.96	-1.77	3.43	-1.63	2.21
			8.64E-03	1.36E-02	1.46E-02	2.00E-02	2.08E-02
			2.75E-03	3.16E-03	2.34E-03	4.04E-03	2.45E-03
3	2	1.09E-02	5.68	-1.30	3.01	-5.05E-01	1.58
			1.18E-02	1.69E-02	1.79E-02	2.04E-02	2.33E-02
			4.90E-03	1.25E-03	2.96E-03	6.24E-04	3.45E-03
4	1	7.82E-03	5.11	-1.60	3.14	-1.60	1.83
			8.26E-03	1.32E-02	1.41E-02	1.95E-02	2.06E-02
			2.37E-03	3.62E-03	2.36E-03	3.93E-03	2.33E-03
4	2	1.05E-02	5.82	-1.26	3.38	-1.50	1.64
			1.13E-02	1.65E-02	1.73E-02	2.26E-02	2.40E-02
			3.95E-03	2.13E-03	3.06E-03	3.98E-03	1.80E-03
5	1	7.80E-03	4.68	-1.41	3.27	-1.60	2.15
			8.21E-03	1.32E-02	1.43E-02	1.94E-02	2.06E-02
			2.58E-03	3.21E-03	2.73E-03	3.66E-03	3.09E-03
5	2	1.04E-02	5.98	-1.52	3.36	-1.70	1.86
			1.12E-02	1.64E-02	1.72E-02	2.28E-02	2.40E-02
			4.65E-03	1.41E-03	3.56E-03	3.47E-03	1.98E-03
6	1	8.17E-03	5.08	-1.57	3.82	-1.67	1.75
			8.49E-03	1.40E-02	1.45E-02	1.98E-02	2.06E-02
			2.85E-03	3.11E-03	2.06E-03	4.21E-03	2.23E-03
6	2	1.08E-02	5.88	-7.28E-01	1.15	-3.68	1.57
			1.15E-02	1.53E-02	1.68E-02	1.75E-02	2.30E-02
			4.08E-03	8.72E-04	1.16E-03	2.91E-03	4.10E-03
7	1	8.30E-03	4.82	-2.40	2.81	-2.02	1.64
			9.06E-03	1.36E-02	1.46E-02	2.03E-02	2.14E-02
			1.85E-03	4.19E-03	1.63E-03	4.66E-03	2.27E-03
7	2	1.10E-02	6.01	-1.16	3.48	-1.58	1.61
			1.17E-02	1.69E-02	1.79E-02	2.30E-02	2.45E-02
			3.94E-03	2.13E-03	3.14E-03	3.74E-03	2.02E-03
8	1	8.06E-03	5.58	-2.01	3.05	-2.20	1.50
			8.51E-03	1.35E-02	1.43E-02	1.98E-02	2.13E-02
			2.51E-03	3.43E-03	2.09E-03	4.14E-03	2.06E-03
8	2	1.07E-02	6.01	-1.39	3.34	-1.77	1.37
			1.13E-02	1.66E-02	1.76E-02	2.27E-02	2.41E-02
			4.64E-03	1.42E-03	2.87E-03	4.02E-03	2.04E-03
9	1	8.33E-03	4.75	-1.66	3.30	-1.58	1.99
			8.74E-03	1.42E-02	1.46E-02	2.02E-02	2.09E-02
			2.81E-03	3.21E-03	2.50E-03	3.84E-03	2.31E-03
9	2	1.09E-02	6.03	-1.29	2.79	-1.43	1.39
			1.18E-02	1.66E-02	1.81E-02	2.35E-02	2.42E-02

continued on next page

continued from previous page							
			Peaks				
Run	T.	t_0	#1	#2	#3	#4	#5
			3.90E-03	2.45E-03	2.64E-03	4.31E-03	1.60E-03
10	1	8.13E-03	4.56 8.54E-03 3.01E-03	-2.31 1.40E-02 3.00E-03	3.39 1.44E-02 2.51E-03	-1.58 2.02E-02 3.63E-03	1.84 2.07E-02 2.53E-03
10	2	1.08E-02	5.99 1.15E-02 3.66E-03	-1.09 1.62E-02 2.49E-03	2.70 1.76E-02 2.94E-03	-1.28 2.26E-02 4.14E-03	1.34 2.44E-02 1.62E-03
11	1	8.42E-03	5.44 8.64E-03 2.90E-03	-1.92 1.27E-02 3.03E-03	3.94 1.47E-02 2.76E-03	-1.50 2.01E-02 3.46E-03	2.02 2.12E-02 3.37E-03
11	2	1.10E-02	5.51 1.17E-02 4.91E-03	-9.60E-01 1.66E-02 1.19E-03	3.16 1.79E-02 3.77E-03	-1.19 2.26E-02 3.22E-03	1.76 2.46E-02 2.65E-03
12	1	8.17E-03	4.74 8.55E-03 2.82E-03	-1.79 1.40E-02 3.09E-03	4.65 1.44E-02 2.76E-03	-1.54 2.00E-02 3.54E-03	2.16 2.06E-02 2.76E-03
12	2	1.08E-02	6.03 1.15E-02 4.02E-03	-1.14 1.64E-02 2.07E-03	2.99 1.77E-02 2.87E-03	-1.61 2.32E-02 4.16E-03	1.58 2.44E-02 1.63E-03

Table E.22: Detailed list of pressure pulse characteristics for Test #22 of Table 4.5

			Peaks				
Run	T.	t_0	#1	#2	#3	#4	#5
1	1	8.30E-03	5.16 9.21E-03 1.59E-03	-1.12 1.10E-02 4.43E-03	1.64 1.49E-02 2.45E-03	-1.03 1.81E-02 4.26E-03	4.24E-01 2.25E-02 2.31E-03
1	2	1.07E-02	3.72 1.18E-02 2.82E-03	-1.25 1.43E-02 3.92E-03	7.67E-01 1.85E-02 2.49E-03	-7.80E-01 2.13E-02 6.14E-03	5.93E-01 2.88E-02 5.54E-03
2	1	7.78E-03	6.03 8.61E-03 2.50E-03	-1.19 1.18E-02 3.64E-03	1.57 1.47E-02 2.31E-03	-1.00 1.76E-02 4.63E-03	4.02E-01 2.14E-02 1.98E-03
2	2	1.02E-02	3.95 1.12E-02 2.82E-03	-1.16 1.48E-02 4.00E-03	5.79E-01 1.78E-02 2.38E-03	-8.27E-01 2.10E-02 6.17E-03	5.93E-01 2.78E-02 6.40E-03
3	1	8.26E-03	4.51 8.93E-03 1.99E-03	-1.21 1.19E-02 3.82E-03	1.89 1.47E-02 2.72E-03	-8.33E-01 1.78E-02 3.50E-03	5.27E-01 2.20E-02 2.92E-03
3	2	1.07E-02	3.59 1.17E-02 2.50E-03	-9.57E-01 1.46E-02 3.45E-03	8.24E-01 1.83E-02 3.16E-03	-5.82E-01 2.11E-02 4.02E-03	2.62E-01 2.49E-02 2.39E-03
			4.74	-1.08	1.03	-1.31	1.08
continued on next page							

continued from previous page

			Peaks				
Run	T.	t_0	#1	#2	#3	#4	#5
4	1	8.28E-03	9.11E-03	1.19E-02	1.37E-02	1.47E-02	1.79E-02
			2.05E-03	1.70E-03	2.21E-03	2.22E-03	4.68E-03
4	2	1.07E-02	3.75	-9.42E-01	6.99E-01	-8.01E-01	6.14E-01
			1.16E-02	1.46E-02	1.84E-02	2.13E-02	2.80E-02
			2.63E-03	3.96E-03	2.38E-03	5.81E-03	1.24E-02
5	1	8.39E-03	4.74	-1.68	1.27	-1.40	2.87E-01
			9.26E-03	1.14E-02	1.52E-02	1.82E-02	2.18E-02
			1.58E-03	4.53E-03	1.98E-03	4.91E-03	1.54E-03
5	2	1.08E-02	3.90	-1.07	7.56E-01	-7.90E-01	1.47E-01
			1.17E-02	1.47E-02	1.83E-02	2.16E-02	2.52E-02
			2.78E-03	3.78E-03	2.61E-03	4.85E-03	1.11E-03
6	1	8.41E-03	4.81	-1.43	1.53	-1.15	3.08E-01
			9.33E-03	1.12E-02	1.53E-02	1.84E-02	2.20E-02
			1.58E-03	4.47E-03	2.18E-03	4.54E-03	2.03E-03
6	2	1.09E-02	4.08	-1.17	7.00E-01	-7.53E-01	4.72E-01
			1.18E-02	1.54E-02	1.83E-02	2.14E-02	2.78E-02
			2.45E-03	4.07E-03	2.41E-03	5.95E-03	1.36E-02
7	1	8.38E-03	4.84	-1.26	1.60	-1.07	3.84E-01
			9.30E-03	1.08E-02	1.53E-02	1.82E-02	2.18E-02
			2.06E-03	3.90E-03	2.27E-03	4.53E-03	1.95E-03
7	2	1.08E-02	4.16	-9.99E-01	7.82E-01	-7.18E-01	1.26E-01
			1.18E-02	1.49E-02	1.86E-02	2.14E-02	2.51E-02
			2.54E-03	3.98E-03	2.42E-03	5.20E-03	8.64E-04
8	1	8.43E-03	4.65	-1.40	1.74	-9.77E-01	4.29E-01
			8.95E-03	1.07E-02	1.54E-02	1.86E-02	2.18E-02
			2.06E-03	3.90E-03	2.38E-03	3.81E-03	2.74E-03
8	2	1.01E-02	3.85	-1.16	7.14E-01	-8.33E-01	1.52E-01
			1.14E-02	1.45E-02	1.77E-02	2.11E-02	2.45E-02
			2.83E-03	3.82E-03	2.54E-03	5.06E-03	1.08E-03
9	1	8.02E-03	4.17	-8.48E-01	1.50	-4.73E-01	1.92
			8.86E-03	1.05E-02	1.16E-02	1.35E-02	1.50E-02
			1.96E-03	1.09E-03	1.39E-03	1.56E-03	2.27E-03
9	2	1.07E-02	4.74	-1.21	6.18E-01	-8.82E-01	6.48E-01
			1.17E-02	1.55E-02	1.85E-02	2.18E-02	2.83E-02
			2.80E-03	3.94E-03	2.27E-03	6.23E-03	5.50E-03
10	1	8.24E-03	5.82	-1.21	1.74	-1.07	2.88E-01
			9.15E-03	1.11E-02	1.52E-02	1.82E-02	2.24E-02
			2.06E-03	4.10E-03	2.24E-03	4.80E-03	1.61E-03
10	2	1.06E-02	4.14	-1.06	5.35E-01	-7.78E-01	1.21E-01
			1.17E-02	1.44E-02	1.83E-02	2.11E-02	2.47E-02
			2.73E-03	4.10E-03	2.38E-03	4.82E-03	1.15E-03
11	1	7.18E-03	4.98	-1.26	1.46	-1.17	2.88E-01
			8.01E-03	1.08E-02	1.44E-02	1.70E-02	2.04E-02

continued on next page

continued from previous page							
			Peaks				
Run	T.	t_0	#1	#2	#3	#4	#5
			2.81E-03	3.27E-03	2.22E-03	4.58E-03	1.77E-03
11	2	9.62E-03	3.99	-1.16	8.07E-01	-7.87E-01	5.52E-01
			1.04E-02	1.41E-02	1.74E-02	2.02E-02	2.67E-02
			2.72E-03	4.30E-03	1.90E-03	5.87E-03	6.17E-03
12	1	8.36E-03	4.51	-1.40	1.65	-1.21	4.31E-01
			9.28E-03	1.18E-02	1.52E-02	1.80E-02	2.19E-02
			1.98E-03	4.15E-03	2.09E-03	4.78E-03	1.68E-03
12	2	1.08E-02	4.71	-1.20	7.70E-01	-8.24E-01	5.89E-01
			1.18E-02	1.47E-02	1.87E-02	2.15E-02	2.77E-02
			2.49E-03	4.21E-03	2.41E-03	6.18E-03	6.32E-03

Table E.23: Detailed list of pressure pulse characteristics for Test #23 of Table 4.5

			Peaks				
Run	T.	t_0	#1	#2	#3	#4	#5
1	1	8.60E-03	4.26	-1.08	1.92	-8.48E-01	5.58E-01
			8.90E-03	1.10E-02	1.51E-02	1.75E-02	2.20E-02
			1.34E-03	4.60E-03	1.96E-03	4.12E-03	2.33E-03
1	2	1.12E-02	2.93	-9.15E-01	7.72E-01	-6.81E-01	2.56E-01
			1.20E-02	1.42E-02	1.84E-02	2.07E-02	2.48E-02
			2.03E-03	3.69E-03	2.85E-03	3.97E-03	2.27E-03
2	1	8.49E-03	5.29	-8.97E-01	1.73	-8.03E-01	5.09E-01
			9.08E-03	1.09E-02	1.52E-02	1.79E-02	2.16E-02
			1.48E-03	4.38E-03	2.19E-03	4.44E-03	2.00E-03
2	2	1.10E-02	3.85	-1.07	8.50E-01	-6.97E-01	2.41E-01
			1.18E-02	1.55E-02	1.83E-02	2.12E-02	2.50E-02
			2.30E-03	4.08E-03	2.35E-03	4.59E-03	1.65E-03
3	1	8.38E-03	4.45	-1.08	1.64	-9.38E-01	5.62E-01
			9.06E-03	1.10E-02	1.52E-02	1.77E-02	2.17E-02
			1.60E-03	4.42E-03	2.01E-03	4.27E-03	2.06E-03
3	2	1.11E-02	3.38	-9.34E-01	8.94E-01	-7.93E-01	2.38E-01
			1.16E-02	1.41E-02	1.83E-02	2.06E-02	2.48E-02
			2.32E-03	3.73E-03	2.49E-03	4.51E-03	1.66E-03
4	1	8.31E-03	4.04	-1.49	1.70	-1.02	5.74E-01
			9.30E-03	1.04E-02	1.49E-02	1.76E-02	2.16E-02
			1.68E-03	4.27E-03	2.10E-03	3.71E-03	2.82E-03
4	2	1.09E-02	3.56	-1.22	1.03	-7.50E-01	2.81E-01
			1.16E-02	1.37E-02	1.82E-02	2.07E-02	2.46E-02
			2.15E-03	3.88E-03	2.62E-03	3.82E-03	2.54E-03
5	1	8.38E-03	3.99	-1.12	1.50	-1.08	4.24E-01
			8.89E-03	1.11E-02	1.53E-02	1.73E-02	2.17E-02
			1.56E-03	4.58E-03	1.71E-03	4.70E-03	1.83E-03
continued on next page							

continued from previous page

			Peaks				
Run	T.	t_0	#1	#2	#3	#4	#5
5	2	1.10E-02	3.81	-7.82E-01	8.58E-01	-6.88E-01	2.49E-01
			1.18E-02	1.39E-02	1.85E-02	2.06E-02	2.50E-02
			2.30E-03	3.79E-03	2.52E-03	4.54E-03	1.72E-03
6	1	8.11E-03	4.46	-1.35	1.60	-9.29E-01	3.83E-01
			8.76E-03	1.20E-02	1.49E-02	1.83E-02	2.16E-02
			1.87E-03	4.11E-03	2.18E-03	4.70E-03	1.78E-03
6	2	1.07E-02	4.99	-1.10	8.64E-01	-7.30E-01	5.89E-01
			1.14E-02	1.53E-02	1.83E-02	2.15E-02	2.75E-02
			2.35E-03	3.96E-03	2.42E-03	5.83E-03	6.60E-03
7	1	8.14E-03	3.89	-1.03	1.64	-9.84E-01	3.75E-01
			8.46E-03	1.07E-02	1.48E-02	1.86E-02	2.15E-02
			1.78E-03	4.17E-03	2.44E-03	4.28E-03	1.62E-03
7	2	1.08E-02	6.00	-1.26	4.73E-01	-9.80E-01	8.92E-02
			1.14E-02	1.40E-02	1.80E-02	2.08E-02	3.88E-02
			2.90E-03	3.83E-03	1.46E-03	1.84E-02	1.65E-03
8	1	8.53E-03	3.74	-8.54E-01	1.44	-9.48E-01	4.59E-01
			8.89E-03	1.09E-02	1.51E-02	1.75E-02	2.15E-02
			1.44E-03	4.43E-03	1.83E-03	4.66E-03	1.77E-03
8	2	1.11E-02	3.90	-8.80E-01	8.55E-01	-7.86E-01	1.99E-01
			1.19E-02	1.43E-02	1.83E-02	2.10E-02	2.47E-02
			2.24E-03	3.56E-03	2.58E-03	4.60E-03	1.49E-03
9	1	8.46E-03	4.69	-1.59	1.18	-9.31E-01	3.81E-01
			8.84E-03	1.09E-02	1.52E-02	1.75E-02	2.17E-02
			1.50E-03	4.38E-03	1.94E-03	4.72E-03	1.89E-03
9	2	1.10E-02	3.86	-9.16E-01	8.65E-01	-7.29E-01	1.62E-01
			1.18E-02	1.52E-02	1.83E-02	2.11E-02	2.49E-02
			2.48E-03	3.67E-03	2.61E-03	4.72E-03	1.26E-03
10	1	7.76E-03	6.01	-1.49	1.46	-1.02	4.28E-01
			8.21E-03	1.12E-02	1.43E-02	1.74E-02	2.13E-02
			2.22E-03	3.82E-03	1.94E-03	4.58E-03	1.84E-03
10	2	1.04E-02	4.67	-9.57E-01	8.24E-01	-8.63E-01	1.21E-01
			1.11E-02	1.41E-02	1.76E-02	2.08E-02	2.41E-02
			2.21E-03	4.03E-03	2.38E-03	4.94E-03	8.32E-04
11	1	8.40E-03	4.51	-1.35	1.74	-9.78E-01	5.22E-01
			8.72E-03	1.12E-02	1.51E-02	1.89E-02	2.16E-02
			1.57E-03	4.28E-03	2.38E-03	4.26E-03	2.02E-03
11	2	1.08E-02	4.37	-1.11	9.01E-01	-8.34E-01	1.98E-01
			1.19E-02	1.49E-02	1.83E-02	2.15E-02	2.50E-02
			2.79E-03	3.77E-03	2.26E-03	4.96E-03	1.06E-03
12	1	8.26E-03	4.28	-8.32E-01	1.75	-7.38E-01	4.34E-01
			8.60E-03	1.29E-02	1.47E-02	1.76E-02	2.14E-02
			1.68E-03	4.12E-03	2.10E-03	4.58E-03	1.75E-03
			4.27	-8.85E-01	8.02E-01	-6.98E-01	9.93E-02

continued on next page

continued from previous page							
			Peaks				
Run	T.	t_0	#1	#2	#3	#4	#5
12	2	1.08E-02	1.15E-02	1.39E-02	1.81E-02	2.07E-02	2.47E-02
			2.45E-03	3.91E-03	2.20E-03	5.21E-03	7.52E-04

Table E.24: Detailed list of pressure pulse characteristics for Test #24 of Table 4.5

			Peaks				
Run	T.	t_0	#1	#2	#3	#4	#5
1	1	8.30E-03	4.69	-1.03	1.73	-8.46E-01	4.20E-01
			8.97E-03	1.08E-02	1.48E-02	1.71E-02	2.16E-02
			1.59E-03	4.24E-03	2.14E-03	4.58E-03	1.74E-03
1	2	1.08E-02	3.31	-9.09E-01	7.78E-01	-6.28E-01	1.69E-01
			1.14E-02	1.37E-02	1.82E-02	2.10E-02	2.48E-02
			2.12E-03	4.35E-03	2.18E-03	4.74E-03	1.46E-03
2	1	8.54E-03	4.97	-9.35E-01	1.78	-8.41E-01	5.65E-01
			8.97E-03	1.19E-02	1.52E-02	1.82E-02	2.18E-02
			1.43E-03	4.46E-03	2.12E-03	4.38E-03	2.16E-03
2	2	1.11E-02	4.13	-8.86E-01	8.95E-01	-7.45E-01	2.39E-01
			1.17E-02	1.43E-02	1.85E-02	2.09E-02	2.54E-02
			2.24E-03	4.25E-03	2.21E-03	4.46E-03	1.74E-03
3	1	8.02E-03	4.60	-5.63	1.12	-1.50	9.36E-01
			8.54E-03	1.09E-02	1.26E-02	1.45E-02	1.85E-02
			1.91E-03	1.50E-03	2.49E-03	2.26E-03	4.73E-03
3	2	1.05E-02	4.02	-9.47E-01	8.35E-01	-6.65E-01	4.78E-01
			1.13E-02	1.50E-02	1.80E-02	2.14E-02	2.72E-02
			2.54E-03	4.14E-03	2.18E-03	5.91E-03	6.35E-03
4	1	7.15E-03	6.00	-1.22	1.55	-1.26	4.70E-01
			9.22E-03	1.15E-02	1.36E-02	1.62E-02	2.04E-02
			2.81E-03	3.02E-03	1.91E-03	4.63E-03	1.79E-03
4	2	9.67E-03	4.05	-1.06	9.58E-01	-7.77E-01	3.01E-01
			1.05E-02	1.35E-02	1.69E-02	1.95E-02	2.37E-02
			2.13E-03	3.89E-03	2.47E-03	4.36E-03	1.94E-03
5	1	7.97E-03	5.23	-8.66E-01	1.76	-8.66E-01	4.47E-01
			9.26E-03	1.14E-02	1.45E-02	1.81E-02	2.14E-02
			1.99E-03	3.94E-03	2.30E-03	4.39E-03	1.91E-03
5	2	1.05E-02	4.21	-1.13	7.44E-01	-7.56E-01	5.69E-01
			1.12E-02	1.50E-02	1.77E-02	2.04E-02	2.75E-02
			2.43E-03	4.06E-03	2.14E-03	6.06E-03	6.40E-03
6	1	7.98E-03	5.12	-1.46	1.12	-1.13	9.29E-01
			8.48E-03	1.10E-02	1.25E-02	1.46E-02	1.77E-02
			1.83E-03	1.65E-03	2.54E-03	2.14E-03	4.78E-03
6	2	1.05E-02	3.61	-9.35E-01	7.53E-01	-7.00E-01	5.13E-01
			1.14E-02	1.50E-02	1.79E-02	2.08E-02	2.72E-02
continued on next page							

continued from previous page

			Peaks				
Run	T.	t_0	#1	#2	#3	#4	#5
			2.63E-03	3.90E-03	2.41E-03	5.83E-03	6.52E-03
			5.17	-9.22E-01	5.00E-01	-8.75E-01	1.66
7	1	8.50E-03	8.99E-03	1.09E-02	1.13E-02	1.30E-02	1.49E-02
			1.49E-03	1.18E-03	6.24E-04	2.58E-03	2.02E-03
			4.18	-1.12	9.92E-01	-7.90E-01	2.89E-01
7	2	1.11E-02	1.18E-02	1.54E-02	1.83E-02	2.08E-02	2.50E-02
			2.15E-03	3.52E-03	2.83E-03	4.06E-03	2.17E-03
			4.22	-9.90E-01	1.69	-9.32E-01	4.74E-01
8	1	7.73E-03	8.24E-03	1.36E-02	1.46E-02	1.69E-02	2.09E-02
			2.25E-03	3.75E-03	2.04E-03	4.45E-03	1.93E-03
			4.23	-9.76E-01	8.99E-01	-7.89E-01	1.49E-01
8	2	1.03E-02	1.10E-02	1.47E-02	1.76E-02	2.05E-02	2.44E-02
			2.46E-03	3.62E-03	2.57E-03	4.90E-03	1.10E-03
			5.34	-1.08	1.64	-9.40E-01	4.66E-01
9	1	8.42E-03	8.83E-03	1.14E-02	1.53E-02	1.82E-02	2.15E-02
			1.77E-03	4.12E-03	2.26E-03	4.40E-03	1.93E-03
			4.08	-1.03	8.00E-01	-8.41E-01	1.43E-01
9	2	1.10E-02	1.18E-02	1.54E-02	1.83E-02	2.16E-02	2.51E-02
			2.54E-03	3.74E-03	2.35E-03	4.92E-03	1.26E-03
			5.17	-7.88E-01	1.65	-7.41E-01	1.84
10	1	8.49E-03	8.93E-03	1.01E-02	1.13E-02	1.27E-02	1.50E-02
			1.53E-03	6.96E-04	1.19E-03	2.49E-03	2.00E-03
			3.76	-1.12	9.00E-01	-7.88E-01	3.37E-01
10	2	1.10E-02	1.17E-02	1.40E-02	1.83E-02	2.10E-02	2.51E-02
			2.22E-03	3.63E-03	2.69E-03	4.17E-03	2.24E-03
			4.46	-1.12	1.55	-9.30E-01	5.70E-01
11	1	8.06E-03	8.55E-03	1.21E-02	1.47E-02	1.73E-02	2.12E-02
			1.90E-03	3.98E-03	2.18E-03	4.29E-03	2.20E-03
			6.02	-9.60E-01	9.15E-01	-8.66E-01	2.59E-01
11	2	1.06E-02	1.12E-02	1.51E-02	1.80E-02	2.11E-02	2.45E-02
			2.48E-03	3.90E-03	2.30E-03	4.65E-03	1.37E-03
			4.10	-5.87E-01	1.34	-1.43	1.01
12	1	7.88E-03	8.30E-03	1.03E-02	1.16E-02	1.48E-02	1.75E-02
			2.00E-03	9.68E-04	3.06E-03	2.21E-03	4.54E-03
			3.78	-1.09	8.31E-01	-7.63E-01	1.75E-01
12	2	1.05E-02	1.13E-02	1.49E-02	1.82E-02	2.10E-02	2.46E-02
			2.58E-03	3.95E-03	2.36E-03	4.91E-03	1.15E-03

Table E.25: Detailed list of pressure pulse characteristics for Test #25 of Table 4.5

			Peaks				
Run	T.	t_0	#1	#2	#3	#4	#5
			5.19	-1.28	1.63	-9.49E-01	4.10E-01
1	1	7.86E-03	8.83E-03	1.10E-02	1.44E-02	1.84E-02	2.13E-02

continued on next page

continued from previous page

			Peaks				
Run	T.	t_0	#1	#2	#3	#4	#5
			2.10E-03	3.81E-03	2.16E-03	4.60E-03	1.90E-03
1	2	1.04E-02	4.23	-1.02	8.50E-01	-7.90E-01	1.94E-01
			1.11E-02	1.48E-02	1.78E-02	2.08E-02	2.48E-02
			2.42E-03	4.06E-03	2.45E-03	4.76E-03	1.42E-03
2	1	8.30E-03	4.04	-1.21	1.42	-1.07	3.84E-01
			8.80E-03	1.22E-02	1.49E-02	1.87E-02	2.15E-02
			1.63E-03	4.33E-03	2.00E-03	4.67E-03	1.94E-03
2	2	1.08E-02	3.90	-9.77E-01	8.98E-01	-7.43E-01	2.42E-01
			1.17E-02	1.53E-02	1.82E-02	2.14E-02	2.50E-02
			2.50E-03	3.92E-03	2.44E-03	4.60E-03	1.50E-03
3	1	8.19E-03	4.33	-4.42	1.11	-1.38	1.02
			8.62E-03	1.10E-02	1.25E-02	1.48E-02	1.87E-02
			1.79E-03	1.32E-03	2.83E-03	2.06E-03	4.84E-03
3	2	1.08E-02	4.01	-9.61E-01	8.67E-01	-7.27E-01	1.64E-01
			1.15E-02	1.45E-02	1.81E-02	2.11E-02	2.48E-02
			2.46E-03	3.90E-03	2.38E-03	5.11E-03	1.16E-03
4	1	8.34E-03	4.70	-1.37	1.25	-1.33	1.02
			8.74E-03	1.06E-02	1.22E-02	1.50E-02	1.88E-02
			2.21E-03	7.28E-04	3.10E-03	1.82E-03	4.67E-03
4	2	1.09E-02	3.76	-1.02	9.47E-01	-6.94E-01	1.97E-01
			1.13E-02	1.47E-02	1.82E-02	2.13E-02	2.47E-02
			2.41E-03	3.94E-03	2.45E-03	4.58E-03	1.51E-03
5	1	7.02E-03	5.03	-1.11	1.61	-8.76E-01	3.90E-01
			7.55E-03	1.10E-02	1.37E-02	1.68E-02	2.04E-02
			2.90E-03	3.05E-03	2.18E-03	4.78E-03	1.50E-03
5	2	9.62E-03	4.43	-8.65E-01	8.69E-01	-7.24E-01	1.19E-01
			1.04E-02	1.38E-02	1.69E-02	2.05E-02	2.36E-02
			2.50E-03	4.05E-03	2.10E-03	5.20E-03	8.56E-04
6	1	1.07E-02	4.43	-1.39	1.19	-1.10	2.09E-01
			1.09E-02	1.52E-02	1.72E-02	2.06E-02	2.39E-02
			2.28E-03	3.68E-03	1.84E-03	5.21E-03	1.13E-03
6	2	1.31E-02	4.13	-1.02	7.12E-01	-7.41E-01	5.53E-01
			1.39E-02	1.76E-02	2.07E-02	2.35E-02	3.00E-02
			2.57E-03	4.01E-03	2.26E-03	5.91E-03	6.29E-03
7	1	8.14E-03	5.02	-1.13	1.03	-1.55	8.91E-01
			8.66E-03	1.12E-02	1.27E-02	1.48E-02	1.87E-02
			1.81E-03	1.59E-03	2.54E-03	2.31E-03	4.48E-03
7	2	1.07E-02	4.27	-9.34E-01	8.94E-01	-6.99E-01	1.44E-01
			1.14E-02	1.47E-02	1.82E-02	2.10E-02	2.49E-02
			2.53E-03	4.07E-03	2.34E-03	5.09E-03	9.44E-04
8	1	1.08E-02	3.48	-2.20	3.81E-01	-1.82	1.00E-01
			1.11E-02	1.30E-02	1.75E-02	2.03E-02	4.31E-02
			1.31E-03	4.88E-03	9.76E-04	2.50E-02	1.09E-03

continued on next page

continued from previous page

			Peaks				
Run	T.	t_0	#1	#2	#3	#4	#5
8	2	1.31E-02	3.75 1.40E-02 2.62E-03	-1.03 1.76E-02 3.89E-03	8.45E-01 2.05E-02 2.38E-03	-7.96E-01 2.38E-02 5.01E-03	1.88E-01 2.73E-02 1.13E-03
9	1	7.94E-03	5.18 8.43E-03 2.25E-03	-3.07 1.05E-02 6.00E-04	1.33 1.20E-02 3.29E-03	-1.15 1.45E-02 1.94E-03	1.01 1.83E-02 4.88E-03
9	2	1.05E-02	4.29 1.12E-02 2.68E-03	-9.11E-01 1.50E-02 3.91E-03	8.24E-01 1.78E-02 2.33E-03	-7.70E-01 2.17E-02 5.54E-03	5.83E-01 2.80E-02 6.47E-03
10	1	8.44E-03	4.97 8.94E-03 1.90E-03	-3.29 1.05E-02 6.16E-04	1.26 1.26E-02 3.43E-03	-1.32 1.51E-02 1.90E-03	1.07 1.81E-02 5.11E-03
10	2	1.10E-02	3.85 1.18E-02 2.34E-03	-8.42E-01 1.48E-02 4.16E-03	7.99E-01 1.83E-02 2.18E-03	-6.54E-01 2.10E-02 4.83E-03	1.42E-01 2.51E-02 1.38E-03
11	1	8.40E-03	3.97 8.86E-03 1.88E-03	-1.38 1.08E-02 1.75E-03	1.14 1.27E-02 2.26E-03	-1.53 1.50E-02 2.08E-03	1.00 1.78E-02 4.46E-03
11	2	1.09E-02	3.41 1.18E-02 2.19E-03	-1.09 1.45E-02 3.67E-03	7.88E-01 1.83E-02 2.88E-03	-7.12E-01 2.13E-02 4.16E-03	2.72E-01 2.50E-02 2.19E-03
12	1	8.36E-03	4.87 8.81E-03 2.15E-03	-1.41 1.15E-02 3.80E-03	1.31 1.50E-02 2.05E-03	-9.43E-01 1.79E-02 4.75E-03	3.69E-01 2.17E-02 1.90E-03
12	2	1.09E-02	3.48 1.18E-02 2.51E-03	-1.02 1.46E-02 4.00E-03	8.10E-01 1.85E-02 2.35E-03	-6.43E-01 2.09E-02 4.70E-03	1.53E-01 2.55E-02 1.50E-03

Table E.26: Detailed list of pressure pulse characteristics for Test #26 of Table 4.5

			Peaks				
Run	T.	t_0	#1	#2	#3	#4	#5
1	1	7.32E-03	5.40 8.05E-03 1.73E-03	-2.96 9.22E-03 9.12E-04	1.68 1.08E-02 3.46E-03	-1.23 1.43E-02 2.30E-03	1.07 1.80E-02 4.75E-03
1	2	9.76E-03	3.56 1.09E-02 2.58E-03	-1.36 1.37E-02 3.93E-03	5.12E-01 1.75E-02 2.67E-03	-5.66E-01 2.05E-02 5.36E-03	1.37E-01 2.45E-02 1.08E-03
2	1	8.57E-03	5.40 9.41E-03 1.38E-03	-1.96 1.10E-02 4.81E-03	1.42 1.56E-02 2.13E-03	-1.07 1.85E-02 4.10E-03	4.81E-01 2.24E-02 2.93E-03
2	2	1.09E-02	2.93 1.23E-02	-1.19 1.46E-02	6.35E-01 1.89E-02	-6.31E-01 2.15E-02	1.66E-01 2.48E-02

continued on next page

continued from previous page

			Peaks				
Run	T.	t_0	#1	#2	#3	#4	#5
			2.49E-03	3.92E-03	2.91E-03	4.26E-03	2.27E-03
3	1	8.51E-03	5.26	-1.11	2.83	-1.67	9.05E-01
			9.26E-03	1.07E-02	1.13E-02	1.24E-02	1.57E-02
			1.44E-03	9.60E-04	9.12E-04	3.10E-03	1.86E-03
3	2	1.10E-02	3.05	-1.12	4.73E-01	-5.58E-01	1.45E-01
			1.21E-02	1.49E-02	1.89E-02	2.21E-02	2.58E-02
			2.54E-03	3.77E-03	3.19E-03	4.32E-03	2.23E-03
4	1	8.53E-03	4.97	-1.68	1.22	-1.07	3.34E-01
			9.24E-03	1.12E-02	1.55E-02	1.87E-02	2.28E-02
			1.45E-03	4.95E-03	1.94E-03	4.69E-03	2.54E-03
4	2	1.10E-02	3.24	-1.17	5.19E-01	-6.06E-01	1.44E-01
			1.22E-02	1.54E-02	1.89E-02	2.16E-02	2.54E-02
			2.68E-03	3.95E-03	2.76E-03	4.59E-03	2.13E-03
5	1	8.48E-03	5.00	-5.52	1.56	-9.23E-01	1.09
			9.21E-03	1.16E-02	1.24E-02	1.56E-02	1.91E-02
			1.49E-03	1.75E-03	3.23E-03	2.23E-03	5.23E-03
5	2	1.10E-02	3.27	-1.19	4.55E-01	-5.76E-01	1.27E-01
			1.20E-02	1.57E-02	1.93E-02	2.29E-02	2.60E-02
			2.67E-03	4.42E-03	2.47E-03	5.18E-03	1.75E-03
6	1	8.53E-03	5.76	-1.17	1.13	-3.31E-01	1.68
			9.37E-03	1.02E-02	1.22E-02	1.39E-02	1.57E-02
			1.45E-03	1.50E-03	2.21E-03	1.06E-03	2.40E-03
6	2	1.10E-02	2.93	-1.24	5.43E-01	-5.82E-01	1.68E-01
			1.20E-02	1.47E-02	1.86E-02	2.22E-02	2.59E-02
			2.49E-03	3.82E-03	3.05E-03	4.63E-03	2.17E-03
7	1	8.62E-03	4.84	-2.09	1.56	-9.23E-01	6.71E-01
			9.32E-03	1.08E-02	1.56E-02	1.88E-02	2.17E-02
			1.36E-03	4.66E-03	2.28E-03	3.58E-03	3.48E-03
7	2	1.11E-02	3.37	-1.32	6.99E-01	-6.61E-01	2.77E-01
			1.19E-02	1.46E-02	1.79E-02	2.14E-02	2.50E-02
			2.20E-03	3.70E-03	3.06E-03	4.06E-03	2.54E-03
8	1	8.38E-03	5.49	-4.23	1.26	-1.46	1.07
			9.04E-03	1.10E-02	1.18E-02	1.55E-02	1.84E-02
			1.55E-03	1.22E-03	3.34E-03	2.27E-03	4.34E-03
8	2	1.09E-02	3.19	-1.12	5.63E-01	-6.55E-01	2.35E-01
			1.20E-02	1.45E-02	1.86E-02	2.16E-02	2.51E-02
			2.53E-03	3.74E-03	3.03E-03	4.09E-03	2.38E-03
9	1	7.22E-03	5.35	-2.78	1.58	-1.14	1.07
			8.15E-03	9.34E-03	1.12E-02	1.43E-02	1.71E-02
			1.51E-03	1.25E-03	3.50E-03	2.10E-03	4.53E-03
9	2	9.64E-03	2.97	-1.20	4.87E-01	-6.38E-01	1.12E-01
			1.09E-02	1.41E-02	1.74E-02	2.06E-02	2.39E-02
			2.64E-03	3.76E-03	2.94E-03	4.54E-03	2.02E-03

continued on next page

continued from previous page							
			Peaks				
Run	T.	t_0	#1	#2	#3	#4	#5
10	1	8.42E-03	4.79	-1.63	1.18	-7.40E-01	4.32E-01
			9.22E-03	1.06E-02	1.54E-02	1.86E-02	2.23E-02
			1.50E-03	4.62E-03	2.41E-03	3.89E-03	3.13E-03
10	2	1.09E-02	3.05	-9.83E-01	4.24E-01	-6.08E-01	1.42E-01
			1.20E-02	1.46E-02	1.87E-02	2.17E-02	2.50E-02
			2.42E-03	3.94E-03	2.82E-03	4.49E-03	1.97E-03
11	1	8.46E-03	5.01	-1.69	1.17	-1.08	3.24E-01
			9.36E-03	1.12E-02	1.55E-02	1.89E-02	2.23E-02
			1.50E-03	4.83E-03	2.02E-03	4.70E-03	2.18E-03
11	2	1.09E-02	3.14	-1.18	4.63E-01	-6.62E-01	1.35E-01
			1.19E-02	1.46E-02	1.85E-02	2.19E-02	2.60E-02
			2.58E-03	3.98E-03	2.72E-03	5.13E-03	1.26E-03
12	1	8.52E-03	5.50	-1.91	1.37	-1.02	3.87E-01
			9.27E-03	1.10E-02	1.56E-02	1.87E-02	2.24E-02
			1.46E-03	4.69E-03	2.26E-03	3.90E-03	3.10E-03
12	2	1.09E-02	2.91	-1.21	5.68E-01	-6.51E-01	1.46E-01
			1.21E-02	1.45E-02	1.88E-02	2.19E-02	2.48E-02
			2.45E-03	3.86E-03	3.03E-03	4.24E-03	2.34E-03

Table E.27: Detailed list of pressure pulse characteristics for Test #27 of Table 4.5

			Peaks				
Run	T.	t_0	#1	#2	#3	#4	#5
1	1	1.10E-02	4.38	-2.33	3.47E-01	-1.62	2.63E-01
			1.14E-02	1.32E-02	1.77E-02	2.06E-02	4.12E-02
			1.06E-03	5.31E-03	1.11E-03	2.00E-02	5.04E-03
1	2	1.32E-02	3.28	-1.22	5.19E-01	-6.06E-01	1.44E-01
			1.43E-02	1.78E-02	2.10E-02	2.36E-02	2.82E-02
			2.54E-03	3.69E-03	3.05E-03	4.71E-03	1.65E-03
2	1	8.50E-03	4.86	-1.89	6.23E-01	-1.30	1.05
			9.37E-03	1.08E-02	1.32E-02	1.54E-02	1.85E-02
			1.46E-03	2.45E-03	2.27E-03	2.08E-03	4.14E-03
2	2	1.10E-02	2.88	-1.25	5.32E-01	-5.93E-01	2.04E-01
			1.20E-02	1.44E-02	1.83E-02	2.16E-02	2.46E-02
			2.18E-03	3.73E-03	3.15E-03	3.83E-03	2.71E-03
3	1	8.71E-03	4.16	-2.03	1.21	-1.14	3.16E-01
			9.29E-03	1.08E-02	1.57E-02	1.84E-02	2.15E-02
			1.26E-03	4.69E-03	2.20E-03	4.04E-03	2.55E-03
3	2	1.11E-02	2.45	-1.26	6.19E-01	-6.46E-01	2.44E-01
			1.20E-02	1.45E-02	1.83E-02	2.17E-02	2.48E-02
			2.29E-03	3.66E-03	3.03E-03	3.90E-03	2.94E-03
4	1	1.04E-02	4.44	-2.07	9.26E-01	-1.23	2.23E-01
			1.11E-02	1.28E-02	1.72E-02	2.01E-02	2.41E-02
continued on next page							

continued from previous page

			Peaks				
Run	T.	t_0	#1	#2	#3	#4	#5
			1.34E-03	4.95E-03	1.64E-03	5.05E-03	1.66E-03
4	2	3.74E-03	2.37E-01	-3.42	1.12	-8.00E-01	5.13E-01
			5.54E-03	1.35E-02	1.63E-02	2.06E-02	2.35E-02
			1.82E-03	9.58E-03	3.63E-03	3.36E-03	3.80E-03
5	1	1.09E-02	4.28	-2.56	1.91	-1.10E-01	1.24E-01
			1.14E-02	1.48E-02	2.05E-02	4.41E-02	4.68E-02
			1.20E-03	5.80E-03	2.56E-02	2.27E-03	3.41E-03
5	2	1.31E-02	3.39	-1.25	6.67E-01	-6.45E-01	1.99E-01
			1.37E-02	1.65E-02	2.10E-02	2.40E-02	2.75E-02
			2.42E-03	3.84E-03	2.96E-03	4.14E-03	2.42E-03
6	1	1.10E-02	4.13	-2.76	2.10	-4.77E-01	1.73
			1.14E-02	1.33E-02	1.45E-02	1.77E-02	2.05E-02
			1.06E-03	1.96E-03	3.24E-03	1.14E-03	2.07E-02
6	2	1.31E-02	3.93	-1.32	6.52E-01	-6.61E-01	1.83E-01
			1.37E-02	1.76E-02	2.10E-02	2.40E-02	2.81E-02
			2.40E-03	4.14E-03	2.65E-03	5.02E-03	1.46E-03
7	1	8.39E-03	4.64	-1.69	1.12	-1.08	2.76E-01
			9.11E-03	1.13E-02	1.55E-02	1.87E-02	2.22E-02
			1.55E-03	4.76E-03	2.06E-03	4.82E-03	2.05E-03
7	2	1.09E-02	3.24	-1.21	5.21E-01	-6.51E-01	1.46E-01
			1.20E-02	1.52E-02	1.90E-02	2.20E-02	2.50E-02
			2.57E-03	3.84E-03	2.99E-03	4.32E-03	2.38E-03
8	1	1.08E-02	4.41	-1.50	1.17	-1.22	1.40E-01
			1.13E-02	1.27E-02	1.75E-02	2.05E-02	2.42E-02
			1.23E-03	4.54E-03	2.10E-03	5.15E-03	1.32E-03
8	2	1.30E-02	3.62	-1.35	6.17E-01	-6.96E-01	2.42E-01
			1.40E-02	1.63E-02	2.08E-02	2.38E-02	2.75E-02
			2.39E-03	3.82E-03	2.91E-03	4.02E-03	2.64E-03
9	1	8.55E-03	4.84	-1.95	1.05	-1.11	2.96E-01
			9.32E-03	1.13E-02	1.57E-02	1.83E-02	2.24E-02
			1.44E-03	4.76E-03	1.94E-03	4.33E-03	2.65E-03
9	2	1.10E-02	3.16	-1.25	5.79E-01	-6.40E-01	2.04E-01
			1.23E-02	1.48E-02	1.86E-02	2.22E-02	2.51E-02
			2.41E-03	3.75E-03	3.08E-03	4.12E-03	2.51E-03
10	1	1.07E-02	4.94	-2.42	6.23E-01	-1.49	6.89E-01
			1.13E-02	1.37E-02	1.77E-02	2.05E-02	2.70E-02
			1.50E-03	4.79E-03	1.58E-03	6.45E-03	5.42E-03
10	2	1.30E-02	3.96	-1.38	6.82E-01	-6.31E-01	2.13E-01
			1.37E-02	1.74E-02	2.08E-02	2.36E-02	2.74E-02
			2.41E-03	3.91E-03	2.94E-03	4.17E-03	2.32E-03
11	1	8.33E-03	4.97	-1.87	8.48E-01	-1.21	1.92E-01
			9.11E-03	1.14E-02	1.54E-02	1.86E-02	2.23E-02
			2.17E-03	4.04E-03	1.94E-03	4.93E-03	1.90E-03

continued on next page

continued from previous page							
			Peaks				
Run	T.	t_0	#1	#2	#3	#4	#5
11	2	1.07E-02	3.77	-1.38	6.80E-01	-5.85E-01	2.58E-01
			1.17E-02	1.49E-02	1.87E-02	2.13E-02	2.52E-02
			2.61E-03	3.91E-03	2.78E-03	4.19E-03	2.66E-03
12	1	8.25E-03	5.97	-1.81	1.15	-1.01	3.02E-01
			9.39E-03	1.13E-02	1.52E-02	1.88E-02	2.21E-02
			1.73E-03	4.30E-03	2.45E-03	4.30E-03	2.48E-03
12	2	1.07E-02	3.62	-1.39	8.09E-01	-6.91E-01	1.53E-01
			1.14E-02	1.53E-02	1.87E-02	2.17E-02	2.50E-02
			2.70E-03	4.12E-03	2.58E-03	4.61E-03	1.94E-03

Table E.28: Detailed list of pressure pulse characteristics for Test #28 of Table 4.5

			Peaks				
Run	T.	t_0	#1	#2	#3	#4	#5
1	1	8.19E-03	4.30	-2.99	9.94E-01	-1.26	9.47E-01
			8.90E-03	1.06E-02	1.19E-02	1.48E-02	1.81E-02
			2.10E-03	7.12E-04	3.07E-03	2.26E-03	4.64E-03
1	2	1.05E-02	3.77	-1.29	6.77E-01	-7.29E-01	2.09E-01
			1.14E-02	1.38E-02	1.81E-02	2.15E-02	2.47E-02
			2.43E-03	3.62E-03	3.16E-03	4.51E-03	1.80E-03
2	1	8.54E-03	4.78	-1.64	7.04E-01	-1.26	9.38E-01
			9.04E-03	1.08E-02	1.33E-02	1.50E-02	1.82E-02
			1.41E-03	2.18E-03	2.27E-03	2.08E-03	4.77E-03
2	2	1.08E-02	3.71	-1.07	8.02E-01	-6.98E-01	2.40E-01
			1.16E-02	1.45E-02	1.85E-02	2.13E-02	2.42E-02
			2.27E-03	3.77E-03	3.11E-03	3.98E-03	2.45E-03
3	1	8.44E-03	4.72	-7.15E-01	1.04	-1.04	1.21
			9.06E-03	1.03E-02	1.09E-02	1.28E-02	1.54E-02
			1.53E-03	6.40E-04	7.28E-04	3.22E-03	2.02E-03
3	2	1.09E-02	3.01	-1.07	6.68E-01	-6.44E-01	1.99E-01
			1.18E-02	1.54E-02	1.87E-02	2.11E-02	2.50E-02
			2.38E-03	3.84E-03	2.90E-03	4.22E-03	2.33E-03
4	1	8.27E-03	4.58	-1.38	1.11	-1.09	3.58E-01
			8.83E-03	1.13E-02	1.53E-02	1.80E-02	2.19E-02
			2.10E-03	3.84E-03	2.09E-03	4.74E-03	2.09E-03
4	2	1.06E-02	3.39	-1.15	8.15E-01	-5.91E-01	2.53E-01
			1.14E-02	1.42E-02	1.83E-02	2.11E-02	2.52E-02
			2.65E-03	3.66E-03	2.98E-03	3.92E-03	2.88E-03
5	1	8.30E-03	4.40	-1.32	1.21	-9.93E-01	4.14E-01
			8.93E-03	1.07E-02	1.49E-02	1.86E-02	2.20E-02
			1.68E-03	4.30E-03	2.19E-03	4.50E-03	2.30E-03
			3.55	-1.09	7.41E-01	-6.65E-01	2.25E-01
continued on next page							

continued from previous page

			Peaks				
Run	T.	t_0	#1	#2	#3	#4	#5
5	2	1.07E-02	1.18E-02	1.51E-02	1.84E-02	2.14E-02	2.52E-02
			2.47E-03	3.51E-03	3.15E-03	4.31E-03	2.20E-03
6	1	8.40E-03	4.36	-2.25	1.22	-1.13	1.08
			9.03E-03	1.07E-02	1.23E-02	1.52E-02	1.83E-02
			1.71E-03	1.11E-03	3.13E-03	2.08E-03	4.63E-03
6	2	1.09E-02	5.87	-1.35	9.03E-01	-8.31E-01	2.94E-01
			1.15E-02	1.43E-02	1.86E-02	2.14E-02	2.46E-02
			2.43E-03	4.22E-03	2.42E-03	3.93E-03	2.44E-03
7	1	8.20E-03	5.20	-7.52E-01	1.13	-1.12	9.86E-01
			9.55E-03	1.08E-02	1.18E-02	1.51E-02	1.74E-02
			2.27E-03	5.84E-04	3.10E-03	2.07E-03	4.61E-03
7	2	1.07E-02	3.17	-1.10	7.32E-01	-6.28E-01	2.16E-01
			1.14E-02	1.43E-02	1.82E-02	2.11E-02	2.51E-02
			2.35E-03	3.72E-03	2.92E-03	3.94E-03	2.40E-03
8	1	1.08E-02	4.41	-2.25	8.48E-01	-1.35	6.99E-01
			1.12E-02	1.40E-02	1.76E-02	2.08E-02	2.74E-02
			1.45E-03	4.60E-03	1.64E-03	6.51E-03	6.95E-03
8	2	1.29E-02	3.38	-1.21	6.62E-01	-6.51E-01	1.46E-01
			1.37E-02	1.74E-02	2.07E-02	2.37E-02	2.76E-02
			2.78E-03	4.00E-03	2.50E-03	4.58E-03	1.99E-03
9	1	8.34E-03	4.32	-1.68	1.13	-1.03	9.83E-02
			9.35E-03	1.13E-02	1.51E-02	1.84E-02	2.19E-02
			1.66E-03	4.45E-03	1.96E-03	5.20E-03	1.50E-03
9	2	1.08E-02	3.62	-1.20	1.25	-7.64E-01	5.96E-01
			1.15E-02	1.40E-02	1.50E-02	1.86E-02	2.13E-02
			2.50E-03	7.68E-04	3.57E-03	2.36E-03	5.14E-03
10	1	6.74E-03	4.62	-1.29	1.05	-1.01	2.56E-01
			7.37E-03	1.13E-02	1.36E-02	1.70E-02	2.05E-02
			3.22E-03	3.07E-03	1.86E-03	4.89E-03	1.70E-03
10	2	9.30E-03	3.95	-9.71E-01	8.11E-01	-8.30E-01	2.01E-01
			1.00E-02	1.40E-02	1.70E-02	2.05E-02	2.37E-02
			2.33E-03	4.23E-03	2.56E-03	5.09E-03	1.13E-03
11	1	8.18E-03	4.61	-1.81	1.00	-1.25	2.51E-01
			8.74E-03	1.12E-02	1.51E-02	1.84E-02	2.20E-02
			2.20E-03	4.11E-03	1.74E-03	4.96E-03	1.78E-03
11	2	1.06E-02	3.29	-1.12	7.56E-01	-6.98E-01	1.93E-01
			1.16E-02	1.45E-02	1.85E-02	2.14E-02	2.47E-02
			2.54E-03	3.51E-03	3.14E-03	4.06E-03	2.42E-03
12	1	8.42E-03	4.59	-1.73	1.22	-1.03	4.23E-01
			8.93E-03	1.14E-02	1.52E-02	1.84E-02	2.20E-02
			1.47E-03	4.46E-03	2.19E-03	4.54E-03	2.27E-03
12	2	1.08E-02	3.71	-1.26	7.55E-01	-6.99E-01	1.92E-01
			1.19E-02	1.54E-02	1.84E-02	2.15E-02	2.47E-02

continued on next page

continued from previous page							
			Peaks				
Run	T.	t_0	#1	#2	#3	#4	#5
			2.57E-03	3.46E-03	3.14E-03	4.53E-03	2.04E-03

Table E.29: Detailed list of pressure pulse characteristics for Test #29 of Table 4.5

			Peaks				
Run	T.	t_0	#1	#2	#3	#4	#5
1	1	8.24E-03	4.59	-9.38E-01	1.27	-7.50E-01	3.75E-01
			8.88E-03	1.14E-02	1.51E-02	1.84E-02	2.21E-02
			1.71E-03	4.42E-03	2.26E-03	4.74E-03	2.05E-03
1	2	1.08E-02	3.09	-7.02E-01	5.63E-01	-5.15E-01	4.68E-01
			1.17E-02	1.49E-02	1.84E-02	2.10E-02	2.78E-02
			2.51E-03	3.38E-03	3.29E-03	6.22E-03	5.24E-03
2	1	8.18E-03	4.65	-9.77E-01	1.18	-7.90E-01	3.35E-01
			8.76E-03	1.05E-02	1.50E-02	1.79E-02	2.19E-02
			1.80E-03	4.33E-03	2.02E-03	4.85E-03	2.00E-03
2	2	1.07E-02	2.95	-7.02E-01	7.04E-01	-5.62E-01	9.47E-02
			1.16E-02	1.42E-02	1.84E-02	2.11E-02	2.54E-02
			2.37E-03	3.43E-03	3.34E-03	4.70E-03	1.59E-03
3	1	7.51E-03	4.09	-4.11E-01	9.26E-01	-1.04	8.33E-01
			8.06E-03	1.04E-02	1.21E-02	1.42E-02	1.67E-02
			2.62E-03	1.16E-03	2.32E-03	1.91E-03	4.98E-03
3	2	9.95E-03	2.77	-7.96E-01	5.63E-01	-5.62E-01	9.47E-02
			1.10E-02	1.46E-02	1.77E-02	2.04E-02	2.40E-02
			2.42E-03	3.49E-03	3.24E-03	4.29E-03	2.06E-03
4	1	8.34E-03	4.07	-9.48E-01	9.27E-01	-8.07E-01	2.71E-01
			8.88E-03	1.14E-02	1.54E-02	1.78E-02	2.23E-02
			1.66E-03	4.60E-03	1.94E-03	5.03E-03	1.82E-03
4	2	1.08E-02	2.34	-6.15E-01	5.10E-01	-5.68E-01	8.82E-02
			1.18E-02	1.43E-02	1.91E-02	2.16E-02	2.51E-02
			2.50E-03	4.30E-03	2.38E-03	5.02E-03	1.20E-03
5	1	6.54E-03	4.28	-7.36E-01	1.14	-7.83E-01	2.01E-01
			7.16E-03	1.14E-02	1.34E-02	1.71E-02	2.03E-02
			3.38E-03	2.79E-03	1.97E-03	5.16E-03	1.48E-03
5	2	9.08E-03	3.11	-6.88E-01	6.24E-01	-5.48E-01	4.54E-01
			1.00E-02	1.37E-02	1.67E-02	1.96E-02	2.64E-02
			2.46E-03	3.48E-03	3.15E-03	6.08E-03	1.38E-02
6	1	8.12E-03	4.57	-1.00	1.01	-9.57E-01	8.24E-01
			8.72E-03	1.10E-02	1.28E-02	1.51E-02	1.83E-02
			2.10E-03	1.49E-03	2.80E-03	1.82E-03	5.24E-03
6	2	1.06E-02	3.13	-6.65E-01	2.26E-01	-4.60E-01	5.24E-01
			1.16E-02	1.40E-02	1.69E-02	1.85E-02	2.14E-02
			2.77E-03	3.32E-03	8.32E-04	2.25E-03	5.87E-03
continued on next page							

continued from previous page

			Peaks				
Run	T.	t_0	#1	#2	#3	#4	#5
7	1	7.56E-03	4.37	-1.51	8.83E-01	-1.04	7.43E-01
			8.22E-03	1.09E-02	1.23E-02	1.46E-02	1.69E-02
			3.03E-03	6.56E-04	2.50E-03	2.05E-03	4.86E-03
7	2	1.01E-02	2.88	-7.30E-01	6.30E-01	-4.95E-01	7.35E-02
			1.12E-02	1.47E-02	1.78E-02	2.01E-02	2.54E-02
			2.37E-03	3.47E-03	3.24E-03	5.24E-03	1.04E-03
8	1	8.14E-03	3.66	-8.37E-01	1.18	-8.37E-01	3.35E-01
			8.68E-03	1.10E-02	1.47E-02	1.89E-02	2.16E-02
			1.76E-03	4.30E-03	2.09E-03	4.75E-03	1.93E-03
8	2	1.06E-02	2.83	-7.83E-01	2.95E-01	-8.58E-01	5.96E-01
			1.18E-02	1.45E-02	1.71E-02	1.83E-02	2.09E-02
			2.49E-03	3.70E-03	5.60E-04	2.27E-03	6.24E-03
9	1	7.06E-03	4.04	-9.31E-01	1.13	-8.84E-01	2.88E-01
			7.69E-03	1.09E-02	1.39E-02	1.73E-02	2.11E-02
			2.90E-03	3.31E-03	2.19E-03	4.80E-03	1.95E-03
9	2	9.54E-03	2.92	-8.30E-01	5.76E-01	-6.42E-01	4.55E-01
			1.08E-02	1.40E-02	1.73E-02	2.08E-02	2.68E-02
			2.73E-03	3.63E-03	2.92E-03	6.10E-03	6.28E-03
10	1	7.70E-03	3.81	-4.57E-01	2.31	-9.26E-01	9.96E-01
			8.39E-03	1.05E-02	1.07E-02	1.25E-02	1.46E-02
			2.27E-03	5.52E-04	9.36E-04	2.57E-03	1.97E-03
10	2	1.02E-02	3.06	-6.89E-01	7.17E-01	-7.36E-01	1.74E-01
			1.11E-02	1.48E-02	1.80E-02	2.12E-02	2.43E-02
			2.90E-03	3.40E-03	2.98E-03	4.68E-03	8.48E-04
11	1	8.22E-03	5.55	-1.20	1.33	-8.22E-01	3.97E-01
			8.80E-03	1.12E-02	1.47E-02	1.80E-02	2.18E-02
			1.95E-03	3.94E-03	2.31E-03	4.23E-03	2.50E-03
11	2	1.06E-02	2.91	-9.77E-01	6.17E-01	-6.02E-01	1.48E-01
			1.07E-02	1.37E-02	1.81E-02	2.08E-02	2.48E-02
			2.46E-03	3.70E-03	2.98E-03	4.64E-03	1.70E-03
12	1	8.04E-03	5.49	-8.89E-01	9.39E-01	-8.42E-01	2.36E-01
			9.29E-03	1.10E-02	1.50E-02	1.80E-02	2.17E-02
			2.71E-03	3.38E-03	2.06E-03	4.98E-03	1.73E-03
12	2	1.05E-02	2.61	-8.08E-01	5.51E-01	-6.20E-01	4.33E-01
			1.16E-02	1.52E-02	1.84E-02	2.08E-02	2.79E-02
			2.68E-03	4.12E-03	2.18E-03	6.45E-03	6.83E-03

Table E.30: Detailed list of pressure pulse characteristics for Test #30 of Table 4.5

			Peaks				
Run	T.	t_0	#1	#2	#3	#4	#5
1	1	8.11E-03	5.21	-1.64	4.25E-01	-7.47E-01	1.43E-01
			9.26E-03	1.15E-02	1.54E-02	1.80E-02	2.28E-02
			1.88E-03	4.97E-03	1.49E-03	5.81E-03	1.70E-03

continued on next page

continued from previous page

			Peaks				
Run	T.	t_0	#1	#2	#3	#4	#5
1	2	1.07E-02	2.24	-6.15E-01	3.23E-01	-3.34E-01	8.82E-02
			1.18E-02	1.42E-02	1.90E-02	2.19E-02	2.63E-02
			2.58E-03	4.65E-03	2.46E-03	5.62E-03	1.01E-03
2	1	8.01E-03	4.57	-1.85	5.84E-01	-9.63E-01	2.56E-01
			8.57E-03	1.13E-02	1.52E-02	1.76E-02	2.20E-02
			1.98E-03	4.54E-03	1.51E-03	5.16E-03	1.95E-03
2	2	1.05E-02	6.02	-8.71E-01	5.35E-01	-4.49E-01	1.13E-01
			1.21E-02	1.42E-02	1.83E-02	2.10E-02	2.46E-02
			2.48E-03	3.73E-03	3.14E-03	4.49E-03	1.87E-03
3	1	8.79E-03	5.08	-1.85	1.29	-7.71E-01	9.63E-01
			9.46E-03	1.11E-02	1.20E-02	1.59E-02	1.83E-02
			1.91E-03	5.44E-04	4.04E-03	1.54E-03	5.35E-03
3	2	1.12E-02	2.36	-8.29E-01	5.30E-01	-4.54E-01	1.55E-01
			1.24E-02	1.49E-02	1.88E-02	2.17E-02	2.59E-02
			2.35E-03	3.86E-03	3.09E-03	4.42E-03	2.15E-03
4	1	7.80E-03	5.04	-4.76	1.61	-2.63E-01	7.22E-01
			8.40E-03	9.54E-03	1.12E-02	1.53E-02	1.78E-02
			1.47E-03	1.20E-03	4.39E-03	9.92E-04	6.84E-03
4	2	1.04E-02	1.83	-4.63E-01	2.40E-01	-3.23E-01	2.76E-01
			1.14E-02	1.39E-02	1.88E-02	2.11E-02	2.88E-02
			2.54E-03	4.74E-03	2.13E-03	6.10E-03	7.83E-03
5	1	7.52E-03	6.00	-1.73	3.24E-01	-1.44E-01	2.38E-01
			9.46E-03	1.11E-02	2.44E-02	3.02E-02	4.30E-02
			2.69E-03	1.26E-02	5.50E-03	5.02E-03	3.46E-02
5	2	1.01E-02	2.01	-4.75E-01	2.75E-01	-2.88E-01	3.35E-01
			1.13E-02	1.41E-02	1.83E-02	2.13E-02	2.92E-02
			2.70E-03	4.69E-03	2.20E-03	7.10E-03	5.01E-03
6	1	8.35E-03	4.74	-1.02	1.26	-1.97E-01	7.41E-01
			8.94E-03	1.02E-02	1.24E-02	1.57E-02	1.79E-02
			1.65E-03	1.72E-03	3.44E-03	1.13E-03	6.98E-03
6	2	1.09E-02	2.31	-5.02E-01	2.48E-01	-3.14E-01	2.67E-01
			1.19E-02	1.44E-02	1.88E-02	2.14E-02	2.83E-02
			2.42E-03	4.61E-03	2.16E-03	6.13E-03	7.14E-03
7	1	8.69E-03	5.02	-1.54	1.77	-2.90E-01	6.47E-01
			9.37E-03	1.05E-02	1.22E-02	1.65E-02	1.84E-02
			1.28E-03	1.82E-03	4.09E-03	1.26E-03	5.75E-03
7	2	1.13E-02	1.70	-6.45E-01	1.99E-01	-3.17E-01	2.70E-01
			1.24E-02	1.56E-02	1.93E-02	2.23E-02	2.98E-02
			2.69E-03	4.71E-03	2.38E-03	7.00E-03	7.74E-03
8	1	8.74E-03	5.20	-2.95	2.06	-9.85E-01	2.35E-01
			9.43E-03	1.09E-02	1.23E-02	1.90E-02	2.51E-02
			1.70E-03	1.13E-03	5.02E-03	7.26E-03	5.54E-03
			2.20	-5.70E-01	2.74E-01	-5.70E-01	2.89E-01

continued on next page

continued from previous page

			Peaks				
Run	T.	t_0	#1	#2	#3	#4	#5
8	2	1.11E-02	1.21E-02	1.49E-02	1.94E-02	2.43E-02	2.92E-02
			2.94E-03	4.48E-03	2.46E-03	6.42E-03	5.78E-03
9	1	8.54E-03	4.89	-1.72	1.34	-2.02E-01	9.70E-01
			9.18E-03	1.05E-02	1.27E-02	1.62E-02	1.93E-02
			1.42E-03	1.58E-03	4.25E-03	9.12E-04	6.72E-03
9	2	1.10E-02	2.04	-7.73E-01	2.58E-01	-3.51E-01	2.10E-01
			1.21E-02	1.50E-02	1.94E-02	2.25E-02	2.93E-02
			2.76E-03	4.61E-03	2.50E-03	6.80E-03	7.48E-03
10	1	8.66E-03	4.92	-4.17	2.25	-1.03	1.43E-01
			9.28E-03	1.05E-02	1.22E-02	1.88E-02	3.00E-02
			1.50E-03	1.28E-03	5.03E-03	1.30E-02	3.94E-03
10	2	1.11E-02	2.41	-7.78E-01	2.06E-01	-4.03E-01	2.63E-01
			1.23E-02	1.54E-02	1.91E-02	2.29E-02	3.03E-02
			2.74E-03	4.81E-03	2.07E-03	6.82E-03	8.07E-03
11	1	8.58E-03	5.45	-2.28	2.69	-1.44	2.51E-01
			9.17E-03	1.06E-02	1.15E-02	1.25E-02	1.60E-02
			1.37E-03	1.20E-03	7.52E-04	3.69E-03	1.00E-03
11	2	1.11E-02	2.27	-6.40E-01	2.98E-01	-3.12E-01	2.18E-01
			1.24E-02	1.46E-02	1.95E-02	2.23E-02	2.91E-02
			2.54E-03	4.56E-03	2.56E-03	6.72E-03	7.14E-03
12	1	8.58E-03	4.98	-2.05	3.89E-01	-6.42E-01	1.54E-01
			9.13E-03	1.10E-02	1.61E-02	1.82E-02	2.33E-02
			1.39E-03	5.46E-03	1.38E-03	5.90E-03	1.83E-03
12	2	1.11E-02	2.03	-5.44E-01	2.53E-01	-3.57E-01	2.63E-01
			1.24E-02	1.50E-02	1.96E-02	2.18E-02	2.92E-02
			2.64E-03	4.75E-03	2.12E-03	6.28E-03	7.34E-03

Table E.31: Detailed list of pressure pulse characteristics for Test #31 of Table 4.5

			Peaks				
Run	T.	t_0	#1	#2	#3	#4	#5
1	1	8.50E-03	4.88	-1.78	2.81E-01	-7.97E-01	2.34E-01
			9.10E-03	1.09E-02	1.59E-02	1.82E-02	2.51E-02
			1.46E-03	5.58E-03	1.08E-03	7.56E-03	4.64E-03
1	2	1.10E-02	2.12	-6.42E-01	3.13E-01	-7.82E-01	3.13E-01
			1.23E-02	1.46E-02	1.96E-02	2.16E-02	2.87E-02
			2.54E-03	5.23E-03	1.39E-03	6.75E-03	7.25E-03
2	1	8.58E-03	4.83	-1.36	4.68E-01	-7.04E-01	9.28E-02
			9.21E-03	1.17E-02	1.62E-02	1.88E-02	2.32E-02
			1.38E-03	5.56E-03	1.49E-03	6.13E-03	8.40E-04
2	2	1.12E-02	2.49	-7.41E-01	2.90E-01	-4.13E-01	5.06E-01
			1.24E-02	1.50E-02	1.94E-02	2.14E-02	2.23E-02
			2.64E-03	5.11E-03	1.66E-03	9.36E-04	6.41E-03

continued on next page

continued from previous page

			Peaks				
Run	T.	t_0	#1	#2	#3	#4	#5
3	1	8.23E-03	5.17	-1.58	2.51E-01	-6.87E-01	7.72E-02
			8.91E-03	1.18E-02	1.57E-02	1.89E-02	2.38E-02
			2.69E-03	4.38E-03	1.36E-03	6.18E-03	1.18E-03
3	2	1.08E-02	2.42	-5.35E-01	1.68E-01	-7.22E-01	3.01E-01
			1.21E-02	1.45E-02	1.95E-02	2.42E-02	2.92E-02
			2.86E-03	5.19E-03	1.22E-03	6.55E-03	8.40E-03
4	1	8.72E-03	4.96	-1.74	1.04	-5.10E-01	6.15E-01
			9.32E-03	1.06E-02	1.29E-02	1.61E-02	1.88E-02
			1.25E-03	2.35E-03	3.30E-03	1.51E-03	5.86E-03
4	2	1.13E-02	1.97	-6.56E-01	2.81E-01	-3.75E-01	2.81E-01
			1.25E-02	1.48E-02	1.95E-02	2.30E-02	2.93E-02
			2.54E-03	5.12E-03	1.99E-03	6.71E-03	7.40E-03
5	1	8.49E-03	4.75	-1.34	1.30	-3.92E-01	5.92E-01
			9.17E-03	1.12E-02	1.22E-02	1.57E-02	1.86E-02
			1.50E-03	1.42E-03	3.80E-03	1.49E-03	5.99E-03
5	2	4.67E-03	4.08E-01	-2.50	7.36E-01	-2.48E-01	4.55E-01
			7.96E-03	1.21E-02	1.46E-02	1.91E-02	2.20E-02
			6.30E-03	2.63E-03	5.05E-03	1.64E-03	1.20E-02
6	1	8.49E-03	5.18	-1.86	3.94E-01	-6.84E-01	1.13E-01
			9.08E-03	1.08E-02	1.61E-02	1.88E-02	2.32E-02
			1.49E-03	5.47E-03	1.52E-03	6.16E-03	1.30E-03
6	2	1.09E-02	1.90	-5.39E-01	1.65E-01	-4.92E-01	2.10E-01
			1.23E-02	1.45E-02	1.95E-02	2.35E-02	2.60E-02
			2.88E-03	4.92E-03	2.04E-03	4.92E-03	1.41E-03
7	1	8.49E-03	4.69	-2.58	1.64	-9.74E-02	9.34E-01
			9.14E-03	1.12E-02	1.31E-02	1.58E-02	1.82E-02
			1.62E-03	1.50E-03	4.02E-03	8.88E-04	1.39E-02
7	2	1.10E-02	1.96	-5.26E-01	1.31E-01	-3.85E-01	5.70E-02
			1.24E-02	1.46E-02	1.91E-02	2.20E-02	4.24E-02
			2.88E-03	4.86E-03	1.96E-03	2.15E-02	1.61E-03
8	1	8.14E-03	4.83	-1.40	3.31E-01	-8.41E-01	3.25E-01
			8.74E-03	1.21E-02	1.57E-02	1.85E-02	2.52E-02
			2.64E-03	4.38E-03	1.24E-03	6.91E-03	5.76E-03
8	2	1.07E-02	2.30	-5.63E-01	1.87E-01	-3.76E-01	9.47E-02
			1.20E-02	1.43E-02	1.90E-02	2.20E-02	4.24E-02
			2.84E-03	4.78E-03	1.78E-03	2.14E-02	4.06E-03
9	1	8.39E-03	4.63	-1.55	1.60	-3.22E-01	8.03E-01
			9.00E-03	1.09E-02	1.29E-02	1.60E-02	1.87E-02
			1.58E-03	1.79E-03	3.84E-03	1.14E-03	6.90E-03
9	2	1.09E-02	2.13	-6.36E-01	2.08E-01	-3.55E-01	2.61E-01
			1.19E-02	1.52E-02	1.92E-02	2.18E-02	2.88E-02
			3.14E-03	4.54E-03	2.02E-03	7.04E-03	8.47E-03
			5.00	-4.82	1.89	-4.09E-01	7.63E-01

continued on next page

continued from previous page

			Peaks				
Run	T.	t_0	#1	#2	#3	#4	#5
10	1	8.47E-03	9.05E-03	1.06E-02	1.16E-02	1.59E-02	1.86E-02
			1.98E-03	8.40E-04	4.14E-03	1.24E-03	6.94E-03
10	2	1.11E-02	2.14	-9.97E-01	1.75E-01	-7.16E-01	4.35E-01
			1.20E-02	1.49E-02	1.92E-02	2.33E-02	3.11E-02
			2.58E-03	5.08E-03	1.45E-03	6.43E-03	1.30E-02
11	1	8.83E-03	4.40	-1.84	2.76	-6.64E-01	7.43E-01
			9.39E-03	1.07E-02	1.18E-02	1.32E-02	1.61E-02
			1.12E-03	1.58E-03	6.56E-04	3.15E-03	1.75E-03
11	2	1.14E-02	1.84	-6.43E-01	2.68E-01	-3.88E-01	3.15E-01
			1.27E-02	1.46E-02	1.70E-02	1.93E-02	2.17E-02
			2.34E-03	3.22E-03	1.49E-03	2.37E-03	4.45E-03
12	1	8.53E-03	4.50	-1.59	4.24E-01	-6.08E-01	9.56E-02
			9.10E-03	1.12E-02	1.59E-02	1.89E-02	2.28E-02
			1.44E-03	5.26E-03	1.59E-03	5.78E-03	1.30E-03
12	2	6.97E-03	1.37E-01	-1.37E-01	1.84E-01	-2.20	4.26E-01
			7.83E-03	9.03E-03	1.04E-02	1.21E-02	1.45E-02
			1.03E-03	1.76E-03	1.22E-03	2.71E-03	4.73E-03

Table E.32: Detailed list of pressure pulse characteristics for Test #32 of Table 4.5

			Peaks				
Run	T.	t_0	#1	#2	#3	#4	#5
1	1	8.37E-03	5.39	-9.87E-01	3.37	-1.13	3.25E-01
			8.90E-03	1.04E-02	1.10E-02	1.24E-02	1.58E-02
			1.46E-03	9.44E-04	7.12E-04	4.10E-03	1.13E-03
1	2	1.09E-02	1.78	-4.22E-01	1.41E-01	-3.28E-01	1.41E-01
			1.23E-02	1.55E-02	1.90E-02	2.23E-02	3.61E-02
			3.03E-03	4.78E-03	2.00E-03	1.37E-02	1.66E-01
2	1	8.30E-03	4.40	-1.03	3.73E-01	-5.17E-01	9.56E-02
			8.90E-03	1.07E-02	1.60E-02	1.94E-02	3.30E-02
			1.59E-03	5.70E-03	1.63E-03	1.51E-02	4.88E-03
2	2	1.09E-02	1.61	-4.09E-01	1.07E-01	-3.62E-01	1.75E-01
			1.24E-02	1.54E-02	2.01E-02	2.31E-02	3.67E-02
			3.29E-03	5.31E-03	1.31E-03	1.36E-02	7.41E-03
3	1	8.39E-03	4.64	-1.08	4.17E-01	-5.67E-01	8.92E-02
			8.98E-03	1.26E-02	1.61E-02	1.88E-02	2.34E-02
			1.58E-03	5.53E-03	1.57E-03	6.21E-03	1.34E-03
3	2	1.10E-02	1.57	-4.50E-01	1.59E-01	-4.03E-01	1.69E-01
			1.21E-02	1.54E-02	1.98E-02	2.25E-02	3.46E-02
			3.00E-03	4.94E-03	1.88E-03	1.34E-02	9.96E-03
4	1	8.39E-03	4.35	-1.13	4.60E-01	-5.25E-01	2.90E-01
			9.00E-03	1.11E-02	1.61E-02	1.92E-02	2.61E-02
			1.49E-03	5.71E-03	1.59E-03	7.02E-03	8.38E-03

continued on next page

continued from previous page

			Peaks				
Run	T.	t_0	#1	#2	#3	#4	#5
4	2	1.10E-02	1.47	-3.55E-01	1.14E-01	-3.55E-01	7.35E-02
			1.24E-02	1.53E-02	1.91E-02	2.25E-02	3.58E-02
			3.14E-03	4.80E-03	1.86E-03	1.49E-02	5.80E-03
5	1	8.50E-03	4.75	-9.69E-01	3.44E-01	-6.88E-01	3.13E-01
			9.06E-03	1.17E-02	1.61E-02	1.86E-02	2.60E-02
			2.67E-03	4.42E-03	1.48E-03	7.38E-03	5.83E-03
5	2	1.11E-02	1.56	-4.07E-01	1.55E-01	-3.60E-01	1.26E-01
			1.23E-02	1.52E-02	1.92E-02	2.29E-02	3.67E-02
			2.96E-03	4.65E-03	1.95E-03	1.52E-02	5.64E-03
6	1	8.34E-03	4.88	-1.49	2.43E-01	-6.01E-01	2.73E-01
			9.00E-03	1.11E-02	1.58E-02	1.84E-02	2.55E-02
			1.62E-03	5.46E-03	1.40E-03	7.23E-03	5.95E-03
6	2	1.09E-02	1.72	-3.43E-01	1.26E-01	-3.43E-01	7.90E-02
			1.22E-02	1.54E-02	1.91E-02	2.20E-02	4.61E-02
			3.13E-03	4.69E-03	1.70E-03	2.55E-02	2.18E-03
7	1	8.49E-03	4.99	-1.11	4.41E-01	-4.49E-01	7.44E-02
			9.09E-03	1.11E-02	1.59E-02	1.91E-02	2.41E-02
			2.14E-03	4.64E-03	1.75E-03	5.89E-03	1.29E-03
7	2	1.11E-02	2.06	-3.30E-01	3.73E-01	-5.17E-01	2.83E-01
			1.19E-02	1.45E-02	2.02E-02	2.21E-02	2.63E-02
			2.82E-03	4.26E-03	2.71E-03	5.27E-03	6.03E-03
8	1	8.52E-03	5.00	-2.19	1.23	-1.29E-01	7.62E-01
			9.10E-03	1.12E-02	1.34E-02	1.60E-02	1.90E-02
			1.45E-03	1.51E-03	4.49E-03	7.44E-04	7.15E-03
8	2	1.12E-02	1.76	-4.46E-01	1.17E-01	-6.80E-01	1.65E-01
			1.25E-02	1.54E-02	1.90E-02	2.99E-02	3.20E-02
			2.75E-03	4.88E-03	1.87E-03	1.12E-02	3.74E-03
9	1	8.50E-03	4.67	-1.38	1.24E-01	-8.13E-01	2.04E-01
			9.01E-03	1.12E-02	1.61E-02	1.94E-02	2.63E-02
			1.78E-03	5.63E-03	7.04E-04	7.10E-03	5.23E-03
9	2	1.12E-02	2.12	-3.69E-01	2.41E-01	-5.56E-01	2.75E-01
			1.22E-02	1.50E-02	1.94E-02	1.64E-01	1.65E-01
			2.77E-03	4.66E-03	1.95E-03	1.44E-01	1.51E-03
10	1	8.22E-03	4.72	-9.53E-01	2.66E-01	-6.25E-01	1.09E-01
			8.82E-03	1.18E-02	1.59E-02	1.86E-02	3.27E-02
			3.07E-03	4.30E-03	1.03E-03	1.57E-02	3.94E-03
10	2	1.09E-02	1.74	-3.73E-01	9.56E-02	-9.56E-02	3.26E-01
			1.22E-02	1.53E-02	1.87E-02	1.95E-02	2.18E-02
			3.34E-03	4.43E-03	7.04E-04	1.28E-03	1.48E-02
11	1	8.39E-03	4.95	-1.47	3.10E-01	-5.81E-01	2.53E-01
			8.96E-03	1.24E-02	1.59E-02	1.89E-02	2.60E-02
			1.74E-03	5.38E-03	1.25E-03	7.21E-03	8.71E-03
			1.82	-3.35E-01	2.74E-01	-3.82E-01	1.48E-01

continued on next page

continued from previous page

			Peaks				
Run	T.	t_0	#1	#2	#3	#4	#5
11	2	1.10E-02	1.22E-02	1.54E-02	1.99E-02	2.98E-02	3.43E-02
			2.89E-03	4.89E-03	1.96E-03	1.35E-02	1.04E-03
12	1	8.00E-03	4.55	-1.64	8.89E-01	-5.17E-01	5.61E-01
			8.58E-03	1.11E-02	1.20E-02	1.56E-02	1.84E-02
			1.92E-03	1.61E-03	3.42E-03	1.74E-03	7.28E-03
12	2	1.06E-02	1.59	-4.22E-01	1.41E-01	-3.28E-01	9.38E-02
			1.20E-02	1.41E-02	1.88E-02	2.22E-02	3.56E-02
			2.87E-03	5.04E-03	1.89E-03	1.52E-02	1.54E-03

Table E.33: Detailed list of pressure pulse characteristics for Test #33 of Table 4.5

			Peaks				
Run	T.	t_0	#1	#2	#3	#4	#5
1	1	8.24E-03	4.59	-9.38E-01	1.27	-7.50E-01	3.75E-01
			8.88E-03	1.14E-02	1.51E-02	1.84E-02	2.21E-02
			1.71E-03	4.42E-03	2.26E-03	4.74E-03	2.05E-03
1	2	1.08E-02	3.09	-7.02E-01	5.63E-01	-5.15E-01	4.68E-01
			1.17E-02	1.49E-02	1.84E-02	2.10E-02	2.78E-02
			2.51E-03	3.38E-03	3.29E-03	6.22E-03	5.24E-03
2	1	8.18E-03	4.65	-9.77E-01	1.18	-7.90E-01	3.35E-01
			8.76E-03	1.05E-02	1.50E-02	1.79E-02	2.19E-02
			1.80E-03	4.33E-03	2.02E-03	4.85E-03	2.00E-03
2	2	1.07E-02	2.95	-7.02E-01	7.04E-01	-5.62E-01	9.47E-02
			1.16E-02	1.42E-02	1.84E-02	2.11E-02	2.54E-02
			2.37E-03	3.43E-03	3.34E-03	4.70E-03	1.59E-03
3	1	7.51E-03	4.09	-4.11E-01	9.26E-01	-1.04	8.33E-01
			8.06E-03	1.04E-02	1.21E-02	1.42E-02	1.67E-02
			2.62E-03	1.16E-03	2.32E-03	1.91E-03	4.98E-03
3	2	9.95E-03	2.77	-7.96E-01	5.63E-01	-5.62E-01	9.47E-02
			1.10E-02	1.46E-02	1.77E-02	2.04E-02	2.40E-02
			2.42E-03	3.49E-03	3.24E-03	4.29E-03	2.06E-03
4	1	8.34E-03	4.07	-9.48E-01	9.27E-01	-8.07E-01	2.71E-01
			8.88E-03	1.14E-02	1.54E-02	1.78E-02	2.23E-02
			1.66E-03	4.60E-03	1.94E-03	5.03E-03	1.82E-03
4	2	1.08E-02	2.34	-6.15E-01	5.10E-01	-5.68E-01	8.82E-02
			1.18E-02	1.43E-02	1.91E-02	2.16E-02	2.51E-02
			2.50E-03	4.30E-03	2.38E-03	5.02E-03	1.20E-03
5	1	6.54E-03	4.28	-7.36E-01	1.14	-7.83E-01	2.01E-01
			7.16E-03	1.14E-02	1.34E-02	1.71E-02	2.03E-02
			3.38E-03	2.79E-03	1.97E-03	5.16E-03	1.48E-03
5	2	9.08E-03	3.11	-6.88E-01	6.24E-01	-5.48E-01	4.54E-01
			1.00E-02	1.37E-02	1.67E-02	1.96E-02	2.64E-02

continued on next page

continued from previous page

			Peaks				
Run	T.	t_0	#1	#2	#3	#4	#5
			2.46E-03	3.48E-03	3.15E-03	6.08E-03	1.38E-02
6	1	8.12E-03	4.57	-1.00	1.01	-9.57E-01	8.24E-01
			8.72E-03	1.10E-02	1.28E-02	1.51E-02	1.83E-02
			2.10E-03	1.49E-03	2.80E-03	1.82E-03	5.24E-03
6	2	1.06E-02	3.13	-6.65E-01	2.26E-01	-4.60E-01	5.24E-01
			1.16E-02	1.40E-02	1.69E-02	1.85E-02	2.14E-02
			2.77E-03	3.32E-03	8.32E-04	2.25E-03	5.87E-03
7	1	7.56E-03	4.37	-1.51	8.83E-01	-1.04	7.43E-01
			8.22E-03	1.09E-02	1.23E-02	1.46E-02	1.69E-02
			3.03E-03	6.56E-04	2.50E-03	2.05E-03	4.86E-03
7	2	1.01E-02	2.88	-7.30E-01	6.30E-01	-4.95E-01	7.35E-02
			1.12E-02	1.47E-02	1.78E-02	2.01E-02	2.54E-02
			2.37E-03	3.47E-03	3.24E-03	5.24E-03	1.04E-03
8	1	8.14E-03	3.66	-8.37E-01	1.18	-8.37E-01	3.35E-01
			8.68E-03	1.10E-02	1.47E-02	1.89E-02	2.16E-02
			1.76E-03	4.30E-03	2.09E-03	4.75E-03	1.93E-03
8	2	1.06E-02	2.83	-7.83E-01	2.95E-01	-8.58E-01	5.96E-01
			1.18E-02	1.45E-02	1.71E-02	1.83E-02	2.09E-02
			2.49E-03	3.70E-03	5.60E-04	2.27E-03	6.24E-03
9	1	7.06E-03	4.04	-9.31E-01	1.13	-8.84E-01	2.88E-01
			7.69E-03	1.09E-02	1.39E-02	1.73E-02	2.11E-02
			2.90E-03	3.31E-03	2.19E-03	4.80E-03	1.95E-03
9	2	9.54E-03	2.92	-8.30E-01	5.76E-01	-6.42E-01	4.55E-01
			1.08E-02	1.40E-02	1.73E-02	2.08E-02	2.68E-02
			2.73E-03	3.63E-03	2.92E-03	6.10E-03	6.28E-03
10	1	7.70E-03	3.81	-4.57E-01	2.31	-9.26E-01	9.96E-01
			8.39E-03	1.05E-02	1.07E-02	1.25E-02	1.46E-02
			2.27E-03	5.52E-04	9.36E-04	2.57E-03	1.97E-03
10	2	1.02E-02	3.06	-6.89E-01	7.17E-01	-7.36E-01	1.74E-01
			1.11E-02	1.48E-02	1.80E-02	2.12E-02	2.43E-02
			2.90E-03	3.40E-03	2.98E-03	4.68E-03	8.48E-04
11	1	8.22E-03	5.55	-1.20	1.33	-8.22E-01	3.97E-01
			8.80E-03	1.12E-02	1.47E-02	1.80E-02	2.18E-02
			1.95E-03	3.94E-03	2.31E-03	4.23E-03	2.50E-03
11	2	1.06E-02	2.91	-9.77E-01	6.17E-01	-6.02E-01	1.48E-01
			1.07E-02	1.37E-02	1.81E-02	2.08E-02	2.48E-02
			2.46E-03	3.70E-03	2.98E-03	4.64E-03	1.70E-03
12	1	8.04E-03	5.49	-8.89E-01	9.39E-01	-8.42E-01	2.36E-01
			9.29E-03	1.10E-02	1.50E-02	1.80E-02	2.17E-02
			2.71E-03	3.38E-03	2.06E-03	4.98E-03	1.73E-03
12	2	1.05E-02	2.61	-8.08E-01	5.51E-01	-6.20E-01	4.33E-01
			1.16E-02	1.52E-02	1.84E-02	2.08E-02	2.79E-02
			2.68E-03	4.12E-03	2.18E-03	6.45E-03	6.83E-03

continued on next page

continued from previous page

			Peaks				
Run	T.	t_0	#1	#2	#3	#4	#5

Table E.34: Detailed list of pressure pulse characteristics for Test #34 of Table 4.5

			Peaks				
Run	T.	t_0	#1	#2	#3	#4	#5
			6.63	-1.81	2.32	-1.99	1.32
1	1	8.31E-03	8.40E-03	1.33E-02	1.42E-02	1.67E-02	2.01E-02
			1.98E-03	3.66E-03	1.41E-03	4.55E-03	1.38E-03
			5.75	-8.71E-01	9.34E-01	-3.25	1.12
1	2	1.09E-02	1.13E-02	1.50E-02	1.63E-02	1.72E-02	2.11E-02
			3.57E-03	1.03E-03	1.21E-03	2.18E-03	3.99E-03
			5.23	-1.98	3.23	-1.58	1.92
2	1	8.18E-03	8.51E-03	1.36E-02	1.39E-02	1.82E-02	2.02E-02
			2.65E-03	2.98E-03	1.54E-03	4.34E-03	1.58E-03
			6.98	-1.15	3.48	-1.21	1.60
2	2	1.07E-02	1.12E-02	1.65E-02	1.70E-02	2.10E-02	2.28E-02
			3.66E-03	2.18E-03	2.01E-03	4.23E-03	1.54E-03
			4.42	-3.30	2.30	-2.20	1.11
3	1	8.68E-03	8.81E-03	1.39E-02	1.44E-02	1.60E-02	2.02E-02
			1.45E-03	3.97E-03	1.18E-03	4.84E-03	1.12E-03
			5.65	-9.77E-01	1.16	-2.96	1.29
3	2	1.10E-02	1.15E-02	1.54E-02	1.68E-02	1.74E-02	2.13E-02
			3.64E-03	8.56E-04	1.31E-03	2.04E-03	4.23E-03
			4.92	-1.89	1.73	-2.52	1.77
4	1	8.46E-03	8.58E-03	1.38E-02	1.46E-02	1.83E-02	2.21E-02
			1.94E-03	3.70E-03	9.84E-04	5.81E-03	5.28E-03
			5.97	-8.39E-01	1.21	-3.10	1.21
4	2	1.11E-02	1.15E-02	1.52E-02	1.68E-02	1.74E-02	2.13E-02
			3.86E-03	7.28E-04	1.32E-03	1.95E-03	4.22E-03
			4.49	-2.24	1.76	-1.99	1.88
5	1	8.76E-03	8.80E-03	9.44E-03	1.39E-02	1.46E-02	1.83E-02
			5.76E-04	1.34E-03	3.47E-03	1.17E-03	4.89E-03
			4.90	-9.74E-01	2.65	-1.16	1.40
5	2	1.11E-02	1.16E-02	1.68E-02	1.72E-02	2.14E-02	2.33E-02
			4.55E-03	1.29E-03	2.02E-03	4.00E-03	1.71E-03
			4.29	-1.21	1.83	-2.17	2.27
6	1	1.00E-02	1.05E-02	1.18E-02	1.50E-02	1.58E-02	1.75E-02
			1.39E-03	9.04E-04	3.17E-03	9.76E-04	5.05E-03
			5.03	-7.79E-01	1.03	-2.60	9.67E-01
6	2	1.24E-02	1.29E-02	1.63E-02	1.81E-02	1.89E-02	2.27E-02
			3.92E-03	6.80E-04	1.26E-03	1.98E-03	4.26E-03
			5.61	-2.32	2.43	-2.70	1.18

continued on next page

continued from previous page

			Peaks				
Run	T.	t_0	#1	#2	#3	#4	#5
7	1	7.98E-03	8.38E-03	1.32E-02	1.38E-02	1.92E-02	1.99E-02
			1.91E-03	3.61E-03	1.43E-03	4.65E-03	1.20E-03
7	2	1.06E-02	7.64	-1.73	3.52	-1.54	1.64
			1.10E-02	1.59E-02	1.67E-02	2.18E-02	2.28E-02
			3.59E-03	2.09E-03	2.56E-03	3.65E-03	1.52E-03
8	1	7.40E-03	6.12	-1.76	2.62	-2.01	1.55
			7.74E-03	1.22E-02	1.32E-02	1.84E-02	1.91E-02
			1.92E-03	3.61E-03	1.46E-03	4.50E-03	1.41E-03
8	2	9.98E-03	7.28	-8.47E-01	1.22	-3.34	1.35
			1.04E-02	1.41E-02	1.55E-02	1.60E-02	2.02E-02
			3.70E-03	8.08E-04	1.20E-03	2.32E-03	3.90E-03
9	1	8.19E-03	6.86	-1.83	3.11	-1.89	1.67
			8.30E-03	1.38E-02	1.41E-02	1.80E-02	1.99E-02
			2.22E-03	3.42E-03	1.40E-03	4.59E-03	1.37E-03
9	2	1.08E-02	6.32	-1.18	3.32	-1.24	1.70
			1.12E-02	1.63E-02	1.69E-02	2.10E-02	2.28E-02
			3.72E-03	2.06E-03	2.04E-03	4.20E-03	1.52E-03
10	1	8.18E-03	6.74	-1.64	3.80	-1.82	1.74
			8.30E-03	1.28E-02	1.39E-02	1.80E-02	1.99E-02
			2.30E-03	3.29E-03	1.62E-03	4.30E-03	1.44E-03
10	2	1.07E-02	7.05	-1.51	3.30	-1.33	1.61
			1.12E-02	1.64E-02	1.69E-02	2.10E-02	2.31E-02
			3.48E-03	2.57E-03	1.79E-03	4.22E-03	1.45E-03
11	1	7.02E-03	5.47	-1.72	2.22	-2.03	1.53
			7.13E-03	1.19E-02	1.29E-02	1.68E-02	1.90E-02
			2.37E-03	3.13E-03	1.51E-03	4.51E-03	1.38E-03
11	2	9.53E-03	6.90	-8.54E-01	1.42	-3.52	1.48
			9.97E-03	1.37E-02	1.53E-02	1.57E-02	2.13E-02
			3.94E-03	8.40E-04	1.02E-03	2.21E-03	4.02E-03
12	1	1.04E-02	5.56	-1.94	2.68	-1.88	1.50
			1.04E-02	1.57E-02	1.60E-02	2.01E-02	2.24E-02
			2.18E-03	3.46E-03	1.35E-03	4.58E-03	1.42E-03
12	2	1.29E-02	6.92	-9.58E-01	1.27	-3.23	1.33
			1.33E-02	1.70E-02	1.87E-02	1.93E-02	2.31E-02
			3.72E-03	9.84E-04	1.06E-03	2.30E-03	3.94E-03

Table E.35: Detailed list of pressure pulse characteristics for Test #35 of Table 4.5

			Peaks				
Run	T.	t_0	#1	#2	#3	#4	#5
1	1	8.36E-03	5.33	-1.61	1.49	-8.90E-01	9.85E-01
			9.14E-03	1.03E-02	1.17E-02	1.52E-02	1.77E-02
			1.60E-03	1.22E-03	3.01E-03	2.05E-03	4.92E-03
			3.79	-1.21	4.74E-01	-6.51E-01	4.63E-01

continued on next page

continued from previous page

			Peaks				
Run	T.	t_0	#1	#2	#3	#4	#5
1	2	1.08E-02	1.13E-02	1.44E-02	1.80E-02	2.10E-02	2.74E-02
			2.27E-03	3.53E-03	2.75E-03	5.86E-03	6.09E-03
2	1	8.31E-03	5.70	-1.68	2.63	-1.55	1.07
			9.08E-03	1.04E-02	1.08E-02	1.17E-02	1.50E-02
			1.67E-03	6.80E-04	5.36E-04	2.90E-03	2.04E-03
2	2	1.07E-02	4.60	-1.53	5.33E-01	-7.17E-01	4.04E-01
			1.13E-02	1.42E-02	1.79E-02	2.04E-02	2.67E-02
			1.99E-03	3.81E-03	2.62E-03	6.26E-03	4.38E-03
3	1	8.25E-03	4.94	-1.81	1.38	-8.75E-01	1.13
			8.99E-03	1.05E-02	1.31E-02	1.46E-02	1.73E-02
			1.71E-03	1.98E-03	2.37E-03	1.74E-03	4.95E-03
3	2	3.67E-03	4.48	-1.39	3.58E-01	-6.70E-01	7.05E-01
			1.15E-02	1.38E-02	1.68E-02	1.80E-02	2.06E-02
			9.29E-03	3.58E-03	7.68E-04	1.87E-03	4.41E-03
4	1	8.52E-03	5.55	-2.27	9.22E-01	-1.20	2.34E-01
			9.29E-03	1.16E-02	1.53E-02	1.84E-02	2.18E-02
			1.74E-03	4.08E-03	2.01E-03	4.77E-03	1.66E-03
4	2	1.10E-02	4.22	-1.41	4.66E-01	-5.97E-01	1.53E-01
			1.17E-02	1.45E-02	1.81E-02	2.13E-02	2.46E-02
			2.18E-03	3.51E-03	2.84E-03	4.21E-03	2.06E-03
5	1	8.39E-03	5.67	-2.29	1.77	-7.32E-01	1.14
			9.23E-03	1.12E-02	1.20E-02	1.46E-02	1.78E-02
			1.48E-03	1.50E-03	2.83E-03	1.91E-03	5.25E-03
5	2	1.09E-02	4.65	-1.42	3.33E-01	-7.92E-01	4.79E-01
			1.15E-02	1.45E-02	1.78E-02	2.06E-02	2.72E-02
			2.08E-03	4.28E-03	1.87E-03	6.17E-03	4.70E-03
6	1	8.32E-03	6.01	-1.81	1.68	-1.01	1.06
			9.02E-03	1.06E-02	1.18E-02	1.51E-02	1.74E-02
			1.61E-03	1.14E-03	3.06E-03	1.94E-03	4.82E-03
6	2	1.07E-02	3.95	-1.42	5.16E-01	-6.09E-01	1.41E-01
			1.13E-02	1.45E-02	1.78E-02	2.15E-02	2.46E-02
			2.20E-03	3.43E-03	2.90E-03	4.45E-03	1.66E-03
7	1	1.06E-02	5.92	-1.83	1.17	-1.15	2.92E-01
			1.12E-02	1.41E-02	1.69E-02	2.03E-02	2.39E-02
			2.76E-03	3.06E-03	2.19E-03	4.78E-03	1.60E-03
7	2	1.30E-02	3.90	-1.35	5.29E-01	-6.58E-01	9.19E-02
			1.36E-02	1.64E-02	2.01E-02	2.30E-02	2.64E-02
			2.28E-03	3.54E-03	2.93E-03	4.62E-03	1.42E-03
8	1	8.27E-03	6.06	-2.13	8.11E-01	-1.13	1.86E-01
			9.00E-03	1.07E-02	1.47E-02	1.76E-02	2.16E-02
			1.70E-03	4.11E-03	1.88E-03	5.04E-03	1.13E-03
8	2	1.07E-02	3.96	-1.35	4.63E-01	-5.99E-01	1.51E-01
			1.14E-02	1.40E-02	1.77E-02	2.06E-02	2.45E-02

continued on next page

continued from previous page

			Peaks				
Run	T.	t_0	#1	#2	#3	#4	#5
			2.19E-03	3.48E-03	2.87E-03	4.36E-03	1.76E-03
9	1	1.05E-02	6.57	-1.99	9.44E-01	-1.18	3.19E-01
			1.12E-02	1.28E-02	1.72E-02	2.05E-02	2.35E-02
			1.69E-03	3.86E-03	2.30E-03	4.34E-03	2.06E-03
9	2	1.29E-02	3.90	-1.48	5.25E-01	-6.63E-01	2.12E-01
			1.36E-02	1.66E-02	2.01E-02	2.32E-02	2.66E-02
			2.28E-03	3.48E-03	2.81E-03	3.91E-03	2.36E-03
10	1	8.34E-03	5.57	-1.93	1.13	-1.18	3.16E-01
			9.07E-03	1.14E-02	1.50E-02	1.83E-02	2.16E-02
			1.62E-03	3.81E-03	2.41E-03	4.35E-03	1.87E-03
10	2	1.07E-02	4.32	-1.50	5.67E-01	-8.08E-01	1.30E-01
			1.14E-02	1.45E-02	1.79E-02	2.08E-02	2.41E-02
			2.14E-03	3.59E-03	2.69E-03	4.70E-03	1.44E-03
11	1	8.36E-03	4.63	-1.12	8.21E-01	-1.18	8.21E-01
			9.04E-03	1.04E-02	1.12E-02	1.30E-02	1.51E-02
			1.62E-03	7.68E-04	1.26E-03	2.38E-03	1.72E-03
11	2	1.08E-02	3.47	-1.09	4.71E-01	-5.92E-01	4.04E-01
			1.13E-02	1.45E-02	1.83E-02	2.06E-02	2.66E-02
			2.24E-03	4.05E-03	2.16E-03	5.98E-03	1.25E-02
12	1	8.43E-03	6.07	-2.43	1.13	-1.12	2.59E-01
			9.22E-03	1.06E-02	1.51E-02	1.75E-02	2.15E-02
			1.54E-03	3.90E-03	2.31E-03	4.54E-03	1.83E-03
12	2	8.68E-03	1.72E-01	-3.42	1.52	-6.72E-01	6.41E-01
			8.90E-03	1.15E-02	1.38E-02	1.78E-02	2.10E-02
			2.14E-03	2.13E-03	3.46E-03	2.87E-03	3.92E-03

Table E.36: Detailed list of pressure pulse characteristics for Test #36 of Table 4.5

			Peaks				
Run	T.	t_0	#1	#2	#3	#4	#5
1	1	8.35E-03	4.51	-1.83	1.67	-1.26	1.05
			8.90E-03	1.08E-02	1.13E-02	1.46E-02	1.77E-02
			1.59E-03	9.68E-04	3.09E-03	1.98E-03	4.30E-03
1	2	1.07E-02	3.36	-1.14	6.75E-01	-5.75E-01	2.38E-01
			1.13E-02	1.42E-02	1.76E-02	2.04E-02	2.43E-02
			2.09E-03	3.35E-03	2.98E-03	3.66E-03	2.37E-03
2	1	7.12E-03	5.47	-1.53	1.28	-9.03E-01	2.84E-01
			7.70E-03	1.04E-02	1.32E-02	1.68E-02	2.01E-02
			2.86E-03	2.86E-03	2.02E-03	4.55E-03	1.66E-03
2	2	9.48E-03	3.93	-1.01	1.80E-01	-6.18E-01	5.07E-01
			1.01E-02	1.31E-02	1.53E-02	1.64E-02	1.90E-02
			2.25E-03	3.42E-03	7.04E-04	2.13E-03	4.45E-03
			7.72	-1.40	9.09E-01	-9.66E-01	2.22E-01

continued on next page

continued from previous page

			Peaks				
Run	T.	t_0	#1	#2	#3	#4	#5
3	1	7.54E-03	9.37E-03	1.07E-02	1.39E-02	1.73E-02	2.08E-02
			2.40E-03	3.52E-03	1.84E-03	5.03E-03	1.15E-03
3	2	9.95E-03	3.37	-7.59E-01	6.16E-01	-6.34E-01	5.09E-01
			1.05E-02	1.37E-02	1.75E-02	2.04E-02	2.59E-02
			2.41E-03	3.97E-03	2.22E-03	5.35E-03	1.25E-02
4	1	8.38E-03	5.22	-1.53	1.34	-1.10	9.01E-01
			8.89E-03	1.04E-02	1.13E-02	1.46E-02	1.73E-02
			1.58E-03	1.05E-03	2.95E-03	2.17E-03	4.23E-03
4	2	7.79E-03	2.35E-01	-3.30	1.14	-6.10E-01	7.02E-01
			7.80E-03	1.12E-02	1.36E-02	1.77E-02	2.03E-02
			2.95E-03	2.01E-03	3.50E-03	2.71E-03	4.83E-03
5	1	8.14E-03	4.47	-1.16	1.16	-6.57E-01	2.81E-01
			8.72E-03	1.12E-02	1.45E-02	1.68E-02	2.13E-02
			2.46E-03	3.34E-03	2.13E-03	4.63E-03	1.64E-03
5	2	7.55E-03	1.79E-01	-1.16E-01	3.37	-7.59E-01	4.91E-01
			7.59E-03	8.53E-03	1.13E-02	1.40E-02	1.77E-02
			9.20E-04	2.00E-03	2.45E-03	4.07E-03	1.96E-03
6	1	1.06E-02	4.95	-1.18	1.49	-1.45	9.25E-01
			1.11E-02	1.27E-02	1.36E-02	1.69E-02	1.91E-02
			1.75E-03	7.20E-04	3.10E-03	2.22E-03	3.78E-03
6	2	1.00E-02	1.79E-01	-3.55	1.32	-7.41E-01	7.59E-01
			1.01E-02	1.36E-02	1.62E-02	1.99E-02	2.28E-02
			2.91E-03	2.06E-03	3.47E-03	2.65E-03	4.07E-03
7	1	8.40E-03	5.03	-1.34	7.16E-01	-9.09E-01	9.03E-01
			8.95E-03	1.12E-02	1.38E-02	1.46E-02	1.75E-02
			1.54E-03	2.72E-03	1.43E-03	1.74E-03	5.18E-03
7	2	1.08E-02	3.52	-9.17E-01	5.83E-01	-5.42E-01	4.17E-01
			1.13E-02	1.41E-02	1.76E-02	2.05E-02	2.63E-02
			2.10E-03	3.33E-03	2.96E-03	5.91E-03	4.91E-03
8	1	8.45E-03	5.45	-1.83	1.17	-7.01E-01	1.11
			9.06E-03	1.10E-02	1.30E-02	1.47E-02	1.76E-02
			2.03E-03	2.00E-03	1.86E-03	1.85E-03	5.26E-03
8	2	1.09E-02	3.41	-9.66E-01	1.59E-01	-5.34E-01	5.91E-01
			1.14E-02	1.43E-02	1.68E-02	1.79E-02	2.05E-02
			2.26E-03	3.48E-03	5.12E-04	2.30E-03	4.13E-03
9	1	8.36E-03	5.96	-1.10	1.48	-7.10E-01	9.15E-01
			8.96E-03	1.04E-02	1.17E-02	1.49E-02	1.76E-02
			1.60E-03	1.26E-03	3.05E-03	1.82E-03	5.14E-03
9	2	1.08E-02	3.30	-9.55E-01	4.83E-01	-5.17E-01	3.92E-01
			1.13E-02	1.41E-02	1.81E-02	2.07E-02	2.67E-02
			2.30E-03	4.24E-03	1.87E-03	5.42E-03	1.40E-02
10	1	8.35E-03	5.26	-8.63E-01	1.49	-9.50E-01	1.05
			8.94E-03	1.02E-02	1.16E-02	1.48E-02	1.73E-02

continued on next page

continued from previous page							
			Peaks				
Run	T.	t_0	#1	#2	#3	#4	#5
			1.60E-03	7.68E-04	3.18E-03	2.12E-03	4.91E-03
10	2	1.07E-02	3.68	-1.13	5.58E-01	-5.67E-01	3.80E-01
			1.13E-02	1.37E-02	1.76E-02	2.03E-02	2.62E-02
			2.14E-03	3.29E-03	2.90E-03	6.15E-03	5.72E-03
11	1	1.06E-02	5.22	-1.22	5.29E-01	-1.03	1.03
			1.11E-02	1.37E-02	1.52E-02	1.68E-02	1.96E-02
			2.53E-03	1.63E-03	1.38E-03	2.07E-03	5.22E-03
11	2	1.30E-02	3.12	-1.01	5.56E-01	-5.69E-01	4.44E-01
			1.35E-02	1.62E-02	2.01E-02	2.26E-02	2.92E-02
			2.04E-03	3.44E-03	2.81E-03	5.91E-03	5.08E-03
12	1	8.49E-03	4.66	-1.84	1.04	-9.63E-01	3.49E-01
			8.98E-03	1.07E-02	1.47E-02	1.68E-02	2.11E-02
			1.50E-03	3.94E-03	1.80E-03	4.48E-03	1.90E-03
12	2	1.08E-02	3.31	-1.13	6.23E-01	-5.65E-01	2.48E-01
			1.14E-02	1.34E-02	1.77E-02	2.00E-02	2.29E-02
			1.82E-03	3.26E-03	2.99E-03	3.61E-03	2.38E-03

Table E.37: Detailed list of pressure pulse characteristics for Test #37 of Table 4.5

			Peaks				
Run	T.	t_0	#1	#2	#3	#4	#5
1	1	8.30E-03	8.00	-1.82	4.81	-2.69	1.81
			8.63E-03	1.32E-02	1.38E-02	1.88E-02	1.99E-02
			2.64E-03	2.46E-03	2.49E-03	3.60E-03	1.74E-03
1	2	1.08E-02	8.16	-2.53	3.97	-2.59	2.10
			1.10E-02	1.62E-02	1.68E-02	2.20E-02	2.27E-02
			3.30E-03	2.44E-03	2.18E-03	3.84E-03	1.52E-03
2	1	8.46E-03	7.77	-6.95	7.33	-2.30	2.64
			8.79E-03	1.38E-02	1.40E-02	1.91E-02	2.01E-02
			2.71E-03	2.68E-03	2.81E-03	2.97E-03	1.97E-03
2	2	1.10E-02	8.19	-1.94	4.88	-2.31	1.88
			1.12E-02	1.64E-02	1.70E-02	2.23E-02	2.28E-02
			3.76E-03	1.77E-03	2.44E-03	3.74E-03	1.53E-03
3	1	1.04E-02	5.31	-3.50	2.81	-3.63	2.38
			1.08E-02	1.52E-02	1.60E-02	2.12E-02	2.72E-02
			1.53E-03	3.86E-03	1.42E-03	5.70E-03	5.10E-03
3	2	1.28E-02	8.17	-2.39	4.24	-2.70	1.49
			1.31E-02	1.83E-02	1.87E-02	2.43E-02	2.47E-02
			3.63E-03	2.06E-03	2.60E-03	3.48E-03	1.58E-03
4	1	8.29E-03	7.49	-3.17	5.11	-2.51	3.36
			8.83E-03	1.35E-02	1.38E-02	1.91E-02	1.95E-02
			2.50E-03	2.69E-03	2.77E-03	3.14E-03	2.39E-03
continued on next page							

continued from previous page

			Peaks				
Run	T.	t_0	#1	#2	#3	#4	#5
			8.17	-2.27	5.61	-2.64	2.17
4	2	1.07E-02	1.10E-02	1.57E-02	1.67E-02	2.18E-02	2.26E-02
			3.71E-03	1.93E-03	2.73E-03	3.30E-03	1.71E-03
			7.19	-4.51	4.94	-2.68	2.01
5	1	8.22E-03	8.52E-03	1.35E-02	1.41E-02	1.91E-02	1.99E-02
			2.54E-03	2.78E-03	1.82E-03	4.09E-03	1.74E-03
			8.18	-2.20	4.24	-2.57	1.74
5	2	1.07E-02	1.10E-02	1.61E-02	1.69E-02	2.20E-02	2.26E-02
			3.45E-03	2.14E-03	2.51E-03	3.70E-03	1.66E-03
			7.89	-1.30	5.51	-2.05	2.57
6	1	8.29E-03	8.63E-03	1.31E-02	1.38E-02	1.89E-02	1.95E-02
			3.22E-03	1.86E-03	3.72E-03	2.29E-03	2.82E-03
			8.18	-2.44	4.31	-2.63	1.74
6	2	1.08E-02	1.10E-02	1.58E-02	1.66E-02	2.20E-02	2.26E-02
			3.66E-03	1.97E-03	2.78E-03	3.26E-03	1.56E-03
			7.95	-2.49	4.32	-3.18	1.70
7	1	8.21E-03	8.66E-03	1.30E-02	1.36E-02	1.86E-02	1.96E-02
			2.66E-03	2.41E-03	2.21E-03	3.75E-03	1.70E-03
			7.95	-2.68	4.64	-3.11	1.70
7	2	1.07E-02	1.09E-02	1.56E-02	1.67E-02	2.18E-02	2.24E-02
			3.83E-03	1.76E-03	2.47E-03	3.45E-03	1.90E-03
			7.83	-2.67	3.40	-2.67	1.90
8	1	8.05E-03	8.11E-03	1.30E-02	1.37E-02	1.88E-02	1.97E-02
			1.73E-03	3.59E-03	1.62E-03	4.28E-03	1.50E-03
			7.88	-1.87	4.56	-2.37	2.19
8	2	1.05E-02	1.08E-02	1.59E-02	1.66E-02	2.19E-02	2.25E-02
			3.85E-03	1.74E-03	2.30E-03	3.90E-03	1.43E-03
			7.99	-2.70	3.36	-3.26	1.43
9	1	8.24E-03	8.33E-03	1.31E-02	1.37E-02	1.87E-02	1.98E-02
			2.02E-03	3.23E-03	1.75E-03	4.26E-03	1.41E-03
			8.18	-2.64	5.30	-2.89	1.74
9	2	1.07E-02	1.10E-02	1.62E-02	1.68E-02	2.20E-02	2.24E-02
			3.84E-03	1.90E-03	2.61E-03	3.32E-03	1.46E-03
			6.05	-1.76	3.36	-2.01	1.74
10	1	1.03E-02	1.06E-02	1.53E-02	1.60E-02	2.13E-02	2.22E-02
			2.17E-03	3.10E-03	1.83E-03	4.26E-03	1.53E-03
			8.11	-1.58	3.86	-2.02	1.80
10	2	1.28E-02	1.32E-02	1.82E-02	1.88E-02	2.44E-02	2.50E-02
			3.87E-03	1.80E-03	2.32E-03	3.93E-03	1.46E-03
			6.93	-2.01	4.30	-2.82	1.74
11	1	7.40E-03	7.87E-03	1.22E-02	1.28E-02	1.80E-02	1.89E-02
			2.45E-03	2.66E-03	2.35E-03	3.68E-03	1.73E-03
			8.17	-2.58	4.17	-2.76	1.36

continued on next page

continued from previous page

			Peaks				
Run	T.	t_0	#1	#2	#3	#4	#5
11	2	9.87E-03	1.01E-02	1.53E-02	1.57E-02	2.11E-02	2.16E-02
			3.73E-03	1.92E-03	2.50E-03	3.54E-03	1.46E-03
12	1	7.74E-03	7.98	-2.52	2.80	-3.02	1.55
			7.81E-03	1.27E-02	1.37E-02	1.84E-02	1.93E-02
			2.22E-03	3.06E-03	1.70E-03	4.52E-03	1.22E-03
12	2	1.02E-02	8.17	-2.27	4.23	-2.58	1.92
			1.05E-02	1.57E-02	1.64E-02	2.16E-02	2.20E-02
			3.71E-03	2.02E-03	2.68E-03	3.33E-03	1.66E-03

Table E.38: Detailed list of pressure pulse characteristics for Test #38 of Table 4.5

			Peaks				
Run	T.	t_0	#1	#2	#3	#4	#5
1	1	1.06E-02	5.34	-2.66	1.41	-5.26E-01	1.54
			1.10E-02	1.32E-02	1.57E-02	1.70E-02	1.99E-02
			1.34E-03	3.27E-03	1.28E-03	1.34E-03	5.35E-03
1	2	1.35E-02	3.57	-4.46E-01	1.57	-4.91E-01	1.16E-01
			1.37E-02	2.77E-02	3.02E-02	4.11E-02	7.16E-02
			9.06E-03	6.00E-03	1.90E-03	4.11E-02	9.76E-04
2	1	1.08E-02	5.02	-4.48	2.11E-01	-3.36E-01	1.48E-01
			1.10E-02	1.37E-02	4.17E-02	5.93E-02	1.35E-01
			7.20E-04	2.92E-02	5.18E-03	8.92E-02	1.38E-03
2	2	1.30E-02	1.78	-5.59	3.47E-01	-9.68E-02	9.68E-02
			1.35E-02	1.50E-02	4.15E-02	1.17E-01	1.19E-01
			6.64E-04	1.89E-02	8.45E-02	1.59E-03	2.02E-03
3	1	8.62E-03	7.22	-2.53	6.57E-01	-1.34	1.57E-01
			9.30E-03	1.20E-02	1.49E-02	1.85E-02	2.17E-02
			2.73E-03	3.06E-03	1.80E-03	5.27E-03	8.96E-04
3	2	1.10E-02	4.13	-1.43	6.31E-01	-5.56E-01	1.31E-01
			1.16E-02	1.49E-02	1.83E-02	2.08E-02	2.37E-02
			2.20E-03	3.42E-03	2.94E-03	3.87E-03	2.30E-03
4	1	8.30E-03	7.95	-2.43	1.32	-1.36	3.25E-01
			8.81E-03	1.13E-02	1.46E-02	1.78E-02	2.15E-02
			1.67E-03	3.96E-03	1.90E-03	4.51E-03	1.88E-03
4	2	1.07E-02	4.30	-1.51	7.39E-01	-7.61E-01	1.76E-01
			1.15E-02	1.40E-02	1.77E-02	2.05E-02	2.32E-02
			2.06E-03	3.35E-03	3.02E-03	3.96E-03	2.10E-03
5	1	8.53E-03	6.03	-2.09	5.97E-01	-1.59	2.84E-01
			9.35E-03	1.06E-02	1.48E-02	1.84E-02	2.19E-02
			1.46E-03	4.46E-03	1.50E-03	5.37E-03	1.10E-03
5	2	1.09E-02	4.53	-1.47	6.51E-01	-6.62E-01	1.51E-01
			1.16E-02	1.43E-02	1.81E-02	2.07E-02	2.37E-02

continued on next page

continued from previous page

			Peaks				
Run	T.	t_0	#1	#2	#3	#4	#5
			2.24E-03	3.32E-03	2.90E-03	4.06E-03	2.15E-03
6	1	7.75E-03	6.18	-2.76	4.31E-01	-1.51	6.31E-01
			9.34E-03	1.13E-02	1.46E-02	1.73E-02	2.36E-02
			2.24E-03	3.90E-03	1.32E-03	6.46E-03	7.18E-03
6	2	7.38E-03	1.65E-01	-4.29	1.33	-4.78E-01	6.47E-01
			8.04E-03	1.08E-02	1.40E-02	1.73E-02	2.02E-02
			2.86E-03	2.15E-03	4.20E-03	2.16E-03	5.94E-03
7	1	8.46E-03	6.12	-2.56	4.36E-01	-1.31	2.49E-01
			9.10E-03	1.15E-02	1.49E-02	1.72E-02	2.17E-02
			1.50E-03	4.56E-03	1.34E-03	5.32E-03	1.42E-03
7	2	1.19E-02	2.05E-01	-9.83E-01	2.67E-01	-9.20E-01	3.30E-01
			1.21E-02	1.27E-02	1.40E-02	1.46E-02	1.63E-02
			6.80E-04	1.24E-03	6.32E-04	1.52E-03	1.06E-03
8	1	8.44E-03	7.02	-2.85	4.00E-01	-1.16	1.50E-01
			9.07E-03	1.06E-02	1.52E-02	1.73E-02	2.17E-02
			1.50E-03	4.60E-03	1.34E-03	5.65E-03	9.28E-04
8	2	1.11E-02	4.33	-1.49	6.38E-01	-6.12E-01	1.38E-01
			1.19E-02	1.44E-02	1.82E-02	2.08E-02	2.39E-02
			2.07E-03	3.40E-03	2.98E-03	3.87E-03	2.34E-03
9	1	8.44E-03	7.02	-2.85	4.00E-01	-1.16	1.50E-01
			9.07E-03	1.06E-02	1.52E-02	1.73E-02	2.17E-02
			1.50E-03	4.60E-03	1.34E-03	5.65E-03	9.28E-04
9	2	1.08E-02	4.15	-1.35	4.58E-01	-4.79E-01	1.46E-01
			1.17E-02	1.42E-02	1.83E-02	2.08E-02	2.44E-02
			2.07E-03	3.74E-03	2.99E-03	3.95E-03	2.30E-03
10	1	8.35E-03	5.96	-2.66	6.51E-01	-1.29	2.13E-01
			8.95E-03	1.14E-02	1.50E-02	1.78E-02	2.18E-02
			1.64E-03	4.34E-03	1.41E-03	5.49E-03	1.07E-03
10	2	1.07E-02	4.45	-1.49	5.11E-01	-6.14E-01	7.35E-02
			1.13E-02	1.44E-02	1.80E-02	2.08E-02	2.34E-02
			2.19E-03	3.78E-03	2.48E-03	4.13E-03	1.86E-03
11	1	8.41E-03	6.01	-2.24	1.14	-1.11	3.26E-01
			9.00E-03	1.14E-02	1.46E-02	1.81E-02	2.16E-02
			1.56E-03	4.18E-03	2.19E-03	4.54E-03	1.82E-03
11	2	1.08E-02	3.88	-1.30	5.09E-01	-5.54E-01	1.34E-01
			1.12E-02	1.42E-02	1.80E-02	2.06E-02	2.46E-02
			2.26E-03	3.76E-03	2.66E-03	4.45E-03	1.71E-03
12	1	1.07E-02	6.15	-3.97	1.53E-01	-2.78E-01	1.53E-01
			1.11E-02	1.35E-02	4.16E-02	5.92E-02	1.13E-01
			9.20E-04	2.95E-02	5.24E-03	6.59E-02	4.90E-03
12	2	1.28E-02	4.45	-1.36	4.53E-01	-6.09E-01	1.09E-01
			1.35E-02	1.63E-02	1.98E-02	2.25E-02	2.73E-02
			2.18E-03	3.31E-03	2.93E-03	4.61E-03	1.49E-03

continued on next page

continued from previous page

			Peaks				
Run	T.	t_0	#1	#2	#3	#4	#5

Table E.39: Detailed list of pressure pulse characteristics for Test #39 of Table 4.5

			Peaks				
Run	T.	t_0	#1	#2	#3	#4	#5
1	1	7.78E-03	6.31	-1.63	7.44E-01	-9.44E-01	1.81E-01
			8.40E-03	1.06E-02	1.41E-02	1.68E-02	2.07E-02
			2.20E-03	3.46E-03	1.87E-03	5.14E-03	1.20E-03
1	2	1.02E-02	4.05	-1.14	1.36E-01	-4.26E-01	6.36E-01
			1.07E-02	1.34E-02	1.63E-02	1.72E-02	1.96E-02
			2.08E-03	3.97E-03	5.20E-04	1.57E-03	5.60E-03
2	1	7.97E-03	5.81	-2.13	6.21E-01	-1.07	2.46E-01
			8.58E-03	1.13E-02	1.44E-02	1.72E-02	2.12E-02
			1.94E-03	3.96E-03	1.64E-03	5.27E-03	1.33E-03
2	2	1.04E-02	3.91	-1.15	4.08E-01	-6.54E-01	9.56E-02
			1.11E-02	1.40E-02	1.75E-02	2.00E-02	2.40E-02
			2.16E-03	4.38E-03	1.74E-03	5.26E-03	1.15E-03
3	1	8.39E-03	6.33	-2.05	8.27E-01	-9.85E-01	2.02E-01
			8.94E-03	1.16E-02	1.45E-02	1.73E-02	2.14E-02
			1.98E-03	3.86E-03	1.74E-03	4.86E-03	1.50E-03
3	2	1.08E-02	4.19	-1.13	6.25E-01	-9.38E-01	6.88E-01
			1.12E-02	1.40E-02	1.73E-02	1.80E-02	2.06E-02
			2.17E-03	3.38E-03	1.10E-03	1.76E-03	5.04E-03
4	1	7.86E-03	8.01	-2.12	6.34E-01	-1.24	1.34E-01
			9.42E-03	1.11E-02	1.41E-02	1.70E-02	2.08E-02
			2.13E-03	3.74E-03	1.54E-03	5.38E-03	1.07E-03
4	2	1.03E-02	4.06	-1.19	2.50E-01	-6.25E-01	6.25E-01
			1.05E-02	1.33E-02	1.59E-02	1.72E-02	2.02E-02
			2.06E-03	3.34E-03	1.07E-03	1.98E-03	6.05E-03
5	1	7.66E-03	8.00	-2.25	3.09E-01	-1.13	5.66E-01
			9.44E-03	1.07E-02	1.40E-02	1.70E-02	2.36E-02
			2.30E-03	3.78E-03	1.19E-03	6.05E-03	1.81E-02
5	2	1.01E-02	3.95	-9.23E-01	4.52E-01	-4.23E-01	4.23E-01
			1.06E-02	1.36E-02	1.72E-02	2.00E-02	2.65E-02
			2.22E-03	4.25E-03	2.31E-03	5.86E-03	2.06E-02
6	1	7.34E-03	6.48	-2.02	4.22E-01	-1.27	1.41E-01
			7.92E-03	1.06E-02	1.36E-02	1.72E-02	3.51E-02
			2.61E-03	3.44E-03	1.18E-03	1.97E-02	1.27E-02
6	2	9.68E-03	4.10	-1.03	4.73E-01	-5.27E-01	8.95E-02
			1.04E-02	1.32E-02	1.69E-02	1.97E-02	3.63E-02
			2.20E-03	4.36E-03	1.98E-03	1.80E-02	2.10E-03
			6.83	-2.49	2.37E-01	-2.01E-01	1.38E-01

continued on next page

continued from previous page							
			Peaks				
Run	T.	t_0	#1	#2	#3	#4	#5
7	1	7.54E-03	8.08E-03	1.12E-02	2.90E-02	3.23E-02	3.57E-02
			2.51E-03	1.73E-02	4.16E-03	3.96E-03	9.68E-04
7	2	9.93E-03	4.08	-9.79E-01	4.58E-01	-6.04E-01	4.17E-01
			1.06E-02	1.41E-02	1.72E-02	1.99E-02	2.64E-02
			2.38E-03	4.02E-03	2.10E-03	5.86E-03	4.83E-03
8	1	7.30E-03	6.40	-2.10	4.62E-01	-1.10	1.50E-01
			7.87E-03	1.08E-02	1.38E-02	1.67E-02	2.06E-02
			2.74E-03	3.31E-03	1.60E-03	5.58E-03	7.04E-04
8	2	9.67E-03	4.08	-1.17	4.51E-01	-6.12E-01	4.24E-01
			1.03E-02	1.34E-02	1.69E-02	2.01E-02	2.61E-02
			2.29E-03	4.24E-03	2.12E-03	5.70E-03	6.62E-03
9	1	7.48E-03	8.08	-2.11	4.53E-01	-1.17	7.84E-02
			8.54E-03	1.07E-02	1.38E-02	1.74E-02	2.08E-02
			2.46E-03	3.53E-03	1.30E-03	5.95E-03	5.60E-04
9	2	9.87E-03	4.01	-1.05	4.49E-01	-6.14E-01	4.26E-01
			1.05E-02	1.36E-02	1.69E-02	2.03E-02	2.53E-02
			2.24E-03	4.23E-03	1.95E-03	5.62E-03	6.51E-03
10	1	8.31E-03	7.38	-2.25	6.29E-01	-1.12	1.91E-01
			9.47E-03	1.13E-02	1.47E-02	1.82E-02	2.17E-02
			1.63E-03	4.28E-03	1.58E-03	5.49E-03	1.13E-03
10	2	1.07E-02	3.69	-1.00	2.50E-01	-5.00E-01	5.00E-01
			1.13E-02	1.42E-02	1.64E-02	1.79E-02	2.09E-02
			2.17E-03	3.34E-03	9.76E-04	2.22E-03	6.06E-03
11	1	1.04E-02	6.10	-2.34	5.34E-01	-1.15	1.59E-01
			1.10E-02	1.39E-02	1.69E-02	2.04E-02	2.37E-02
			2.14E-03	3.89E-03	1.35E-03	5.59E-03	1.02E-03
11	2	1.29E-02	4.03	-1.03	2.19E-01	-5.32E-01	5.31E-01
			1.33E-02	1.65E-02	1.87E-02	1.99E-02	2.28E-02
			2.09E-03	3.28E-03	1.18E-03	1.82E-03	4.12E-03
12	1	1.04E-02	8.11	-2.08	6.68E-01	-1.14	1.68E-01
			1.15E-02	1.35E-02	1.68E-02	1.99E-02	2.37E-02
			1.80E-03	4.15E-03	1.58E-03	5.58E-03	8.48E-04
12	2	1.29E-02	4.14	-1.04	6.43E-01	-5.44E-01	4.82E-01
			1.34E-02	1.60E-02	1.99E-02	2.26E-02	2.91E-02
			2.12E-03	3.33E-03	3.08E-03	5.62E-03	5.60E-03

E.2 Detailed Listing of Pressure Histories for Large-Scale Annular Jet Experiments

In this section, characteristics of the pressure histories recorded for the large-scale annular jet experiments (see Table 4.6), are presented. Experiments with different values of the shock strength, superficial liquid velocity, and initial homogeneous void

fraction have been conducted. Referring to Table 4.6, the amplitudes and locations of the first six pressure pulses for test numbers 1 through 3 and for test numbers 6 through 15 are presented in Tables E.41 through E.43 and in Tables E.44 through E.53, respectively. For each combination of test conditions, the experiment is repeated 10 times, except for the test conditions # 4 and 5 (see Table 4.5), where the input energy of 2.4 kJ was too low to produce a sufficiently strong shock to propagate through the two-phase jet.

The pressure histories for large-scale annular jet experiments conducted with radially- and axially-confined shocks have the same general trend as that shown in Figure E.4. The time location t_0 corresponds to the initial time of the experiment, i.e. the time at which the oscilloscope detects a significant change in pressure and is triggered by the first channel. The amplitudes and time locations of the first six pressure pulses (A_1 through A_6 and t_1 through t_6, respectively) are noted in Figure E.4 and reported in a table for each combination of test conditions, as it is shown in Table E.40.

Table E.40: Table example for data related to large-scale annular jet experiments conducted with radially- and axially-confined shocks

		Peaks					
Run	t_0 $\times 10^3$	#1	#2	#3	#4	#5	#6
Test #	Initial time (s)	Amplitude of the pulse (psig) Location of the pulse (s)					
Test	$t_0 \times 10^3$	A_1 t_1	A_2 t_2	A_3 t_3	A_4 t_4	A_5 t_5	A_6 t_6

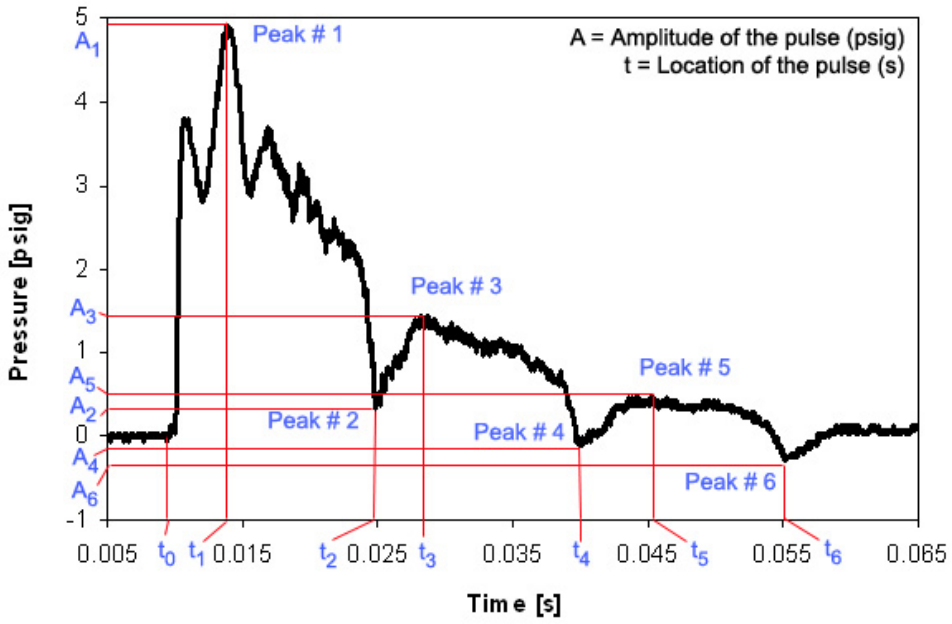

Figure E.4: Figure example for data related to large-scale annular jet experiments conducted with radially- and axially-confined shocks

Table E.41: Detailed list of pressure pulse characteristics for Test #1 of Table 4.6

		Peaks					
Run	t_0 $\times 10^3$	#1	#2	#3	#4	#5	#6
1		3.70	1.54	2.34	-9.93E-02	0.00	0.00
	9.96	1.18E-02	2.52E-02	2.66E-02	4.27E-02	0.00	0.00
2		3.84	1.64	2.34	-1.42E-01	0.00	0.00
	9.94	1.07E-02	2.51E-02	2.63E-02	4.26E-02	0.00	0.00
3		3.70	1.59	2.34	-1.42E-01	0.00	0.00
	10.1	1.14E-02	2.51E-02	2.67E-02	4.27E-02	0.00	0.00
4		3.62	1.46	2.21	-1.33E-01	0.00	0.00
	9.96	1.06E-02	2.52E-02	2.66E-02	4.26E-02	0.00	0.00
5		3.85	1.50	2.16	-9.19E-02	0.00	0.00
	9.98	1.09E-02	2.51E-02	2.66E-02	4.26E-02	0.00	0.00
6		3.18	1.07	2.10	-2.86E-01	0.00	0.00
	10.0	1.22E-02	2.56E-02	2.67E-02	4.32E-02	0.00	0.00
7		3.43	1.46	2.26	-1.80E-01	0.00	0.00
	10.0	1.19E-02	2.52E-02	2.64E-02	4.28E-02	0.00	0.00
8		3.78	1.39	2.23	-2.09E-01	0.00	0.00
	9.98	1.09E-02	2.51E-02	2.63E-02	4.26E-02	0.00	0.00

continued on next page

continued from previous page							
		Peaks					
Run	t_0 $\times 10^3$	#1	#2	#3	#4	#5	#6
9		3.51	1.44	2.15	-1.03E-01	0.00	0.00
	9.94	1.22E-02	2.51E-02	2.61E-02	4.32E-02	0.00	0.00
10		3.65	1.59	2.25	-9.74E-02	0.00	0.00
	9.96	1.22E-02	2.50E-02	2.62E-02	4.25E-02	0.00	0.00

Table E.42: Detailed list of pressure pulse characteristics for Test #2 of Table 4.6

		Peaks					
Run	t_0 $\times 10^3$	#1	#2	#3	#4	#5	#6
1		1.96	-4.26E-01	6.05E-01	-4.73E-01	2.77E-01	-3.80E-01
	9.95	1.42E-02	2.41E-02	2.72E-02	3.80E-02	4.47E-02	5.25E-02
2		2.16	5.33E-02	9.91E-01	-2.28E-01	3.81E-01	-3.22E-01
	9.96	1.44E-02	2.49E-02	2.80E-02	3.92E-02	4.23E-02	5.37E-02
3		2.42	8.00E-02	8.77E-01	-2.48E-01	3.14E-01	-2.95E-01
	9.9	1.42E-02	2.44E-02	2.72E-02	3.81E-02	4.19E-02	5.19E-02
4		2.15	3.77E-02	1.02	-2.44E-01	4.13E-01	-2.90E-01
	9.96	1.44E-02	2.45E-02	2.78E-02	3.88E-02	4.20E-02	5.27E-02
5		2.53	-3.68E-03	9.81E-01	-1.91E-01	3.71E-01	-2.38E-01
	9.95	1.40E-02	2.38E-02	2.72E-02	3.77E-02	4.10E-02	5.15E-02
6		2.32	1.14E-01	7.70E-01	-1.20E-01	2.55E-01	-2.14E-01
	9.98	1.42E-02	2.54E-02	2.88E-02	4.08E-02	4.42E-02	5.62E-02
7		1.54	-1.96E-01	6.48E-01	-2.43E-01	3.20E-01	-2.90E-01
	9.97	1.44E-02	2.49E-02	2.81E-02	3.99E-02	4.47E-02	5.48E-02
8		2.25	-2.80E-01	7.98E-01	-3.74E-01	3.29E-01	-3.74E-01
	9.94	1.41E-02	2.46E-02	2.79E-02	3.93E-02	4.62E-02	5.38E-02
9		2.34	-2.42E-01	9.77E-01	-3.82E-01	3.68E-01	-3.35E-01
	10.5	1.48E-02	2.67E-02	2.90E-02	4.01E-02	4.36E-02	5.43E-02
10		2.76	4.41E-02	8.41E-01	-3.31E-01	2.32E-01	-4.25E-01
	9.94	1.38E-02	2.42E-02	2.66E-02	3.80E-02	4.15E-02	5.23E-02

Table E.43: Detailed list of pressure pulse characteristics for Test #3 of Table 4.6

		Peaks					
Run	t_0 $\times 10^3$	#1	#2	#3	#4	#5	#6
1		2.85	3.95E-02	9.30E-01	-3.35E-01	2.27E-01	-3.82E-01
	10.5	1.48E-02	2.47E-02	2.87E-02	3.90E-02	4.25E-02	5.33E-02
2		2.01	-4.73E-01	6.05E-01	-4.26E-01	2.77E-01	-3.80E-01
	9.98	1.41E-02	2.41E-02	2.74E-02	3.81E-02	4.54E-02	5.27E-02
3		2.02	-1.86E-01	8.46E-01	-3.26E-01	3.77E-01	-3.26E-01
	9.94	1.42E-02	2.38E-02	2.76E-02	3.79E-02	4.17E-02	5.18E-02
continued on next page							

continued from previous page							
		Peaks					
Run	t_0 $\times 10^3$	#1	#2	#3	#4	#5	#6
4		2.00	-2.01E-01	8.30E-01	-3.89E-01	3.61E-01	-3.42E-01
	9.98	1.37E-02	2.39E-02	2.75E-02	3.79E-02	4.18E-02	5.16E-02
5		2.32	-2.62E-01	6.76E-01	-4.03E-01	2.54E-01	-3.56E-01
	9.98	1.40E-02	2.40E-02	2.74E-02	3.81E-02	4.49E-02	5.22E-02
6		1.49	-4.76E-01	6.96E-01	-3.35E-01	3.21E-01	-2.42E-01
	9.92	1.40E-02	2.50E-02	2.83E-02	3.95E-02	4.29E-02	5.41E-02
7		2.38	-1.00E-01	8.37E-01	-2.88E-01	2.75E-01	-3.35E-01
	9.54	1.35E-02	2.44E-02	2.80E-02	3.88E-02	4.21E-02	5.32E-02
8		2.82	5.24E-02	1.08	-3.69E-01	3.81E-01	-4.63E-01
	9.96	1.43E-02	2.43E-02	2.78E-02	3.85E-02	4.18E-02	5.27E-02
9		1.92	-5.15E-01	7.04E-01	-5.15E-01	2.82E-01	-4.68E-01
	9.94	1.39E-02	2.42E-02	2.78E-02	3.82E-02	4.18E-02	5.25E-02
10		2.72	-4.96E-02	8.41E-01	-3.31E-01	2.78E-01	-3.78E-01
	10.5	1.49E-02	2.48E-02	2.76E-02	3.86E-02	4.58E-02	5.25E-02

Table E.44: Detailed list of pressure pulse characteristics for Test #6 of Table 4.6

		Peaks					
Run	t_0 $\times 10^3$	#1	#2	#3	#4	#5	#6
1		4.92	1.07	2.34	-2.85E-01	6.99E-01	-9.88E-01
	10.3	1.12E-02	2.48E-02	2.79E-02	3.91E-02	4.21E-02	5.36E-02
2		5.47	1.25	2.42	-3.42E-01	7.36E-01	-9.51E-01
	9.97	1.03E-02	2.45E-02	2.86E-02	3.88E-02	4.25E-02	5.32E-02
3		4.44	8.26E-01	2.00	-6.27E-01	6.39E-01	-1.00
	9.98	1.22E-02	2.44E-02	2.76E-02	3.87E-02	4.49E-02	5.33E-02
4		5.60	8.19E-01	2.27	-3.53E-01	6.78E-01	-1.10
	9.98	1.18E-02	2.45E-02	2.76E-02	3.87E-02	4.24E-02	5.33E-02
5		5.28	1.25	2.43	-4.81E-01	7.85E-01	-9.03E-01
	9.70	1.18E-02	2.44E-02	2.73E-02	3.87E-02	4.13E-02	5.33E-02
6		4.50	7.46E-01	2.06	-2.85E-01	7.93E-01	-8.01E-01
	10.3	1.21E-02	2.46E-02	2.73E-02	3.92E-02	4.25E-02	5.36E-02
7		4.83	8.89E-01	2.11	-3.30E-01	7.48E-01	-6.11E-01
	9.98	1.27E-02	2.47E-02	2.76E-02	3.89E-02	4.16E-02	5.31E-02
8		5.30	1.27	2.21	-2.28E-01	8.50E-01	-6.97E-01
	9.98	1.03E-02	2.45E-02	2.68E-02	3.88E-02	4.13E-02	5.33E-02
9		4.90	1.01	2.09	-5.82E-01	7.78E-01	-6.76E-01
	10.3	1.07E-02	2.48E-02	2.79E-02	3.91E-02	4.28E-02	5.35E-02
10		5.48	1.63	2.85	8.46E-02	1.07	-4.78E-01
	10.1	1.13E-02	2.47E-02	2.78E-02	3.92E-02	4.20E-02	5.35E-02

Table E.45: Detailed list of pressure pulse characteristics for Test #7 of Table 4.6

		Peaks					
Run	t_0 $\times 10^3$	#1	#2	#3	#4	#5	#6
1		1.86	-4.83E-01	7.35E-01	-3.43E-01	4.54E-01	-2.02E-01
	10.4	1.48E-02	2.47E-02	2.89E-02	4.03E-02	4.58E-02	5.42E-02
2		3.96	2.60E-01	1.48	-6.80E-02	4.48E-01	-3.02E-01
	10.3	1.42E-02	2.46E-02	2.78E-02	3.91E-02	4.23E-02	5.42E-02
3		2.78	-4.05E-01	1.19	-2.18E-01	5.32E-01	-1.71E-01
	10.3	1.48E-02	2.57E-02	2.92E-02	4.06E-02	4.41E-02	5.53E-02
4		1.86	-6.22E-01	8.78E-01	-2.00E-01	6.43E-01	-1.29E-02
	10.1	1.44E-02	2.47E-02	2.87E-02	3.98E-02	4.31E-02	5.34E-02
5		4.03	3.72E-01	1.45	-2.76E-03	4.66E-01	-2.37E-01
	10.1	1.41E-02	2.47E-02	2.80E-02	3.89E-02	4.18E-02	5.35E-02
6		4.32	3.37E-01	1.13	-7.88E-01	-2.72E-01	-1.02
	9.94	1.42E-02	2.62E-02	2.95E-02	4.19E-02	4.52E-02	5.71E-02
7		1.78	-1.03	5.18E-01	-8.41E-01	4.96E-02	-5.13E-01
	10.0	1.46E-02	2.68E-02	3.01E-02	4.23E-02	4.59E-02	5.77E-02
8		3.73	-5.39E-01	8.68E-01	-7.73E-01	2.39E-02	-5.85E-01
	9.95	1.44E-02	2.64E-02	3.02E-02	4.18E-02	4.61E-02	5.65E-02
9		2.47	-4.34E-01	1.02	-2.93E-01	4.57E-01	-2.93E-01
	10.1	1.43E-02	2.62E-02	2.91E-02	4.07E-02	4.51E-02	5.57E-02
10		2.71	-3.38E-01	1.11	-3.85E-01	5.06E-01	-2.91E-01
	10.3	1.46E-02	2.53E-02	2.91E-02	4.01E-02	4.71E-02	5.51E-02

Table E.46: Detailed list of pressure pulse characteristics for Test #8 of Table 4.6

		Peaks					
Run	t_0 $\times 10^3$	#1	#2	#3	#4	#5	#6
1		2.15	-4.72E-01	1.36	4.65E-01	1.40	6.99E-01
	9.64	1.38E-02	2.54E-02	3.35E-02	3.94E-02	4.60E-02	5.43E-02
2		4.91	3.15E-01	1.44	-1.07E-01	4.56E-01	-2.94E-01
	9.66	1.38E-02	2.48E-02	2.81E-02	3.99E-02	4.36E-02	5.51E-02
3		3.99	4.26E-01	1.32	3.68E-03	3.79E-01	-2.31E-01
	9.95	1.38E-02	2.49E-02	2.75E-02	4.03E-02	4.32E-02	5.49E-02
4		3.21	-1.64E-01	1.01	-2.57E-01	3.05E-01	-3.04E-01
	10.3	1.45E-02	2.51E-02	2.82E-02	3.99E-02	4.42E-02	5.46E-02
5		2.99	-2.90E-01	1.07	-2.90E-01	4.60E-01	-1.96E-01
	9.62	1.40E-02	2.39E-02	2.71E-02	3.85E-02	4.13E-02	5.24E-02
6		2.61	-3.94E-01	1.11	2.76E-02	1.01	3.09E-01
	9.93	1.42E-02	2.53E-02	2.92E-02	3.99E-02	4.61E-02	5.51E-02
7		2.45	-8.46E-02	1.23	-3.77E-02	6.65E-01	5.61E-02
	9.62	1.41E-02	2.43E-02	2.87E-02	3.91E-02	4.31E-02	5.38E-02
8		3.41	-3.87E-01	1.11	-4.34E-01	4.10E-01	-4.81E-01
	9.94	1.40E-02	2.41E-02	2.91E-02	3.83E-02	4.31E-02	5.27E-02
9		2.20	-7.56E-01	7.91E-01	-2.87E-01	5.10E-01	-1.46E-01

continued on next page

continued from previous page							
		Peaks					
Run	t_0 $\times 10^3$	#1	#2	#3	#4	#5	#6
	9.94	1.42E-02	2.38E-02	2.70E-02	3.75E-02	4.84E-02	5.20E-02
10		2.86	4.23E-01	1.22	2.35E-01	3.76E-01	3.29E-01
	9.94	1.44E-02	2.59E-02	2.83E-02	4.53E-02	4.58E-02	4.60E-02

Table E.47: Detailed list of pressure pulse characteristics for Test #9 of Table 4.6

		Peaks					
Run	t_0 $\times 10^3$	#1	#2	#3	#4	#5	#6
1		2.18	-5.88E-01	6.77E-01	-4.48E-01	3.02E-01	-3.54E-01
	10.4	1.41E-02	2.55E-02	3.17E-02	4.02E-02	4.57E-02	5.50E-02
2		2.62	-3.32E-01	6.99E-01	-3.32E-01	2.31E-01	-3.32E-01
	10.0	1.42E-02	2.49E-02	2.81E-02	3.91E-02	4.70E-02	5.37E-02
3		2.50	-6.88E-01	6.71E-01	-4.54E-01	2.96E-01	-4.07E-01
	10.4	1.40E-02	2.48E-02	2.86E-02	3.93E-02	4.61E-02	5.47E-02
4		3.63	-5.40E-01	1.10	-3.99E-01	3.98E-01	-4.46E-01
	10.3	1.41E-02	2.46E-02	2.83E-02	3.86E-02	4.52E-02	5.31E-02
5		2.43	-8.95E-01	7.92E-01	-5.67E-01	4.17E-01	-3.80E-01
	9.65	1.36E-02	2.42E-02	2.81E-02	3.87E-02	4.47E-02	5.30E-02
6		3.41	-6.34E-02	1.25	-2.51E-01	5.46E-01	-4.38E-01
	10.4	1.47E-02	2.43E-02	2.83E-02	3.80E-02	4.24E-02	5.21E-02
7		2.72	-2.82E-01	8.90E-01	-2.35E-01	5.15E-01	-4.78E-02
	9.96	1.43E-02	2.53E-02	2.96E-02	4.04E-02	4.58E-02	5.54E-02
8		2.48	-3.81E-01	7.91E-01	-2.87E-01	5.10E-01	-2.40E-01
	10.0	1.42E-02	2.57E-02	2.93E-02	4.06E-02	4.56E-02	5.58E-02
9		2.62	-1.43E-01	9.35E-01	-2.84E-01	3.25E-01	-2.84E-01
	10.1	1.42E-02	2.61E-02	3.11E-02	4.06E-02	4.61E-02	5.57E-02
10		3.03	-3.00E-01	8.72E-01	-4.40E-01	1.22E-01	-4.87E-01
	10.3	1.41E-02	2.53E-02	2.92E-02	4.11E-02	4.41E-02	5.59E-02

Table E.48: Detailed list of pressure pulse characteristics for Test #10 of Table 4.6

		Peaks					
Run	t_0 $\times 10^3$	#1	#2	#3	#4	#5	#6
1		2.38	-5.72E-01	7.41E-01	-3.84E-01	4.60E-01	-1.50E-01
	9.69	1.35E-02	2.49E-02	3.08E-02	3.98E-02	4.62E-02	5.49E-02
2		2.57	-2.86E-01	8.39E-01	-3.80E-01	4.17E-01	-2.86E-01
	10.4	1.39E-02	2.50E-02	3.05E-02	3.97E-02	4.57E-02	5.43E-02
3		2.50	-4.57E-01	7.62E-01	-3.63E-01	4.34E-01	-2.69E-01
	9.95	1.38E-02	2.46E-02	3.08E-02	3.92E-02	4.57E-02	5.40E-02
4		2.53	-3.26E-01	1.03	-2.79E-01	4.71E-01	-2.33E-01
continued on next page							

continued from previous page							
		Peaks					
Run	t_0 $\times 10^3$	#1	#2	#3	#4	#5	#6
	9.99	1.40E-02	2.49E-02	2.90E-02	3.94E-02	4.44E-02	5.38E-02
5		1.45	-1.08	6.07E-01	-4.25E-01	4.19E-01	-1.90E-01
	9.97	1.35E-02	2.38E-02	2.74E-02	3.77E-02	4.16E-02	5.19E-02
6		2.15	-6.62E-01	6.98E-01	-5.68E-01	3.23E-01	-3.81E-01
	10.1	1.40E-02	2.51E-02	2.87E-02	3.92E-02	4.50E-02	5.34E-02
7		2.39	-5.61E-01	7.05E-01	-5.14E-01	2.83E-01	-3.26E-01
	10.1	1.43E-02	2.48E-02	2.87E-02	3.91E-02	4.46E-02	5.35E-02
8		3.05	-3.70E-01	9.42E-01	-5.58E-01	2.39E-01	-5.11E-01
	9.98	1.35E-02	2.45E-02	2.81E-02	3.92E-02	4.26E-02	5.33E-02
9		2.30	-5.16E-01	7.97E-01	-3.75E-01	4.69E-01	-2.34E-01
	10.3	1.39E-02	2.50E-02	3.11E-02	3.93E-02	4.58E-02	5.41E-02
10		1.75	-8.29E-01	8.58E-01	-3.60E-01	6.71E-01	-1.73E-01
	10.4	1.39E-02	2.53E-02	3.15E-02	3.99E-02	4.62E-02	5.49E-02

Table E.49: Detailed list of pressure pulse characteristics for Test #11 of Table 4.6

		Peaks					
Run	t_0 $\times 10^3$	#1	#2	#3	#4	#5	#6
1		7.72	2.02	3.66	5.32E-01	1.39	-2.50E-01
	9.80	1.03E-02	2.45E-02	2.66E-02	3.85E-02	4.00E-02	5.32E-02
2		6.88	1.49	2.90	2.42E-01	1.10	-3.05E-01
	9.78	1.03E-02	2.45E-02	2.67E-02	3.85E-02	4.08E-02	5.31E-02
3		6.20	1.51	2.84	2.59E-01	1.04	-2.88E-01
	9.78	1.03E-02	2.44E-02	2.66E-02	3.85E-02	3.99E-02	5.24E-02
4		6.30	1.61	2.31	4.37E-01	1.30	-2.67E-01
	9.80	1.03E-02	3.17E-02	3.17E-02	3.85E-02	4.06E-02	5.31E-02
5		7.20	1.81	2.52	4.84E-01	1.34	-2.97E-01
	9.82	1.04E-02	3.15E-02	3.18E-02	3.87E-02	4.03E-02	5.32E-02
6		6.33	8.61E-01	2.74	-5.45E-01	1.02	-1.01
	9.91	1.04E-02	2.42E-02	2.76E-02	3.84E-02	4.32E-02	5.39E-02
7		6.48	7.81E-01	2.73	-7.03E-01	9.38E-01	-7.81E-01
	9.97	1.03E-02	2.43E-02	2.70E-02	3.84E-02	4.22E-02	5.35E-02
8		6.64	8.56E-01	2.65	-1.59E-01	9.34E-01	-3.94E-01
	9.80	1.04E-02	2.44E-02	2.68E-02	3.85E-02	4.04E-02	5.31E-02
9		6.71	1.39	2.80	-1.69E-01	1.00	-4.81E-01
	9.94	1.13E-02	2.42E-02	2.60E-02	3.84E-02	4.04E-02	5.31E-02
10		6.63	1.24	2.73	-6.13E-03	1.01	-3.97E-01
	9.80	1.03E-02	2.43E-02	2.66E-02	3.86E-02	3.99E-02	5.32E-02

Table E.50: Detailed list of pressure pulse characteristics for Test #12 of Table 4.6

		Peaks					
Run	t_0 $\times 10^3$	#1	#2	#3	#4	#5	#6
1		3.37	-1.42E-01	1.64	3.26E-01	1.12	2.79E-01
	1.0.2	1.46E-02	2.39E-02	2.78E-02	3.78E-02	4.24E-02	5.15E-02
2		3.83	-3.44E-01	1.39	-1.09E-01	7.81E-01	-1.09E-01
	10.2	1.45E-02	2.42E-02	2.95E-02	3.81E-02	4.38E-02	5.24E-02
3		3.47	-2.34E-01	1.31	3.28E-01	6.56E-01	1.41E-01
	10.0	1.46E-02	2.61E-02	3.04E-02	4.18E-02	4.50E-02	5.74E-02
4		5.02	3.28E-01	1.73	9.38E-02	8.44E-01	4.69E-02
	10.0	1.46E-02	2.60E-02	2.90E-02	4.06E-02	4.46E-02	5.54E-02
5		5.05	2.25E-01	1.82	2.72E-01	1.02	1.78E-01
	10.0	1.44E-02	2.50E-02	2.90E-02	3.99E-02	4.42E-02	5.45E-02
6		2.66	-2.46E-01	9.26E-01	-5.88E-02	5.97E-01	3.49E-02
	10.0	1.46E-02	2.52E-02	3.11E-02	3.88E-02	4.57E-02	5.29E-02
7		4.77	-6.25E-02	1.44	-2.03E-01	6.41E-01	-2.03E-01
	10.2	1.35E-02	2.59E-02	2.99E-02	4.12E-02	4.69E-02	5.71E-02
8		5.95	4.67E-01	1.73	2.79E-01	6.54E-01	-4.87E-02
	10.1	1.46E-02	2.66E-02	3.01E-02	4.12E-02	4.43E-02	5.63E-02
9		3.42	4.04E-02	1.82	3.22E-01	1.12	3.22E-01
	10.1	1.38E-02	2.56E-02	3.00E-02	3.96E-02	4.43E-02	5.44E-02
10		2.28	-5.36E-01	1.48	1.20E-01	1.10	2.61E-01
	10.3	1.40E-02	2.51E-02	2.92E-02	3.94E-02	4.38E-02	5.45E-02

Table E.51: Detailed list of pressure pulse characteristics for Test #13 of Table 4.6

		Peaks					
Run	t_0 $\times 10^3$	#1	#2	#3	#4	#5	#6
1		2.78	-7.78E-01	9.57E-01	-2.15E-01	5.82E-01	-1.21E-01
	10.1	1.42E-02	2.42E-02	3.11E-02	3.83E-02	4.46E-02	5.30E-02
2		2.81	-5.18E-01	8.88E-01	-2.37E-01	4.19E-01	-2.37E-01
	10.0	1.43E-02	2.43E-02	2.90E-02	3.92E-02	4.48E-02	5.35E-02
3		3.93	-9.93E-02	1.31	-5.24E-02	7.44E-01	-5.24E-02
	10.0	1.40E-02	2.47E-02	2.98E-02	3.99E-02	4.44E-02	5.34E-02
4		5.84	7.31E-01	1.67	-1.60E-01	3.56E-01	-3.94E-01
	10.1	1.44E-02	2.55E-02	2.80E-02	3.98E-02	4.27E-02	5.31E-02
5		4.02	1.25E-01	1.34	-1.56E-02	5.47E-01	-1.56E-01
	10.3	1.45E-02	2.42E-02	2.79E-02	3.84E-02	4.21E-02	5.25E-02
6		2.78	-7.78E-01	9.57E-01	-2.15E-01	5.82E-01	-1.21E-01
	10.1	1.42E-02	2.42E-02	3.11E-02	3.83E-02	4.46E-02	5.30E-02
7		4.92	7.92E-01	1.54	-4.60E-03	8.92E-02	-3.80E-01
	9.72	1.36E-02	2.60E-02	2.84E-02	4.59E-02	4.78E-02	5.97E-02
8		2.60	-7.73E-01	1.06	7.08E-02	9.15E-01	2.58E-01
	10.1	1.43E-02	2.58E-02	3.17E-02	4.11E-02	4.69E-02	5.73E-02
9		5.18	4.01E-01	1.20	-2.09E-01	3.07E-01	-3.49E-01

continued on next page

continued from previous page							
		Peaks					
Run	t_0 $\times 10^3$	#1	#2	#3	#4	#5	#6
	10.0	1.45E-02	2.49E-02	2.91E-02	4.02E-02	4.71E-02	5.58E-02
10		4.08	-9.28E-02	1.17	-2.80E-01	3.76E-01	-2.80E-01
	10.0	1.44E-02	2.44E-02	2.84E-02	3.89E-02	4.54E-02	5.34E-02

Table E.52: Detailed list of pressure pulse characteristics for Test #14 of Table 4.6

		Peaks					
Run	t_0 $\times 10^3$	#1	#2	#3	#4	#5	#6
1		3.06	-5.50E-01	1.09	-3.15E-01	5.28E-01	-3.15E-01
	10.0	1.39E-02	2.46E-02	3.14E-02	3.90E-02	4.59E-02	5.39E-02
2		2.51	-8.13E-01	9.68E-01	-3.92E-01	5.46E-01	-2.04E-01
	10.3	1.39E-02	2.46E-02	3.10E-02	3.89E-02	4.56E-02	5.34E-02
3		2.04	-8.63E-01	8.24E-01	-1.60E-01	7.78E-01	2.62E-01
	10.3	1.45E-02	2.44E-02	3.03E-02	3.89E-02	4.77E-02	5.32E-02
4		2.53	-9.42E-01	9.33E-01	-3.33E-01	6.99E-01	-5.15E-02
	10.0	1.40E-02	2.46E-02	3.07E-02	3.92E-02	4.59E-02	5.36E-02
5		2.53	-7.08E-01	1.03	-1.45E-01	6.05E-01	1.36E-01
	10.0	1.39E-02	2.44E-02	3.17E-02	3.93E-02	4.50E-02	5.35E-02
6		2.71	-9.42E-01	9.33E-01	-5.67E-01	3.70E-01	-5.20E-01
	9.60	1.35E-02	2.41E-02	3.03E-02	3.90E-02	4.58E-02	5.43E-02
7		3.22	-2.91E-01	8.34E-01	-2.91E-01	2.71E-01	-3.38E-01
	10.0	1.40E-02	2.46E-02	2.99E-02	3.92E-02	4.63E-02	5.41E-02
8		1.47	-1.07	8.56E-01	-2.22E-01	7.15E-01	5.88E-02
	10.1	1.41E-02	2.47E-02	3.14E-02	3.89E-02	4.58E-02	5.37E-02
9		2.21	-7.47E-01	8.47E-01	-3.25E-01	5.65E-01	-1.38E-01
	10.0	1.43E-02	2.44E-02	3.11E-02	3.88E-02	4.54E-02	5.32E-02
10		3.00	-3.77E-01	9.83E-01	-9.56E-02	6.08E-01	-1.84E-03
	10.0	1.39E-02	2.45E-02	3.17E-02	4.04E-02	4.61E-02	5.52E-02

Table E.53: Detailed list of pressure pulse characteristics for Test #15 of Table 4.6

		Peaks					
Run	t_0 $\times 10^3$	#1	#2	#3	#4	#5	#6
1		2.48	-6.63E-01	9.31E-01	-3.35E-01	5.56E-01	-1.00E-01
	10.0	1.36E-02	2.49E-02	3.09E-02	3.95E-02	4.55E-02	5.49E-02
2		2.98	-5.79E-01	1.25	-1.65E-02	9.21E-01	-1.65E-02
	10.3	1.36E-02	2.49E-02	3.26E-02	4.00E-02	4.69E-02	5.44E-02
3		2.94	-6.65E-01	1.21	-1.02E-01	8.82E-01	8.55E-02
	10.0	1.36E-02	2.47E-02	3.13E-02	3.95E-02	4.62E-02	5.39E-02
4		2.09	-9.14E-01	1.10	-1.17E-01	9.15E-01	1.18E-01
continued on next page							

continued from previous page							
		Peaks					
Run	t_0 $\times 10^3$	#1	#2	#3	#4	#5	#6
	10.3	1.38E-02	2.49E-02	3.14E-02	4.00E-02	4.56E-02	5.42E-02
5		2.19	-8.53E-01	9.75E-01	-3.84E-01	6.94E-01	-1.03E-01
	10.0	1.36E-02	2.46E-02	3.08E-02	3.89E-02	4.57E-02	5.38E-02
6		2.88	-5.42E-01	1.24	-7.35E-02	9.11E-01	6.71E-02
	10.3	1.37E-02	2.46E-02	3.24E-02	3.95E-02	4.72E-02	5.45E-02
7		4.40	-9.65E-02	1.22	-2.84E-01	4.66E-01	-2.37E-01
	10.1	1.35E-02	2.49E-02	3.05E-02	4.01E-02	4.60E-02	5.47E-02
8		2.71	-5.74E-01	8.32E-01	-3.87E-01	4.57E-01	-1.53E-01
	10.0	1.38E-02	2.55E-02	3.11E-02	4.05E-02	4.67E-02	5.53E-02
9		1.54	-1.14	6.93E-01	-4.79E-01	5.06E-01	-1.04E-01
	10.0	1.39E-02	2.47E-02	3.03E-02	3.93E-02	4.54E-02	5.38E-02
10		2.96	-2.78E-01	1.13	-1.38E-01	5.65E-01	-1.38E-01
	10.0	1.37E-02	2.51E-02	3.13E-02	4.04E-02	4.63E-02	5.58E-02

APPENDIX F

ERROR ANALYSIS

This appendix summarizes the methods used to quantify the uncertainties in the experimental measurements. Results of this analysis are given followed by a general description of the method used and a brief explanation of the source of each reported measurement uncertainty.

Uncertainty A (U_A), also known as imprecision, is due to statistical fluctuations and is obtained using the generic formula:

$$U_A = k_c \times \sigma \tag{F.1}$$

where k_c is a multiplier computed from an appropriate distribution such that 95% of the data should fall within statistical fluctuations; σ is the sample standard deviation. Uncertainty B (U_B), also known as inaccuracy, is due to the inaccuracy of the instrumentation. Combined uncertainty (U_C) is calculated using the rule for combining uncertainties, where the total uncertainty is the root-mean square of U_A and U_B:

$$U_C = \sqrt{U_A^2 + U_B^2} \tag{F.2}$$

The overall standard uncertainty of an indirect measurement y, dependent on N indirect measurements x_i, is defined in Equation F.3. The standard uncertainty associated with an indirect measurement is analogous to the standard deviation of a statistical population.

$$[U_y]^2 = \sum_{i=1}^{N} \left[\frac{\partial y}{\partial x_i} \cdot U_{x_i} \right]^2 \tag{F.3}$$

Here, U is used to define standard uncertainty.

F.1 Uncertainty in Bubble Size and Sauter Diameter Measurements

F.1.1 Uncertainty in Bubble Size Measurements

For the uncertainty in the bubble size, both uncertainties due to statistical fluctuations and instrumentation are considered. The equivalent spherical bubble diameters for $N = 40$ different bubbles distributed over a distance of nearly 12 cm downstream of the nozzle exit, $d_{b,s,i}$, were photographed and measured for different superficial liquid velocities $j_{l,e}$ and homogeneous exit void fraction α_e (see Section 4.1.2). The sample standard deviations $\sigma_{d_{b,s}}$ were calculated. The Student's t-distribution with 39 degrees of freedom is used to determine that the multiplier k_c should 2.023 for 95% of the measurements to fall within the uncertainty. The size of a pixel was calculated for each picture and is used as the uncertainty due to the instrumentation. Finally, the total uncertainty is found by taking the root-mean-square of the two sources of error computed for different superficial liquid velocities and homogeneous exit void fraction. The results for uncertainties in the bubble size for planar jets are shown in Table F.1. The relative uncertainties are high due to the large range of bubble diameters measured on each picture.

Table F.1: Listing of uncertainties in the bubble size for planar jets

$j_{l,e}$ (m/s)	α_e (%)	$d_{b,s,avg}$ (mm)	$\sigma_{d_{b,s}}$ (mm)	size of a pixel (mm)	$U_{d_{b,s}}$ (mm)	Relative Uncertainty (%)
1.26	1.00	2.414	0.748	0.224	1.529	63.34
	2.50	3.054	0.809	0.224	1.653	54.11
	5.00	3.574	0.668	0.224	1.370	38.34
	10.0	3.607	0.665	0.224	1.363	37.79
	25.0	3.876	0.743	0.224	1.520	39.22
2.52	1.00	1.441	0.405	0.225	0.849	58.93
	2.50	1.921	0.539	0.226	1.114	57.96
	5.00	2.722	0.517	0.225	1.069	39.28
	10.0	3.264	0.532	0.225	1.099	33.66
	15.0	3.087	0.790	0.224	1.613	52.24
4.92	1.00	1.259	0.244	0.224	0.543	43.11
	2.50	1.562	0.297	0.225	0.641	41.05
	5.00	1.544	0.244	0.224	0.542	35.13
	7.50	1.957	0.495	0.225	1.026	52.45
	10.0	1.964	0.628	0.224	1.291	65.73

F.1.2 Uncertainty in Sauter Mean Diameter

The total uncertainty in the Sauter mean diameter (see Equation F.4) is found by using an error propagation formula (see Equation F.5). It is dependent on the uncertainties of the bubble size ($d_{b,s,i}$), which were computed in Section F.1.1. The uncertainty in the bubble size ($U_{d_{b,s}}$) is assumed to be constant for each set of nozzle exit homogeneous void fraction and liquid superficial velocity. The results for uncertainties in the Sauter diameter for planar jets are shown in Table F.2. The total relative uncertainties in the Sauter diameter for planar jets vary from 8.38% to 18.32% depending on the homogeneous void fraction at the nozzle exit and the liquid superficial velocity. The relatively high uncertainties are due to the large range of bubble diameters measured on each picture.

$$d_{Sauter} = \frac{\sum_{i=1}^{N} \left(N_i \cdot {d_{b,s,i}}^3 \right)}{\sum_{i=1}^{N} \left(N_i \cdot {d_{b,s,i}}^2 \right)} \tag{F.4}$$

$$U_{d_{Sauter}} = \sqrt{\left[\frac{U_{d_{b,s}}}{\sum_{i=1}^{N} N_i \cdot {d_{b,s,i}}^2} \right]^2 \cdot \sum_{j=1}^{N} \left(N_j \cdot d_{b,s,j} \right)^2 \cdot \left(3 \cdot d_{b,s,j} - 2 \cdot d_{Sauter} \right)^2} \tag{F.5}$$

Table F.2: Listing of uncertainties in the Sauter diameter for planar jets

$j_{l,e}$ (m/s)	α_e (%)	$d_{b,s,avg}$ (mm)	$U_{d_{b,s}}$ (mm)	d_{Sauter} (mm)	$U_{d_{Sauter}}$ (mm)	Relative Uncertainty (%)
1.26	1.00	2.414	1.529	2.819	0.481	17.05
	2.50	3.054	1.653	3.475	0.474	13.64
	5.00	3.574	1.370	3.816	0.393	10.31
	10.0	3.607	1.363	3.844	0.351	9.14
	25.0	3.876	1.520	4.151	0.398	9.58
2.52	1.00	1.441	0.849	1.657	0.304	18.32
	2.50	1.921	1.114	2.152	0.386	17.91
	5.00	2.722	1.069	2.911	0.295	10.14
	10.0	3.264	1.099	3.442	0.288	8.38
	15.0	3.087	1.613	3.473	0.524	15.09
4.92	1.00	1.259	0.543	1.369	0.185	13.53
	2.50	1.562	0.641	1.670	0.201	12.03
	5.00	1.544	0.542	1.622	0.189	11.65
	7.50	1.957	1.026	2.241	0.312	13.91
	10.0	1.964	1.291	2.380	0.419	17.60

F.2 Uncertainty in Void Fraction and Slip Ratio Distribution Measurements

F.2.1 Uncertainty in the Numbers of Counts Measured with each Medium

For the uncertainty in the numbers of counts, both uncertainties due to statistical fluctuations and instrumentation are considered. Calibration of the gamma-ray densitometer was performed every day before and after conducting a experimental test run; ten values for I_l and I_g were obtained, from which the sample standard deviations were calculated. The Student's t-distribution with nine degrees of freedom is used to determine that the multiplier k_c should 2.262 for 95% of the measurements to fall within the uncertainty. The manufacturer stated tolerance for the ORTEC photomultiplier is 0.02%. This tolerance is used to determine the uncertainty from instrumentation based on the average values of intensity for both the liquid and gas, $I_{l,avg}$ and $I_{g,avg}$. Finally, the total uncertainty is found by taking the root-mean-square of the two sources of error computed for the numbers of counts measured with each medium. The uncertainty in the numbers of counts measured with two-phase jets, $U_{I_{2-phase}}$, is assumed to be equal to the higher of the two values for the liquid and gas. The results for the planar and the circular jets are shown in Tables F.3 and F.4, respectively. The relative uncertainties are very low (less than 1%), except for two tests whose uncertainties are between 1 and 3%.

Table F.3: Listing of uncertainties in the numbers of counts measured with each medium for planar jets

Day		Average (-)	σ (-)	U_A (-)	U_B (-)	U_C (-)	Relative Uncertainty (%)
1	I_g	10,746,860	5,112	11,563	2,149	11,761	0.11
	I_l	4,006,629	6,210	14,046	801	14,069	0.35
	$I_{2-phase}$					14,069	
2	I_g	10,737,189	3,504	7,925	2,147	8,211	0.08
	I_l	4,001,339	7,186	16,254	800	16,273	0.41
	$I_{2-phase}$					16,273	

continued on next page

continued from previous page

Day		Average (-)	σ (-)	U_A (-)	U_B (-)	U_C (-)	Relative Uncertainty (%)
3	I_g	10,726,369	3,406	7,703	2,145	7,996	0.07
	I_l	4,002,947	4,396	9,943	801	9,975	0.25
	$I_{2-phase}$					9,975	
4	I_g	10,747,718	7,578	17,142	2,150	17,276	0.16
	I_l	4,005,225	3,270	7,397	801	7,441	0.19
	$I_{2-phase}$					17,276	
5	I_g	10,740,977	8,741	19,773	2,148	19,889	0.19
	I_l	4,005,225	1,933	4,373	801	4,446	0.11
	$I_{2-phase}$					19,889	
6	I_g	10,740,061	4,264	9,646	2,148	9,882	0.09
	I_l	4,003,375	3,066	6,936	801	6,982	0.17
	$I_{2-phase}$					9,882	
7	I_g	10,734,680	7,424	16,793	2,147	16,929	0.16
	I_l	4,001,714	3,732	8,441	800	8,479	0.21
	$I_{2-phase}$					16,929	
8	I_g	10,726,369	3,406	7,703	2,145	7,996	0.07
	I_l	4,002,947	4,396	9,943	801	9,975	0.25
	$I_{2-phase}$					9,975	
9	I_g	10,719,804	5,039	11,399	2,144	11,599	0.11
	I_l	4,003,321	6,715	15,189	801	15,211	0.38
	$I_{2-phase}$					15,211	
10	I_g	10,740,809	5,862	13,260	2,148	13,433	0.13
	I_l	4,004,580	1,801	4,074	801	4,152	0.10
	$I_{2-phase}$					13,433	
11	I_g	10,765,259	9,910	22,416	2,153	22,519	0.21
	I_l	4,009,842	3,038	6,872	802	6,919	0.17
	$I_{2-phase}$					22,519	
12	I_g	10,713,979	13,376	30,256	2,143	30,332	0.28
	I_l	4,008,986	8,026	18,154	802	18,172	0.45
	$I_{2-phase}$					30,332	

Table F.4: Listing of uncertainties in the numbers of counts measured with each medium for circular jets

Day		Average (-)	σ (-)	U_A (-)	U_B (-)	U_C (-)	Relative Uncertainty (%)
1	I_g	10,728,333	30,054	67,981	2,146	68,015	0.63
	I_l	3,962,258	52,541	118,849	792	118,851	3.00
	$I_{2-phase}$					118,851	
2	I_g	10,705,353	12,878	29,130	2,141	29,208	0.27
	I_l	3,932,646	29,518	66,770	787	66,775	1.70
	$I_{2-phase}$					66,775	

continued on next page

continued from previous page							
Day		Average (-)	σ (-)	U_A (-)	U_B (-)	U_C (-)	Relative Uncertainty (%)
3	I_g	10,735,401	16,804	38,010	2,147	38,071	0.35
	I_l	3,970,995	12,223	27,648	794	27,659	0.70
	$I_{2-phase}$					38,071	
4	I_g	10,744,156	6,293	14,236	2,149	14,397	0.13
	I_l	3,981,605	3,538	8,003	796	8,042	0.20
	$I_{2-phase}$					14,397	
5	I_g	10,752,614	2,720	6,154	2,151	6,519	0.06
	I_l	3,974,793	3,559	8,051	795	8,091	0.20
	$I_{2-phase}$					8,091	
6	I_g	10,760,007	4,786	10,826	2,152	11,037	0.10
	I_l	3,975,533	9,849	22,279	795	22,293	0.56
	$I_{2-phase}$					22,293	
7	I_g	10,757,906	5,052	11,427	2,152	11,628	0.11
	I_l	3,966,807	2,779	6,285	793	6,335	0.16
	$I_{2-phase}$					11,628	
8	I_g	10,762,786	3,596	8,135	2,153	8,415	0.08
	I_l	3,978,978	8,822	19,955	796	19,970	0.50
	$I_{2-phase}$					19,970	

F.2.2 Uncertainty in the Averaged Void Fraction across the Container

The total uncertainty in the average void fraction across the container (see Equation F.6) is found by using an error propagation formula (see Equation F.7). It is dependent on the uncertainties for the numbers of counts measured with liquid ($I_{l,avg}$), gas ($I_{g,avg}$), and two-phase jets ($I_{2-phase}(x)$), which are computed in Section F.2.1. The partial derivatives of Equation F.7 are shown in Equations F.8, F.9, and F.10. The total relative uncertainties in the average void fraction across the container for planar and circular jets vary from 0.14% to 0.47% and from 0.32% to 4.77%, respectively, depending on the geometry of the jet, the homogeneous void fraction at the nozzle exit, and the liquid superficial velocity. At low liquid superficial velocity, the relative uncertainty decreases as the homogeneous void fraction at the nozzle exit increases. At high liquid superficial velocity, the inverse is observed (i.e., the relative uncertainty

increases as the homogeneous void fraction at the nozzle exit increases).

$$\alpha_C(x) = \frac{\ln\left(\frac{I_{2-phase}(x)}{I_{l,avg}}\right)}{\ln\left(\frac{I_{g,avg}}{I_{l,avg}}\right)} \tag{F.6}$$

$$U_{\alpha_C(x)} = \sqrt{\left[U_{I_{2-phase}(x)} \cdot \frac{\partial \alpha_C(x)}{\partial I_{2-phase}(x)}\right]^2 + \left[U_{I_{l,avg}} \cdot \frac{\partial \alpha_C(x)}{\partial I_{l,avg}}\right]^2 + \left[U_{I_{g,avg}} \cdot \frac{\partial \alpha_C(x)}{\partial I_{g,avg}}\right]^2} \tag{F.7}$$

$$\frac{\partial \alpha_C(x)}{\partial I_{2-phase}(x)} = \left[\ln\left(\frac{I_{g,avg}}{I_{l,avg}}\right) \cdot I_{2-phase}(x)\right]^{-1} \tag{F.8}$$

$$\frac{\partial \alpha_C(x)}{\partial I_{l,avg}} = -\frac{1-\alpha_C(x)}{I_{l,avg} \cdot \ln\left(\frac{I_{g,avg}}{I_{l,avg}}\right)} \tag{F.9}$$

$$\frac{\partial \alpha_C(x)}{\partial I_{g,avg}} = -\frac{\alpha_C(x)}{I_{g,avg} \cdot \ln\left(\frac{I_{g,avg}}{I_{l,avg}}\right)} \tag{F.10}$$

F.2.3 Uncertainty in the Collapsed Liquid Thickness of the Jet

The total uncertainty in the collapsed liquid thickness of the jet is found by using an error propagation formula (see Equation F.12). The collapsed liquid thickness has an influence coefficient and a standard uncertainty for the inner length of the container cross section (δ_C) and the average void fraction across the container (see Equation F.11). The uncertainties in the average void fraction across the container were computed in Section F.2.2. The uncertainty for the inner length of the container cross section is due to the precision of the depth micrometer used to measure δ_C; based on the smallest unit measurement on the micrometer, it is assumed to be 7.62 $\times$ 10^{-4} m. The total relative uncertainties in the collapsed liquid thickness of the jet for planar and circular jets vary from 1.53% to 4.81% and from 1.26% to 5.42%, respectively, depending on the geometry of the jet, the homogeneous void fraction at the nozzle exit, and the liquid superficial velocity. The relative uncertainty increases as the homogeneous void fraction at the nozzle exit increases.

$$\delta_{CLT}(x) = \delta_C \cdot (1 - \alpha_C(x)) \tag{F.11}$$

$$U_{\delta_{CLT}(x)} = \sqrt{\left[U_{\delta_C} \cdot (1-\alpha_C(x))\right]^2 + \left[U_{\alpha_C(x)} \cdot \delta_C\right]^2} \tag{F.12}$$

F.2.4 Uncertainty in the Void Fraction of the Jet

The total uncertainty in the void fraction of the jet is found by using an error propagation formula (see Equation F.14). The void fraction of the jet has an influence coefficient and a standard uncertainty for the jet collapsed liquid thickness ($\delta_{CLT}(x)$) and the jet measured thickness ($\delta_{jet}(x)$) (see Equation F.13). The uncertainties in the jet collapsed liquid thickness were computed in Section F.2.3. The uncertainty for the jet measured thickness is due to the precision of the depth micrometer used to measure $\delta_{jet}(x)$; it is assumed to be 6.35×10^{-5} m. The total absolute uncertainties in the void fraction of the jet for planar and circular jets vary from 1.50% to 2.58% and from 1.18% to 5.37%, respectively, depending on the geometry of the jet, the homogeneous void fraction at the nozzle exit, and the liquid superficial velocity. Since low void fractions $\alpha_{jet}(x)$ were measured in this investigation (between 1% and 15%), the total relative uncertainties in the void fraction of the jet can be extremely high; they vary from 17% to 158% and from 14% to 230% for the planar and circular jets, respectively. The relative uncertainty decreases as the homogeneous void fraction at the nozzle exit and the liquid superficial velocity increase.

$$\alpha_{jet}(x) = 1 - \frac{\delta_{CLT}(x)}{\delta_{jet}(x)} \tag{F.13}$$

$$U_{\alpha_{jet}(x)} = \sqrt{\left[U_{\delta_{CLT}(x)} \cdot \frac{-1}{\delta_{jet}(x)}\right]^2 + \left[U_{\delta_{jet}(x)} \cdot \frac{\delta_{CLT}(x)}{\delta_{jet}^2(x)}\right]^2} \tag{F.14}$$

F.2.5 Uncertainty in the Slip Ratio

The total uncertainty in the slip ratio within the jet is found by using an error propagation formula (see Equation F.16). The slip ratio within the jet has an influence coefficient and a standard uncertainty for the void fraction of the jet ($\alpha_{jet}(x)$) and the homogeneous void fraction at the nozzle exit (α_e) (see Equation F.15). The error on α_e is assumed to be small compared to the error in α_{jet}(x). The uncertainties in the slip ratio within the jet were computed in Section F.2.4. The total absolute

uncertainties in the slip ratio for planar and circular jets vary in average from 0.15 to 0.68 and from 0.08 to 0.41, respectively, depending on the geometry of the jet, the homogeneous void fraction at the nozzle exit, and the liquid superficial velocity; the higher uncertainties are found for very low void fractions. As aforementioned, the total relative uncertainties in the slip ratio can be extremely high; they vary from 20% to 149% and from 10% to 117% for the planar and circular jets, respectively. The relative uncertainty decreases as the homogeneous void fraction at the nozzle exit and the liquid superficial velocity increase.

$$S(x) = \frac{\alpha_e}{\alpha_{jet}(x)} \cdot \frac{1 - \alpha_{jet}(x)}{1 - \alpha_e} \tag{F.15}$$

$$U_{S(x)} = \sqrt{\left[U_{\alpha_{jet}(x)} \cdot \frac{\alpha_e}{(1-\alpha_e) \cdot (\alpha_{jet}(x))^2}\right]^2} = \left|U_{\alpha_{jet}(x)} \cdot \frac{\alpha_e}{(1-\alpha_e) \cdot (\alpha_{jet}(x))^2}\right| \tag{F.16}$$

F.3 Uncertainty in Shock Attenuation Measurements

For the uncertainty in the shock attenuation measurements, both uncertainties due to statistical fluctuations and instrumentation are considered in this subsection. The uncertainty due to statistical fluctuations is obtained for the transient pressure histories for 12 experiments conducted without a jet present in the enclosure; the experiments were conducted using the radial-and-axial confinement boundary configuration with pulser input energy of 2.4 kJ (referring to Table 4.5 test # 21). The pressure signal captured by the transducer at the bottom of the confinement tube is shown in Figure 4.29. For each transient pressure history, $25,000$ instantaneous pressure samples were recorded at a data rate of 125 kHz and the sample standard deviations were calculated. The Student's t-distribution with 11 degrees of freedom is used to determine that the multiplier k_c should 2.201 for 95% of the measurements to fall within the uncertainty. The uncertainty due to instrumentation in the pressure transducer reading is found by using the manufacturer stated instrumental uncertainty of +/-

1%. The total absolute uncertainty in shock attenuation measurements is found to be in average approximately +/-0.18 psi.

As shown in Figure 4.29, the overall profile of the pressure histories is in good qualitative agreement, given the sensitivity of the pressure transducer to slight changes in initial conditions.

APPENDIX G

MODELING IN $FLUENT^{®}$

In this Appendix, the single- and two-phase jet models in $FLUENT^{®}$ are presented. Section G.1 describes the model options used for single-phase jets and their effects, while Section G.2 contains the two-phase modeling options.

G.1 Single-Phase Jet Modeling

G.1.1 Selection of the Single-Phase Model Options in $FLUENT^{®}$

- Selecting the Multiphase Model:

$FLUENT^{®}$'s documentation recommends to use the *Volume Of Fluid* (*VOF*) model for stratified/free-surface flows ($FLUENT^{®}$, 2004). The *VOF* model is a surface-tracking technique applied to a fixed Eulerian mesh. It is designed for two or more immiscible fluids where the position of the interface between the fluids is of interest. In the *VOF* model, a single set of momentum equations is shared by the fluids, and the volume fraction of each of the fluids in each computational cell is tracked throughout the domain. Applications of the *VOF* model include stratified flows, free-surface flows, filling, sloshing, the motion of large bubbles in a liquid, the motion of liquid after a dam break, the prediction of jet breakup (surface tension), and the steady or transient tracking of any liquid-gas interface. For each additional phase that is added to the model, a variable is introduced: the volume fraction of the phase in the computational cell. In each control volume, the volume fractions of all phases sum to unity. The fields for all variables and properties are shared by the phases and represent volume-averaged values, as long as the volume fraction of each of the phases is known at each location. Thus the variables and properties in any given cell

are either purely representative of one of the phases, or representative of a mixture of the phases, depending upon the volume fraction values. In other words, if the q^{th} fluid's volume fraction in the cell is denoted as α, then the following three conditions are possible:

- $\alpha = 0$: the cell is empty (of the q^{th} fluid).

- $\alpha = 1$: the cell is full (of the q^{th} fluid)

- $0 < \alpha < 1$: the cell contains the interface between the q^{th} fluid and one or more other fluids.

Based on the local value of α, the appropriate properties and variables are assigned to each control volume within the domain ($FLUENT$®, 2004).

For the *VOF* model, it is necessary to specify the *VOF* formulation as well. The time-dependent with the *implicit* interpolation scheme can be used if the user is looking for a steady-state solution and is not interested in the intermediate transient flow behavior, but the final steady-state solution is dependent on the initial flow conditions. While the *implicit* time-dependent formulation is less computationally expensive than the *geometric reconstruction* scheme (default *VOF* scheme), the interface between phases is not as sharp as that predicted with the *geometric reconstruction* scheme. To reduce this diffusivity, it is recommended to use the *second-order* discretization scheme for the volume fraction equations (see Section "Selecting the Solver, the Controls and Discretization Parameters:"). In addition, turning the *geometric reconstruction* scheme back on after calculating a solution with the implicit scheme may help to obtain a sharper interface ($FLUENT$®, 2004).

- Defining the Phases:

In general, there is no rule as to how to specify the primary and secondary phases. However, since it is necessary to patch an initial volume fraction of 1 for the air

phase in all the domain, it is more convenient to make that phase a secondary phase. Therefore, the water phase has been selected as the primary phase. In order to model the free surface, the surface tension effects between water and air are turned on and the coefficient is set to a constant equal to 72.8 mN/m, which is the surface tension coefficient between water and air at $T_{room} = 295$ K $= 22^{o}$C. Note that the calculation of surface tension effects are more accurate if a quadrilateral or hexahedral mesh is used in the areas of the computational domain where surface tension is significant (see Section 5.1.1). For calculations involving surface tension, $FLUENT$®'s documentation recommends to turn on the *implicit body force* treatment for the body force formulation in the multiphase model panel. This treatment improves solution convergence by accounting for the partial equilibrium of the pressure gradient and surface tension forces in the momentum equations (see Section "Including Body Forces:") ($FLUENT$®, 2004).

- Including Body Forces:

In this investigation, the motion of the phases is strongly influenced by gravitational effects. Therefore, gravity is turned on in the operating conditions panel and the gravitational acceleration is set to 9.81 m/s^2.

For *VOF* calculations, the *specified operating density* option in the operating conditions panel needs to be activated and the operating density is set to the density of the lightest phase (i.e., air). This excludes the buildup of hydrostatic pressure within the lightest phase, improving the round-off accuracy for the momentum balance ($FLUENT$®, 2004).

For *VOF* calculations involving body forces, it is recommended to also turn on the *implicit body force* treatment for the body force formulation in the multiphase model panel. When large body forces (e.g., gravity or surface tension forces) exist in multiphase flows, the body force and pressure gradient terms in the momentum equation are almost in equilibrium. *Segregated* algorithms converge poorly unless partial

equilibrium of pressure gradient and body forces is taken into account. $FLUENT^{®}$ provides an optional *implicit body force* treatment that can account for this effect, making the solution more robust. The basic procedure involves augmenting the correction equation for the face flow rate with an additional term involving corrections to the body force. This results in extra body force correction terms and allows the flow to achieve a realistic pressure field very early in the iterative process. In addition, $FLUENT^{®}$ allows control of the change in the body forces through the use of an under-relaxation factor for body forces ($FLUENT^{®}$, 2004).

- Setting the Turbulence Model:

The simplest complete models of turbulence are the two-equation models in which the solution of two separate transport equations allows the turbulent velocity and length scales to be independently determined. The $k-\epsilon$ model in $FLUENT^{®}$ falls within this class of turbulence models and has become the workhorse of practical engineering flow calculations. Robustness, economy, and reasonable accuracy for a wide range of turbulent flows explain its popularity. It is a semi-empirical model, and the derivation of the model equations relies on phenomenological considerations and empiricism ($FLUENT^{®}$, 2004). The default parameters of the *standard* and *realizable* $k-\epsilon$ models with *standard wall functions* are used in this study. For the inlet and the outlets, the turbulence intensity and the hydraulic diameter are specified (see Table G.1).

Another turbulence model has been studied and compared to the $k-\epsilon$ options. Turbulent flows are characterized by eddies with a wide range of length and time scales. The largest eddies are typically comparable in size to the characteristic length of the mean flow. The smallest scales are responsible for the dissipation of turbulence kinetic energy. In the *Large Eddy Simulation* model *LES*, large eddies are resolved directly, while small eddies are modeled. The rationale behind *LES* is that

by modeling less of turbulence (and resolving more), the error introduced by turbulence modeling can be reduced ($FLUENT$®, 2004). It is also believed to be easier to find a "universal" model for the small scales, since they tend to be more isotropic and less affected by the macroscopic features like boundary conditions, than the large eddies ($FLUENT$®, 2004). In this study, the stochastic components of the flow at the velocity-specified inlet boundary are neglected. Individual instantaneous velocity components are simply set equal to their mean velocity counterparts, since the level of turbulence at the inflow boundary is negligible due to the flow conditioner.

- Setting the Boundary Conditions:

By default, the reference pressure location is the center of the cell at or closest to the point (0,0,0). The site of the reference pressure is moved to a location that will result in less round-off in the pressure calculation by specifying a new reference pressure location in the operating conditions panel. The position must be in a region that will always contain the least dense of the fluids (i.e., the gas phase). This is because variations in the static pressure are larger in a more dense fluid than in a less dense fluid, given the same velocity distribution. If the zero of the relative pressure field is in a region where the pressure variations are small, less round-off will occur than if the variations occur in a field of large non-zero values ($FLUENT$®, 2004). Therefore, the reference pressure location is chosen to be at the intersection of the outlet boundary and the outer-wall.

The detailed list of the boundary conditions and their different parameters is given in Table G.1. Note that the inlet velocity specified at the "Inlet" corresponds to the water velocity at the nozzle entrance, which is three times less than the average water velocity at the nozzle exit. Referring to the case presented in Table G.1, it corresponds to a jet with a liquid superficial velocity at the nozzle exit $j_{l,e} = 3$ m/s.

The hydraulic diameter is calculated according to the following formula:

$$D_H = 4 \cdot \frac{Flow\ Area}{Wetted\ Perimeter} \tag{G.1}$$

For the outlets "Air-Outlet" and "Water-Outlet", the hydraulic diameters are calculated from $\delta(x = 15.9\text{ cm})$ and $w(x = 15.9\text{ cm})$, the experimentally-measured thickness and width along the y- and z-axis, respectively, assuming that the cross section of the water flow at the outlet is a rectangle. The turbulence intensity at the core of a fully-developed duct flow can be estimated from the following formula derived from an empirical correlation for pipe flows ($FLUENT$®, 2004):

$$I = 0.16 \cdot (Re_{D_H})^{-1/8} \tag{G.2}$$

This formula is used to approximate the turbulence intensity both at the inlet and the outlets. The Reynolds number Re_{D_H} is based on the water velocity at the inlet.

If the jet is assumed to have the same shape and cross section from the nozzle exit along the x-axis, the backflow volume fraction of air across the "Water-Outlet" would be zero. In reality, the jet changes geometry downstream of the imposed rectangular nozzle exit condition. The jet width and thickness decrease along the flow direction due to surface tension forces and gravitational acceleration of the flow. Therefore, the backflow volume fraction of air across the "Water-Outlet" is greater than zero. It is estimated to be:

$$Backflow\ Volume\ Fraction = 1 - \frac{Cross\ Section\ of\ the\ Jet\ at\ x = 15.9\ cm}{Cross\ Section\ of\ the\ Jet\ at\ the\ Nozzle\ Exit} \tag{G.3}$$

The cross section of the jet at x = 15.9 cm is calculated from $\delta(x = 15.9\text{ cm})$ and $w(x = 15.9\text{ cm})$, the experimentally-measured thickness and width along the y- and z-axis, respectively, assuming that the cross section of the water flow at that location is a rectangle. The backflow volume fraction is found to be 0.12 for a liquid superficial velocity at the nozzle exit $j_{l,e} = 3$ m/s.

The boundaries labeled as "Wall-Nozzle" and "Wall-Thickness" (see Table G.1) are real and, therefore, no slip is assumed at the wall. The boundary labeled as "Outer-Wall" has no real physical existence, and its only purpose is to close the numerical domain. Thus, the stress at this virtual wall can be specified and set to zero.

Table G.1: Detailed list of the boundary conditions and their parameters

Name	Mixture	Water	Air
Inlet	***Velocity-Inlet*** - Velocity specification method: magnitude, normal to the boundary - Velocity magnitude: 1 m/s - Turbulence specification method: intensity and hydraulic diameter - Turbulence Intensity: 4.18% - Hydraulic diameter: 4.62 cm		Volume fraction: 0
Air-Outlet	***Pressure-Outlet*** - Gauge pressure: 0 Pa - Backflow direction specification method: normal to the boundary - Turbulence specification method: intensity and hydraulic diameter - Turbulence intensity: 5.00% - Hydraulic diameter: 1.10 cm		Backflow volume: 1

continued on next page

continued from previous page

Name	Mixture	Water	Air
Water-Outlet	***Pressure-Outlet*** - Gauge Pressure: 0 Pa - Backflow direction specification method: normal to the boundary - Turbulence specification method: intensity and hydraulic diameter - Turbulence intensity: 4.82% - Hydraulic diameter: 1.48 cm		Backflow volume: 0/0.12
Wall-Nozzle	***Wall*** - Shear condition: no slip		
Wall-Thickness	***Wall*** - Shear condition: no slip		
Outer-Wall	***Wall*** - Shear condition: specified stress (0,0,0)		

- Selecting the Solver, the Controls and Discretization Parameters:

The *segregated* solver is traditionally used for incompressible and mildly compressible flows. Moreover, the *segregated* solver provides several physical models that are not available with the coupled solvers (e.g., *VOF* model) ($FLUENT^{®}$, 2004). Thus, a 3D unsteady calculation with the *segregated* solver has been for this investigation.

A number of pressure interpolation schemes are available when the *segregated* solver is used in $FLUENT^{®}$. The default *standard* scheme interpolates the pressure values at the faces using momentum equation coefficients. This procedure works well

as long as the pressure variation between cell centers is smooth. When there are jumps or large gradients in the momentum source terms between control volumes, the pressure profile has a high gradient at the cell face, and cannot be interpolated using this scheme. If this scheme is used, the discrepancy shows up in overshoots/undershoots of cell velocity. Flows for which the *standard* pressure interpolation scheme may experience difficulty include flows with large body forces. In such cases, it is necessary to pack the mesh in regions of high gradient to resolve the pressure variation adequately. Another source of error is that $FLUENT^{®}$ assumes that the normal pressure gradient at the wall is zero. This is valid for boundary layers, but not in the presence of body forces or curvature. Again, the failure to correctly account for the wall pressure gradient is manifested in velocity vectors pointing in/out of walls. The *body-force-weighted* scheme computes the face pressure by assuming that the normal gradient of the difference between pressure and body forces is constant. This works well if the body forces are known a priori in the momentum equations (e.g., buoyancy). The *second-order* scheme is not applicable for flows with discontinuous pressure gradients imposed by the use of the *VOF* for multiphase flow. For most cases the *PRESTO* scheme is acceptable, but for problems involving large body forces and *VOF* calculations, the *body-force-weighted* scheme is recommended ($FLUENT^{®}$, 2004).

When the flow is aligned with the grid, the *first-order* upwind discretization scheme may be acceptable. If the flow is not aligned with the grid, however, *first-order* convective discretization increases the numerical discretization error (numerical diffusion). For quad/hex grids, better results will be obtained using the *second-order* discretization, especially for complex flows. While the *first-order* discretization scheme generally yields better convergence than the *second-order* scheme, it will generally yield less accurate results. For *VOF* calculations, when the *implicit* scheme is used, the *modified HRIC*, *second-order*, or *QUICK* discretization schemes should be used

for the volume fraction equations in order to improve the sharpness of the interface between phases; it is also less computationally intensive than the *Geo-Reconstruct* scheme ($FLUENT^{®}$, 2004).

Steady-state calculations generally use *SIMPLE* or *SIMPLEC* for the pressure-velocity coupling scheme, while *PISO* is recommended for transient calculations. Using *PISO* allows for increased values on all under-relaxation factors, without a loss of solution stability. *PISO* can maintain a stable calculation with a larger time step and an under-relaxation factor of 1.0 for both momentum and pressure ($FLUENT^{®}$, 2004).

- Setting the Time-Dependent Parameters:

Since the $FLUENT^{®}$ formulation is fully implicit, there is no stability criterion that needs to be met in determining the time step. However, to model transient phenomena properly, it is necessary to set the time step at least one order of magnitude smaller than the smallest time constant in the system being modeled. A good way to judge the choice of the time step is to observe the number of iterations $FLUENT^{®}$ needs to converge at each time step. The ideal number of iterations per time step is 5-10. If $FLUENT^{®}$ needs substantially more iterations, the selected time step may be too large. If $FLUENT^{®}$ needs only a few iterations per time step, the time step can be increased. For a stable, efficient calculation, the Courant number within the domain should not exceed a value of 20-40 in most sensitive transient regions of the domain ($FLUENT^{®}$, 2004).

By default, $FLUENT^{®}$ solves the volume fraction equation once for each time step. This means that the convective flux coefficients appearing in the other transport equations are not completely updated each iteration, since the volume fraction field does not change from iteration to iteration. When $FLUENT^{®}$ performs a time-dependent *VOF* calculation, the time step used for the volume fraction calculation is not the same as the time step used for the rest of the transport equations. $FLUENT^{®}$

refines the time step for *VOF* automatically, based on the default input for the maximum Courant Number allowed near the free surface (its default value is set to 0.25) (*FLUENT*®, 2004).

- Setting the Initial Volume Fraction:

Once the flow is initialized from the inlet, the initial distribution of the phases needs to be defined. For a transient simulation, this distribution will serve as the initial condition at $t = 0$. The initial volume fraction for the secondary phase, i.e. air, is set equal to 1 in the entire domain.

- Checking the Convergence:

At the end of each solver iteration, the residual sum for each of the conserved variables is computed and stored, thereby recording the convergence history. On a computer with infinite precision, these residuals would go to zero as the solution converges. On an actual computer, the residuals decay to some small value ("round-off") and then stop changing ("level out"). The scaled residual is an appropriate indicator of convergence. A popular approach to judging convergence is to require that the unscaled residuals drop by three orders of magnitude. Lax's equivalence theorem states that for non-linear problems consistency and stability are necessary conditions for convergence. Therefore, ensuring convergence of the model also proves its stability and consistency (*FLUENT*®, 2004).

At the end of each solver iteration or time step, the average, mass average, integral, flow rate, or other integral report of a field variable or function can be monitored on a surface. Monitoring surface integrals can be used to check for both iteration convergence and grid independence. For example, the average value of a certain variable can be monitored on a surface. When this value stops changing, one can stop iterating. Then the grid can be adapted and the solution can be reconverged. The solution can be considered grid-independent when the average value on the surface

stops changing between adaptions. In this investigation, the mass flow rates at the inlet and the outlets are monitored; when the net mass flow rate stops changing, the solution can be considered to have reached steady-state ($FLUENT$®, 2004).

G.1.2 Parametric Analysis

In order to assess the $FLUENT$® models ability to predict the contours of a single-phase jet, a baseline case is created and the simulated contours of the jet are compared with the experimental results obtained in this investigation. The baseline case simulates a laminar planar jet with a liquid superficial velocity at the nozzle exit $j_{l,e}$ = 3 m/s. The used scheme are *VOF-Implicit*, *first-order* discretization scheme for the volume fraction equation, and the *PISO* scheme as the pressure-velocity coupling scheme. The mesh is built with the mesh size Δx = 1 mm, Δy = 0.25 mm, and Δz = 0.5 mm for the x-, y-, and z-directions, respectively. The backflow volume fraction of air across the "Water-Outlet" is set to 0. The time step is Δt = 0.8 ms. The jet thickness in the y-direction and the jet width in the z-direction calculated by the code are plotted in pink in the following figures of Section G.1.2 and are compared with the experimental values measured at $j_{l,e}$ = 3 m/s which are plotted in green. The error bars shown on the experimental values are 0.127 mm and 0.225 mm for the thickness and the width, and correspond to the errors due to the depth micrometer and the pixel size, respectively. On each figure different water isosurfaces ($0.6 \leq \alpha_{water} \leq 1$) are plotted; the isosurface $\alpha_{water} = 1$ pertains the case where the contours border the region containing only water, while the isosurface $\alpha_{water} = 0.6$ pertains the case where the contours border a region containing the water jet and its boundaries at 60% water. The predicted curves in the following figures of Section G.1.2 successively represent from the bottom to the top the water isosurfaces $\alpha_{water} = 1$, $\alpha_{water} = 0.99$, $\alpha_{water} = 0.9$, $\alpha_{water} = 0.8$, $\alpha_{water} = 0.7$, and $\alpha_{water} = 0.6$.

Different simulation parameters are studied in order to examine their effect on the

calculated results. The effects of the mesh size Δx and Δz, the time step Δt, the backflow volume fraction of air across the "Water-Outlet", the turbulence, and the controls and discretization schemes are successively examined and compared to the baseline case.

- Effect of Mesh Size:

The effect of mesh size in the x-direction is studied. Comparison is made between experimental and predicted values when two mesh sizes with a mesh step in the x-direction (i.e., in the flow direction) $\Delta x = 1$ mm and $\Delta x = 2$ mm are used (see Section 5.1.1). Both the jet thickness and the jet width of the experimental and predicted values are examined and compared for different x-positions from the nozzle (between x = 0 cm and x = 16 cm). The experimental data are plotted in green while the baseline case, $\Delta x = 1$ mm, is plotted in pink, and the second simulated case with a coarser mesh, $\Delta x = 2$ mm, is plotted in blue. The mesh step Δz in both cases is 0.5 mm. Figures G.1 and G.2 show the evolution along the x-axis of the jet thickness and width, respectively, when the mesh size in the x-direction is varied. Results for the jet thickness show good agreement for 0 cm $<$ x $<$ 13 cm between the experimental and the baseline case values for a water isosurface α_{water} = 0.6; differences are within the experimental errors bars (see Figure G.1). For the case $\Delta x = 2$ mm, the simulation is dependent on the grid size; the predicted values increasingly diverge from the experimental values for 0 cm $<$ x $<$ 9 cm. For 9 cm $<$ x $<$ 16 cm, the predicted values using $\Delta x = 2$ mm show good agreement with the predicted results for $\Delta x = 1$ mm; however, they begin diverging around $x = 16$ cm.

Figure G.2 has the same characteristics as Figure G.1. Results for the jet width show good agreement between the experimental and the baseline case values for 0 cm $<$ x $<$ 13 cm and a water isosurface $\alpha_{water} = 0.6$; differences are within the experimental errors bars (see Figure G.2). For the case $\Delta x = 2$ mm, the simulation shows again its dependence on the grid size; a strong non-physical discontinuity appears at

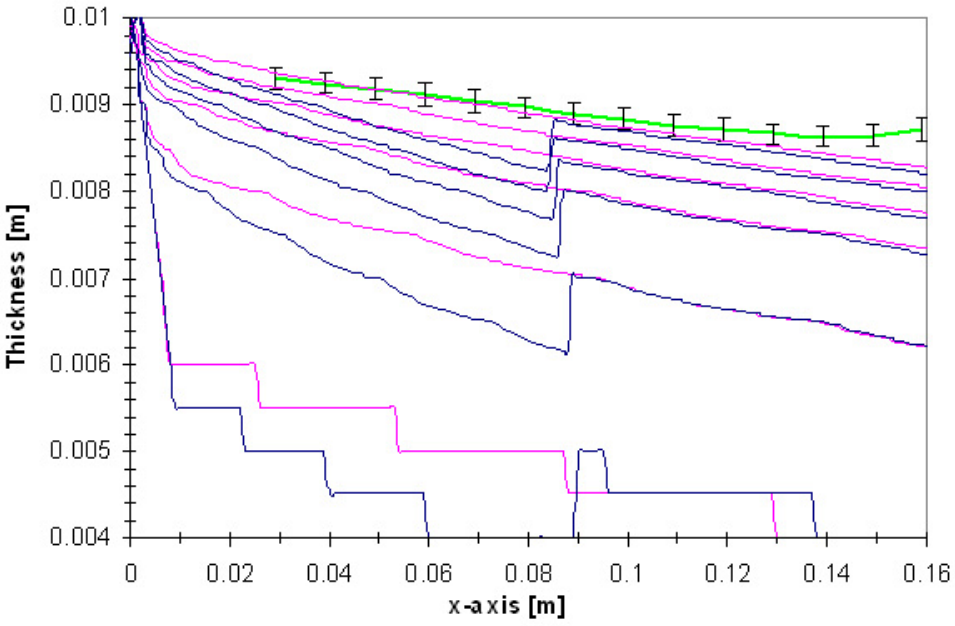

Figure G.1: Comparison of the jet thicknesses (y-direction) along the x-axis, between experimental (green) and predicted values when $\Delta x = 1$ mm (pink) and $\Delta x = 2$ mm (blue). Predicted curves of a same color (pink or blue) successively represent from the bottom to the top the water isosurfaces $\alpha_{water} = 1$, $\alpha_{water} = 0.99$, $\alpha_{water} = 0.9$, $\alpha_{water} = 0.8$, $\alpha_{water} = 0.7$, and $\alpha_{water} = 0.6$.

x = 9 cm.

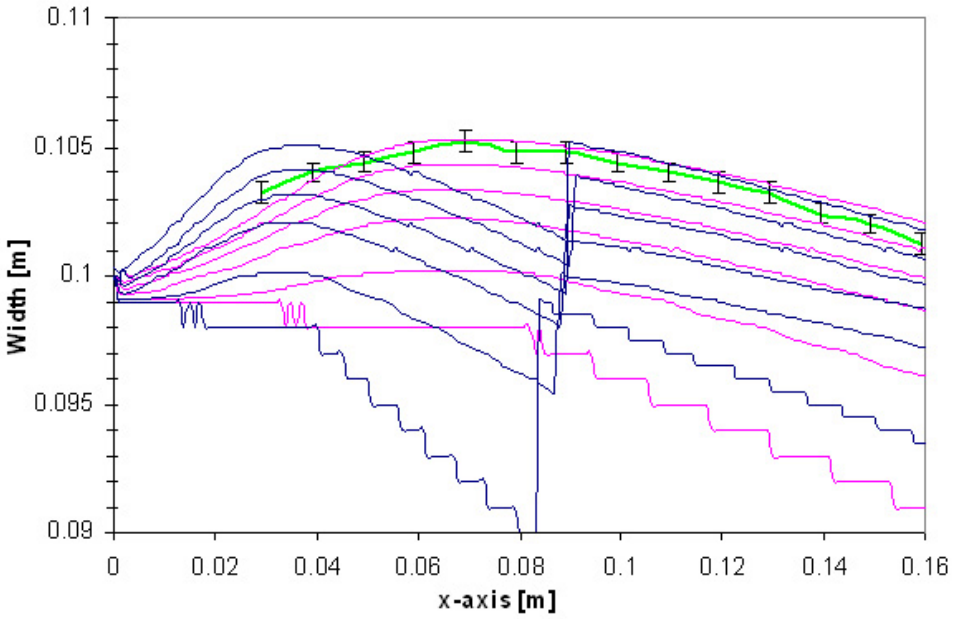

Figure G.2: Comparison of the jet widths (z-direction) along the x-axis, between experimental (green) and predicted values when $\Delta x = 1$ mm (pink) and $\Delta x = 2$ mm (blue). Predicted curves of a same color (pink or blue) successively represent from the bottom to the top the water isosurfaces $\alpha_{water} = 1$, $\alpha_{water} = 0.99$, $\alpha_{water} = 0.9$, $\alpha_{water} = 0.8$, $\alpha_{water} = 0.7$, and $\alpha_{water} = 0.6$.

The mesh size study shows that $\Delta x = 1$ mm is the largest value for Δx for which the simulation result is independent of the mesh grid.

The effects of the mesh size in the z-direction are now investigated. Comparison is made between experimental and predicted values for two mesh sizes in the z-direction: $\Delta z = 0.5$ mm and $\Delta z = 0.25$ mm. The baseline case with a mesh step $\Delta z = 0.5$ mm is plotted in pink, while the second case simulated with a finer mesh, $\Delta z = 0.25$ mm, is plotted in blue. The mesh step Δx in both cases equals 1 mm. Figures G.3 and G.4 show the evolution along the x-axis of the jet thickness and width, respectively, when the effects of the mesh size in the z-direction are studied. Referring to Figure G.3, the case $\Delta z = 0.25$ mm shows excellent agreement with the baseline case; the errors on the water isosurface $\alpha_{water} = 1$ increase due to the propagation of the error at each discontinuity.

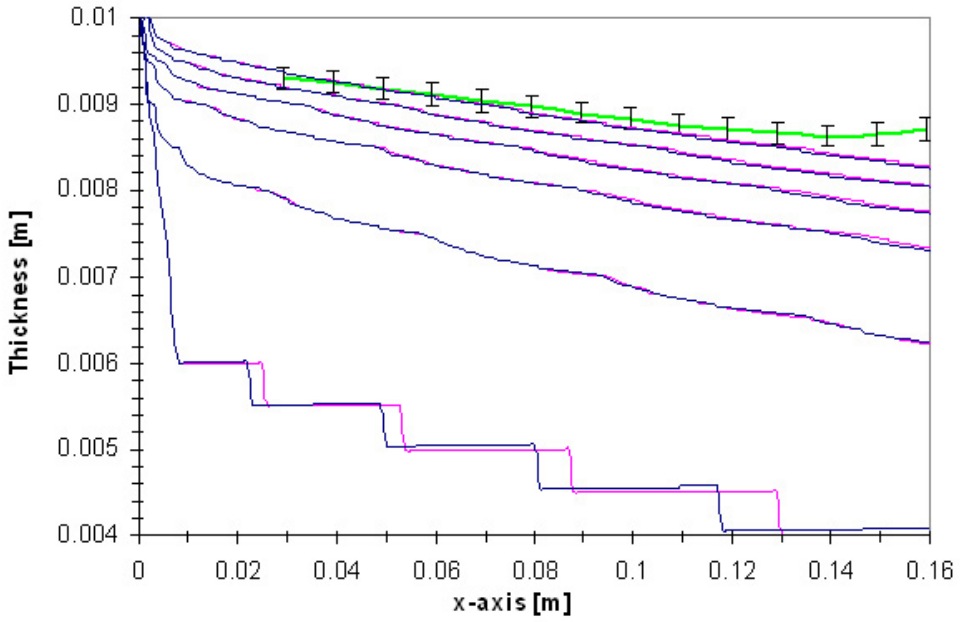

Figure G.3: Comparison of the jet thicknesses (y-direction) along the x-axis, between experimental (green) and predicted values when $\Delta z = 0.5$ mm (pink) and $\Delta x = 0.25$ mm (blue). Predicted curves of a same color (pink or blue) successively represent from the bottom to the top the water isosurfaces $\alpha_{water} = 1$, $\alpha_{water} = 0.99$, $\alpha_{water} = 0.9$, $\alpha_{water} = 0.8$, $\alpha_{water} = 0.7$, and $\alpha_{water} = 0.6$.

Figure G.4 also show good agreement between the baseline case ($\Delta z = 0.5$ mm) and the second simulated case ($\Delta z = 0.25$ mm), when water isosurfaces are in the range $0.6 \leq \alpha_{water} \leq 0.9$; the errors are within the size of the mesh. For $\alpha_{water} = 0.99$ or 1, significant differences are observed between the baseline case and the case with a finer mesh. However, the improvement of the free surface sharpness is not significant

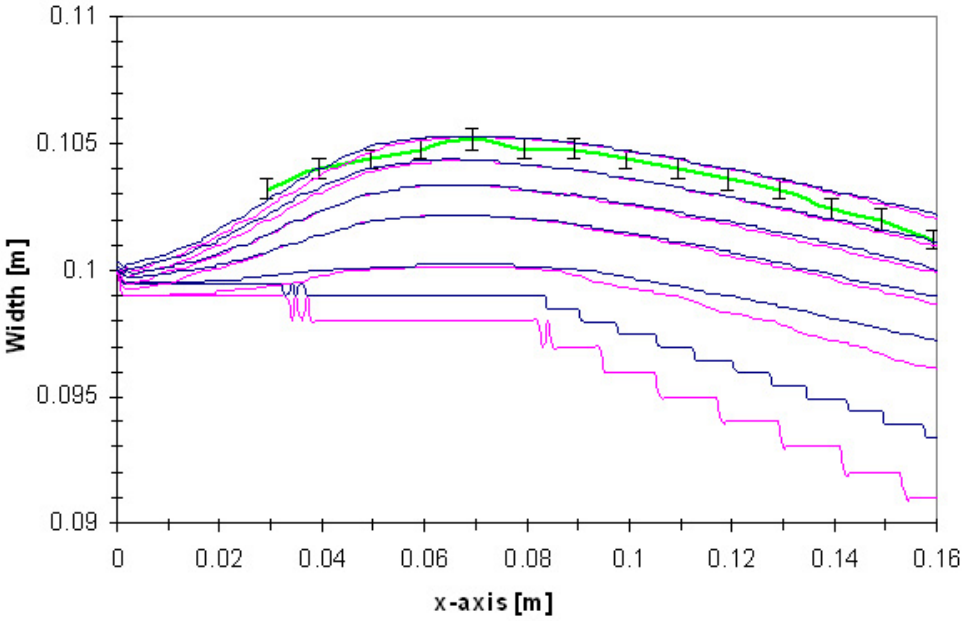

Figure G.4: Comparison of the jet widths (z-direction) along the x-axis, between experimental (green) and predicted values when $\Delta x = 0.5$ mm (pink) and $\Delta x = 0.25$ mm (blue). Predicted curves of a same color (pink or blue) successively represent from the bottom to the top the water isosurfaces $\alpha_{water} = 1$, $\alpha_{water} = 0.99$, $\alpha_{water} = 0.9$, $\alpha_{water} = 0.8$, $\alpha_{water} = 0.7$, and $\alpha_{water} = 0.6$.

enough to justify the use of a finer mesh for Δz, and it increases the cost of the solution in terms of necessary computer hardware and calculation time. Therefore, with $\Delta x = 1$ mm, $\Delta y = 0.25$ mm, and $\Delta z = 0.5$ mm, the errors due to the coarseness of the grid appear to be eliminated.

- Effect of Time Step:

The effect of time step of the simulation is now considered. Comparison is made between experimental and predicted values when two time steps $\Delta t = 0.8$ ms and Δt

= 5 ms are studied. The baseline case, Δt = 0.8 ms, is plotted in pink, while the second simulated case with a larger time step, Δx = 5 ms, is plotted in blue. The mesh size (Δx = 1 mm, Δy = 0.25 mm, and Δz = 0.5 mm) is the same in both cases. Figures G.5 and G.6 show the evolution along the x-axis of the jet thickness and width, respectively, when the effects of time step of the simulation are studied. Results for the jet thickness show excellent agreement between the baseline case Δt = 0.8 ms and the case Δt = 5 ms (see Figure G.5); the errors in the water isosurface α_{water} = 1 slightly increase due to the propagation of the error at each discontinuity.

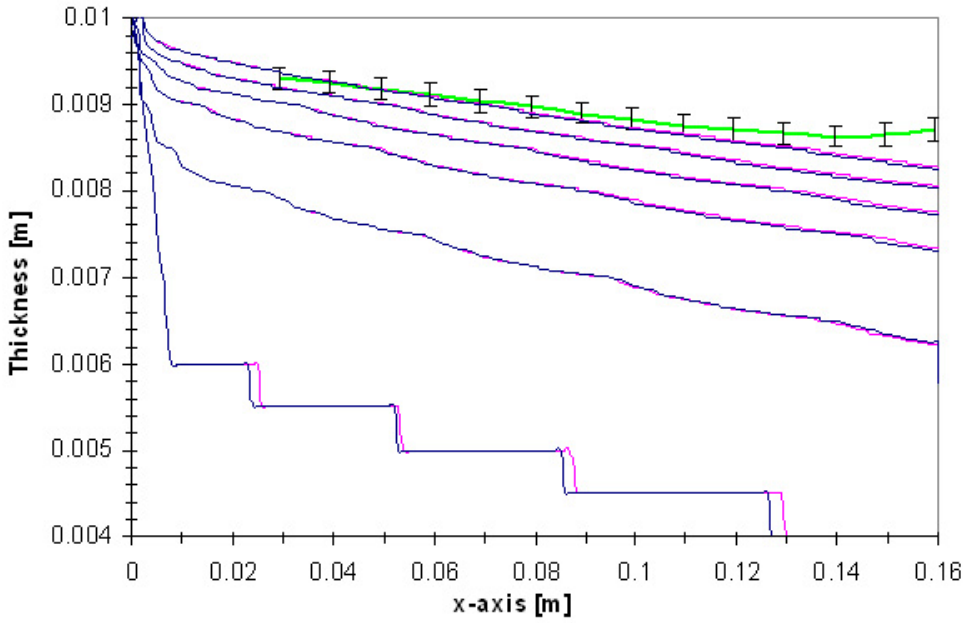

Figure G.5: Comparison of the jet thicknesses (y-direction) along the x-axis, between experimental (green) and predicted values when Δt = 0.8 ms (pink) and Δt = 5 ms (blue). Predicted curves of a same color (pink or blue) successively represent from the bottom to the top the water isosurfaces α_{water} = 1, α_{water} = 0.99, α_{water} = 0.9, α_{water} = 0.8, α_{water} = 0.7, and α_{water} = 0.6.

Figure G.6 has the same characteristics as Figure G.5. Results for the jet width show almost perfect agreement between the baseline case with Δt = 0.8 ms and the case with Δt = 5 ms for a water isosurface α_{water} = 0.6. Therefore, the time step Δt = 0.8 ms is assumed to be small enough not to influence the simulation.

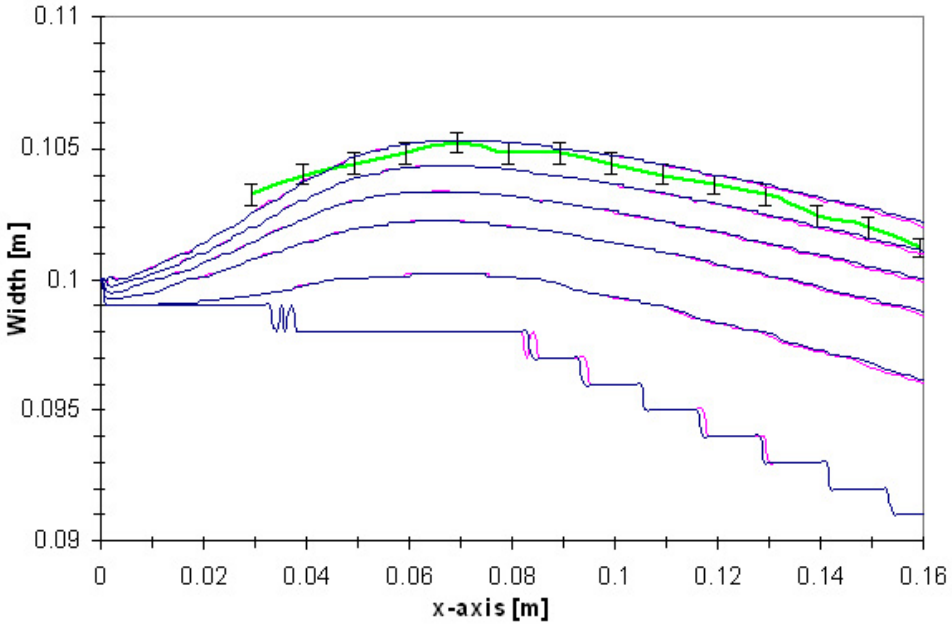

Figure G.6: Comparison of the jet widths (z-direction) along the x-axis, between experimental (green) and predicted values when $\Delta t = 0.8$ ms (pink) and $\Delta t = 5$ ms (blue). Predicted curves of a same color (pink or blue) successively represent from the bottom to the top the water isosurfaces $\alpha_{water} = 1$, $\alpha_{water} = 0.99$, $\alpha_{water} = 0.9$, $\alpha_{water} = 0.8$, $\alpha_{water} = 0.7$, and $\alpha_{water} = 0.6$.

- Effects of the Backflow Volume Fraction of Air at the Outlet Boundary Condition:

The effects of the backflow volume fraction of air at the outlet boundary condition are here examined. Comparison is made between experimental and predicted values when two backflow volume fractions of air $\alpha_{backflow} = 0$ and $\alpha_{backflow} = 0.12$ are studied (see Section G.1.1 "Setting the Boundary Conditions:"). The baseline case, $\alpha_{backflow} = 0$, is plotted in pink, while the second simulated case with a non-zero backflow, $\alpha_{backflow} = 0.12$, is plotted in blue. The mesh and time steps are the same in both cases (i.e., the ones selected for the baseline case). Figures G.7 and G.8 show the evolution along the x-axis of the jet thickness and width, respectively, when the effects of the backflow volume fraction of air at the outlet boundary condition are studied. Results for the jet thickness show excellent agreement between the baseline case $\alpha_{backflow} = 0$ and the case with $\alpha_{backflow} = 0.12$ (see Figure G.7).

Figure G.8 leads to the same conclusions as Figure G.7. Therefore, the backflow volume fraction of air at the outlet boundary condition appears to have no influence on the predicted solution. The simplest backflow volume fraction condition can be used, i.e. $\alpha_{backflow} = 0$.

- Effect of Turbulence Model:

The effects of the turbulence models are now examined. Comparison is made between experimental and predicted values when the flow is assumed to be either laminar or turbulent according to the *standard* k-ϵ model (see Section G.1.1 "Setting the Turbulence Model:"). The baseline case, laminar flow, is plotted in pink, while the second simulated case with the *standard* k-ϵ model is plotted in blue. The other parameters of these two cases are the same as those of the baseline case given in Section G.1.1. Figures G.9 and G.10 show the evolution along the x-axis of the jet thickness and width, respectively, when the effects of the *standard* k-ϵ model are

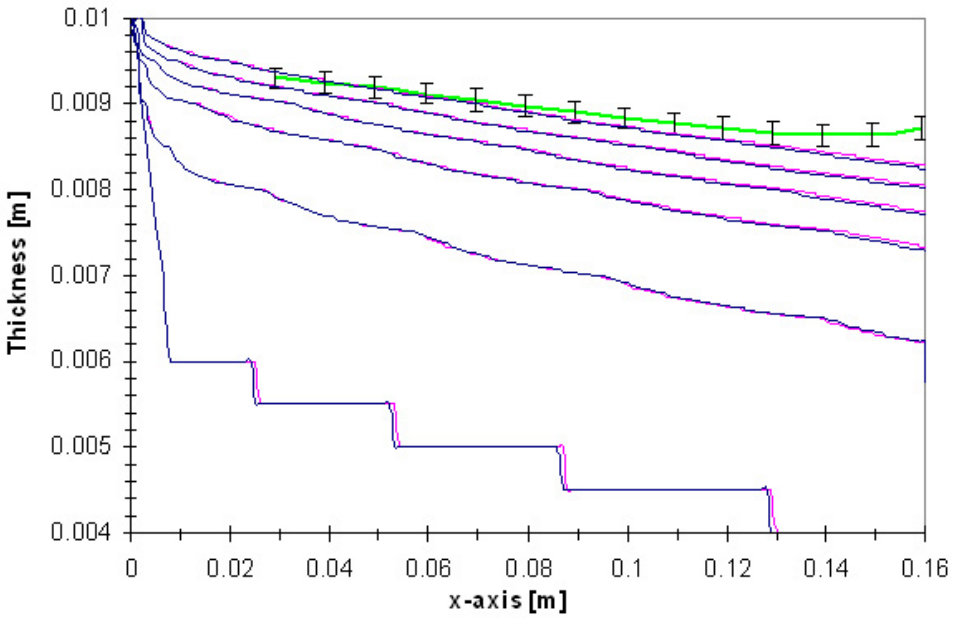

Figure G.7: Comparison of the jet thicknesses (y-direction) along the x-axis, between experimental (green) and predicted values when the backflow volume fraction of air at the outlet boundary condition is 0 (pink) or 0.12 (blue). Predicted curves of a same color (pink or blue) successively represent from the bottom to the top the water isosurfaces $\alpha_{water} = 1$, $\alpha_{water} = 0.99$, $\alpha_{water} = 0.9$, $\alpha_{water} = 0.8$, $\alpha_{water} = 0.7$, and $\alpha_{water} = 0.6$.

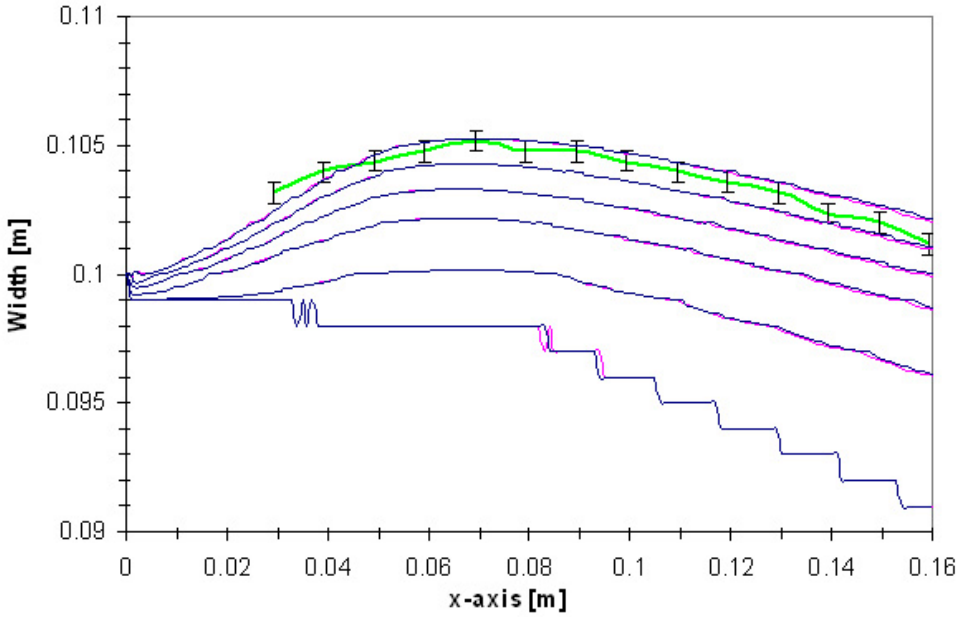

Figure G.8: Comparison of the jet widths (z-direction) along the x-axis, between experimental (green) and predicted values when the backflow volume fraction of air at the outlet boundary condition is 0 (pink) or 0.12 (blue). Predicted curves of a same color (pink or blue) successively represent from the bottom to the top the water isosurfaces $\alpha_{water} = 1$, $\alpha_{water} = 0.99$, $\alpha_{water} = 0.9$, $\alpha_{water} = 0.8$, $\alpha_{water} = 0.7$, and $\alpha_{water} = 0.6$.

studied. Results for the jet thickness show small difference between the laminar baseline case and the turbulent case with the *standard k-ϵ* model; the *standard k-ϵ* model predicts a slightly thicker jet. The errors in the water isosurface $\alpha_{water} = 1$ increases due to the propagation of the error at each discontinuity. There is better agreement for 0 cm < x < 14 cm between the experimental and the *standard k-ϵ* case values rather than between the experimental and the baseline case values, for a water isosurface $\alpha_{water} = 0.6$.

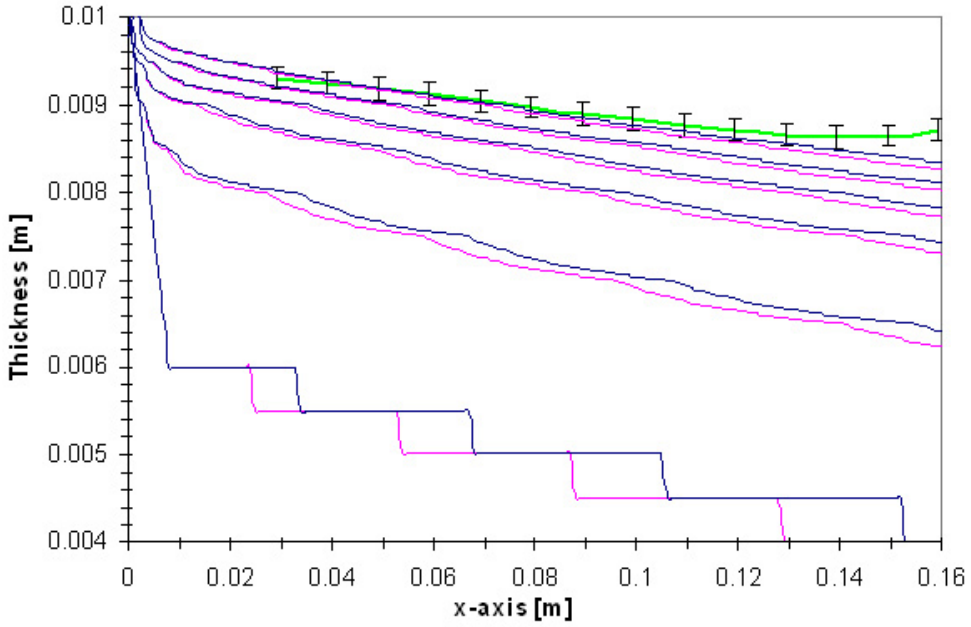

Figure G.9: Comparison of the jet thicknesses (y-direction) along the x-axis, between experimental (green) and predicted values when the flow is assumed to be laminar (pink) and turbulent according to the *standard k-ϵ* model (blue). Predicted curves of a same color (pink or blue) successively represent from the bottom to the top the water isosurfaces $\alpha_{water} = 1$, $\alpha_{water} = 0.99$, $\alpha_{water} = 0.9$, $\alpha_{water} = 0.8$, $\alpha_{water} = 0.7$, and $\alpha_{water} = 0.6$.

Figure G.10 shows the jet width along the x-axis. For the baseline case, water isosurfaces are plotted for $0.6 \leq \alpha_{water} \leq 1$, while for the *standard k-ϵ* case, water isosurfaces are plotted for $0.5 \leq \alpha_{water} \leq 1$. The jet appears to be denser in the case of the turbulent flow. For a given value of α_{water}, the water isosurface predicted for the baseline case appears to match that for the *standard k-ϵ* model with a 10%

lower value of α_{water} (e.g., 0.5 versus 0.6 or 0.8 versus 0.9. The curve pattern of the the *standard* k-ϵ case is slightly different from that of the baseline case. In the case of the the *standard* k-ϵ model, the jet width expands immediately after the nozzle exit, instead of shrinking as is the case for the baseline laminar case. There is better agreement for 0 cm $<$ x $<$ 13 cm between the experimental values and the *standard* k-ϵ water isosurface $\alpha_{water} = 0.5$ rather than between the experimental values and the baseline water isosurface $\alpha_{water} = 0.6$.

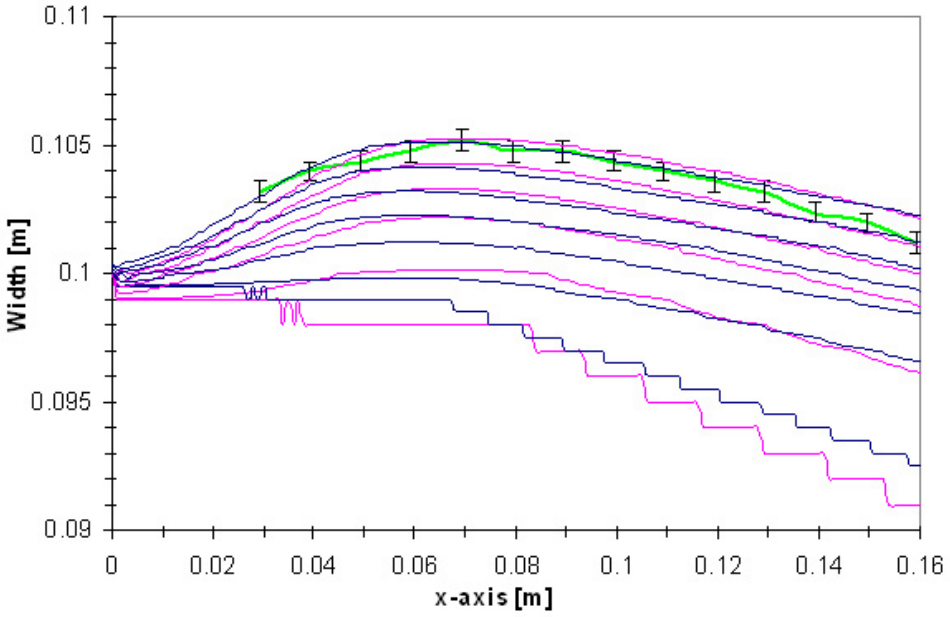

Figure G.10: Comparison of the jet widths (z-direction) along the x-axis, between experimental (green) and predicted values when the flow is assumed to be laminar (pink) and turbulent according to the *standard* k-ϵ (blue). Predicted curves of a same color (pink or blue) successively represent from the bottom to the top the water isosurfaces $\alpha_{water} = 1$, $\alpha_{water} = 0.99$, $\alpha_{water} = 0.9$, $\alpha_{water} = 0.8$, $\alpha_{water} = 0.7$, and $\alpha_{water} = 0.6$. The highest blue curve represents the water isosurfaces $\alpha_{water} = 0.5$.

Successful computations of turbulent flows require some consideration during the mesh generation. Since turbulence (through the spatially-varying effective viscosity) plays a dominant role in the transport of mean momentum and other parameters, turbulence quantities in complex turbulent flows must be properly resolved if high accuracy is required. Due to the strong interaction of the mean flow and turbulence,

the numerical results for turbulent flows tend to be more susceptible to grid dependency than those for laminar flows. The near-wall mesh can be checked by displaying or plotting the values of y^+ and $y^\star$ which are both available in the postprocessing panels. The log-law, which is valid for equilibrium boundary layers and fully developed flows, provides upper and lower bounds on the acceptable distance between the cell centroid and the wall for wall-adjacent cells. The distance is usually measured in the wall unit, y^+ ($\equiv \rho u_t y/\mu$), or $y^\star$. Note that y^+ and $y^\star$ have comparable values when the first cell is placed in the log-layer ($FLUENT$®, 2004). In the k-ϵ case, y^+ is around 24. This is close enough to 30 to support the use of *standard wall functions*, and too far from 1 to allow the use of *enhanced wall functions*. In other words, the mesh selected for this study is a little too fine for *standard wall functions* but too coarse for *enhanced wall functions*.

The *realizable* k-ϵ model is a relatively recent development and differs from the *standard* k-ϵ model in two important ways: (a) the *realizable* k-ϵ model contains a new formulation for the turbulent viscosity; and (b) a new transport equation for the dissipation rate ϵ has been derived from an exact equation for the transport of the mean-square vorticity fluctuation. This model has been extensively validated for a wide range of flows, including rotating homogeneous shear flows, free flows including jets and mixing layers, channel and boundary layer flows, and separated flows. For all these cases, the performance of the model has been found to be substantially better than that of the standard k-ϵ model. Especially noteworthy is the fact that the realizable k-ϵ model resolves the round-jet anomaly; i.e., it predicts the spreading rate for axisymmetric jets as well as that for planar jets ($FLUENT$®, 2004).

Comparison is made between experimental and predicted values when the flow is assumed to be turbulent according to the *standard* and the *realizable* k-ϵ models (see Section G.1.1 "Setting the Turbulence Model:"). The simulated case with the *realizable* k-ϵ model is plotted in pink, while the case simulated with the *standard*

k-ϵ model is plotted in blue. The other parameters for these two cases are the same as those of the baseline case given in Section G.1.1. Figures G.11 and G.12 show the evolution along the x-axis of the jet thickness and width, respectively, when the effects of the *realizable* k-ϵ model are studied. Results for the jet thickness show very good agreement between the results obtained using the *realizable* and the *standard* k-ϵ models; the *standard* k-ϵ model predicts a slightly thicker jet (see Figure G.11).

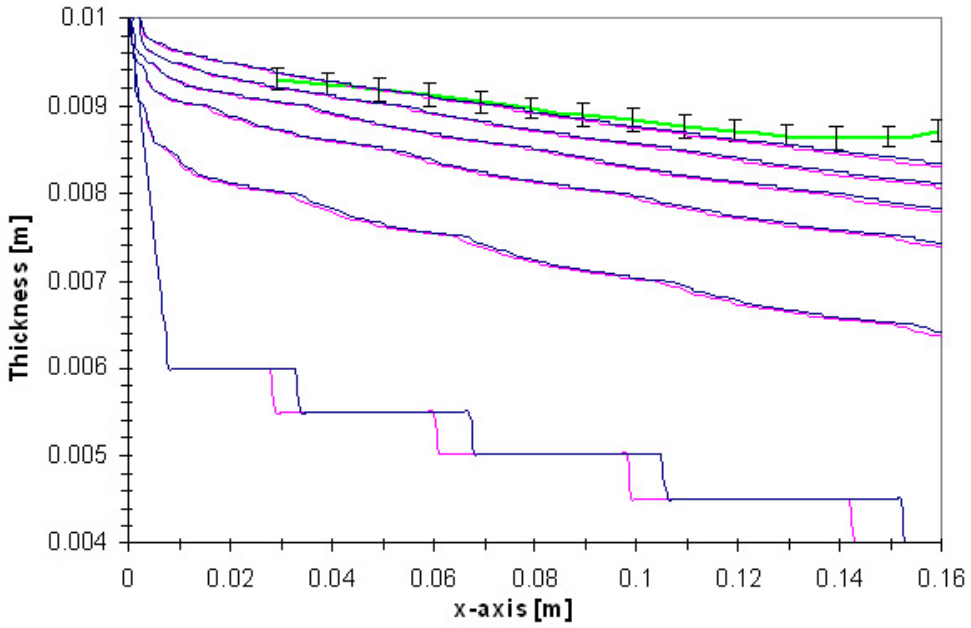

Figure G.11: Comparison of the jet thicknesses (y-direction) along the x-axis, between experimental (green) and predicted values when the flow is assumed to be turbulent according to the *standard* (blue) and the *realizable* (pink) k-ϵ models. Predicted curves of a same color (pink or blue) successively represent from the bottom to the top the water isosurfaces $\alpha_{water} = 1$, $\alpha_{water} = 0.99$, $\alpha_{water} = 0.9$, $\alpha_{water} = 0.8$, $\alpha_{water} = 0.7$, and $\alpha_{water} = 0.6$.

Figure G.12 shows the jet width along the x-axis. For the *realizable* k-ϵ case, water isosurfaces are plotted for $0.6 \leq \alpha_{water} \leq 1$, while for the *standard* k-ϵ case, water isosurfaces are plotted for $0.5 \leq \alpha_{water} \leq 1$. The *realizable* k-ϵ seems to predict the spreading rate better than the *standard* k-ϵ model, especially for 11 cm $<$ x $<$ 16. The water isosurface $\alpha_{water} = 0.6$ of the *realizable* k-ϵ case show better agreement with the experimental values than the water isosurface $\alpha_{water} = 0.5$ of the *standard*

k-ϵ case. Therefore, the *realizable* k-ϵ model is chosen over the *standard* k-ϵ model.

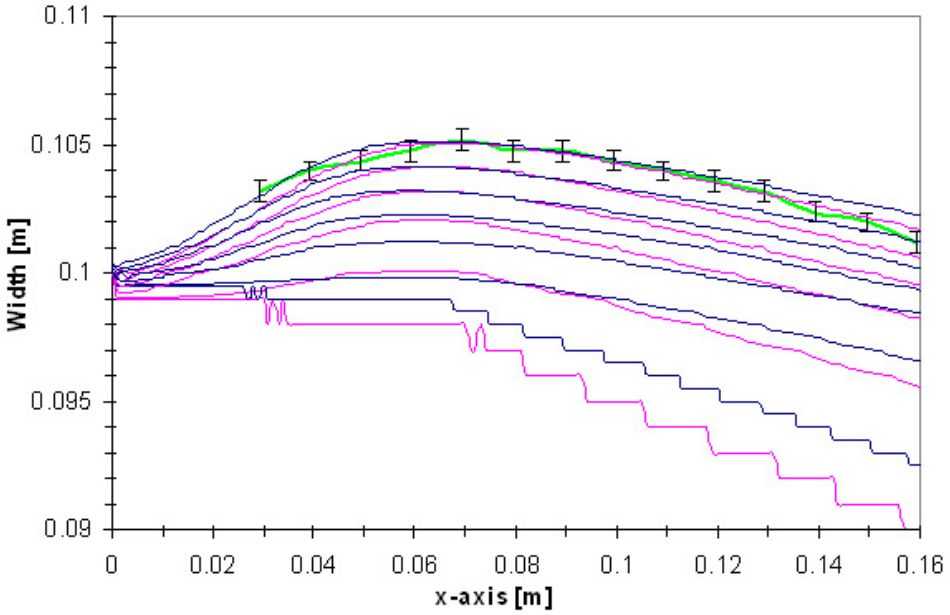

Figure G.12: Comparison of the jet widths (z-direction) along the x-axis, between experimental (green) and predicted values when the flow is assumed to be turbulent according to the *standard* (blue) and the *realizable* (pink) k-ϵ models. Predicted curves of a same color (pink or blue) successively represent from the bottom to the top the water isosurfaces $\alpha_{water} = 1$, $\alpha_{water} = 0.99$, $\alpha_{water} = 0.9$, $\alpha_{water} = 0.8$, $\alpha_{water} = 0.7$, and $\alpha_{water} = 0.6$. The highest blue curve represents the water isosurfaces $\alpha_{water} = 0.5$.

The effects of the *LES* turbulence model are now investigated. Comparison is made between experimental and predicted values when the flow is assumed to be either laminar or turbulent following the *LES* model (see Section G.1.1 "Setting the Turbulence Model:"). The laminar baseline case is plotted in pink, while the second case simulated with the *LES* model is plotted in blue. Figures G.13 and G.14 show the evolution along the x-axis of the jet thickness and width, respectively when the effects of the *LES* turbulence model are studied. Results for the jet thickness show good agreement between the laminar baseline case and the turbulent case with the *LES* model; the errors on the water isosurface $\alpha_{water} = 1$ remain constant at each discontinuity.

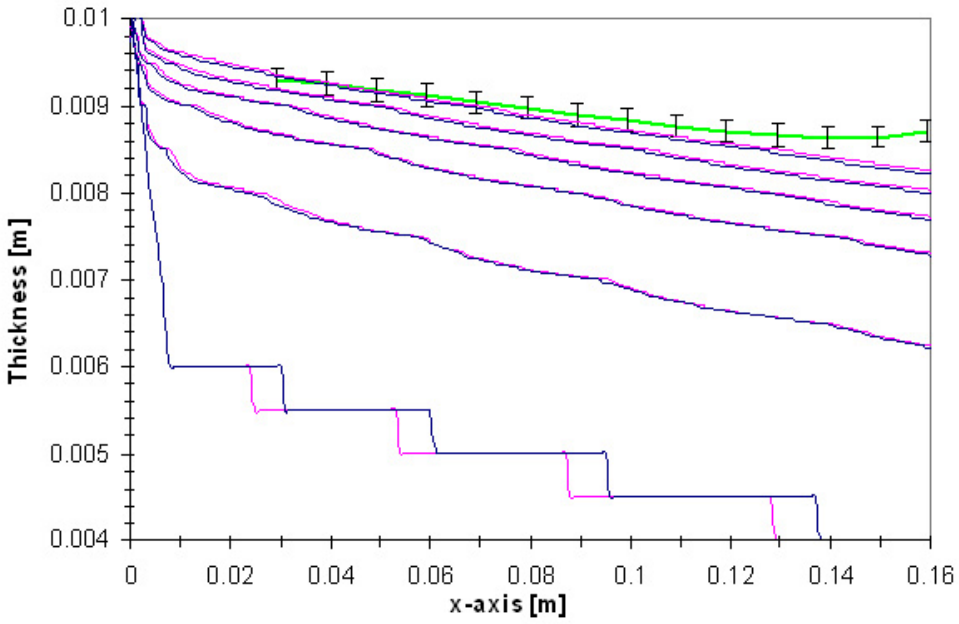

Figure G.13: Comparison of the jet thicknesses (y-direction) along the x-axis, between experimental (green) and predicted values when the flow is assumed to be laminar (pink) and turbulent according to the *LES* model (blue). Predicted curves of a same color (pink or blue) successively represent from the bottom to the top the water isosurfaces $\alpha_{water} = 1$, $\alpha_{water} = 0.99$, $\alpha_{water} = 0.9$, $\alpha_{water} = 0.8$, $\alpha_{water} = 0.7$, and $\alpha_{water} = 0.6$.

Results on the jet width show good agreement between the experimental values and the turbulent case with the *LES* model for a water isosurface $\alpha_{water} = 0.6$; differences are within the experimental errors bars (see Figure G.14). For water isosurfaces $0.6 \leq \alpha_{water} \leq 0.9$, the *LES* model predicts that the jet contracts more in the z-direction than the baseline case, thereby further accelerating the jet at the outlet.

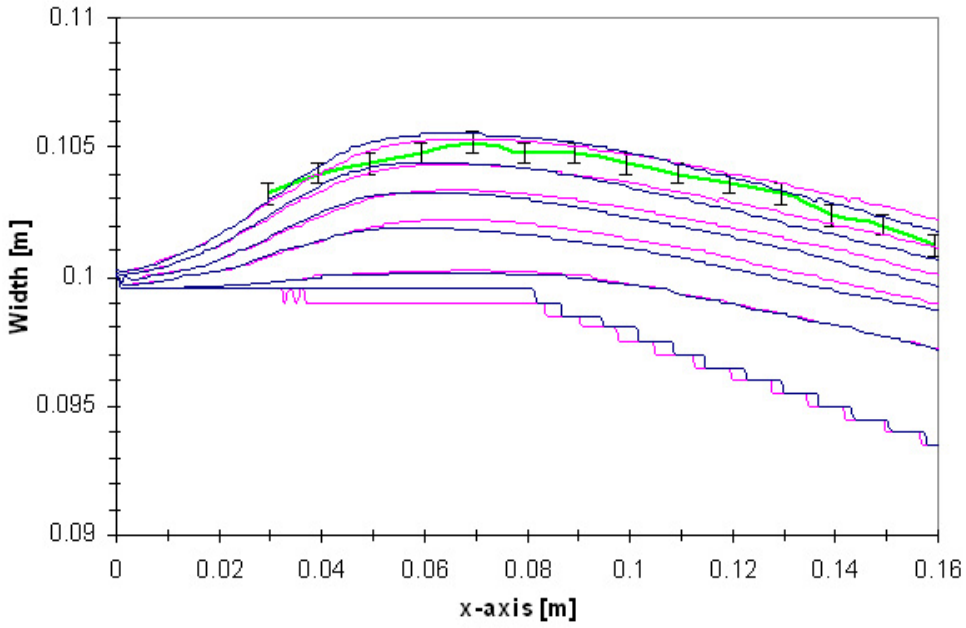

Figure G.14: Comparison of the jet widths (z-direction) along the x-axis, between experimental (green) and predicted values when the flow is assumed to be laminar (pink) and turbulent according to the *LES* model (blue). Predicted curves of a same color (pink or blue) successively represent from the bottom to the top the water isosurfaces $\alpha_{water} = 1$, $\alpha_{water} = 0.99$, $\alpha_{water} = 0.9$, $\alpha_{water} = 0.8$, $\alpha_{water} = 0.7$, and $\alpha_{water} = 0.6$.

For the *LES* implementation in $FLUENT^{®}$, the wall boundary conditions have been implemented using a *law-of-the-wall* approach. This means that there are no computational restrictions on the near-wall mesh spacing.

The use of the *LES* turbulence model does not significantly improve the sharpness of the free surface in the y-direction; however, in the z-direction, use of the *LES* model allows good prediction of the free surface. Nevertheless, the *realizable* k-ϵ model gives

the most satisfactory predictions among the turbulence models.

- Effects of Controls and Discretization:

The effects of the discretization scheme for the volume fraction equations are now examined. Comparison is made between experimental and predicted values when the discretization scheme for the volume fraction equations is either *first-* or *second-order* (see Section G.1.1 "Selecting the Solver, the Controls and Discretization Parameters:"). The *first-order* baseline case is plotted in pink, while the *second-order* case is plotted in blue. The other parameters of these two cases are the same as those of the baseline case given in Section G.1.1. Figures G.15 and G.16 show the evolution along the x-axis of the jet thickness and width, respectively, when the effects of the discretization scheme for the volume fraction equations are studied with the *second-order*. Results for the jet thickness show large differences between the *first-order* baseline case and the *second-order* case. For the water isosurface $\alpha_{water} = 0.6$, the *second-order* shows good agreement with the *first-order* and the experimental values, whereas the other water isosurfaces show that the *second-order* predict a thicker jet than the *first-order* (see Figure G.15).

Results for the jet width show poor agreement between the the *first-order* and the *second-order* schemes (see Figure G.16). The experimental values corresponds to the water isosurface $\alpha_{water} = 0.6$ of the first-order case, while they follow the water isosurface $\alpha_{water} = 0.9$ of the second-order case for $4 \leq x \leq 15$; differences are within the experimental errors bars for both predicted cases. The *second-order* scheme predicts a wider and denser jet with stronger slopes $0 \leq x \leq 7$. Using the *second-order* scheme slightly increases the cost of the solution in terms of calculation time but provides a sharper prediction of the free surface.

The effects of the discretization scheme for the volume fraction equations are studied with the *HRIC* scheme. Comparison is made between experimental and predicted values when the discretization scheme for the volume fraction equations is

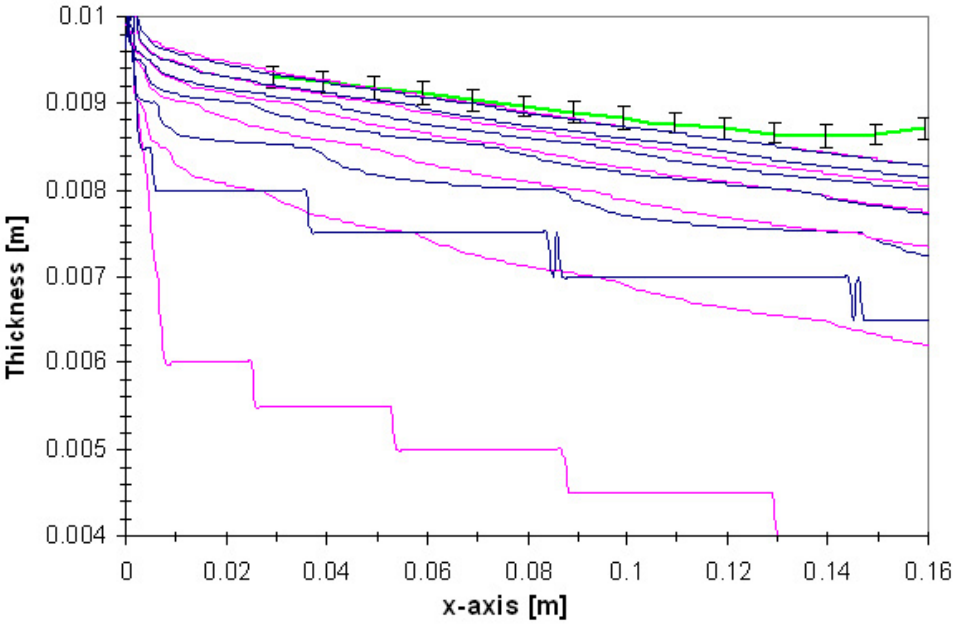

Figure G.15: Comparison of the jet thicknesses (y-direction) along the x-axis, between experimental (green) and predicted values when the volume fraction equations use the *first-order* discretization scheme (pink) and the *second-order* discretization scheme (blue). Predicted curves of a same color (pink or blue) successively represent from the bottom to the top the water isosurfaces $\alpha_{water} = 1$, $\alpha_{water} = 0.99$, $\alpha_{water} = 0.9$, $\alpha_{water} = 0.8$, $\alpha_{water} = 0.7$, and $\alpha_{water} = 0.6$.

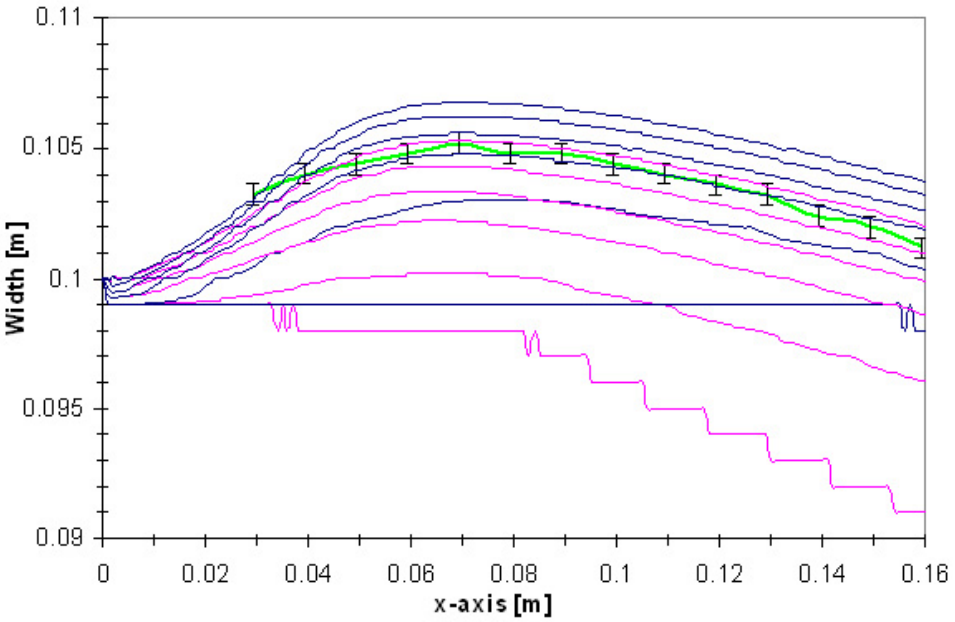

Figure G.16: Comparison of the jet widths (z-direction) along the x-axis, between experimental (green) and predicted values when the volume fraction equations use the *first-order* discretization scheme (pink) and the *second-order* discretization scheme (blue). Predicted curves of a same color (pink or blue)successively represent from the bottom to the top the water isosurfaces $\alpha_{water} = 1$, $\alpha_{water} = 0.99$, $\alpha_{water} = 0.9$, $\alpha_{water} = 0.8$, $\alpha_{water} = 0.7$, and $\alpha_{water} = 0.6$.

either *first-order* or *HRIC* (see Section G.1.1 "Selecting the Solver, the Controls and Discretization Parameters:"). The *first-order* baseline case is plotted in pink, and the *HRIC* case is plotted in blue. The other parameters of these two cases are the same as those of the baseline case given in Section G.1.1. Figures G.17 and G.18 show the evolution along the x-axis of the jet thickness and width, respectively, when the effects of the discretization scheme for the volume fraction equations are studied with the *HRIC*. Like the *second-order* case, results for the jet thickness show large differences between the *first-order* baseline case and the *HRIC* case (see Figure G.17). For the water isosurface $\alpha_{water} = 0.6$, the *HRIC* model show good agreement with the *first-order* scheme and the experimental values. The jet density predicted by the *HRIC* model is even higher than that predicted using the *second-order* model.

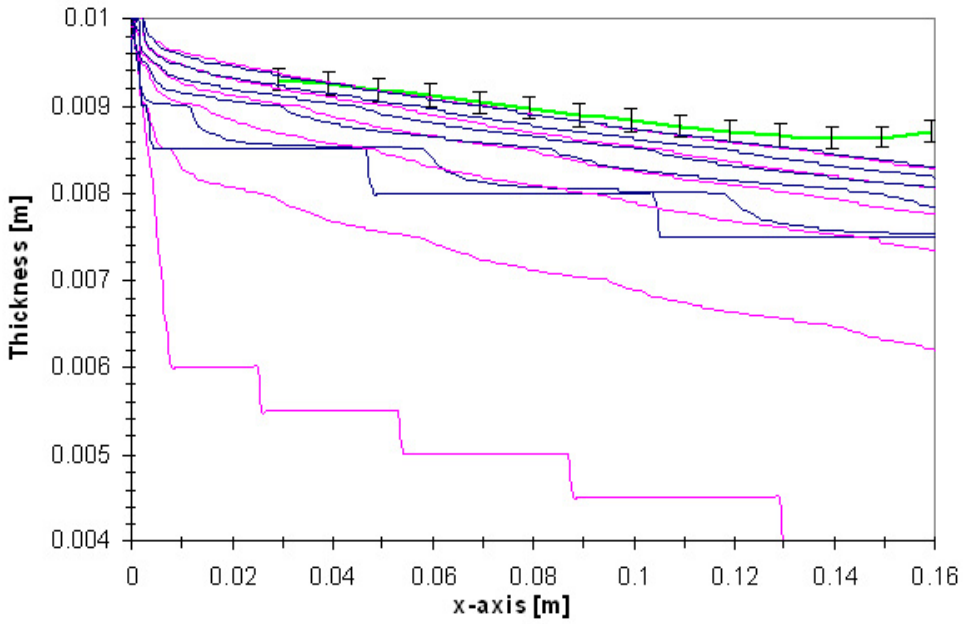

Figure G.17: Comparison of the jet thicknesses (y-direction) along the x-axis, between experimental (green) and predicted values when the volume fraction equations use the *first-order* discretization scheme (pink) and the *HRIC* discretization scheme (blue). Predicted curves of a same color (pink or blue) successively represent from the bottom to the top the water isosurfaces $\alpha_{water} = 1$, $\alpha_{water} = 0.99$, $\alpha_{water} = 0.9$, $\alpha_{water} = 0.8$, $\alpha_{water} = 0.7$, and $\alpha_{water} = 0.6$.

Like the *second-order* case, results on the jet width show poor agreement between

the the *first-order* and the *HRIC* schemes (see Figure G.18). The experimental values corresponds to the water isosurface $\alpha_{water} = 0.6$ of the *first-order* case, while they follow a water isosurface of the *HRIC* case $0.9 \leq \alpha_{water} \leq 0.99$ for $4 \leq \text{x} \leq 15$. The *HRIC* scheme predicts an even wider and denser jet than the *second-order* scheme.

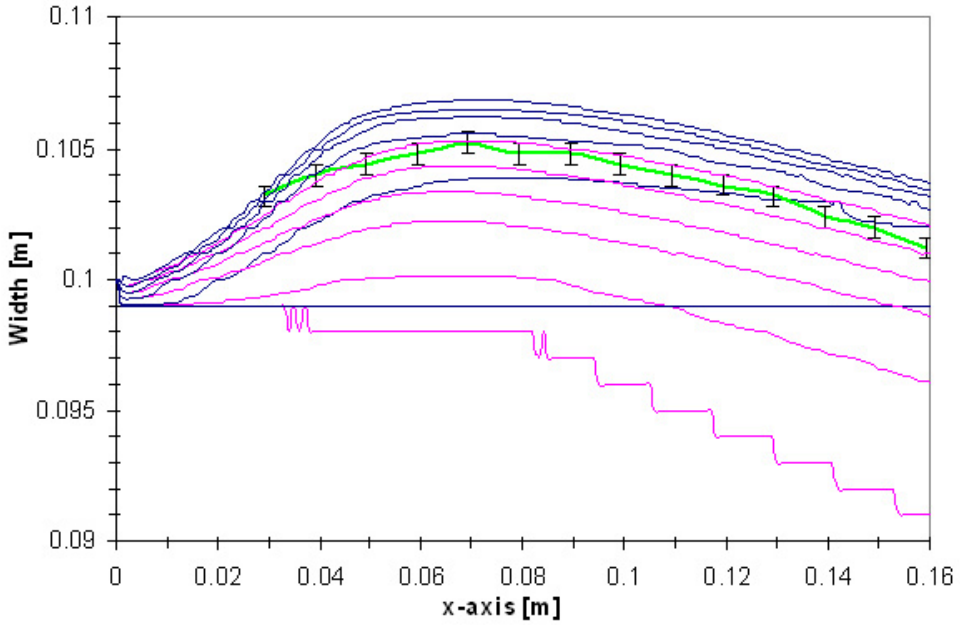

Figure G.18: Comparison of the jet widths (z-direction) along the x-axis, between experimental (green) and predicted values when the volume fraction equations use the *first-order* discretization scheme (pink) and the *HRIC* discretization scheme (blue). Predicted curves of a same color (pink or blue) successively represent from the bottom to the top the water isosurfaces $\alpha_{water} = 1$, $\alpha_{water} = 0.99$, $\alpha_{water} = 0.9$, $\alpha_{water} = 0.8$, $\alpha_{water} = 0.7$, and $\alpha_{water} = 0.6$.

The effects of the discretization scheme for the volume fraction equations are also studied usiing the *QUICK* scheme. The results show this model to be unstable and convergence cannot be established. The curve pattern obtained with the *second-order* better fits the experimental data than that obtained with the *HRIC* model. Thus, the *second-order* discretization scheme is chosen for the volume fraction equations.

The effects of the pressure-velocity coupling scheme are analyzed. Comparison is made between experimental and predicted results when two pressure-velocity coupling schemes, namely, *PISO* and *SIMPLE*, are studied (see Section G.1.1 "Selecting

the Solver, the Controls and Discretization Parameters:"). The baseline case using the *PISO* pressure-velocity coupling scheme is plotted in pink, while the second case simulated with the *SIMPLE* scheme is plotted in blue. The other parameters for these two cases are the same as those of the baseline case given in Section G.1.1. Figures G.19 and G.20 show the evolution along the x-axis of the jet thickness and width, respectively, when the effects of the pressure-velocity coupling scheme are studied. Referring to Figure G.19, results for the jet thickness show excellent agreement between the baseline case (*PISO*) and the second simulated case (*SIMPLE*).

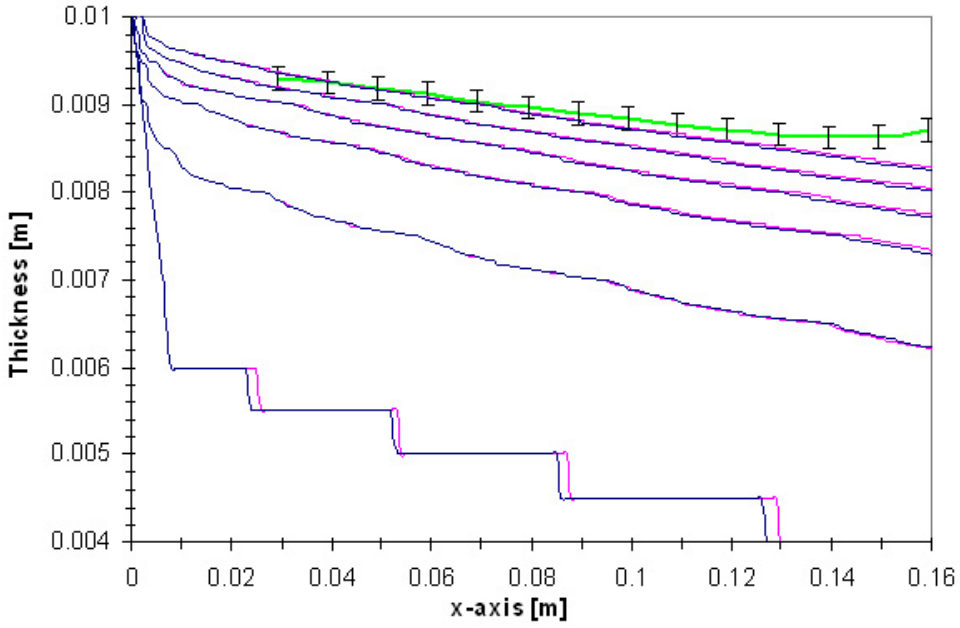

Figure G.19: Comparison of the jet thicknesses (y-direction) along the x-axis, between experimental (green) and predicted values when the pressure-velocity coupling uses the *PISO* scheme (pink) and the *SIMPLE* scheme (blue). Predicted curves of a same color (pink or blue) successively represent from the bottom to the top the water isosurfaces $\alpha_{water} = 1$, $\alpha_{water} = 0.99$, $\alpha_{water} = 0.9$, $\alpha_{water} = 0.8$, $\alpha_{water} = 0.7$, and $\alpha_{water} = 0.6$.

Figure G.20 has the same characteristics as Figure G.19. While the pressure-velocity coupling scheme has no influence on the sharpness of predicted free surface, using *PISO* allows for increased values on all under-relaxation factors without a loss of solution stability, thereby decreasing the calculation time.

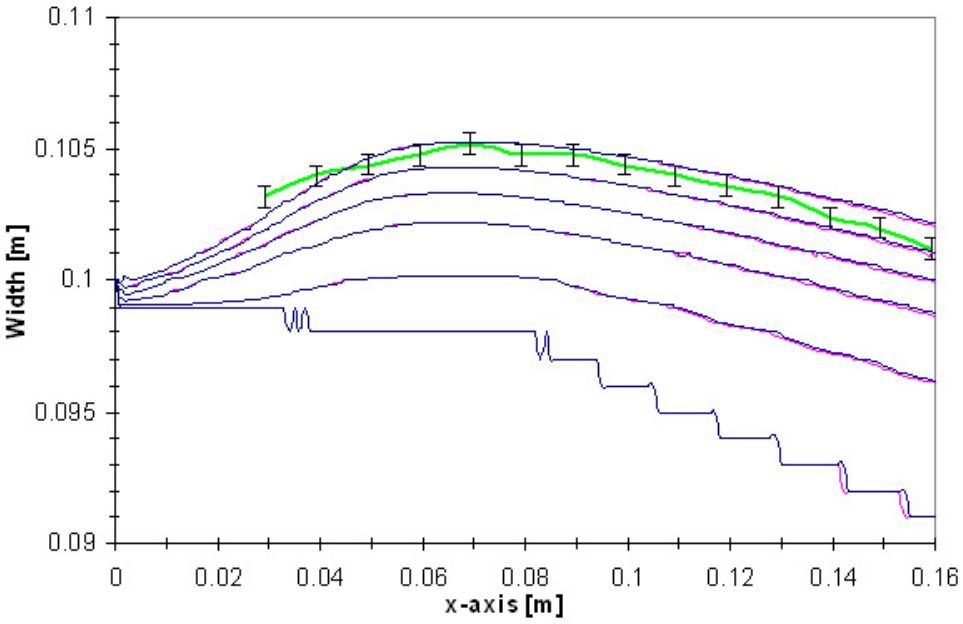

Figure G.20: Comparison of the jet widths (z-direction) along the x-axis, between experimental (green) and predicted values when the pressure-velocity coupling uses the *PISO* scheme (pink) and the *SIMPLE* scheme (blue). Predicted curves of a same color (pink or blue) successively represent from the bottom to the top the water isosurfaces $\alpha_{water} = 1$, $\alpha_{water} = 0.99$, $\alpha_{water} = 0.9$, $\alpha_{water} = 0.8$, $\alpha_{water} = 0.7$, and $\alpha_{water} = 0.6$.

G.2 Two-Phase Jet Modeling

G.2.1 Selection of the Two-Phase Model Options in $FLUENT^{®}$

$FLUENT^{®}$ has also been used to predict the characteristics and the behavior of a two-phase (gas-liquid) vertical jet. The main difficulty here is to select an appropriate multiphase model to simulate this complex problem since two flow types are involved: (a) free surface flow; and (b) two-phase bubbly flow with discrete gaseous bubbles in a continuous liquid.

- Selecting the Multiphase Model:

The *Lagrangian discrete phase* model in $FLUENT^{®}$ follows the Euler-Lagrange approach. The fluid phase is treated as a continuum by solving the time-averaged Navier-Stokes equations, while the dispersed phase is solved by tracking a large number of particles, i.e bubbles or droplets, through the calculated flow field. The dispersed phase can exchange momentum, mass, and energy with the fluid phase. A fundamental assumption made in this model is that the dispersed second phase occupies a low volume fraction, even though high mass loading is acceptable. The particle or droplet trajectories are computed individually at specified intervals during the fluid phase calculation. This makes the model appropriate for modeling of spray dryers, coal and liquid fuel combustion, and some particle-laden flows, but inappropriate for modeling of liquid-liquid mixtures, fluidized beds, or any application where the volume fraction of the second phase is not negligible ($FLUENT^{®}$, 2004).

In the Euler-Euler approach, the different phases are treated mathematically as interpenetrating continua. Since the volume of a phase cannot be occupied by the other phases, the concept of phasic volume fraction is introduced. These volume fractions are assumed to be continuous functions of space and time and their sum is equal to one. Conservation equations for each phase are derived to obtain a set of equations, which have similar structure for all phases. These equations are closed

by providing constitutive relations that are obtained from empirical information. In $FLUENT$®, three different Euler-Euler multiphase models are available: the *Volume Of Fluid* (*VOF*) model, the *Mixture* model, and the *Eulerian* model ($FLUENT$®, 2004).

The *VOF* model is described in Section G.1.1 "Selecting the Multiphase Model". The *mixture* model is designed for two or more phases (fluid or particulate); similar to the *Eulerian* model, the phases are treated as interpenetrating continua. The *mixture* model solves the mixture momentum equation and prescribes relative velocities to describe the dispersed phases. Applications of the *mixture* model include particle-laden flows with low loading, bubbly flows, sedimentation, and cyclone separators. The *mixture* model can also be used without relative velocities for the dispersed phases to model homogeneous multiphase flow.

The *Eulerian* model is the most complex of the multiphase models in $FLUENT$®. It solves a set of momentum and continuity equations for each phase. Coupling is achieved through the pressure and interphase exchange coefficients. The manner in which this coupling is handled depends upon the type of phases involved; granular (fluid-solid) flows are handled differently than non-granular (fluid-fluid) flows. Momentum exchange between the phases is also dependent upon the type of mixture being modeled. $FLUENT$®'s user-defined functions allow you to customize the calculation of the momentum exchange. Applications of the *Eulerian* multiphase model include bubble columns, risers, particle suspension, and fluidized beds .

$FLUENT$®'s documentation recommends use of the *VOF* model for stratified/free-surface flows. For bubbly, droplet, and particle-laden flows in which the dispersed-phase volume fractions are less than or equal to 10%, the *discrete phase* model is recommended. For bubbly, droplet, and particle-laden flows in which the phases mix and/or dispersed-phase volume fractions exceed 10%, either the *mixture* model or the *Eulerian* model can be used.

Particulate loading β has a major impact on phase interactions. The particulate loading is defined as the mass density ratio of the dispersed phase d (air) to that of the carrier phase c (water):

$$\beta = \frac{\alpha_d \cdot \rho_d}{\alpha_c \cdot \rho_c} \tag{G.4}$$

In this investigation, the maximum homogeneous void fraction at the nozzle exit is 10% and 15% for the planar and circular jets, respectively; the "corresponding particle" loadings are 1.36×10^{-4} and 2.17×10^{-4}, respectively. For very low loading, the coupling between the phases is one-way; i.e., the fluid carrier (water) influences the particles (air bubbles) via drag and turbulence, but the particles have no influence on the fluid carrier. The *discrete phase*, *mixture*, and *Eulerian* models can all handle this type of problem adequately. Since the *Eulerian* model requires excessive computing time, either the *discrete phase* or *mixture* model is recommended. It is important to keep in mind that the use of the discrete phase model is limited to low volume fractions. Also, the *discrete phase* model is the only multiphase model that allows the user to specify the particle distribution. The *mixture* and *Eulerian* models also assume that the two-phase flow domain has fixed boundaries (walls). In this investigation, the contours of the free jet are directly calculated by the code, but not set as walls. Therefore, the *discrete phase* and *VOF* models are the only multiphase models that allow for the simulation of free two-phase jets.

- Setting the Calculation Procedures for the *Discrete Phase*:

Since the $FLUENT$® model used in this investigation includes prediction of a coupled two-phase flow, one must begin with a fully converged continuous-phase flow field. The injections of discrete particles are then created and the coupled calculation is set up. For each *discrete-phase* iteration, $FLUENT$® computes the particle/droplet trajectories and updates the interphase exchange of momentum, heat, and mass in each control volume. These interphase exchange terms then impact the continuous phase

when the continuous phase iteration is performed. During the coupled calculation, $FLUENT^{®}$ performs the *discrete phase* iteration at specified intervals during the continuous-phase calculation. The coupled calculation continues until the continuous phase flow field no longer changes with further calculations (i.e., all convergence criteria are satisfied). When convergence is reached, the *discrete phase* trajectories no longer change, since changes in the discrete phase trajectories would result in changes in the continuous phase flow field. The steps for setting up the coupled calculation are as follows ($FLUENT^{®}$, 2004):

1. The continuous phase flow field is solved.

2. In the *discrete phase* model panel, the *interaction with continuous phase* option is enabled. In addition, another option exists which allows the user to control the numerical treatment of the source terms and how they are applied to the continuous phase equations. *Update DPM sources every flow iteration* is turned on when doing unsteady simulations; at every DPM Iteration, the particle source terms are recalculated.

3. The frequency with which the particle trajectory calculations are introduced in the *number of continuous phase iterations per DPM iteration* field is set. In this investigation, this parameter is set to 5, i.e. a *discrete phase* iteration is performed every fifth continuous phase iteration. If the *number of continuous phase iterations per DPM iteration* is less than the number of iterations required to converge the continuous phase between time steps, then sub-iterations are done. Here, particles are tracked to their new positions during a time step and DPM sources are updated; particles are then returned to their original state at the beginning of the time step. At the end of the time step, particles are advanced to their new positions based on the continuous-phase solution. If the *number of continuous phase iterations per DPM iteration* is larger than the

number of iterations specified to converge the continuous phase between time steps, the particles are advanced at the beginning of the time step to compute the particle source terms.

- Setting the Transient Treatment of Particles:

In the *discrete phase* model panel, the particles can be treated in an unsteady or a steady fashion. This option can be chosen independent of the settings for the solver. Since the *breakup* and *collision* models are important in this case, the *unsteady particle tracking* is switched on automatically. When *unsteady particle tracking* is enabled several new options appear. When solving unsteady equations for the continuous phase, one chooses for simplicity to *use fluid flow time step* to inject the particles ($FLUENT$®, 2004).

- Setting the Tracking Parameters for the *Discrete Phase* Model:

Two parameters are used to control the time integration of the particle trajectory equations: (a) the length scale or step length factor to set the time step for integration within each control volume; and (b) the maximum number of time steps to abort trajectory calculations when the particle never exits the flow domain. One simple rule of thumb to follow when setting the parameters above is that for the particles to advance through a domain consisting of N grid cells into the main flow direction, the step length factor times N should be approximately equal to the maximum number of time steps ($FLUENT$®, 2004). The maximum number of time steps keeps its default value of 500 time steps and, therefore, for approximately 220 cells into the main flow direction, the step length factor is set to 2.

- Setting the Physical Models for the *Discrete Phase* Model:

There are five drag laws for the particles that can be selected in the drag law drop-down list. The *dynamic* drag law is recommended only when one of the droplet breakup models is used in conjunction with unsteady tracking ($FLUENT$®, 2004).

Particles can damp or produce turbulent eddies. In $FLUENT^{®}$, the work done by the turbulent eddies on the particles is subtracted from the turbulent kinetic energy. To consider these effects in the chosen turbulence model, the *two-way turbulence coupling* option is turned on ($FLUENT^{®}$, 2004).

The *droplet breakup* option is turned on and the *wave* model is selected. The *wave* model is appropriate for high-speed injections ($We \geq 100$) ($FLUENT^{®}$, 2004). The default values of the *Wave* model are used: ($B0 = 0.61$ and $B1 = 1.73$).

The effect of *droplet collisions* is also allowed. There are no further inputs for this model.

The numerics tab gives control over the numerical schemes for particle tracking as well as solutions of heat and mass equations. Default selections are used in this investigation.

- Specifying the Initial Conditions and Particle Size Distributions:

The primary inputs that must be provided for the *discrete phase* calculations in $FLUENT^{®}$ are the initial conditions that define the starting positions, velocities, and other parameters for each particle stream. In this investigation, the type of injection is a group injection; it allows the user to define a range for one or more of the initial conditions (a range of initial positions). For group injections, the properties are set for the first point and the last point of the group. A range of values, ϕ_1 through ϕ_N, is defined for each initial condition ϕ by setting values for ϕ_1 and ϕ_N. $FLUENT^{®}$ assigns a value of ϕ to the i^{th} injection in the group using a linear variation between the first and last values. N is chosen to be 10. Four similar group injections are created at the nozzle inlet and linearly set every 5 mm with 0 mm $\leq y \leq$ 15 mm. Each stream injects inert particles of *Nitrogen*. *Discrete random walk model* as well as *random eddy life* options are selected in order to include the effect of turbulent velocity fluctuations on the particle trajectories. The list of the different initial conditions for the injection # 1 is provided in Table G.2. The injections # 2 through # 4 have the

same initial conditions, except for the Y-Position. Referring to the case presented in Table G.2, it corresponds to a jet with a liquid superficial velocity at the nozzle exit $j_{l,e} = 3$ m/s and an exit homogeneous void fraction $\alpha_e = 5\%$. The particle diameter at the nozzle inlet is set to 0.5 mm; using a higher value leads to errors with the *droplet collisions* model (see Section 5.2.2). For an exit homogeneous void fraction α_e = 5%, the mass flow rate of air at the nozzle inlet corresponds to 1.2125×10^{-5} kg/s; in this investigation, only a quarter of the nozzle is modeled and four injections are created within this volume. Therefore, the total mass flow rate of air for one injection equals 1.2125×10^{-5} kg/s divided by 16 (i.e., 1.2125×10^{-5} kg/s).

Table G.2: Detailed list of the injection # 1 and its characteristics

	First Point	Last Point
X-Position (m)	0.001	0.001
Y-Position (m)	0	0
Z-Position (m)	0.005	0.055
X-Velocity (m/s)	0	0
Y-Velocity (m/s)	0	0
Z-Velocity (m/s)	0	0
Diameter (m)	0.0005	0.0005
Flow rate (kg/s)	1.2125×10^{-5}	1.2125×10^{-5}
Start Time (s)	0	
Stop Time (s)	0	

- Setting Boundary Conditions for the *Discrete Phase*:

Five different boundary conditions are available for the *discrete phase* model ($FLUENT$®, 2004).

- The "reflect" boundary rebounds the particle off the boundary in question with a change in its momentum as defined by the coefficient of restitution.

- The "trap" boundary terminates the trajectory calculations and records the fate of the particle as "trapped".

- The “escape” boundary reports the particle as having “escaped” when it encounters the boundary in question. Trajectory calculations are terminated.

- The “wall-jet” boundary means that the direction and velocity of the droplet particles are given by the resulting momentum flux.

- The “interior” boundary means that the particles will pass through the internal boundary. This option is available only for internal boundary zones, such as a radiator or a porous jump.

The list of the different boundary conditions for the *discrete phase* model is provided in Table G.3. At the non-physical wall boundary “Outer-Wall”, the particles can escape the domain.

Table G.3: List of the different boundary conditions for the *discrete phase* model

Name	Type of boundary
Inlet (m)	“escape”
Air-Outlet (m)	“escape”
Water-Outlet (m)	“escape”
Wall-Nozzle (m/s)	“reflect”
Wall-Thick (m/s)	“reflect”
Outer-Wall (m/s)	“escape”

REFERENCES

Abbott, R. "The dynamic response of thick-liquid shielding in Z-IFE reactors". In *Proceedings of 21st IEEE/NPSS Symposium on Fusion Engineering SOFE 05*, Knoxville, Tenessee USA, September 2005. ORNL.

Aly, M. S. and Rashed, M. "Experimental investigation of an annular jet". *Journal of Wind Engineering and Industrial Aerodynamics*, **37**(2):155–166, 1991. ISSN 0167-6105.

Anderson, M., Oakley, J., Vigil, V., Rodriquez, S., and Bonazza, R. "Shock mitigation studies of solid foams for Z-Pinch chamber protection". In *Proceedings of 21st IEEE/NPSS Symposium on Fusion Engineering SOFE 05*, Knoxville, Tenessee USA, September 2005. ORL.

Anderson, M. et al. "Shock mitigation studies of solid foams for Z-Pinch chamber protection". Z-Pinch IFE program - Final report for FY05, University of Wisconsin, November 2006.

Armand, A. and Treschev, G. "Investigation of the resistance during movement of the steam-water mixtures in heated boiler pipe at high pressure". *Izvestia User. Teplo. Inst. AERE Lib/Trans*, **816**(4):1–5, 1947.

Azzopardi, B. and Hills, J. *Modelling and experimentation on two-phase flow*, chapter One dimensionnel models for pressure drop, Empirical correlations for void fractions and frictional pressure drop and pressure drop and other effects in fittings, pages 157–220. Springer-Verlag Wien New York, 2003.

Baird, M. and Davidson, J. "Annular jets". *Chemical Engineering Science*, **17**: 467–480, 1962.

Bankoff, S. "Variable density single-fluid model for two-phase flow with particular reference to steam-water flow". *American Society of Mechanical Engineers – Transactions – Journal Heat Transfer Series C*, **82**(4):265–272, 1960.

Beggs, H. D. and Brill, J. R. "Study of two-phase flow in inclined pipes.". *JPT, Journal of Petroleum Technology*, **25**:607–617, 1973.

Bertola, V. *Modelling and experimentation on two-phase flow*, chapter Two-phase flow measurement techniques, pages 281–324. Springer-Verlag Wien New York, 2003.

Binnie, A. and Squire, H. "Liquid jets of annular cross section". *Engineer*, **171** (4448):236–238, 1941.

Bouré, J. *Two-phase flows and heat transfer with application to nuclear reactor design problems*, chapter 9 - Constitutive equations for two-phase flows. Von Karman Inst. Book, Hemisphere, New York, 1978.

Bouré, J. and Reocreux, M. "General equations of two-phase flows - applications to critical flows and to non-steady flows". In *4th All-Union Heat Transfer Conference, Minsk*, 1972.

Boussinesq, J. "Essais sur la théorie des ondes liquides périodiques". *Comptes Rendus des séances de l'Académie des Sciences*, **68**:905–908, 1869.

Chace, G. "Exploding wires". In *Conference on Exploding Wire Phenomenon*, **volume 1**, pages 373–, Boston, MA, United States, 1959. Plenum Press, New York, United States.

Chace, G. "Exploding wires". In *Conference on Exploding Wire Phenomenon*, **volume 2**, pages 321–, Boston, MA, United States, 1962. Plenum Press, New York, United States.

Chace, G. "Exploding wires". In *Conference on Exploding Wire Phenomenon*, **volume 3**, pages 409–, Boston, MA, United States, 1964. Plenum Press, New York, United States.

Chace, G. "Exploding wires". In *Conference on Exploding Wire Phenomenon*, **volume 4**, pages 348–, Boston, MA, United States, 1968. Plenum Press, New York, NY, United States.

Charmin, C., Shatoff, H., and Gallix, R. "Shock mitigation". Z-Pinch IFE program - Final report for FY05, General Atomics, November 2006.

Chisholm, D. *Two-phase flow in pipelines and heat exchangers*. George Godwin, London and New York, 1983.

Collier, J. and Thome, J. *Convective Boiling and Condensation*. Oxford University Press, 3rd edition, 1994.

Couvert, A., Roustan, M., and Chatellier, P. "Two-phase hydrodynamic study of a rectangular air-lift loop reactor with an internal baffle". *Chemical Engineering Science*, **54**(21):5245–5252, 1999. ISSN 0009-2509.

Debonel, C. "Gas dynamics in a thick-liquid protected Z-IFE power plant". Z-Pinch IFE program - Final report for FY05, University of California, Berkeley, November 2006.

Delhaye, J. *Two-phase flows and heat transfer in the power and process industries*, chapter Basic equations for two-phase flow modelling. Hemisphere, New York, 1990.

Dix, G. *Vapor void fraction for forced convection with subcooled boiling at low flow rates*. PhD thesis, University of California-Berkeley, Berkeley, CA, 1971.

Duda, J. and Vrentas, J. "Fluid mechanics of laminar liquid jets". *Chemical Engineering Science*, **22**(6):855–869, 1967.

Dumbleton, J. "Effect of gravity on the shape of water bells". *Journal of Applied Physics*, **40**(10):3950–4, 1969.

Durbin, S. G. *Dynamics and free-surface geometry of turbulent liquid sheets*. PhD thesis, Mechanical Engineering, Georgia Institute of Technology, 2005. URL `http://etd.gatech.edu/theses/available/etd-03032005-095517/`. (Last checked: July 30, 2007).

Elperin, T., Klecorin, N., and Krylov, A. "Nondissipative shock waves in two-phase flows". *Physica D: Nonlinear Phenomena*, **74**(3-4):372–385, 1994. ISSN 0167-2789.

Esser, P. D. and Abdel-Khalik, S. I. "Dynamics of vertical annular liquid jets". *Journal of Fluids Engineering, Transactions of the ASME*, **106**(1):45–51, 1984. ISSN 0098-2202.

FLUENT®. "FLUENT 6.2 Documentation". 2004. URL `http://www.fluent.com/`. (Last checked: July 30, 2007).

Fukano, T. and Kariyasaki, A. "Characteristics of gas-liquid two-phase flow in a capillary tube". *Nucl. Eng. Des. (Netherlands)*, **141**(1-2):59–68, June 1993. ISSN 0029-5493.

Grimshaw, R. H. and Khusnutdinova, K. "The effect of bubbles on internal waves". *Journal of Physical Oceanography*, **34**(2):477–489, 2004. ISSN 0022-3670.

Hasan, M., Mitsutake, Y., and Monde, M. "Shape of an annular liquid jet". *Journal of Fluids Engineering, Transactions of the ASME*, **119**(3):591–596, 1997. ISSN 0098-2202.

Hewitt, G. *Measurement of two phase flow parameters*. Academic Press, 1978.

Hibiki, T., Goda, H., Kim, S., Ishii, M., and Uhle, J. "Experimental study on interfacial area transport of a vertical downward bubbly flow". *Experiments in Fluids*, **35**(1):100–111, 2003. ISSN 0723-4864.

Hoffman, M. A., Takahashi, R. K., and Monson, R. D. "Annular liquid jet experiments". *Journal of Fluids Engineering, Transactions of the ASME*, **102**(3):344–349, 1980. ISSN 0098-2202.

Hovingh, J. "First wall response to energy deposition in conceptual laser-fusion reactors". *Journal of Nuclear Materials*, **63**:158–162, 1976.

Hovingh, J. "Stability of a flowing circular annular liquid curtain". Internal Memo SS&A-77-108, Lawrence Livermore Laboratory, August 1977.

Hughmark, G. "Holdup in gas-liquid flow". *Chemical Engineering Progress*, **58** (4):62–65, 1962.

Incropera, F. and DeWitt, D. *Fundamentals of Heat and Mass Transfer*. John Wiley & Sons, 5th edition, 2002.

Iordansky, S. "Equations of motion of liquid containing gas bubbles". *Zh. Prikl. Mekh Tekh. Fiz.*, **3**:102–110, 1960.

Ishii, M. *Thermo-fluid dynamic theory of two-phase flow*, chapter IX and X. Eyrolles, Paris, Scientific and Medical Publication of France, NY, 1975.

Ishii, M. "One dimensional drift-flux model and constitutive equations for relative motion between phases in various two-phase flow regimes.". Technical Report ANL-77-47, Argonne National Laboratories, October 1977.

Ishii, M. *Multiphase Science and Technology*, **volume 5**, chapter 1 - Two fluid model for two-phase flow. Hemisphere, New York, 1990.

Ishii, M. and Zuber, N. "Drag coefficient and relative velocity in bubbly, droplet or particulate flows.". *AIChE Journal*, **25**(5):843–855, 1979. ISSN 0001-1541.

Kedrinskii, V. "The Iordansky-Kogarko-van Wijngaarden model: shock and rarefaction wave interactions in bubbly media". *Appl. Sci. Res. (Netherlands)*, **58**(1-4): 115–30, 1997-1998. ISSN 0003-6994.

Kendall, J. "Experiments on annular liquid jet instability and on the formation of liquid shells". *Physics of Fluids*, **29**(7):2086–94, July 1986. ISSN 0031-9171.

Kern, B. "Experimental investigation of the hydrodynamics of a plunging two-phase plane jet". Master's thesis, Mechanical Engineering, Georgia Institute of Technology, 2007. URL `http://etd.gatech.edu/theses/available/etd-06212006-153659/`. (Last checked: July 30, 2007).

Khismatullin, D. and Akhatov, I. "Sound-ultrasound interaction in bubbly fluids: Theory and possible applications". *Physics of Fluids*, **13**(12):3582–3598, 2001. ISSN 1070-6631.

Kocamustafaogullari, G. and Ishii, M. "Foundation of the interfacial area transport equation and its closure relations". *International Journal of Heat and Mass Transfer*, **38**(3):481–493, 1995. ISSN 0017-9310.

Kogarko, B. "A [possible] model of liquid cavitation". *Doklady Akademii Nauk SSSR*, **137**(6):1331–1333, April 1961.

Kolesnikov, P., Korotkov, V., and Nesvetailov, G. "The investigation of the volt-ampere characteristics of exploding wires". *Soviet Physics - Technical Physics*, **40**(7):1520–6, 1970. ISSN 0038-5662.

Lance, G. and Perry, R. "Water bells". *Proceedings of the Physical Society. Section B*, **66**:1067–1072, December 1953.

Lawrence, J. "Simple models for aspect of IFE shock mitigation". Z-Pinch IFE program - Final report for FY05, Sandia National Laboratories, November 2006.

Levy, S. "Steam slip – theoretical prediction from momentum model". *American Society of Mechanical Engineers – Transactions – Journal of Heat Transfer Series C*, **82**(2):113–124, 1960.

Li, X. and Shen, J. "Experiments on annular liquid jet breakup". In *Proceedings of the Engineering Technology Conference on Energy*, **volume A**, pages 1–10, Houston, TX, United States, 2001. American Society of Mechanical Engineers, New York, NY 10016-5990, United States.

Lisitsyn, I. V., Muraki, T., and Akiyama, H. "Wire induced flashover as a source of shock waves for destruction of solid materials". *Japanese Journal of Applied Physics, Part 1: Regular Papers & Short Notes & Review Papers*, **36**(3A): 1258–1263, 1997.

LLNL. "Inertial Fusion Energy: Opportunity for Fusion Innovation", January 1997. URL `http://www.llnl.gov/nif/library/ife.pdf`. (Last checked: July 30, 2007).

Lockhart, R. and Martinelli, R. "Proposed correlation of data for isothermal two-phase, two-component flow in pipes". *Chemical Engineering Progress*, **45**(1): 39–45, 1949.

Majumdar, B. and Shambaugh, R. L. "Velocity and temperature fields of annular jets". *Industrial & Engineering Chemistry Research*, **30**(6):1300–1306, 1991. ISSN 0888-5885.

Majumder, S. K., Kundu, G., and Mukherjee, D. "Bubble size distribution and gas-liquid interfacial area in a modified downflow bubble column". *Chemical Engineering Journal*, **122**(1-2):1–10, 2006. ISSN 1385-8947.

Maniscalco, J. A., Meier, W. R., and Monsler, M. J. "Conceptual design of a laser fusion power plant". *AIChE Symposium Series*, **75**(191):174–181, 1979. ISSN 0065-8812.

Mankowski, J. and Kristiansen, M. "Review of short pulse generator technology". *IEEE Transactions on Plasma Science*, **28**(1):102–108, 2000. ISSN 0093-3813.

Marchaterre, J. and Hoglund, B. "Correlation for two-phase flow". *Nucleonics*, **8**:142, 1968.

Mcgrath, J. "Scaling laws for underwater exploding wires". *J. Acoustic Soc. Amer.*, **50**(3 pt 2):1030–3, 1971.

Meekunnasombat, P., Oakley, J., Anderson, M., and Bonazza, R. "Experimental investigation of a shock-accelerated liquid layer with imaging and pressure measurement". *Fusion Sci. Technol. (USA)*, **44**(2):351–5, 2003. ISSN 1536-1055.

Meekunnasombat, P., Oakley, J., Anderson, M., and Bonazza, R. "Protection of IFE first wall surfaces from impulsive loading by multiple liquid layers". *Fusion Science and Technology*, **47**(4):1170–4, May 2005. ISSN 1536-1055.

Nakoriakov, V. E., Nakoryakov, V. E., and Pokusaev, B. G. *Wave Propagation in Gas-Liquid Media*. CRC Press, 2nd sub edition, June 1993.

Nuttall, W. J. *Nuclear renaissance : technologies and policies for the future of nuclear power*. Taylor&Francis, 2005.

Olson, C. et al. "Development path for Z-pinch IFE". *Fusion Sci. Technol. (USA)*, **47**(3):633–40, April 2005a. ISSN 1536-1055.

Olson, C. et al. "Z-Pinch IFE program". Final report for FY04, Sandia National Laboratories, April 2005b.

Olson, C. et al. "Z-Pinch IFE program". Final report for FY05, Sandia National Laboratories, November 2006.

Olson, C. et al. "Z-Pinch IFE program". Final report for FY06, Sandia National Laboratories, January 2007.

Olson, C. *Landolt-Boernstein Handbook on Energy Technologies*, **volume VIII** of *Fusion Technologies (Edited by K. Heinloth)*, chapter Z-Pinch Inertial Fusion Energy. Springer-Verlag (Berlin-Heidelberg) in Press, 2004.

Otsuka, M., Hida, E., and Itoh, S. "Development of high-pressure container using wire explosion". In *American Society of Mechanical Engineers, Pressure Vessels and Piping Division (Publication) PVP*, **volume 485**, pages 133–138, San Diego, CA, United States, 2004. American Society of Mechanical Engineers, New York, NY 10016-5990, United States.

Peterson, P. "VHEX facility to study shock mitigation with liquid jets". Z-Pinch IFE program - Final report for FY05, University of California, Berkeley, November 2006.

Peterson, P. F. "Inertial fusion energy: A tutorial on the technology and economics", September 1998. URL `http://www.nuc.berkeley.edu/thyd/icf/IFE.html`. (Last checked: July 30, 2007).

Piper, T. "Dynamic gamma attenuation density measurements". Ancr-1160, Aerojet Nuclear Company, 1974.

Premoli, A., Di Francesco, D., and Prina, A. "Adimensional correlation for evaluating two- phase mixture density, (una correlazione adminensionale per la determinazione della densita di miscele bifasiche)". *Termotecnica (Milan)*, **25**(1): 17–26, 1971.

Prosperetti, A. and Kim, D. "Pressure waves in bubbly liquids at small gas volume fractions". In *American Society of Mechanical Engineers, Fluids Engineering Division (Publication) FED*, **volume 72**, pages 19–27, Chicago, IL, USA, 1988. Publ by American Soc of Mechanical Engineers (ASME), New York, NY, USA.

Ramos, J. "Annular liquid jets and other axisymmetric free-surface flows at high Reynolds numbers". *Applied Mathematical Modelling*, **22**(6):423–452, 1998. ISSN 0307-904X.

Rayleigh. "Pressure due to collapse of bubbles". *Philosophical Magazine*, **34**: 94–98, August 1917.

Ripoche, J. "Générateur de flashes fonctionnant par explosion de fils métalliques". *Journal de Physique et le Radium (Physique Appliquée)*, **22**(2):48–52, 1961.

Rockett, P. D. and Bach, D. R. "Holographic interferometry of a high-energy-density exploding lithium wire plasma". *Journal of Applied Physics*, **50**(4):2670–2674, 1979. ISSN 0021-8979.

Rodriguez, S. et al. "Z-IFE power plant shock mitigation experiments, modeling philosophy, and code assessment". Z-Pinch IFE program - Final report for FY05, Sandia National Laboratories, November 2006.

Shoji, M. "A study of laminar free liquid-film flow". *Journal of the Faculty of Engineering, University of Tokyo*, **Series A**(9):22–3, 1971. ISSN 0563-7945.

Shoji, M., Ueno, I., Yamazaki, M., and Wakamatsu, K. "Pressure generation by rapid heating of a metal wire in water". *Nippon Kikai Gakkai Ronbunshu, B Hen/Transactions of the Japan Society of Mechanical Engineers, Part B*, **62**(598): 2331–2337, 1996. ISSN 0387-5016.

Sivakumar, D. and Raghunandan, B. "Study on converging thin annular jets". *Journal of Fluids Engineering, Transactions of the ASME*, **119**(4):923–928, 1997. ISSN 0098-2202.

Smith, S. "Void fractions in two-phase flow: a correlation based upon an equal velocity head model". *Proceedings of the Institution of Mechanical Engineers*, **184** (36):647–57, 1969-1970. ISSN 0020-3483.

Stacey, W.M., J. *Fusion: An introduction to the physics and technology of magnetic confinement fusion*. Wiley, 1984.

Stahl, P. and von Rohr, P. R. "On the accuracy of void fraction measurements by single-beam gamma-densitometry for gas-liquid two-phase flows in pipes". *Experimental Thermal and Fluid Science*, **28**(6):533–544, 2004. ISSN 0894-1777.

Sun, X., Vasavada, S., Choi, S., Kim, S., Ishii, M., and Beus, S. "Interfacial structure in an air-water planar bubble jet". *Experiments in Fluids*, **38**(4):426–439, 2005. ISSN 0723-4864.

Taylor, G. "The dynamics of thin sheets of fluid. i. water bells". *Proceedings of the Royal Society of London, Series A (Mathematical and Physical Sciences)*, **253**: 289–295, December 1959.

Thom, J. "Prediction of pressure drop during forced circulation boiling of water". *International Journal of Heat and Mass Transfer*, **7**(7):709–724, July 1964.

Todreas, N. and Kazimi, M. *Nuclear Systems I.* Hemisphere Press, 1990.

Tuck, E. "Annular water jets". *IMA Journal of Applied Mathematics*, **29**(1):45–58, 1982.

Van Wijngaarden, L. "On equations of motion for mixtures of liquid and gas bubbles". *Journal of Fluid Mechanics*, **33**(Part 3):465–474, 1968.

Vigil, V. and Rodriguez, S. "Foamed liquid and cellular metal shock attenuation analysis for Z-IFE". In *Proceedings of 21st IEEE/NPSS Symposium on Fusion Engineering SOFE 05*, Knoxville, Tenessee USA, September 2005. ORNL.

Vijayan, T. and Rohatgi, V. K. "Characteristics of exploding-wire plasmas". *IEEE Transactions on Plasma Science*, **PS-13**(4):197–201, 1985. ISSN 0093-3813.

Wallis, G. *One dimensional two-phase flow.* McGraw-Hill, 1969.

Whalley, P. *Boiling, condensation and gas-liquid flow.* Oxford University Press, 1987.

Wikipedia. "Inertial Confinement Fusion", December 2006. URL `http://en.wikipedia.org/wiki/Inertial_confinement_fusion`. (Last checked: July 30, 2007).

Wikipedia. "Fusion Power", February 2007. URL `http://en.wikipedia.org/wiki/Fusion_power`. (Last checked: July 30, 2007).

Zhang, C., Yang, J., and Chi, X. "Research on plasma explosion of metal wire in water". In *Conference Record of IEEE International Symposium on Electrical Insulation*, pages 257–260, Indianapolis, IN, United States, 2004. Institute of Electrical and Electronics Engineers Inc., Piscataway, NJ 08855-1331, United States.

Zhilin, A. A., Fedorov, A. V., and Fomin, V. M. "Wave propagation in a two-phase mixture of compressible mediums characterized by a difference in pressure and velocity between components". *Physics - Doklady*, **41**(9):430–434, 1996. ISSN 1063-7753.

Zivi, S. "Estimation of steady state steam void fraction by means of the principle of minimum entropy production". *Journal of Heat Transfer*, **86**:247–252, 1964.

Zuber, N. and Findlay, J. "Average volumetric concentration in two-phase flow systems". *Journal of Heat Transfer*, **87**:453–68, 1965.